

ELECTROSTATIC CHARGING OF SPACECRAFT IN GEOSYNCHRONOUS ORBIT

by

Andrew John Sims

A thesis submitted to the University of London
for the degree Doctor of Philosophy

Space Department,
Royal Aerospace Establishment,
Farnborough,
Hampshire.

Mullard Space Science Laboratory,
Department of Physics and Astronomy,
University College London.

ProQuest Number: 10610052

All rights reserved

INFORMATION TO ALL USERS

The quality of this reproduction is dependent upon the quality of the copy submitted.

In the unlikely event that the author did not send a complete manuscript and there are missing pages, these will be noted. Also, if material had to be removed, a note will indicate the deletion.



ProQuest 10610052

Published by ProQuest LLC (2017). Copyright of the Dissertation is held by the Author.

All rights reserved.

This work is protected against unauthorized copying under Title 17, United States Code
Microform Edition © ProQuest LLC.

ProQuest LLC.
789 East Eisenhower Parkway
P.O. Box 1346
Ann Arbor, MI 48106 – 1346

ABSTRACT

Any satellite whose orbit passes through the terrestrial magnetosphere will encounter several plasma regimes with widely differing temperatures, densities and compositions. The spacecraft itself will act as a plasma probe; each surface element changes its potential until no net current flows between it and the plasma. Differential charge build-up between adjacent surfaces (for example of different material or geometrical characteristics) can induce electrostatic discharges. The resulting current pulse, or RF interference gives rise to 'operational anomalies' (spurious switchings, telemetry drop-outs etc), or in extreme cases leads to permanent damage (eg short circuits in strings of solar cells).

This thesis is a study of the spacecraft charging phenomenon applicable to satellites in geosynchronous orbit. Results are derived from three sources. Firstly, Meteosat F2 (a meteorological satellite launched by ESA in July 1981) which carried an electron spectrometer to make direct measurements of the geosynchronous orbit electron environment, and in addition, suffered a series of operational anomalies and surface charging events. Secondly, an experimental test programme was undertaken using a monoenergetic electron beam to irradiate some common spacecraft surface materials, and thereby examine their electrostatic charging properties. Thirdly, numerical simulation codes were written and employed to model several different situations, ranging from the electron beam experiment to a full three-dimensional simulation of Meteosat F2.

Analysis of the electron beam irradiation data shows that the surface conductivity of some common insulating materials (Kapton and Teflon) plays a much greater role in the current balance equation than was thought previously. Furthermore, the process whereby bulk and surface conductivity is enhanced by large electric fields (deviations from pure Ohmic behaviour) is also shown to be a significant factor in the current balance equation. These results are of importance both to satellite surface design, and to high voltage insulating systems.

Spacecraft charging simulation codes must accurately model the detailed interaction between plasma energy spectra and the energy dependent material surface properties (such as secondary electron emission). The thesis demonstrates that it is vital to use real, measured spectra (for example from the Meteosat spectrometer) rather than simple Maxwellian plasma definitions, if spacecraft charging is to be modelled successfully. Also, the need for an improved database of reliable secondary electron yield measurements is demonstrated.

CONTENTS

1. Introduction.	8
1.1 Electrostatic Hazards and Spacecraft Charging.	8
1.2 Objectives.	10
2. Electrostatic Charging of Meteosat.	12
2.1 The Meteosat Spacecraft and Mission.	12
2.2 Previous Studies of Meteosat Electrostatic Charging.	14
2.2.1 ESD tests.	15
2.2.2 NASCAP Simulation of Meteosat F2 Charging.	16
2.3 The Meteosat F2 Electron Spectrometer.	16
3. Theory of Spacecraft Charging in Geostationary Orbit.	22
3.1 Current Collection by Plasma Probes.	22
3.1.1 A Review of Plasma Kinetic Theory.	22
3.1.2 Calculating Macroscopic Quantities.	23
3.1.3 The Maxwell-Boltzmann Distribution Function.	25
3.1.4 Debye Shielding.	27
3.1.5 Current Collection by a Spherical Probe.	29
3.1.6 Current Collection in a Maxwellian Plasma.	32
3.2 Surface Material Physics.	40
3.2.1 SEE Due to Electron Impact.	40
3.2.2 Backscattering of Incident Electrons.	48
3.2.3 Secondary Electron Emission due to Ion Impact.	51
3.2.4 Photoemission.	53
3.2.5 Bulk Conductivity of an Insulator.	54
3.2.6 Surface Conductivity.	57
3.3 The Plasma Environment at Geosynchronous Orbit.	65
3.3.1 Geostationary Orbit and the Magnetosphere.	65
3.3.2 Geomagnetic Storms and Substorms.	67
3.3.3 Geomagnetic Indices.	70
4. The Simulation Codes; EQUIPOT, BEAM and NASCAP.	76
4.1 EQUIPOT.	76
4.1.1 Voltage Stepping Algorithm.	76
4.1.2 A Three Parameter Model of SEE.	77
4.1.3 Material and Environment Definitions.	79
4.2 BEAM.	80
4.2.1 Theory of Electron Beam Charging.	80
4.2.2 Code Description.	82
4.3 NASCAP.	82
5. The Electron Environment at Geostationary Orbit.	86
5.1 Data Reduction.	86
5.2 Results.	87
5.2.1 Plasma Regions in GEO.	87
5.2.2 Average Plasmasheet Spectra.	90
5.2.3 Frequency and Intensity of Substorm Events.	90
5.2.4 Changes of Density and Pressure During Substorms.	93
5.3 Discussion.	93

6. Charging Properties of Satellite Surface Materials.	108
6.1 Experiment and Simulation Details.	108
6.1.1 Experimental Facility and Test Method.	108
6.1.2 Simulation Using the BEAM Code.	110
6.1.3 Simulation Using NASCAP Test-Tank.	110
6.2 Results.	111
6.2.1 Gold on a Teflon Insulator.	111
6.2.2 Gold on a Kapton Insulator.	114
6.3 Discussion.	115
7. Sensitivity Analysis With EQUIPOT.	127
7.1 Results of Varying Material Parameters.	127
7.1.1 Sensitivity to Conduction.	127
7.1.2 Sensitivity to Changes in Electron Backscatter.	128
7.1.3 Sensitivity to Changes in Electron SEE Current.	129
7.1.4 Sensitivity to Changes in Ion-Induced SEE.	130
7.2 Results of Varying the Environment.	130
7.2.1 A Threshold Temperature for Charging.	130
7.2.2 Charging Properties of Average Plasmasheet Spectra.	131
7.2.3 Charging in a Model Substorm Environment.	133
7.2.4 Charging in Measured Substorm Environments.	133
8. Barrier Charging Events on Meteosat F2.	142
8.1 Statistical Study.	142
8.2 NASCAP Simulation.	144
9. Conclusions.	156
Acknowledgements.	160
Appendix A.	161
References.	162

LIST OF FIGURES

2.1 Exploded view of Meteosat F2.	20
2.2 Meteosat F2 radiometer optics (schematic).	21
2.3 Electrostatic analyzer curved plates geometry.	21
3.1 Slanted cylinder used for flux calculation.	37
3.2 Accelerating probe; orbit limited collection.	37
3.3 Accelerating probe; sheath limited collection.	38
3.4 Accelerating probe collection region.	38
3.5 Retarding probe; orbit limited collection.	39
3.6 Retarding probe collection region.	39
3.7 SEE yield curve for Kapton.	59
3.8 SEE yield curve for Teflon.	59
3.9 SEE yield curve for clean Al.	60
3.10 SEE yield curve for Al ₂ O ₃ .	60
3.11 SEE yield curve for gold.	61
3.12 Backscatter yields at normal incidence for Al and Ag.	61
3.13 Ions incident on a solid surface.	62
3.14 SEE yield curve for protons incident on Al.	62
3.15 Solar spectrum and photoemission yields for Al and Au.	63
3.16 Modification of atomic potential well by an applied field	63
3.17 Electric field enhancement of bulk conductivity.	64
3.18 Schematic for surface conductivity calculation.	64
3.19 Schematic diagram of the magnetosphere.	73
3.20 Location of the plasmopause.	73
3.21 The process of reconnection.	74
3.22 Reconnection in the magnetosphere.	74
3.23 Field collapse during a substorm.	75
3.24 Grad-B guiding centre drift.	75
4.1 Emission limited behaviour of Kapton.	85
5.1 Meteosat spectrometer scatter plot (LT 00-01).	97
5.2 Meteosat spectrometer scatter plot (LT 03-04).	97
5.3 Meteosat spectrometer scatter plot (LT 12-13).	98
5.4 Meteosat spectrometer scatter plot (LT 20-21).	98
5.5 Percentage times spent in different plasma regimes.	99
5.6 Region I Probability Distribution.	99
5.7 Region II Probability Distribution.	100
5.8 Plasmasheet Probability Distribution.	100
5.9 Average plasmasheet spectra.	101
5.10 Electron spectrogram for 6th June 1982.	101
5.11 Local time distribution of substorm onsets.	102
5.12 Correlation of substorm onsets with a_p	103
5.13 Correlation of substorm onsets with Dst.	103
5.14 Correlation of substorm onsets with solar flare count.	104
5.15 Substorm onset rate versus solar flare count.	104
5.16 Substorm onset spectra on 6th June 1982.	105
5.17 Density enhancement distribution at substorm onset.	105
5.18 Pressure enhancement distribution at substorm onset.	106

5.19	Plasmasheet inner edge; quiet conditions.	106
5.20	Plasmasheet inner edge; disturbed conditions.	107
5.21	Plasmasheet inner edge; energy distribution.	107
6.1	Vacuum chamber and sample holder.	119
6.2	Vacuum chamber and instrumentation.	120
6.3	Sample holder and probe assembly.	120
6.4	NASCAP model of beam experiment.	121
6.5	Gold on Teflon; Surface potential versus beam energy.	121
6.6	Gold on Teflon; Dynamic NASCAP, BEAM and experiment.	122
6.7	Gold on Teflon; Static NASCAP, BEAM and experiment.	122
6.8	Gold on Kapton; Surface potential versus beam energy.	123
6.9	Gold on Kapton; charging time history.	123
6.10	NASCAP test-tank contour plot.	124
6.11	Fowler-Nordheim theory for field emission.	125
6.12	Field emission current from sample.	125
6.13	Sensitivity of surface potential to incident current.	126
7.1	Effect of changing sample thickness and temperature.	137
7.2	Effect of altering bulk conductivity.	137
7.3	Effect of atomic number on backscatter current.	138
7.4	Effect of emission coefficient and n on SEE current.	138
7.5	Effect of changing SEE current due to ion impact.	139
7.6	Threshold plasma temperature versus energy loss power.	139
7.7	Current-voltage curves for plasmasheet spectra.	140
7.8	Equilibrium potential contours for various substorms.	140
7.9	Electron spectra at peak of 11 substorms.	141
7.10	Analysis of 63 substorm spectra.	141
8.1	Meteosat F2 summary plot for 20th July 1982.	149
8.2	Local time distribution of Meteosat barrier events.	149
8.3	Solar aspect angle distribution.	150
8.4	K_p values at start of barrier events.	150
8.5	Plasmasheet mean energy versus a_p for barrier events.	151
8.6	NASCAP model of Meteosat F2 (+Y view).	151
8.7	NASCAP model of Meteosat F2 (+X view).	152
8.8	NASCAP model of Meteosat F2 (+Z view).	152
8.9	Barrier charging process.	153
8.10	NASCAP contour plot, $Y=3$ plane after 1 cycle.	153
8.11	NASCAP contour plot, $Z=15$ plane after 1 cycle.	154
8.12	NASCAP contour plot, $Y=2$ plane after 21 cycles.	154
8.13	NASCAP contour plot, $Z=15$ plane after 21 cycles.	155
8.14	Solar cell potentials predicted by NASCAP.	155

LIST OF TABLES

2.1 Physical characteristics of Meteosat F2.	19
2.2 SSJ/3 electron spectrometer geometry.	19
2.3 SSJ/3 electron spectrometer characteristics.	19
3.1 Debye lengths and Larmor radii.	36
3.2 Grad-B drift velocities at $6.6R_E$.	72
4.1 EQUIPOT material property list.	85
5.1 Correlation between substorm onsets and SSCs.	102
6.1 Specifications for the electron beam facility.	119
6.2 Upper crossover points of SEE yield for gold.	124
6.3 Measured and predicted insulator resistances.	126
6.4 Normal incidence SEE yields for gold.	126
7.1 Default material properties for Al and Kapton.	135
7.2 Modified SCATHA worst-case environment.	135
7.3 Equilibrium potentials for average plasmashet spectra.	136
7.4 Equilibrium potential for 11 substorm events.	136

1. INTRODUCTION

1.1 ELECTROSTATIC HAZARDS AND SPACECRAFT CHARGING

Since the launch of Sputnik 1 in October 1957, several thousand artificial Earth satellites have been placed in orbit with altitudes ranging from as little as 180km up to the geosynchronous earth orbit (GEO) height of 6.6 earth radii (R_E). Such orbits lie within the magnetosphere, a region surrounding the Earth where the geomagnetic field excludes the tenuous solar wind plasma, but controls the behaviour of several plasma populations contained within. Artificial Earth satellites within the magnetosphere are continuously immersed in a plasma, whose temperature and density vary by several orders of magnitude according to the orbital parameters, orbital position and degree of geomagnetic and solar activity.

In the context of this work, it is important to think of the satellite as a complex, floating plasma probe whose only reference potential is given by the bulk neutrality of the surrounding plasma population. The floating potential of each individual facet of the satellite surface (with respect to plasma "ground") is given by the solution of a current balance equation;

$$-I_e + I_i + I_{se} + I_b + I_{si} + I_{phot} + I_c = 0 \quad (1.1)$$

where I_e is the current due to incident electrons, I_i is the current due to incident ions, I_{se} is due to the emission of true secondary electrons from the surface, I_b is due to backscattered electrons from the surface, I_{si} is due to the emission of true secondary electrons from the surface as a result of ion impact, I_{phot} is the current due to photoemission, and I_c is the conduction current to or from other parts of the satellite. The second, third, fourth and fifth terms depend on the characteristics of the surface, as well as its potential and (apart from photoemission) the incident current. The first and second terms depend on the ambient plasma conditions, the potential of the facet, and of surrounding facets (ie the potential configuration around the satellite) whilst the final term depends on the potential as well as surface and bulk electrical conductivities. This equation reduces to its simplest form for the case of a uniform, shadowed, conducting, non-emissive sphere immersed in a stationary, Maxwellian plasma with Debye length much greater than the sphere radius. This has a solution (given in section 3.1.5) that the equilibrium potential (in Volts) is numerically equal to approximately - 2.5 times the plasma temperature (in eV). Since high altitude satellites (eg those in GEO) may encounter plasma populations with temperatures of several keV, it is apparent that surface potentials of several thousand volts negative with respect to plasma potential can develop in certain circumstances¹. For example, DeForest² has measured potentials of several

kilovolts negative on the geostationary satellite ATS-5 and Olsen et al³ have recorded a potential of -19kV on ATS-6 (also GEO) during eclipse.

High negative potentials need not pose a problem to a mission, given that the entire satellite achieves a uniform voltage; but this is rarely achieved since surfaces of different materials will not reach the same equilibrium potentials by virtue of equation 1.1, even if they are subjected to identical incident currents. It is this differential charging, with the associated possibility of discharge which poses a greater risk to satellites. Modes of discharge between differentially charged surfaces are grouped as "flashover" discharges between neighbouring surface elements, and "punchthrough" discharges between charged surfaces and an underlying conductor (eg through an insulating thermal blanket). A third class of discharge occurs when a charged surface element discharges to the space plasma (a "blowoff" discharge). In each case, the current pulse associated with the discharge may be injected onto the spacecraft ground plane, or into some electrical subsystem. Alternatively, the effects of the discharge may be propagated via inductive coupling (RF interference).

It is possible to define three areas where electrostatic charging represents a hazard to reliable spacecraft operation. Firstly (and most commonly), differential charging can lead to discharges which may result in anomalous operation, or in rare cases can lead to complete subsystem failure. Secondly, scientific spacecraft equipped with probes or spectrometers designed to sample the surrounding plasma must be maintained at plasma potential for successful measurements. Thirdly, satellites equipped with ion thrusters for propulsion must also incorporate a neutraliser system to compensate for the flow of positive charge away from the vehicle. The latter two cases are different from the first in that the necessity for preventing electrostatic charging is appreciated from the earliest stages of design, whilst in the first category, measures to prevent electrostatic charging and discharge (ESD)^{4,5} tend to be incorporated towards the end of the satellite design phase, if at all. If they have any impact on a mission, electrostatic discharges tend to cause anomalous behaviour ("anomalies", or "soft" errors), such as execution of phantom commands, interruptions of telemetry, and unauthorised subsystem shut-downs which do not generally result in catastrophic failure of subsystems or entire satellites but constitute a nuisance to the operators which may lead to loss of data. An important example of permanent damage due to ESD is the loss of strings of solar cells due to discharges through the cells themselves, or through cell insulation which leads to a reduction of available power. A data-base has been compiled of reported operational anomalies⁶ which lists the anomaly time, satellite, type (eg phantom command, telemetry loss) and anomaly diagnosis (eg ESD, single event upset, mission control error). This data base presently contains about 2000 anomaly reports. The European communications satellite ECS-1 suffered a sudden power loss⁷ after 15 months in orbit, followed by further losses at later stages

during the mission. This has been attributed to electrostatic charge build-up on either the solar cell cover glasses, or the layer of Kapton insulating the cells and interconnects from the carbon fibre array structure, leading to discharges.

Whilst many of the operational anomalies have been attributed to electrostatic discharge, they do not all necessarily result from high altitude surface charging. Two other types of spacecraft charging have been studied; Firstly, a mechanism known as "deep dielectric charging" has been proposed to account for some operational anomalies. In this process, energetic electrons (several hundred keV and higher) are able to penetrate distances of up to tens of microns into dielectric layers (eg cable insulation) near the surface of the satellite causing charge accumulation at a rate which exceeds the rate at which charge may be re-distributed within the insulator, leading ultimately to discharge events which apparently occur almost at random. Secondly, it has been assumed that levels of charging in the ionosphere are limited to a few volts relative to the plasma potential due to the presence of high density, cold plasma, but there is now some interest in low earth orbit charging of large space structures which create a sizeable wake region devoid of cold plasma. If the "rear" surface of the structure, adjacent to the wake is in shadow, and is subjected to high fluxes of auroral electrons, high levels of charging (up to 1 kV) may be observed.

1.2 OBJECTIVES

This thesis has four major objectives which are set out below;

- a. To quantify the spacecraft charging plasma environment in geosynchronous Earth orbit (GEO) in terms of the effect of local time (LT) and of the effect of solar and geomagnetic activity. Particular attention is paid to the conditions which prevail during magnetic storms and substorms when surface charging is most likely.
- b. To measure the surface properties of some common spacecraft materials using an electron beam, and to incorporate these results into new spacecraft charging simulation codes.
- c. To perform an extensive sensitivity analysis to investigate the influence of plasma characteristics and material surface properties on equilibrium potentials. The results of such an analysis may be used to determine those areas of the subject which are of great importance to charging, but where the current level of knowledge is inadequate.
- d. To study a series of surface charging events observed on an operational satellite and attempt to model them using simulation codes.

Results are presented from three distinct sources. Firstly, from analysis of a data set generated by an electron spectrometer flown on Meteosat F2, an ESA meteorological satellite. Secondly, from laboratory tests of surface materials using an electron beam facility, and finally from three numerical simulation codes. The Meteosat F2 satellite is used throughout as a case study since it was the platform from which the five year long electron spectrometer data set was derived, and itself suffered

a series of operational anomalies, which were recorded. Also, two types of surface charging event were observed, based on the evidence of the electron spectrometer data. Whilst no clear link has previously been identified between the observed surface charging events and recorded anomalies, Meteosat F2 still presents an ideal opportunity for the study of GEO surface charging. Chapter 2 reviews the previous work on Meteosat F2 anomaly analysis, gives an overall description of the satellite and its mission, and describes the electron spectrometer. Chapter 3 contains a review of the theory of spacecraft charging in geostationary orbit. This consists of three sections; collection of plasma particles by a charged probe, the interaction between magnetospheric plasmas and surface materials, and finally a review of the physics of the plasma environment encountered in GEO. Chapter 4 briefly describes the three numerical simulation codes which are employed; EQUIPOT, which was developed by the author to perform the sensitivity analysis presented in Chapter 7, and its derivative, the BEAM code which simulates laboratory electron beam irradiation experiments. Chapter 4 concludes with a brief review of the NASCAP code.

The results are presented in four chapters. In Chapter 5, long-term (5 year) statistical studies are presented for the location of plasma boundaries observed in GEO, and for the occurrence frequency and intensity of substorm events. Chapter 6 presents electron beam irradiation and simulation results which lead to values for the bulk and surface resistivities of Kapton and Teflon, and for the secondary emission properties of gold. Chapter 7 contains the results of a sensitivity analysis using EQUIPOT which investigates the importance of material properties and plasma characteristics on the equilibrium potential of a surface in space. Finally, Chapter 8 presents a statistical study of barrier charging events observed on Meteosat F2, and the results of a NASCAP simulation of such an event.

2. ELECTROSTATIC CHARGING OF METEOSAT

A brief description of the Meteosat F2 satellite, and the Meteosat project is presented. The results of previous investigations into electrostatic discharges on the F1 and F2 satellites are reviewed. The chapter concludes with a description of the electron spectrometer flown on the F2 satellite.

2.1 THE METEOSAT SPACECRAFT AND MISSION

The Meteosat project was conceived during the 1970s to meet three central requirements⁹; (i) To provide European nations with global meteorological images and data, (ii) To form part of the World Meteorological Organisation (WMO) World Weather Watch (WWW) programme, (iii) To contribute to the WMO's Global Atmospheric Research Programme (GARP).

The overall Meteosat programme consists of the following four segments;

(i) The space segment; a single operational geosynchronous satellite stationed at 0° longitude and equipped with a radiometer (operating in both visible and infra-red wavebands and capable of imaging the full Earth disc in 50 minutes) and a data transmission and relay package operating in the L,S and low UHF bands. The imaging system is designed to provide information on cloud cover, cloud-top and sea surface temperatures, water vapour content of the upper troposphere, radiation balance, and wind determination.

(ii) Facilities at the ESA Space Operations Centre (ESOC), Darmstadt, Germany, which receives raw image data from several sources, including the Meteosat spacecraft, processes it into user form and transmits it back to the Meteosat spacecraft for broadcasting to users throughout Europe and Africa.

(iii) Remote Data Collection Platforms (DCP's) at fixed land sites, or mobile sites such as ships which collect local meteorological data and transmit it to the Meteosat spacecraft.

(iv) Primary and secondary data user stations (PDUS and SDUS) throughout Europe and Africa which receive processed, corrected images, broadcast by the Meteosat spacecraft.

Meteosat provides imaging and telecommunications coverage to the European and African sector of the globe, and forms part of a global network of such geostationary spacecraft; two US GOES satellites at 140° W and 70°W, GOMS at 70°E (USSR) and GMS at 140°E (Japan). The Earth imaging radiometer provides visible (0.4 to 1.1 μm) and infra-red (10.5 to 12.5 μm and 5.7 to 7.1 μm) pictures of the Earth's disc. The longer wavelength infra-red band is able to penetrate the atmosphere, and may be used to infer sea surface temperatures, whilst the shorter IR wavelength band is at the water vapour absorption wavelength. The satellite is spin-stabilised about an axis perpendicular to the equatorial plane and has a spin rate of 100 rpm. This spinning motion

provides East-West scanning, and the radiometer mirror is used to scan in the North-South direction; the mirror is moved by two pixels per satellite revolution. Each visible image consists of 5000x5000 pixels, and requires a southward and a northward scan, which takes 50 minutes. IR images, however, have a resolution of 2500x2500 pixels, and may be captured in a single southward or northward sweep, which takes 25 minutes. Resolution at the sub-satellite point is 2.5km (visible channel) and 5km (infra-red channels). The synchronisation and image channel (SIC) subsystem ensures that the radiometer movement and data routing are correctly synchronised with satellite spin rate and phase.

To date, there have been three Meteosat spacecraft; Meteosat F1, launched in November 1977; Meteosat F2, launched in July 1981, and Meteosat P2, launched in May 1988. An exploded diagram of Meteosat F2 is shown in Figure 2.1; all satellites in the series are of similar construction. The overall spacecraft characteristics are given in Table 2.1. The design is unusual⁹ in that the spacecraft has been built around the radiometer assembly, and not the apogee boost motor (ABM). This approach leads to a stable spinning configuration during the operational life of the satellite, but necessitates that the ABM and its adaptor are jettisoned after firing. The structure consists of two circular shelves which surround the radiometer assembly; the upper shelf carries most of the essential subsystems, such as the station-keeping hydrazine propulsion system, Sun, Earth and nutation sensors and the power system. The lower shelf, mounted above the lower thermal shield supports some of the radiometer electronics and telecommand and telemetry units. Part of the upper shelf is removed to accommodate the radiometer baffle, and both shelves are enclosed by six solar panels which form the cylindrical body. The northern face of this cylinder is partly formed by a thermal control surface, and partly by the antenna assembly. The main L-band antenna consists of arrays of radiating elements placed around a cylindrical shell to form an electrically de-spun antenna (EDA) whilst the S and UHF band antennae are mounted at the very north of the spacecraft and generate a toroidal radiation pattern. A narrow "bellyband" has been positioned approximately one third of the way down the solar panels to accommodate some thermal control surfaces and optical sensors.

A schematic diagram of the radiometer optical assembly¹⁰ is shown in Figure 2.2. It consists of a Ritchey-Chretien primary and secondary mirror assembly, together with a system of 45° folding mirrors to reflect the image onto the IR and visible charge coupled device (CCD) sensor system. Scanning in the vertical plane is achieved by rotating the entire telescope assembly by up to 10 degrees above and below the equatorial plane. All mirrors are fabricated from "Zerodur" which has a very low coefficient of expansion, and are coated with a chrome silver reflective surface. Constraints imposed by the physical mounting and the passive thermal control system have resulted in the mirror assembly being electrically isolated from the main structure.

In summary, a very large percentage of the surface of the spacecraft is covered with electrically insulating material¹¹. These include thermal control surfaces made from double-sided aluminised Kapton, second surface mirrors with an outer layer of Teflon, and solar cells coated with fused silica cover glasses. In addition, the radiometer assembly is also electrically isolated, which gives ample scope for accumulation of surface charge.

2.2 PREVIOUS STUDIES OF METEOSAT ELECTROSTATIC CHARGING

Meteosat F1 suffered from a series of anomalies throughout its operational life, which did not cause major disruption to the Meteosat programme, but proved to be a considerable source of nuisance to the satellite operators. During its first year, 119 anomalies were recorded and classified¹¹ according to the subsystem affected. The most common type (63.8%) were associated with the radiometer assembly which would either jump an extra pixel, or stop during a scan. Other classes of anomaly affected the radiometer calibration, synchronisation and telecommunications system (6.7%), the power system (23.5%) and the attitude control system (5.8%). Suspecting that many of these anomalies were due to electrostatic discharges, Robbins¹¹ studied their distribution with respect to local time, the Ap geomagnetic index, and magnetometer data from stations close to the foot of the magnetic field line which maps to the satellite. He found that the distribution in local time did not differ significantly from a random one, but that a positive correlation existed between the occurrence of an anomaly and the level of magnetic activity measured one or two days prior to the event.

The second satellite in the series, Meteosat F2 was equipped with an electron spectrometer (see section 2.3) to make in-situ measurements of electrons in the energy range responsible for surface charging. In addition, this satellite also suffered many operational anomalies which were similar in character to those reported for Meteosat F1. Johnstone et al¹² studied the distribution of anomalies with respect to local time and geomagnetic activity and found similar results to that of Robbins. They also studied the monthly distribution of anomalies and found, most significantly, that radiometer system anomalies tended to occur near the equinoxes. Johnstone et al¹² identified two types of surface charging event from the spectrometer data; eclipse events which occur when the whole satellite is in shadow, and barrier events which are initiated when an isolated surface is shadowed for an entire spin period, but the remainder of the satellite is sunlit (see Chapter 8). Significantly, no correlation existed between charging events and anomalies. However, the radiometer primary mirror was identified as the element in permanent shadow close to the solstices which gave rise to barrier events.

In summary, Meteosat operational anomalies correlate with environmental effects via geomagnetic indices, and with seasonal effects, but do not correlate with the surface charging events observed on Meteosat F2. There are two explanations; Firstly, anomalies may be

induced by surface charging which is local to the affected subsystem, and does not produce effects which are detectable by the spectrometer. Secondly, anomalies may be due to deep dielectric charging^{13,14} resulting from high energy electrons. In either case, Meteosat F2 has proved to be a unique laboratory for studying spacecraft charging since it is an operational satellite which has suffered anomalies, made extensive measurements of the electron environment and suffered regular surface charging. Two other pieces of work have produced results pertinent to this thesis and are summarised here.

2.2.1 ESD tests

As a result of operational anomalies on Meteosat F1, some thermal control surface materials, the radiometer mirror and the satellite engineering model were irradiated using an electron beam facility.

The thermal shields consisted of 25 μm thick Kapton, aluminised on both sides. Normally, the outer conducting surface was connected to the spacecraft structure by means of grounding straps, but the test program examined the behaviour of thermal blanket material both with and without such straps. Samples were irradiated with monoenergetic electron beams of energy 5, 10 and 20 keV at current densities ranging from 0.1 nA/cm² to 1.25 nA/cm². Test results¹⁵ show that the equilibrium surface potential is greatly affected by the detailed configuration of the sample. The most negative potential (-1700 V) was measured over an additional piece of blanket isolated by an epoxy glue from the primary one which reached -600V on its floating outer surface. When the outer aluminised surface was connected to Earth, only the blanket attached by epoxy glue charged.

A specimen of radiometer mirror material measuring 125 cm², was irradiated with a beam of intensity 1nA/cm² and energy in the range 5 to 20 keV¹⁶. The sample reached a maximum negative potential of -4700V for 20 keV electrons; no discharges were observed and the sample discharged quickly when exposed to UV illumination. When a bias potential (0 to 10 kV) was applied directly to the reflecting surface of the mirror, small discharges were observed near the mounting bracket and near the corners of the mirror for the highest voltages.

High voltages were injected directly at several points onto an electrically active engineering model¹⁵. No anomalies were recorded except when current was injected directly onto the tripod supporting the radiometer secondary mirror when some switching anomalies similar to the synchronisation and radiometer anomalies were observed. In a second group of tests, the entire engineering model was irradiated with an electron beam (1 nA/cm², 0-30 keV). The spacecraft could not be operated electrically during the tests, so that discharges had to be monitored visually, or by RF pulse detection and surface potentials were measured with non-contacting Trek probes. At beam energies below 10 keV, little arcing was observed, but at beam energies above 13 keV, many arc discharges were observed visually and by measurement of associated RF pulses. These occurred mainly on the top and bottom thermal shields and

around the solar panels. During the test, several of the thermal control surfaces were grounded which greatly reduced the number of discharges, although as Hoge and Leverington¹⁷ point out, this modification alone is not enough to prevent anomalous behaviour.

Most importantly, these tests show that large potentials can be applied to the radiometer primary mirror, before arc discharges occur, and also that current injected onto the radiometer secondary mirror can induce anomalous behaviour similar to that observed operationally.

2.2.2 NASCAP simulation of Meteosat F2 charging

Frezet et al¹⁸ simulated charge accumulation on the Meteosat F2 satellite using the NASCAP code¹⁹. The radiometer cavity was modelled as accurately as possible, and the overall shape and surface material ratios for the satellite were preserved. An environment definition (12 keV, 1.2 cm⁻³ electrons; 29.5 keV, 1.0 cm⁻³ ions) was chosen such that exposed Kapton charged to a potential of -12 kV. Surface material property data from tests of materials used on the ECS⁷ and Hipparcos²⁰ satellites were used throughout. Since the satellite spin period is much less than characteristic differential charging times for typical insulating layers, an average illumination was computed for equinox and northern hemisphere summer solstice conditions.

At equinox, the satellite rotates such that the top and bottom thermal shields are continuously in shadow. These surfaces charge negatively, forming potential barriers which prevent photoelectrons escaping from the solar cells near to the top and bottom surfaces. In addition to this large potential gradient which develops across the solar array, the radiometer secondary mirror also develops a large negative potential.

At the solstice, the top thermal shield is now illuminated, but the bottom thermal shield develops a negative potential barrier which extends over part of the solar array. Large negative potentials are again observed within the radiometer cavity.

2.3 THE METEOSAT F2 ELECTRON SPECTROMETER

Following the discovery of a clear link between Meteosat F1 anomalies and geomagnetic activity, ESA decided to directly monitor the energetic electron environment in-situ for the second Meteosat spacecraft, denoted F2. The SSJ/3 detector^{12,21,23} was supplied by the Air Force Geophysics Laboratory, USA, and is similar to others flown on the DMSP satellite program. The spectrometer consists of two curved plate electrostatic analysers which measure different energy ranges. A schematic diagram of a curved plate analyser is shown in Figure 2.3; an electron arriving at the entrance aperture is deflected by the electric field applied across the plates. If the initial energy of the particle is such that the centrifugal force due to its circular motion matches the Lorentz force due to the electric field, the particle will follow a

circular path and will emerge from the plates to be detected by an electron multiplier.

A rigorous calculation for the electric field within such a curved plate system requires Laplace's equation to be solved in cylindrical polar co-ordinates, which gives a solution in the form of a Bessel function. However, an adequate relationship between the voltage, V applied between the plates and the energy of admitted electrons may be obtained by assuming that the electric field, \underline{E} , is the same as for a parallel plate capacitor. Balancing centrifugal force for an electron of mass m and velocity v with the Lorentz force of the same electron in an electric field, \underline{E} , gives

$$\frac{m \cdot v^2}{r} \underline{r} = -eE\underline{r} \quad (2.1)$$

where unit vector \underline{r} is defined within the coordinate system shown in Figure 2.3. If the electric field is related to the applied plate voltage, V , and separation, d , as follows,

$$E = \frac{V}{d} \quad (2.2)$$

then the energy (in eV) of particles able to reach the multiplier for a given V is

$$\epsilon = \frac{r}{2d} V \quad (2.3)$$

The quantity $r/2d$ is called the "analyser constant". Note that an electron following a trajectory exactly mid-way between the plates will follow a surface where $V = 0$, thereby suffering no net acceleration whilst traversing the analyser.

By using a different radius of curvature for the two sets of plates, the same potential difference can be applied across both sets of plates in order to sample two different energy ranges simultaneously. In this case, however, the voltage applied to the low energy analyser was one half that applied to the high energy analyser. Physical characteristics of the two analysers are given in Table 2.2 and the channel energies in Table 2.3. Note that the highest energy of the low energy analyser, and the lowest energy of the high energy analyser are nearly coincident, allowing a continuous comparison of the two different multiplier count rate efficiencies. The energy values given in Table 2.3 represent the centre of an energy band; some electrons are able to reach the multiplier by a trajectory which is slightly more or less curved than the optimal path; the width of each energy band is determined by the geometry of the plates. Furthermore, the acceptance angle of each analyser will depend on plate geometry and the local electric field configuration at the entrance of each analyser. Energy resolution and acceptance angles were

found from a series of calibration tests with an electron beam; the analyser resolutions ($d\epsilon/\epsilon$) were found to be about 4.0% for high energies, and about 7.22% for low energies; such that adjacent energy ranges do not overlap. The approximate width of each channel is given in Table 2.3. Results of these calibration tests allow the electron multiplier count rates to be converted into a differential number flux, with dimension $(\text{cm}^2 \text{ st s eV})^{-1}$, by application of an "integrated geometric factor", $G^*(\epsilon)$, obtained from calibration. This relation may be written as follows;

$$N(\epsilon) = \frac{C(\epsilon)}{G^*(\epsilon) \cdot t} \quad (2.4)$$

where $N(\epsilon)$ is the differential number flux and $C(\epsilon)$ is the raw electron multiplier count over time period t . Values of G^* (units of $(\text{cm}^2 \text{ st eV})$) used for the routine data processing are given in Table 2.3. The dwell time at each energy is 12.583 seconds (imposed by telemetry considerations), so that a full 16 point spectrum is obtained in 100.6 seconds. Note that the dwell time at each energy is very much greater than the satellite spin period of 0.6 seconds; since the analyser openings are in the satellite "bellyband", each spectrum represents an average over many rotations.

The data set from this detector begins in August 1981 and extends continuously until a partial failure of the detector during September 1987. The calibration factor, G^* was amended during early 1982 as a result of comparison of the overlapping energy channels. Analysis presented in this thesis is based on a continuous, five-year long data set which extends from April 1982 through to March 1987.

Table 2.1 Physical Characteristics of Meteosat F2

Weight	697 kg (at launch) including 345 kg (ABM) and 60 kg for ABM + 3rd stage fittings.
Dimensions	210 cm diameter 319.5 cm high (without ABM)
Power	200W (end of life)

Table 2.2
SSJ/3 electron spectrometer geometry

Analyser :	High Energy	Low Energy
Mean plate radius (mm)	100.13	30.00
Plate separation (mm)	2.50	7.52
Analyser constant (eV/V)	20.03	1.99

Table 2.3
SSJ/3 electron spectrometer characteristics

Low Energy Analyser			High Energy Analyser		
ϵ (eV)	$d\epsilon$ (eV)	G^* ($\text{cm}^2 \cdot \text{st} \cdot \text{eV}$)	ϵ (eV)	$d\epsilon$ (eV)	G^* ($\text{cm}^2 \cdot \text{st} \cdot \text{eV}$)
49	3.5	1.72E-3	984	39	6.34E-2
75	5.4	3.53E-3	1510	60	8.72E-2
116	8.4	5.65E-3	2320	93	1.17E-1
177	12.8	8.42E-3	3540	142	1.64E-1
274	19.8	1.30E-2	5480	219	2.18E-1
418	30.2	2.00E-2	8360	334	2.92E-1
644	46.5	3.17E-2	12880	515	3.88E-1
990	71.5	4.74E-2	19800	792	4.80E-1

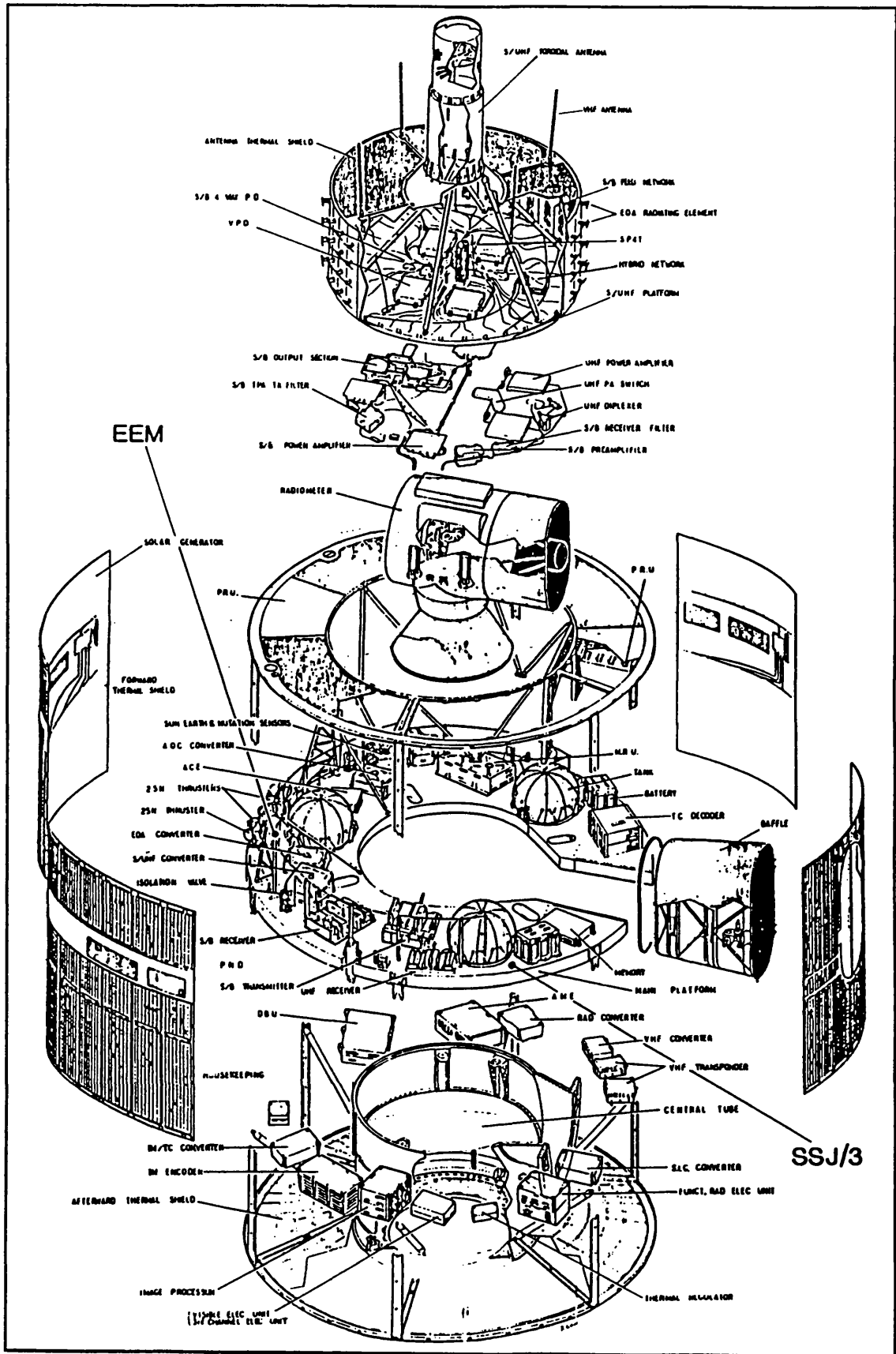


Figure 2.1 Exploded view of Meteosat F2

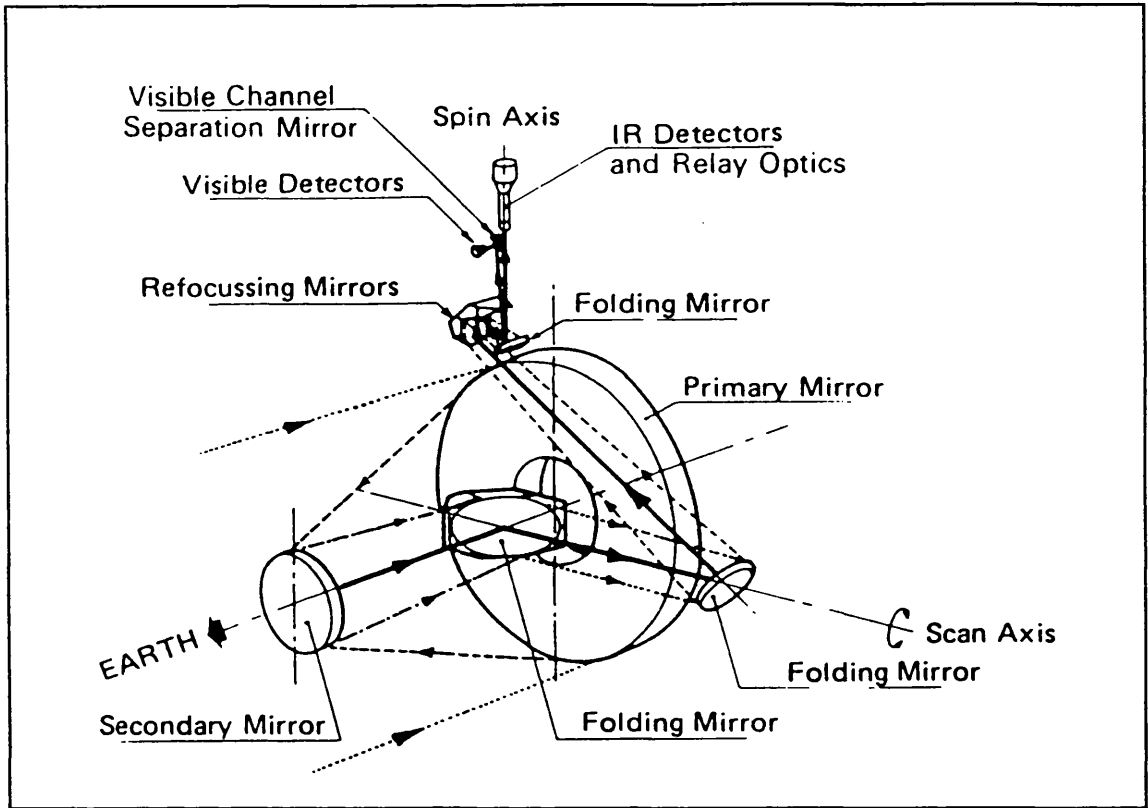


Figure 2.2 Meteosat F2 radiometer optics (schematic)

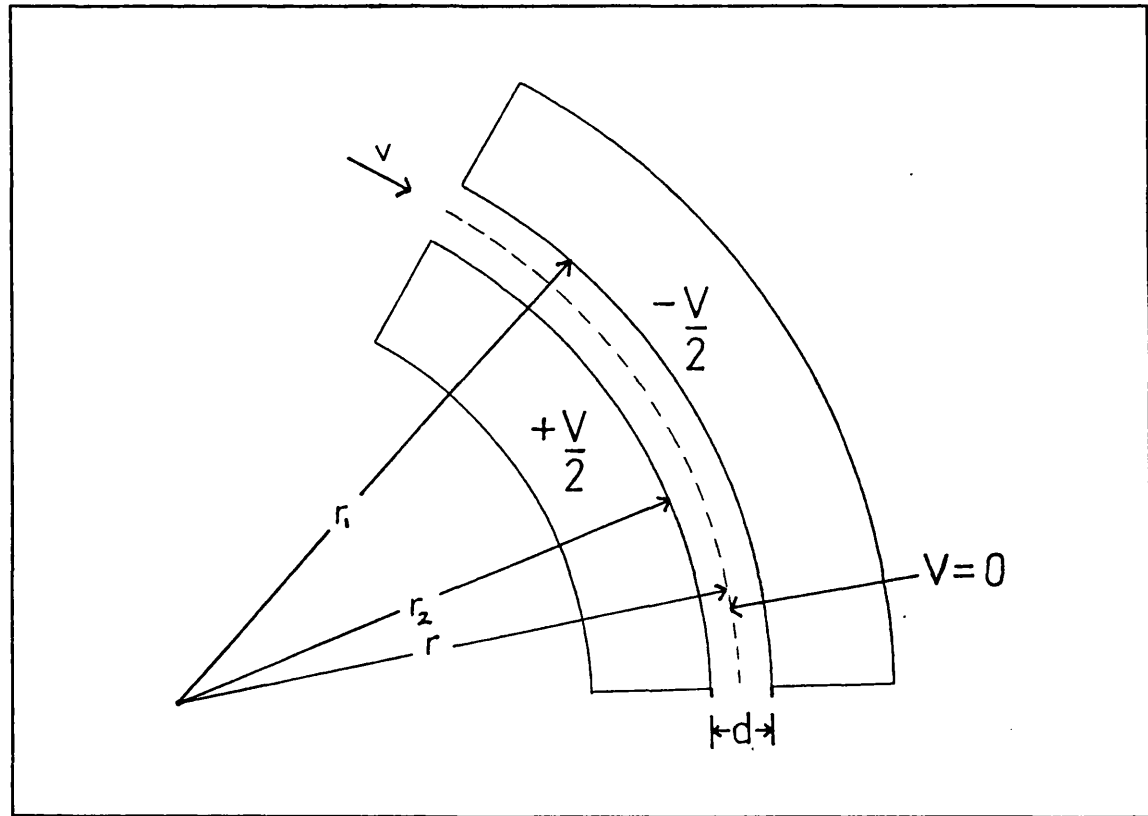


Figure 2.3 SSJ/3 spectrometer; curved plates geometry

3. THEORY OF SPACECRAFT CHARGING IN GEOSYNCHRONOUS ORBIT

The theory of spacecraft charging in geosynchronous orbit is reviewed. This is divided logically into three topics; current collection by plasma probes (within the density and temperature region appropriate to spacecraft charging); surface material / particle interaction physics and an overview of the magnetospheric processes which control plasma conditions around geosynchronous satellites.

3.1 CURRENT COLLECTION BY PLASMA PROBES

A body immersed in a plasma will acquire a net positive or negative charge due to ions and electrons which bombard its surface. As a result of this finite body potential, the electric field due to the probe affects the plasma surrounding the probe, which in turn affects the net current collected. In general, a negative feedback situation develops; for example, in a plasma with equal electron and ion density and temperature, the probe will initially receive a net current of electrons since their thermal velocity exceeds that of the ions. However, as the probe becomes more negatively charged, electrons are repelled and ions attracted, until the probe reaches a potential where the net incident current is zero.

A general theory of current collection by plasma probes is extremely complex since it must extend to all types of "probe" from the grounded walls of a vacuum chamber to a multi-faceted spacecraft, and to all types of plasma whose density and temperature vary by many orders of magnitude. Even for the restricted case of spacecraft sized probes (radii of the order of 1m) immersed in magnetospheric plasmas involves several different branches of the theory. A brief review of plasma kinetic theory is presented, since this is a pre-requisite for calculating the current collected by plasma probes. The Maxwell-Boltzmann distribution function (both with and without an external electric field) is introduced as a step towards deriving the characteristic plasma length scale, the Debye length; general probe collection expressions are then derived for a spherical probe without making any implicit assumption of the form of plasma distribution function.

3.1.1 A review of plasma kinetic theory

Plasmas consist of very large numbers of interacting charged particles which enables their behaviour to be described using statistical techniques similar to those used in the kinetic theory of natural gases. The concepts of phase space and distribution function are necessary for a statistical description of a plasma. At any instant in time, the state of a single particle may be completely defined by six values; its position in some co-ordinate frame (x, y, z) and its velocity vector in the same frame (v_x, v_y, v_z). The state of a particle is represented by a single point in this six-dimensional phase space. A system of N particles is represented by N points in phase space and the time evolution of a

single particle may be described by a trajectory in phase space.

An assembly of particles of a particular species may be described by a distribution function, f which specifies the density of particles in a volume of phase space around a given region of phase space at time t ;

$$f(\underline{r}, \underline{v}, t) = \frac{dn(\underline{r}, \underline{v}, t)}{d^3r \cdot d^3v} \quad (3.1)$$

Note that a plasma in thermal equilibrium is characterised by a distribution function which is homogeneous (does not depend on \underline{r}); isotropic (depends on the magnitude of \underline{v} , not its direction) and independent of time. The dependence of the distribution function, f , on \underline{r} , \underline{v} and t is given by the Boltzmann equation²³. For a collisionless plasma, subject to an external, conservative force \underline{F} , the Boltzmann equation may be written as;

$$\frac{\partial f}{\partial t} + \underline{v} \cdot \nabla f + \frac{\underline{F}}{m} \cdot \frac{\partial f}{\partial \underline{v}} = 0 \quad (3.2)$$

which may be re-written as

$$\frac{Df}{Dt} = 0; \quad \frac{D}{Dt} = \frac{\partial}{\partial t} + \underline{v} \cdot \nabla + \frac{\underline{F}}{m} \cdot \frac{\partial}{\partial \underline{v}} \quad (3.3)$$

D/Dt is the substantive derivative, of which the latter two terms are due to the change in elemental volume, $d^3r \cdot d^3v$ with time. Equation 3.3 states that the density of points in phase space is constant with time for the case where collisions may be ignored; this is known as Liouville's theorem.

3.1.2 Calculating macroscopic quantities from the distribution function

Number density, $n(\underline{r}, t)$ is given by integrating the distribution function over all possible velocities;

$$n(\underline{r}, t) = \int_{\underline{v}} f(\underline{r}, \underline{v}, t) \cdot d^3v \quad (3.4)$$

Average velocity, $\underline{u}(\underline{r}, t)$ is calculated by weighting each velocity by the number of particles moving at that velocity, dividing by the total number of particles and assuming that the distribution function f tends to zero as the velocity approaches infinity;

$$\underline{u}(\underline{r}, t) = \frac{1}{n(\underline{r}, t)} \int_{\underline{v}} \underline{v} \cdot f(\underline{r}, \underline{v}, t) \cdot d^3v \quad (3.5)$$

The number of particles of a single species crossing a surface element per unit time is directly related to the current collected by a surface. Figure 3.1 shows an infinitesimal element of surface $d\underline{S}$ at position \underline{r} ; in time dt , the number of particles dn_v from the plasma which cross $d\underline{S}$ from a single direction is given by the number of particles in the

slanted cylinder which have a velocity \underline{v} in the direction indicated;

$$dn_v = (\underline{v} \cdot d\underline{S}) \cdot (v dt) \cdot f(\underline{r}, \underline{v}, t) \quad (3.6)$$

where $\underline{v} \cdot d\underline{S}$ is the component of area $d\underline{S}$ in the direction of \underline{v} . The total number of particles, N which cross $d\underline{S}$ from all directions is found by integrating equation 3.6 over all possible values of \underline{v} . Note that in most practical cases, $d\underline{S}$ forms part of a solid surface, so the calculation is separated into integrals over scalar v , and over azimuth and elevation angles for one hemisphere of total solid angle.

$$N(\underline{r}, t) = \int_{\underline{v}} (\underline{v} \cdot d\underline{S}) \cdot f(\underline{r}, \underline{v}, t) \cdot dt \cdot d^3v \quad (3.7)$$

The number flux, Γ (typical units $\text{cm}^{-2} \cdot \text{s}^{-1}$), is equal to the number of particles, N crossing per unit area, per unit time, and is given by

$$\Gamma(\underline{r}, t) = \int_{\underline{v}} (\underline{n} \cdot \underline{v}) \cdot f(\underline{r}, \underline{v}, t) \cdot d^3v \quad (3.8)$$

where \underline{n} is a unit vector normal to the surface $d\underline{S}$. Note that equations 3.4 and 3.5 are the first two moments of the distribution function; higher moments (integrals of various powers of \underline{v} multiplied by the distribution function over all values of \underline{v}) give rise to additional physical quantities such as momentum transfer and energy flux.

Calculating moments of the distribution function is greatly simplified when the plasma is both homogeneous (f does not depend on \underline{r}) and isotropic, so that f is a function only of particle speed, or energy. In this case, it is useful to re-cast $f(\underline{r}, \underline{v}, t)$ as a distribution of speeds, $F(v)$. To integrate over all possible velocities, it is necessary to integrate over every "shell" of width dv in velocity space, so that the elemental volume of velocity space becomes (with the usual notation for azimuth and elevation angles)

$$d^3v = dv \cdot (v \cdot d\phi) \cdot (v \cdot \sin\theta \cdot d\theta) \quad (3.9)$$

The expression for computing the n^{th} moment, I_n becomes

$$I_n = \int_{\underline{v}} v^n \cdot f(\underline{r}, \underline{v}, t) \cdot d^3v = \int_{\underline{v}} v^n \cdot f(v) \cdot v^2 \cdot dv \cdot \int_0^\pi \sin\theta \cdot d\theta \cdot \int_0^{2\pi} d\phi \quad (3.10)$$

$$\therefore I_n = \int_{\underline{v}} v^n \cdot F(v) \cdot dv; \quad F(v) = 4\pi v^2 f(v) \quad (3.11, 12)$$

Strictly, this approximation applies equally well to a non-homogeneous plasma which is isotropic, provided that the distribution function is separable into the product of a position dependent part, and a velocity distribution, for example if a homogeneous, isotropic plasma is subject to an electric field.

Finally, it is useful to consider how the expression for particle

flux (equation 3.8) may be simplified for the case of an isotropic distribution function, $f(v)$. From Figure 3.1, it is clear that the term $(\underline{n} \cdot \underline{v})$ may be replaced, for an isotropic distribution by $v \cdot \cos(\theta)$, where θ is the azimuthal particle arrival direction. The element of velocity space $d^3\underline{v}$ can be replaced with integrals over speed and direction (equation 3.9) with arrival directions considered from one hemisphere only. Equation 3.8 now reduces to

$$\Gamma = \int_0^{\frac{\pi}{2}} \sin(\theta) \cos(\theta) d\theta \cdot \int_0^{2\pi} d\phi \cdot \int_0^{\infty} v^3 \cdot f(v) \cdot dv \quad (3.13)$$

By evaluating the integrals over arrival angle, and also using expression 3.12 for the definition of $F(v)$, equation 3.13 becomes

$$\Gamma = \frac{1}{4} \int_0^{\infty} v \cdot F(v) \cdot dv \quad (3.14)$$

which represents the total number of particles crossing a plane surface of unit area per unit time.

3.1.3 The Maxwell-Boltzmann distribution function

Two forms of the distribution function $f(\underline{r}, \underline{v}, t)$ are introduced for a single species in equilibrium with no external forces, and for the same species with an applied external electric field. For a particle species in equilibrium, with no external force applied, the first and third terms of equation 3.2 are zero, which requires that ∇f is also zero, so that the distribution function is isotropic. The familiar Maxwell-Boltzmann distribution function, derived originally for an assembly of neutral gas particles is one solution. The number of particles per unit volume, of a single species, with velocity between \underline{v} and $\underline{v} + d\underline{v}$ is given by

$$f(\underline{v}) \cdot d^3v = n \left(\frac{m}{2 \cdot \pi \cdot k \cdot T} \right)^{\frac{3}{2}} \exp \left(- \frac{m \cdot v^2}{2 \cdot k \cdot T} \right) \cdot d^3v \quad (3.15)$$

Only the magnitude of \underline{v} appears in the definition of f , so that the Maxwell-Boltzmann distribution is, by definition, isotropic. More generally, many space plasmas have been modelled by regarding each species as being a superposition of two or three single Maxwellian components, ie

$$f(\underline{v}) = \sum_j^N n_j \cdot \left(\frac{m}{2 \cdot \pi \cdot k \cdot T_j} \right)^{\frac{3}{2}} \exp \left(- \frac{m \cdot v^2}{2 \cdot k \cdot T_j} \right) \quad (3.16)$$

The distribution of speeds, $F(v)$, for this isotropic distribution is

found from equations 3.12 and 3.15;

$$F(v)dv = 4 \cdot \pi \cdot n \cdot \left(\frac{m}{2 \cdot \pi \cdot k \cdot T} \right)^{\frac{3}{2}} \cdot v^2 \cdot \exp\left[-\frac{m \cdot v^2}{2 \cdot k \cdot T}\right] \cdot d^3v \quad (3.17)$$

noting that

$$\int_0^{\infty} F(v)dv = n \quad (3.18)$$

Equation 3.15 implies that the mean velocity of the Maxwell-Boltzmann distribution is zero, since for any speed, there are as many particles moving in one direction as in the opposite one. The mean speed, however is finite and is given by

$$\int_0^{\infty} v \cdot F(v) \cdot dv = \left(\frac{8 \cdot k \cdot T}{\pi \cdot m} \right)^{\frac{1}{2}} \quad (3.19)$$

Equation 3.15 is one solution of the Boltzmann equation (3.2) for the case where there is no time dependence and no externally applied force. If the force term \underline{F} becomes finite, and is allowed only to depend on position, \underline{r} , the particle distribution function is longer homogeneous, but may be expressed as a product of a homogeneous, isotropic part (depending on v only) and a position dependent part;

$$f(\underline{r}, \underline{v}) = f_o(\underline{v}) \cdot \Psi(\underline{r}) \quad (3.20)$$

this can be substituted into Boltzmann's equation to give;

$$f_o(\underline{v}) \cdot [\underline{v} \cdot \nabla \Psi(\underline{r})] - \frac{\nabla U(\underline{r})}{m} \cdot \Psi(\underline{r}) \cdot \frac{\partial f_o(\underline{v})}{\partial \underline{v}} = 0 \quad (3.21)$$

where the conservative force, \underline{F} , has been expressed as the gradient of potential $U(\underline{r})$;

$$\underline{F}(\underline{r}) = -\nabla U(\underline{r}) \quad (3.22)$$

In order to proceed further, the form of f_o must be known, so that the final term of equation 3.21 can be evaluated. Taking f_o to be the isotropic, homogeneous Maxwellian distribution (equation 3.15), the partial derivative of f_o with respect to \underline{v} is

$$\frac{\partial f_o(\underline{v})}{\partial \underline{v}} = \frac{-m}{kT} \cdot f_o(\underline{v}) \cdot \underline{v} \quad (3.23)$$

Substituting this into equation 3.21 yields the following equation, noting that a factor $\underline{v} \cdot f(\underline{v})$ has been cancelled from both terms;

$$\nabla \Psi(\underline{r}) + \frac{\nabla U(\underline{r})}{k \cdot T} \Psi(\underline{r}) = 0 \quad (3.24)$$

Since U and Ψ are functions of \underline{r} only, equation 3.24 may be re-arranged

into the following integral expression;

$$\int_{\mathcal{L}} \frac{d\Psi(\mathcal{L})}{\Psi(\mathcal{L})} = -\frac{1}{kT} \int_{\mathcal{L}} dU(\mathcal{L}) \quad (3.25)$$

which has a solution of the form

$$\Psi(\mathcal{L}) = A. \exp\left[-\frac{U(\mathcal{L})}{kT}\right] \quad (3.26)$$

The value of the constant, A is unity since equation 3.4 holds, which also implies that

$$n(\mathcal{L}) = n_o. \exp\left[-\frac{U(\mathcal{L})}{kT}\right] \quad (3.27)$$

where n_o is the density of the particle species when no field is present.

The distribution function for an isotropic plasma in an external force field, \underline{F} , introduced here, is important for calculating the size of the space charge sheath which forms around a charged object immersed in a plasma, and will be used in the following section.

3.1.4 Debye shielding

Consider a negatively charged probe immersed in a hydrogen plasma which is in thermal equilibrium, and whose distribution function is a single Maxwellian (equation 3.15). Assume that the timescale over which the plasma near the probe re-arranges itself is short, such that the inertia of the ion population prevents significant re-distribution of positive charges. The electrons surrounding the probe are repelled by the electric field and migrate away, leaving an excess of ions. Eventually, the electric field arising from the imbalance of electron and ion density near the probe cancels the field from the charged probe itself at a certain distance from the probe. The plasma has re-arranged itself in order to shield out the initial potential applied to the probe. The characteristic length scale over which this shielding occurs is called the Debye length and the region surrounding the probe, to a distance of the order of a Debye length is called the plasma sheath, within which overall charge neutrality is not preserved and there is a net electric field due to the probe itself. Outside the sheath region, the electric field due to the probe has been completely shielded and the plasma is in its ambient state. In order to preserve overall charge neutrality, the net charge imbalance within the sheath is equal and opposite to the total charge on the probe itself.

Expressions for the Debye length in terms of plasma density and temperature, as well as the potential within the sheath may be derived from the Maxwell-Boltzmann distribution function for a plasma in thermal equilibrium in a conservative force field, equations 3.15, 3.19 and 3.26, together with Poisson's equation. For simplicity, consider a negatively charged, spherical probe, where the electric field and potential are a

function of radial distance only,

$$E(r) = -V\Phi(r) \quad (3.28)$$

According to equation 3.27, electron density in the region of an electric field is given by

$$n_e = n_0 \cdot \exp\left(\frac{+q \cdot \Phi}{k \cdot T_e}\right) \quad (3.29)$$

where q is the magnitude of the electronic charge and T_e is the electron temperature. The approximation of fixed ions mentioned above implies that the ion density is everywhere equal to the ambient ion and electron density, n_0 ;

$$n_i(r) = n_0 \quad (3.30)$$

These expressions may be substituted into Poisson's equation;

$$\nabla^2\Phi(r) = -\frac{\rho(r)}{\epsilon_0} = -\frac{q}{\epsilon_0}(-n_e(r) + n_i(r)) \quad (3.31)$$

to give

$$\nabla^2\Phi(r) = \frac{q \cdot n_0}{\epsilon_0} \left[\exp\left[\frac{q \cdot \Phi}{k \cdot T_e}\right] - 1 \right] \quad (3.32)$$

which may be solved for the electrostatic potential as a function of r . Making the further assumption that the electrostatic potential energy is smaller than the thermal energy of the electrons, then the exponential form may be approximated by

$$\exp(x) \approx 1 + x \quad (x \ll 1) \quad (3.33)$$

whereupon equation 3.32 reduces to

$$\nabla^2\Phi(r) = \frac{q \cdot n_0}{\epsilon_0} \left[1 + \frac{q \cdot \Phi(r)}{k \cdot T_e} - 1 \right] = \frac{q^2 \cdot n_0}{\epsilon_0 \cdot k \cdot T_e} \Phi(r) \quad (3.34)$$

The constants which appear in this differential equation imply a characteristic length scale: the Debye length, which is defined as

$$\lambda_D = \left(\frac{\epsilon_0 \cdot k \cdot T_e}{n_0 \cdot q^2} \right)^{\frac{1}{2}} \quad (3.35)$$

with which equation 3.34 becomes

$$\nabla^2\Phi(r) = \frac{1}{\lambda_D^2} \Phi(r) \quad (3.36)$$

At this stage, there are several points to note. Firstly, the Debye length decreases with increasing plasma density simply because the net

positive charge (for a negative probe) within the sheath region which is required to neutralise the effects of the charged probe is achieved over a much smaller region for high ambient plasma density. Secondly, the Debye length increases with electron (rather than ion) temperature since it is the electrons which re-distribute themselves to provide the necessary charge distribution in the sheath region. Thirdly, the expression for Debye length reflects the idea that the sheath radius is close to the radius where the electric potential energy is equal to the electron thermal energy. Clearly, a solution of equation 3.36 for any geometry yields a potential function which falls away on a length scale of the order of a Debye length; there will be a finite electric field beyond the Debye length.

Finally, it is interesting to solve equation 3.36 for the simple case of a negatively charged sphere. The potential is expected to fall off with increasing r faster than a Coulomb potential, so that the potential function may be written as

$$\Phi(r) = \frac{A}{r} F(r) \quad (3.37)$$

where A is constant, and F is some decreasing function of r . Substituting equation 3.37 into 3.36 yields the following differential equation for $F(r)$;

$$\frac{d^2 F(r)}{d^2 r} = \frac{F(r)}{\lambda_D^2} \quad (3.38)$$

which may be solved such that F decreases exponentially with r , on a distance scale of one Debye length;

$$F(r) = A_2 \cdot \exp\left[-\frac{r}{\lambda_D}\right] = A_3 \cdot \exp\left[-\frac{(r-r_0)}{\lambda_D}\right] \quad (3.39)$$

where r_0 is the probe radius and the factor $\exp(r_0)$ is considered to be part of the constant of integration. The Debye potential then becomes

$$\Phi(r) = \frac{\Phi(r_0)}{r} \cdot \exp\left[-\frac{(r-r_0)}{\lambda_D}\right] \quad (3.40)$$

It can be seen that at one Debye length from the probe, the potential has dropped to $1/e$ of the corresponding free-space Coulomb potential at that distance.

3.1.5 Current collection by a spherical probe

Discussions in the previous four sections have introduced the concepts of a plasma distribution function and a characteristic plasma length scale; the Debye length. With these ideas, it is now possible to address a problem central to the study of spacecraft charging; what will be the current of ions and electrons collected by a probe immersed in a plasma as a function of probe potential and plasma density and

temperature?. In fact, the general (and complex) problem of current collection by a plasma probe has been studied extensively; both computationally and experimentally with space and laboratory plasmas. It turns out that for a plasma with a Debye length which is long compared to the characteristic length scale of a probe, and in the collisionless plasma limit, simple analytical formulae may be derived for current collection as a function of probe potential and plasma density and temperature.

Medicus²⁴ re-visited the original work of Mott-Smith and Langmuir²⁵, but instead of assuming a Maxwell-Boltzmann distribution function, he sub-divided each species into a series of monoenergetic "swarms" of particles. For this approach, it is necessary to assume that a definite sheath boundary exists, beyond which no electric fields due to the probe are present. This is not quite consistent with the form of the Debye potential derived in the previous section, but as will be justified later, it is quite acceptable when the Debye length greatly exceeds probe radius. Consider Figure 3.2 which depicts a spherical probe of radius r_p , surrounded by a spherical sheath of radius r_s , on which several trajectories have been drawn. Under the influence of a central force, the trajectory of a particle is confined to a plane containing the initial location of the particle and the origin (probe centre). This is evident from the law of conservation of angular momentum, and allows all trajectories to be considered in two dimensions only. Furthermore, without any loss of generality, circular symmetry allows the direction of the x and y axes to be defined such that any incident particle initially approaches the probe parallel to the x axis.

Accelerating probe:

Figure 3.2 represents the case when particles are accelerated towards the probe; either electron trajectories towards a positive probe, or ion trajectories towards a negative probe. All four trajectories represent a particle with velocity v_{ix} approaching the probe parallel to the x axis with impact parameter y_i . Trajectory T4, with impact parameter greater than sheath radius, never enters the sheath region, and is not subject to an accelerating field at any stage of its trajectory. Trajectories T1, T2 and T3 all enter the sheath region, so that the particles are subject to an accelerating field. Trajectory T2 just grazes the probe, which represents the limiting value of impact parameter, for this initial velocity; all particles approaching the probe with velocity v_{ix} and impact parameter less than this critical value, y_c will be collected. The value of y_c may be calculated easily from conservation of

energy and angular momentum²⁶; Conservation of energy requires that

$$\frac{1}{2} \cdot m \cdot v_{ix}^2 = \frac{1}{2} \cdot m \cdot v_{iy}^2 + q \cdot \Phi(r_p) \quad (3.41)$$

and conservation of angular momentum requires that

$$-m \cdot y_c \cdot v_{ix} = -m \cdot r_p \cdot v_{iy} \quad (3.42)$$

Eliminating the final velocity gives the following expression for critical impact parameter, y_c ;

$$y_c^2 = r_p^2 \left(1 - \frac{q \cdot \Phi(r_p)}{\frac{1}{2} \cdot m \cdot v_{ix}^2} \right) = r_p^2 \left(1 - \frac{q \cdot \Phi(r_p)}{E_o} \right) \quad (3.43)$$

Since the potential is accelerating, the product of charge and potential is always negative, so that the critical impact parameter always exceeds probe radius. The critical impact parameter gives the effective collection area of the probe for a monoenergetic population of particles having velocity v_{ix} . Note that equation 3.43 applies only when the critical impact parameter is less than the sheath radius; this behaviour is termed "impact parameter limited collection", or "orbit limited collection". Figure 3.3 illustrates the case where the converse is true; the sheath thickness is less than the (theoretical) limiting impact parameter, so that all particles entering the sheath are collected. This behaviour is termed "sheath limited collection" and applies when the Debye length is small compared to the probe radius, or for very low energy monoenergetic "swarms". The energy range for which sheath limited probe collection applies may be found from equation 3.43, by setting the critical impact parameter, y_c to be equal to the sheath radius, r_s . This gives a critical energy, E_c which (when normalised by the probe potential energy) is a function of probe and sheath radius;

$$\frac{E_c}{-q \cdot \Phi(r_p)} = \frac{r_p^2}{r_s^2 - r_p^2} \quad (3.44)$$

Figure 3.4 shows a region of parameter space defined by particle impact parameter and normalised incident particle energy, for an accelerating probe. Sheath limited behaviour occurs for particle energies to the left of the dashed vertical line. Consider a probe of radius 1m. In a Low Earth orbit type of plasma with a Debye length of around 1mm, sheath limited behaviour applies until incident particle energy exceeds probe potential energy by a factor of nearly 500, whilst in a more tenuous, hotter plasma such as encountered in the plasmashet, the Debye length may approach 100m and orbit limited behaviour applies for particle energies greater than 1.0×10^{-4} times the probe potential energy. The shaded region of Figure 3.4 represents that part of the parameter space where particles are collected, according to equation 3.43. Note that when particle energy greatly exceeds probe potential energy, only particles

with impact parameter less than or equal to probe radius are collected, which is the limiting case for an uncharged probe.

Retarding probe:

Consider Figure 3.5 which is identical to Figure 3.2 except that the particle trajectories illustrated apply to the case of a retarding probe; electrons approaching a negative probe, or ions approaching a positive probe. Whatever the size of the sheath, the behaviour is always "impact parameter limited" since all particles with initial velocity v_{ix} and impact parameter less than some critical value y_c will reach the probe, providing, of course that the particle has sufficient kinetic energy initially to climb the potential barrier. The method of calculating critical impact parameter, y_c proceeds identically to the calculation for the accelerating case, so that equation 3.43 is still applicable. Note, however that the product of particle charge and probe potential is now positive, so that the critical impact parameter is always less than the probe radius; ie the effective collection area of the probe is reduced. Figure 3.6 represents the behaviour of particle collection by a retarding probe in impact parameter/ normalised energy space. Orbit limited behaviour applies everywhere and the collection region (given by equation 3.43) is shaded. As for an accelerating probe, note that when incident energy greatly exceeds probe potential energy, behaviour approaches that of an uncharged probe.

The preceding theory assumes that the deflection of electrons and ions inside the sheath by the ambient magnetic field is negligible. This is justified by the work of Rubinstein and Laframboise²⁷ who note that the probe current may be sensitive to magnetic fields if $r_L \gg r_p$ (r_L = Larmor radius, r_p = probe radius), if in addition, $r_L \ll \lambda_D$ (Debye length or sheath size). Table 3.1 gives values of r_L and λ_D for electrons and protons moving at the thermal velocity, for several plasma densities and temperatures assuming a dipolar geomagnetic field at $6.6R_E$. From this table, is evident that ions suffer little deflection due to the ambient magnetic field whilst they are in the sheath region, since the proton Larmor radius exceeds the Debye length by a factor of more than 100. For electrons, r_L exceeds λ_D by a factor of 3 for particles moving at the thermal velocity, and is comparable to λ_D for the lower energy particles of the population, but well outside the regime where magnetic field effects are important.

3.1.6 Current collection by a spherical, charged probe in a Maxwellian plasma

The results derived in the previous section for a monoenergetic "swarm" can be applied to any distribution of speeds by integrating over all energies and including the probe collection factor applicable to that energy. For the case of an accelerating probe, this necessitates breaking the energy integral into two parts, one for the sheath limited region, and one for the orbit limited collection region.

The current of particles of a given species collected by a

infinitesimal plane surface in a Maxwellian plasma may be obtained directly from equations 3.14 and 3.17. Multiplying the flux by the charge on each particle, and the total surface area of the probe (of radius r_p) gives the current collected by an uncharged, spherical probe;

$$I_o = 4\pi \cdot r_p^2 \cdot q \cdot \frac{1}{4} \cdot \int_0^\infty v \cdot F(v) \cdot dv = n_o \cdot \pi \cdot q \cdot r_p^2 \cdot \left(\frac{8 \cdot kT}{\pi \cdot m} \right)^{\frac{1}{2}} \quad (3.45)$$

The current incident on the probe, dI_v , due to a single monoenergetic "swarm" of particles with velocity v may be obtained from equation 3.14 to give

$$dI_v = \pi \cdot q \cdot r^2(v) \cdot v \cdot F(v) \cdot dv \quad (3.46)$$

where $r(v)$ is the effective collection radius of the probe, derived in the previous section and given by equation 3.43. In the case of an accelerating probe, the total current is therefore given by

$$I_{acc} = \pi \cdot q \cdot r_s^2 \cdot \int_0^{v_f} v \cdot F(v) \cdot dv + \pi \cdot q \cdot r_p^2 \cdot \int_{v_c}^\infty v \cdot F(v) \cdot \left[1 + \frac{-q \cdot \phi_o}{\frac{1}{2} \cdot m \cdot v^2} \right] \cdot dv \quad (3.47)$$

where v_c is the transition velocity at which sheath limited collection to orbit limited collection occurs. In the long Debye length limit, v_c tends to zero, and the first term of this expression may be ignored. Expanding the second term, and making use of the definition 3.12 for $F(v)$ gives

$$I_{acc} = \pi \cdot q \cdot r_p^2 \cdot \left[\int_0^\infty v \cdot F(v) \cdot dv + \frac{(-q \cdot \phi_o)}{\frac{1}{2} m} \frac{1}{4\pi} \int_0^\infty v \cdot f(v) \cdot dv \right] \quad (3.48)$$

From the definition of the Maxwellian distribution function, equation 3.15, it may be easily verified that, by defining K_i as

$$K_i = \int_0^\infty v^i \cdot f(v) \cdot dv \quad (3.49)$$

then the following recursion relation may be established;

$$K_i = \frac{m}{(i+1) \cdot kT} K_{i+2} \quad (3.50)$$

Using this relation, together with the definition of current collection at zero probe potential gives the following expression for I_{acc} ;

$$I_{acc} = I_o \left[1 + \frac{(-q \cdot \phi_o)}{kT} \right] \quad (3.51)$$

For a retarding probe, there is no contribution to the integral from a sheath limited part, and equation 3.47 still holds, except that only those particles with incident energy greater than the probe potential energy should be considered, and that the product of particle charge and

probe potential becomes positive;

$$I_{ret} = \pi \cdot q \cdot r_p^2 \left[\int_{v_m}^{\infty} v \cdot F(v) \cdot dv - \frac{(q \cdot \phi)}{\frac{1}{2}m} \frac{1}{4\pi} \int_{v_m}^{\infty} v \cdot f(v) \cdot dv \right] \quad (3.52)$$

where the minimum velocity v_m is

$$v_m = \left(\frac{2(q \cdot \phi)}{m} \right)^{\frac{1}{2}} \quad (3.53)$$

Equation 3.52 may be integrated by parts directly to give the following expression for I_{ret} in terms of the current collected by an uncharged probe;

$$I_{ret} = I_o \exp\left[-\frac{q \cdot \phi}{kT}\right]^{\frac{1}{2}} \quad (3.54)$$

Equations 3.51 and 3.54 describe the collection of plasma particles for both accelerating and retarding spherical probes in a Maxwellian plasma with a Debye length much greater than probe radius.

By way of an introduction to spacecraft charging in geostationary plasmas, the two major probe collection equations derived in this section may be combined to predict the equilibrium potential attained by a non-emissive, spherical probe immersed in a stationary, Maxwellian hydrogen plasma where electrons and ions have equal density, n_o , and temperature, T . From equation 3.45, the incident electron and ion currents, I_{eo} and I_{io} , for an uncharged probe (at plasma potential) are given by;

$$I_{eo} = -\pi \cdot e \cdot n_o \cdot r_p^2 \left(\frac{8 \cdot kT}{\pi \cdot m_e} \right)^{\frac{1}{2}} \quad (3.55)$$

$$I_{io} = \pi \cdot e \cdot n_o \cdot r_p^2 \left(\frac{8 \cdot kT}{\pi \cdot m_i} \right)^{\frac{1}{2}} \quad (3.56)$$

where m_e and m_i are the electron and proton mass respectively, and e is the magnitude of the electronic charge. Assuming that the probe acquires a negative potential of magnitude V , then the current collection

equations become;

$$I_e = I_{e0} \cdot \exp\left(-\frac{eV}{kT}\right) \quad (3.57)$$

$$I_i = I_{i0} \left(1 + \frac{eV}{kT}\right) \quad (3.58)$$

At equilibrium, the net current to the probe is zero;

$$I_e + I_i = 0 \quad (3.59)$$

This equation may be rearranged by substituting equations 3.57, 3.58, 3.55 and 3.56 and then cancelling common terms;

$$\left(\frac{m_i}{m_e}\right)^{\frac{1}{2}} \cdot \exp\left(-\frac{eV}{kT}\right) = 1 + \frac{eV}{kT} \quad (3.60)$$

If the ions are protons, then the square root of the proton to electron mass ratio is equal to 42.85. Replacing eV/kT by the dimensionless quantity, x , one obtains a transcendental expression which can only be solved numerically;

$$42.85e^{-x} - x - 1 = 0 \quad (3.61)$$

A simple Newton-Raphson iteration process gives the value $x = 2.5037$. Physically, a spherical, non-emissive probe immersed in a stationary Maxwellian plasma composed of protons and electron populations of equal density and temperature will acquire a negative potential equal to 2.5 times the plasma temperature, provided that the probe is much smaller than the Debye length of the plasma.

This simple, idealised calculation illustrates two important points to note concerning spacecraft charging. Firstly, even the simplest possible physical situation which can be modelled requires solution by a numerical method. Secondly the calculation shows that in the plasmashet region, where plasma temperature frequently reaches several keV, exposed spacecraft surfaces may acquire potentials of several kV negative relative to the plasma, or more importantly, to other parts of the spacecraft.

Table 3.1
Debye Lengths and Larmor Radii for several particle populations

n (cm ⁻³)	kT (eV)	λ_D (m)	(e ⁻) r _L (m)	(p ⁺) r _L (m)
0.5	10 ¹	33	96	4,103
0.5	10 ²	105	303	12,973
0.5	10 ³	332	958	41,024
0.5	10 ⁴	1051	3028	129,731
1.0	10 ¹	24	96	4,102
1.0	10 ²	74	303	12,973
1.0	10 ³	235	958	41,024
1.0	10 ⁴	743	3028	129,731

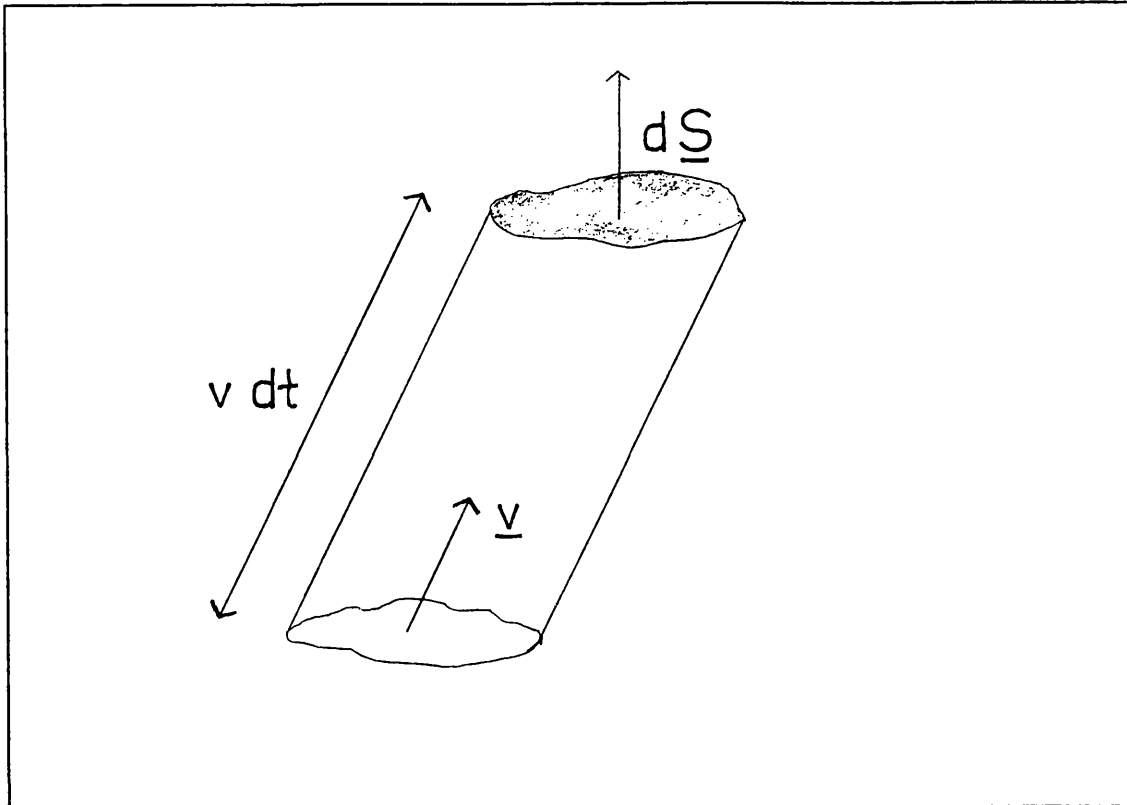


Figure 3.1 Slanted cylinder for incident flux calculation

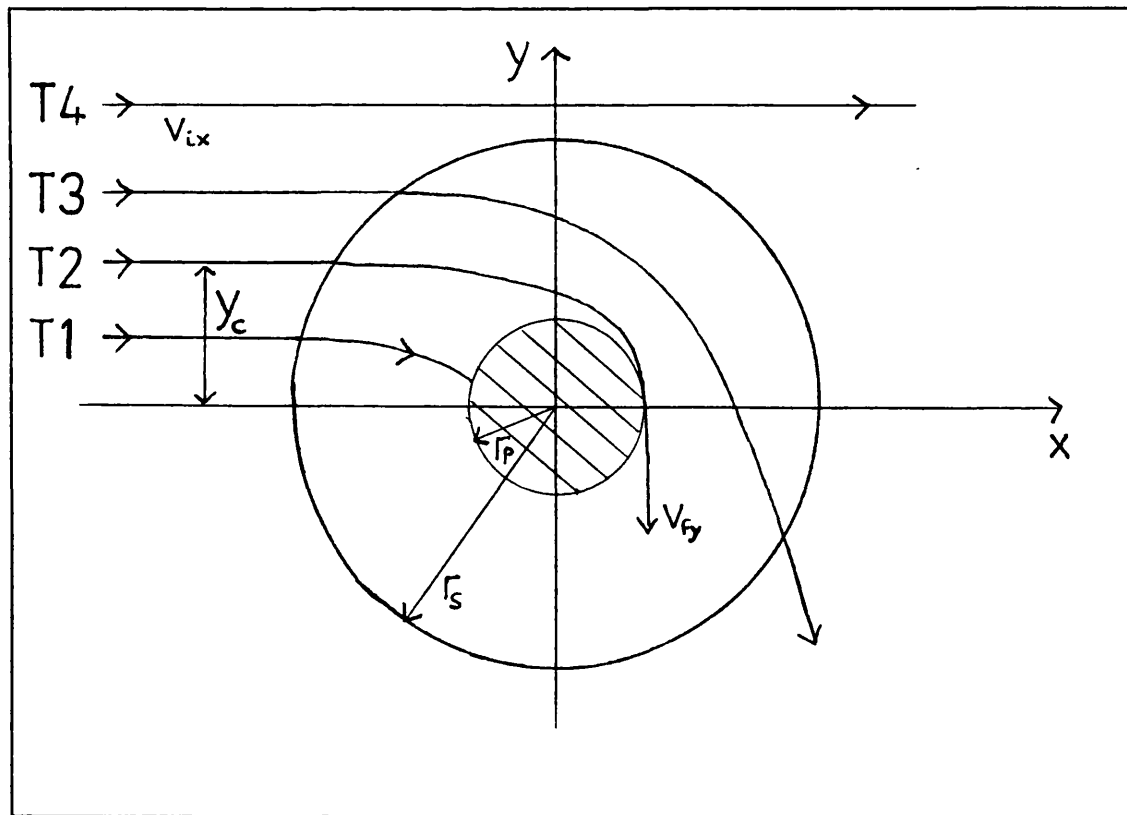


Figure 3.2 Accelerating probe; orbit limited collection

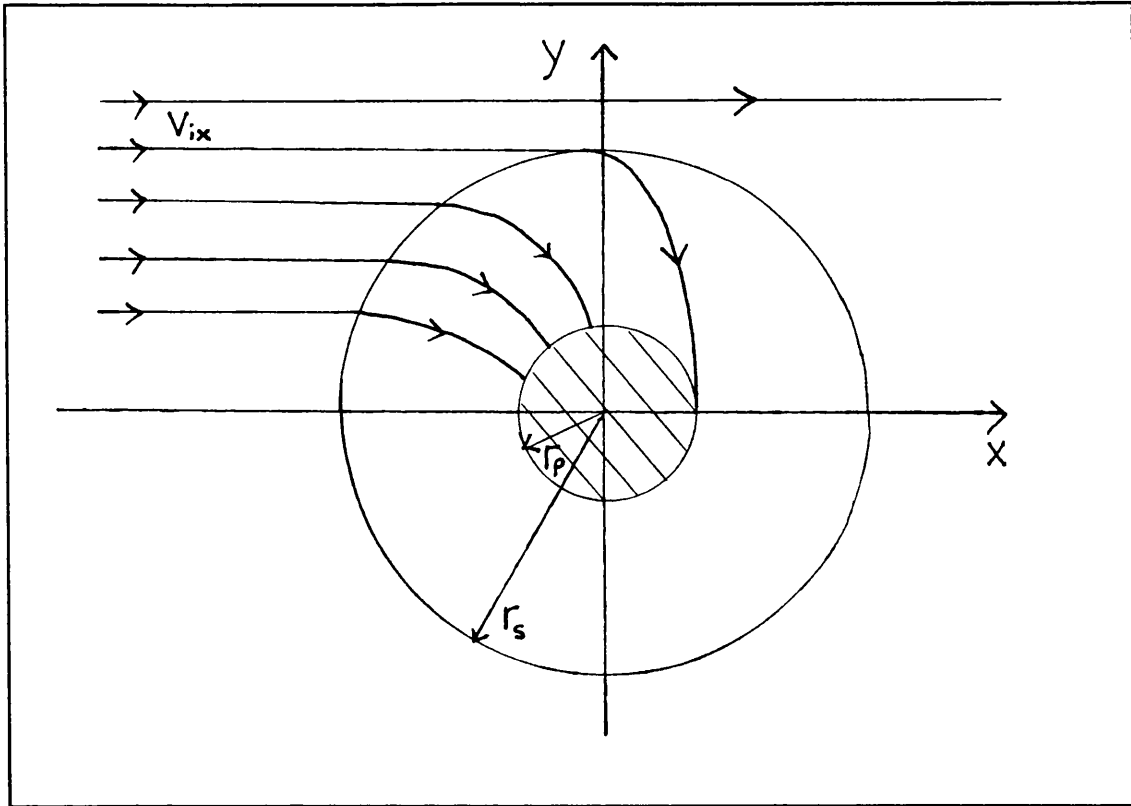


Figure 3.3 Accelerating probe; sheath limited collection

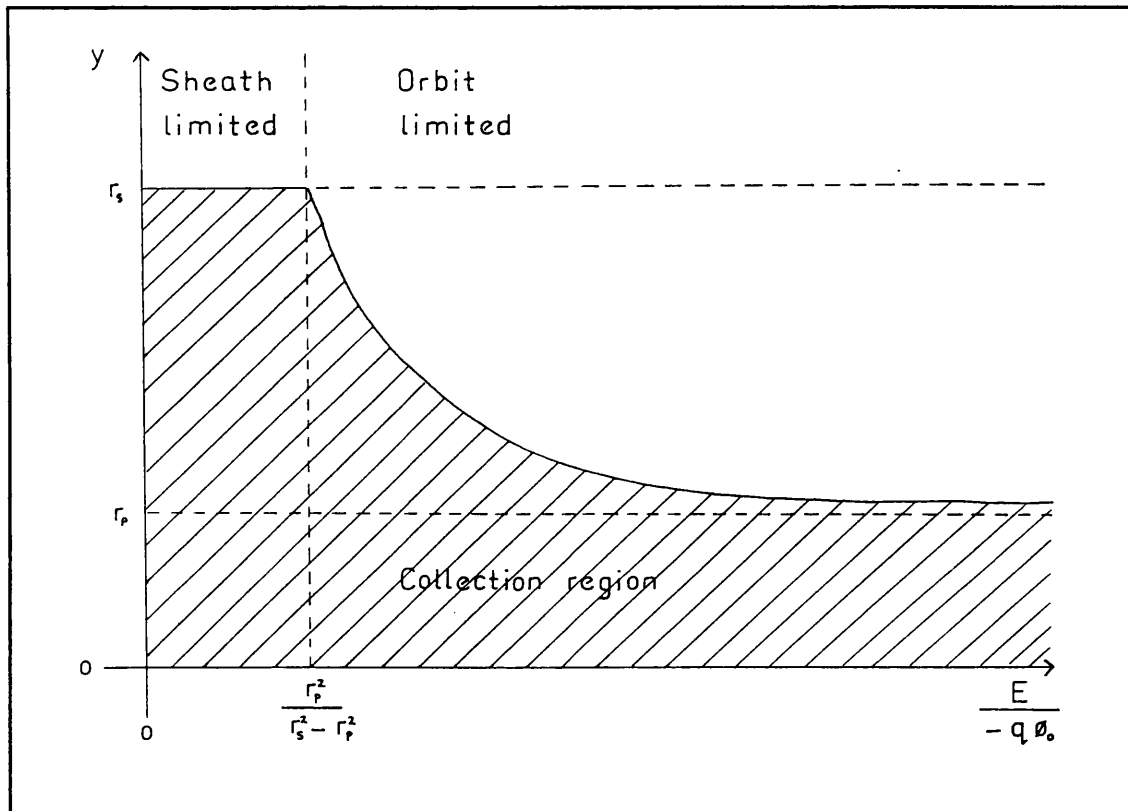


Figure 3.4 Accelerating probe collection region

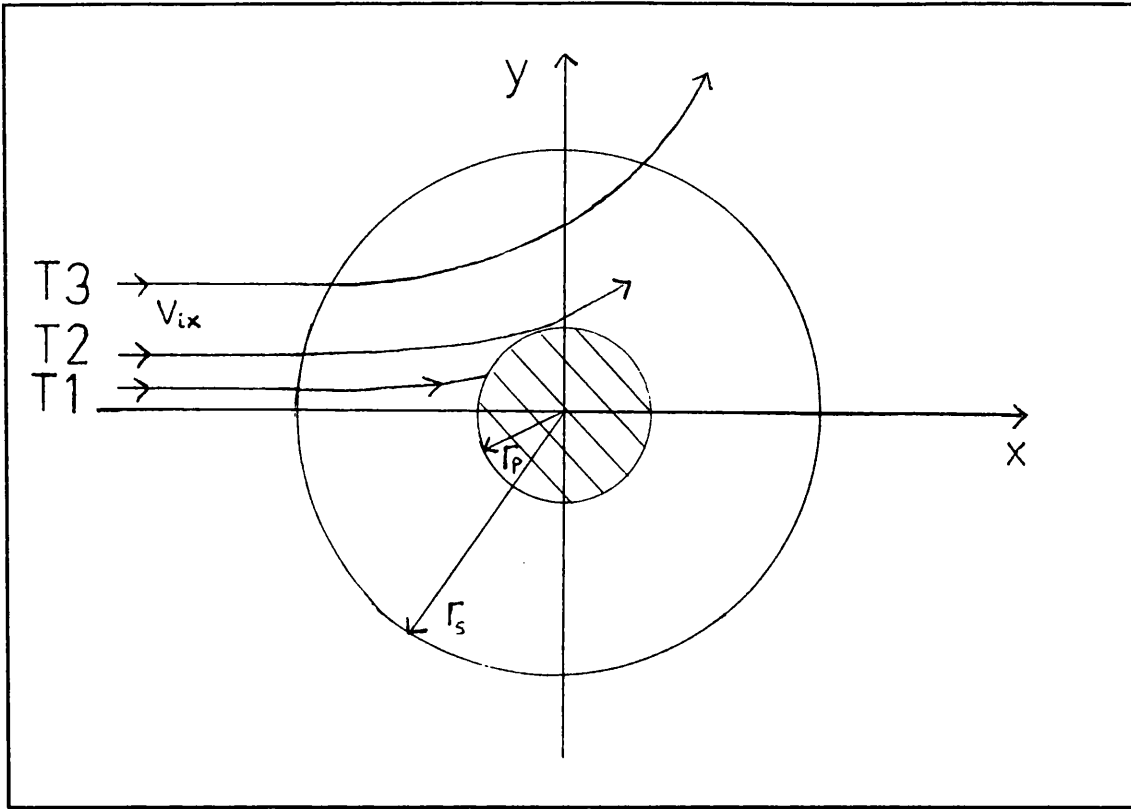


Figure 3.5 Retarding probe; orbit limited collection

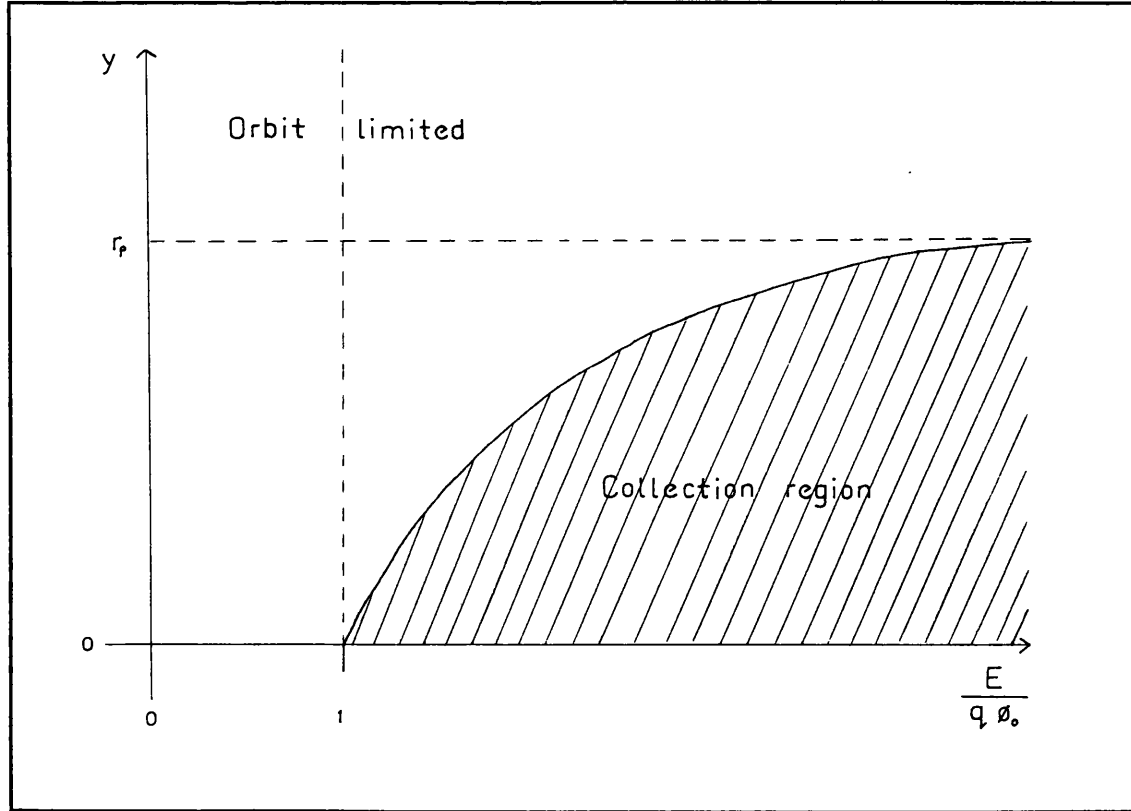


Figure 3.6 Retarding probe collection region

3.2 SURFACE MATERIAL PHYSICS

A review is presented of theory and models for secondary emission due to electron impact, electron backscatter, secondary electron emission due to ion impact, photoemission, bulk conductivity and surface conductivity.

3.2.1 Secondary electron emission due to electron impact.

When electrons impinge on a solid surface, they suffer both elastic and inelastic collisions at scattering centres within the target. Those electrons within the target material which are ionised by inelastic collisions with primary electrons, then migrate back to the surface and emerge as true "secondary electrons". This phenomenon was first discovered by Austin and Starke²⁸ in 1902. Primary electrons which undergo elastic collisions near the surface of the target, and re-emerge from the surface without significant energy loss are termed "backscattered electrons" and are discussed more fully in section 3.2.2.

The secondary electron emission (SEE) yield is defined as the number of true secondary electrons emitted per primary electron, and often exceeds unity for certain target materials within some energy range, but is always a non-negligible component of the current balance equation. Indeed, in many cases, the equilibrium potential of a surface is determined by the balance between the incident and secondary (including backscatter) currents. Accurately known secondary electron emission yields are necessary²⁹ for modelling spacecraft charging, and indeed for spacecraft surface design. However, there is a marked shortage of SEE yield measurements in the literature, particularly at high incident energies (5 to 50 keV), and for oblique angles of beam incidence.

Several theoretical and semi-empirical models for SEE yield have been proposed, and will be discussed later, but all agree on the basic physical principles which are involved. Consider a monoenergetic, unidirectional electron beam incident normally on a solid target of any material. Apart from those electrons which suffer elastic collisions at the first few scattering centres, most of the primary electrons suffer a series of inelastic collisions with lattice electrons, to which they lose energy. As the primary electron loses energy by ionisation, the collision cross-section with lattice electrons increases until the primary electron finally is "stopped" as it deposits all its remaining energy in a Bragg peak near the limit of its range. Secondary electrons are therefore excited at a rate proportional to the local energy loss rate of the primaries (termed the "stopping power"). Each scattering event produces a secondary electron whose energy and direction are determined by the dynamics of the scattering process; factors include arrival direction of the primary relative to the lattice, lattice structure, chemical composition of the target and energy of the primary electron. Once a secondary electron has been liberated, it must migrate back to the surface of the material³⁰; a process which is identical to the

passage of the primary. Secondaries also suffer inelastic collisions which may liberate tertiary (and possibly higher order) electrons since the secondary electron has a much smaller mean free path between collisions than the primary electrons. Migrating secondaries must also overcome the work function (for a metal) or the band gap energy plus electron affinity (for an insulator or semi-conductor) before emerging into vacuum, so it is apparent that only a very thin layer near the surface of the target material contributes to the secondary yield. Due to the nature of the scattering and migration processes, secondary electrons tend to be emitted isotropically from the surface with an approximately Maxwellian energy distribution with a characteristic temperature of about 2 eV³¹. When the monoenergetic electron beam is not normally incident, the total yield increases since the secondary electrons are liberated closer to the vacuum surface than they were in the case of a normal beam. The net yield for an isotropically incident population is obtained by integrating unidirectional yield functions for every value of incident angle, and is always greater than the yield for normal incidence at the same incident energy.

These processes may be modelled mathematically to give a theoretical expression for the secondary yield. A general expression for the secondary yield of electrons with energy E_0 and normally incident can be written as follows (Dionne³²);

$$\delta = \int_0^{\infty} n(x, E_0) \cdot f(x) \cdot dx \quad (3.62)$$

where $n(x, E_0) \cdot dx$ is the average number of secondary electrons produced by each incident primary electron at depth x within the slab dx and $f(x)$ is the probability that the secondary electron migrates and finally escapes from the surface. The function $n(x, E_0)$ is equal to the stopping power dE/dx (for particles of incident energy E_0 at depth x in the target material) divided by the energy required to liberate a single secondary electron from the lattice, e_0 ;

$$n(x, E_0) = -\frac{1}{e_0} \left(\frac{dE(x, E_0)}{dx} \right) \quad (3.63)$$

Thus far, the expressions presented are completely general. To proceed further, it is necessary to make approximations for the form of the stopping power, dE/dx , and of the escape probability, $f(x)$. The latter must combine the directional effects of the scattering process which liberated the secondary, together with the effects of further scatters during the migration process, which may itself include some dependence on dE/dx (albeit at very low energies). Several workers have formulated expressions for dE/dx and $f(x)$ to arrive at an expression for the total yield which is based on a small number of parameters deduced from fitting with experimental data. Some of these differing approaches are given below:

(a) **The Dionne Expression**^{32,33};

Dionne assumes that the stopping power may be expressed as a power law;

$$\frac{dE}{dX} = -\frac{A}{E^{n-1}} \quad (3.64)$$

where A is a constant and $n > 1$. From the turning point of the E(x) function, the maximum penetration depth, d for a given incident energy E_0 is given by

$$d = \frac{E_0^n}{A \cdot n} \quad (3.65)$$

In order to take into account the scattering of primary electrons, a further assumption is made that the number of secondaries produced per unit pathlength is constant, and that the number of primaries decreases linearly with increasing depth. This leads to the following expression for $n(x, E_0)$;

$$n(E_0) = \frac{1}{E_0} (A \cdot n)^{\frac{1}{n}} \cdot d^{\frac{(1-n)}{n}} \quad (3.66)$$

For a one-dimensional model, Dionne assumes that the migration and escape probability function, $f(x)$ decreases exponentially with depth;

$$f(x) = B \cdot \exp(-\alpha \cdot x) \quad (3.67)$$

where B is the escape probability and α is an inverse migration distance (or inverse mean free path). Substituting equations 3.66 and 3.67 into the general expression 3.62, and noting that the maximum penetration depth is d, gives the following expression for total yield;

$$\delta = \frac{B}{E_0} \int_0^d (An)^{\frac{1}{n}} \cdot d^{(1-n)/n} \cdot e^{-\alpha x} \cdot dx \quad (3.68)$$

which may be integrated directly to give

$$\delta = \frac{B}{E_0} \left(\frac{An}{\alpha} \right)^{\frac{1}{n}} \cdot (\alpha d)^{\frac{1}{n}-1} \cdot (1 - e^{-\alpha d}) \quad (3.69)$$

This expression includes several constants which are peculiar to the target material (the energy dependence enters via the d parameter), and it is customary to re-formulate 3.69 in terms of the maximum yield, and the energy at maximum yield. The maximum yield (with respect to $\alpha \cdot d$) is found by setting the derivative of 3.69 to zero which gives rise to the

following transcendental expression for $\alpha \cdot d$;

$$\alpha d_m = \left(1 - \frac{1}{n}\right) (e^{\alpha d_m} - 1) \quad (3.70)$$

At this point, one is forced to choose a value for n , the energy loss power-law index. Dionne suggests $n = 1.35$ for the energy range 0.3 to 7.25 keV, but $n = 1.66$ for energies up to 40 keV. Putting $n = 1.35$ into 3.70 gives the result that $\alpha \cdot d$ (at maximum yield) = 2.28. Equation 3.69 may now be re-expressed in terms of the maximum yield, and energy at maximum yield, E_{om} ;

$$\delta(E_o) = 1.114 \delta_m \left(\frac{E_{om}}{E_o}\right)^{0.35} \left\{1 - \exp\left[-2.28 \left(\frac{E_o}{E_{om}}\right)^{1.35}\right]\right\} \quad (3.71)$$

It is a simple matter to extend this idea to include non-normal incidence. The parameter d is the distance through the target material to which the primaries penetrate, so the depth to which they penetrate (important in the definition of the function $f(x)$), is given by $d \cdot \cos(\theta)$ where θ is the angle between the beam and surface normal. This can be incorporated into the preceding theory by replacing alpha with $\alpha \cdot \cos(\theta)$, to give the following result;

$$\delta(\theta, E_o) = \frac{1.114 \delta_m}{\cos(\theta)} \left(\frac{E_{om}}{E_o}\right)^{0.35} \left\{1 - \exp\left[-2.28 \cos(\theta) \left(\frac{E_o}{E_{om}}\right)^{1.35}\right]\right\} \quad (3.72)$$

where δ_m and E_{om} are the maximum yield and energy at maximum yield for normal incidence (which, of course is the minimum yield for a given energy for all angles of incidence). When the distribution of primaries is isotropic, or random, the "angle-averaged yield" becomes the important parameter. This is the average yield obtained per single primary arriving from a random direction, given by

$$\bar{\delta}(E_o) = \frac{\int_0^1 \cos\theta \cdot \delta(\cos\theta) \cdot d(\cos\theta)}{\int_0^1 \cos\theta \cdot d(\cos\theta)} \quad (3.73)$$

which results in the following expression for the angular dependent yield expression of equation 3.72;

$$\bar{\delta}(E_o) = 1.114 \delta_m \left(\frac{E_{om}}{E_o}\right)^{0.35} \left\{\frac{2(Q-1+e^{-Q})}{Q}\right\} \quad (3.74)$$

where

$$Q = 2.28 \left(\frac{E_o}{E_{om}}\right)^{1.35} \quad (3.75)$$

Whipple³⁴ notes that the effect of an isotropic primary distribution is

to increase the yield, and shift the position of the maximum isotropic yield to a higher energy.

(b) **The NASCAP/KATZ expression³⁵**;

This is identical to Dionne's theory except for the formulation of stopping power, dE/dx , which includes an extra term in the power series expansion. Defining electron range as R , dE/dx is evaluated from the following equation;

$$R = r_1 E^{n_1} + r_2 E^{n_2} \quad (3.76)$$

where r_1 , r_2 , n_1 and n_2 are constants which depend on the target material. The stopping power is assumed to be linear in x , and may be evaluated as follows;

$$\frac{dE}{dx} = \left(\frac{dR}{dE_0}\right)^{-1} + \frac{d^2R}{dE_0^2} \left(\frac{dR}{dE_0}\right)^{-3} x \quad (3.77)$$

Using an identical definition for $f(x)$ (equation 3.67), and substituting 3.67 and 3.77 into 3.62 gives the following expression for total yield, noting that the integration has been taken to the particle range, R_0 which is determined by either $dE/dx = 0$, or the point where the primary has lost all energy;

$$\delta(E, \theta) = \frac{B}{e_0} \left[R_0 \left(\frac{dR}{dE_0}\right)^{-1} \left(\frac{1-e^{-Q}}{Q}\right) + R_0^2 \frac{d^2R}{dE_0^2} \left(\frac{dR}{dE_0}\right)^{-3} \left(\frac{1-(Q+1)e^{-Q}}{Q^2}\right) \right] \quad (3.78)$$

where

$$Q = \alpha R_0 \cos(\theta) \quad (3.79)$$

note that the first term of this expression is the same as that of Dionne (equation 3.69), since R and d are identical. It is now impossible to find an analytical expression for the maximum yield, and the energy of the maximum yield due to the addition of this second, higher order term. Instead, these quantities are specified (from experimental data) along with the constants which appear in equation 3.76 to enable the yield to be computed for any energy. The angle-averaged yield is computed in the same fashion as the Dionne expression and is given by the following;

$$\bar{\delta}(E) = \frac{B}{e_0} \left[R_0 \left(\frac{dR}{dE_0}\right)^{-1} Z_1(Q) + R_0^2 \left(\frac{d^2R}{dE_0^2}\right) \left(\frac{dR}{dE_0}\right)^{-2} Z_2(Q) \right] \quad (3.80)$$

where

$$Z_1(Q) = \frac{2(Q-1+e^{-Q})}{Q} \quad (3.81)$$

and

$$Z_2(Q) = 2 \int_0^1 u \cdot du \frac{1 - (Qu+1)e^{-Qu}}{Q^2 u^2} \quad (3.82)$$

and Q has been evaluated for normal incidence.

(c) **Estimates of maximum yield; Ono and Kanaya³⁶.**

Ono and Kanaya give expressions for secondary yield in a very similar fashion to (a) and (b), above, but they also give semi-empirical relationships which relate the maximum yield, and energy at maximum yield to atomic number Z , first ionization energy I (in eV), and backscatter coefficient, r ;

$$E_m = 57.9Z^{1/5} I^{4/5} (1+5r^2)^{4/5} \text{ (eV)} \quad (3.83)$$

$$\delta_m = 0.12Z^{1/5} I^{4/5} (1+1.26r) \quad (3.84)$$

r is a function of Z and n (the range energy power)³⁶. The parameter r increases smoothly with increasing Z from 0.07 (for Li, $Z=3$) to 0.45 (Th, $Z=90$). Other useful values are Al ($Z=13$, $r=0.20$), Cu ($Z=29$, $r=0.34$), Au ($Z=79$, $r=0.45$).

(d) **Emission from Polymers; Burke³⁷.**

Burke's analysis is identical to that of Dionne, except that he chooses a value of $n=1.725$ (see equation 3.65) for the range-energy formula, instead of 1.35, although both theories may be easily modified to accommodate a different value of n . Burke introduces an "emission coefficient", K for polymers, which, when combined with the empirical constant relationship between maximum yield and energy at maximum yield enables these quantities to be derived for lightly halogenated polymers, from their chemical compositions. The empirical relationship between K and the number of valence electrons, N in a repeating polymer unit (1,4,5,6 for H,C,N,O) and M (the gram molecular weight) is

$$K = 10.64 \left(\frac{N}{M} \right) - 3.15 \quad (3.85)$$

the energy at maximum yield (in keV) is related to K as follows;

$$E_{om} = \left(\frac{K}{12.09} \right)^{0.580} \quad (3.86)$$

and the maximum yield is related to E_{om} by;

$$\delta_m = 9.5E_{om} \quad (3.87)$$

Although this holds for most of the polymers studied by Burke, only Teflon (CF_2) was heavily halogenated and has a constant of proportionality

of 5.3. By means of a derivation identical to that of Dionne, Burke gives the following equation for yield as a function of incident energy;

$$\delta(E_o) = 1.526\delta_n g_n(Z) \quad (3.88)$$

where

$$g_n(Z) = \frac{1 - \exp(-Z^{1.725})}{Z^{0.725}} \quad (3.89)$$

and

$$Z = 1.284 \frac{E_o}{E_{om}} \quad (3.90)$$

Values of the emission constant, K for some common polymers are Teflon (CF_2 , $K=1.546$), Mylar ($C_{10}H_8O_4$, $K=0.847$) and Kapton ($C_{22}H_{10}O_5N_2$, $K=0.682$).

Having summarised the four main theoretical formulations which appear in the literature, it is instructive to compare these expressions with published experimental data. Five target materials are chosen; Kapton, Teflon, Aluminium, Al_2O_3 , and Gold since they represent a wide range of material types, and are frequently to be found on spacecraft surfaces. One problem encountered whilst surveying the literature for such data is that workers frequently fit their data to one of the approaches above, and quote the maximum yield, and energy at maximum yield rather than the measured data points. Also, some authors quote data for total secondary yield (true SEE + backscatter), rather than true secondary yield which necessitates a correction for backscatter before a realistic comparison can be made. Principal measurements of yield for metals and some oxides have been performed by Kollath³⁸, Bruining^{39,40}, and Dekker⁴¹ whilst measurements on polymers have been made by Willis and Skinner⁴², Matskevitch⁴³ and Levy⁴⁴. The data is presented as five yield versus energy curves for Kapton, Teflon, Aluminium, Al_2O_3 , and Gold; Figures 3.7 to 3.11 respectively.

Figure 3.7 shows the normal incidence true secondary electron yield for Kapton. The curve marked "NASCAP" is a plot based on the Katz formulation, equation 3.78, using data fitted to measurements by Levy et al⁴⁴ (max yield = 1.90, energy at max yield = 200 eV, $r_1 = 70\text{\AA}$, $n_1 = 0.6$, $r_2 = 300\text{\AA}$, $n_2 = 1.75$). The curve marked "Dionne" is a plot of the Dionne expression (equation 3.71) for the values of max yield and energy given above; the curve marked "Burke" is a plot of equation 3.88 where the maximum yield is 1.806 at 190 eV, based on properties of the polymer given by equations 3.85 and 3.86. The experimental points marked "W+S" are taken from the work of Willis and Skinner⁴², and corrected for backscatter yield by equation 3.102 (the Burke expression for backscatter yield in polymers, marked "W+S (1)") and equations 3.94, 3.99 and 3.100 (the Everhart theory of backscatter, marked "W+S (2)"). Experimental

points are also shown from Gair⁴⁵ and from Levy⁴⁴ (corrected for backscatter by the two expressions noted above, denoted "Levy (1)" and "Levy (2)"). Several points are evident from this figure; at high incident energies, the Dionne expression gives a much higher yield than the NASCAP formula for the same maximum, but the Burke expression and NASCAP formula agree well, although the maxima are not quite coincident. Apart from the position of the maximum, the Burke and Dionne formulae are identical (both are based on a constant energy loss approximation), except for the energy loss power law, (Burke assumes that dE/dx is proportional to $E^{-0.725}$ whilst Dionne assumes dE/dx is proportional to $E^{-0.35}$). Consider next the experimental data for energies above 500 eV. The NASCAP curve has been computed by means of a fit to the data of Levy, so the agreement here is expected. Furthermore, Burke based his choice of power law on the high energy data of Gair which accounts for the good agreement at high energy. However, the most striking feature of Figure 3.7 is the discrepancy between the experimental data of Willis and Skinner and that of Levy et al. The reason for this is unclear; apart from a systematic experimental error (for example the measurement of incident current or leakage current) in one or both sets of measurements, the most likely reasons are the standard of surface cleanliness of the test samples, or possibly their previous irradiation history (and hence internal charge distribution). If the discrepancy is indeed due to one of the latter reasons, then such variability in the SEE properties of Kapton should be incorporated into any charging simulations. At lower energies, the three expressions all appear to underestimate the height of the peak, although they correctly predict its energy. This should be treated with care, since the models employed to correct for backscatter are least accurate at these energies, and appear to underestimate the backscatter yield.

Turning next to a Teflon target, Figure 3.8 shows the three theoretical models along with some experimental data points. The curve marked "NASCAP" is based on equation 3.78 using the standard NASCAP materials data¹⁹ (max yield = 3.0, energy at maximum = 300 eV, $r_1 = 45.4\text{\AA}$, $n_1 = 0.4$, $r_2 = 218\text{\AA}$, $n_2 = 1.77$); the curve marked "Dionne" was computed using equation 3.71 with the same maximum as the NASCAP expression, and the curve marked "Burke" based on equation 3.88 and a maximum yield of 2.882 at 303 eV. (These parameters are based on a measured value of emission constant, $K = 1.546$, since Teflon is a heavily halogenated polymer and does not fit well with Burke's theoretical values for K). The experimental data points are taken from measurements by Willis and Skinner⁴² and corrected for backscatter by the two methods mentioned for Kapton. This time, the NASCAP and Burke equations agree closely, and are in good agreement with the experimental data. The equation of Dionne once again predicts a higher yield at high energies. There is complete agreement at low energies and near the peak.

Figure 3.9 shows the theoretical and experimental data for a clean aluminium sample (ie without an oxide layer). The "NASCAP" curve is based

on data from the NASCAP code¹⁹ (max yield = 0.97 at 300 eV, $r_1 = 154\text{\AA}$, $n_1 = 0.8$, $r_2 = 220\text{\AA}$, $n_2 = 1.76$) and the "Dionne" curve based on equation 3.71 with the same maximum as the NASCAP expression. Experimental data is taken from Bruining and de Boer³⁹ (marked "Bruining") and Kollath³⁸. The NASCAP and Dionne expressions exhibit the familiar discrepancy at high energy, but both agree well with experimental data near the peak. Throughout the literature, there is a marked dearth of data for clean aluminium at high (>1 keV) incident energy.

Figure 3.10 shows the yield curve for Al_2O_3 , or more correctly for an Aluminium sample with an oxide layer. The "NASCAP" curve is based on a fit to the data of Levy et al⁴⁴ (max yield = 3.20 at 350 eV, $r_1 = 50\text{\AA}$, $n_1 = 0.66$, $r_2 = 100\text{\AA}$, $n_2 = 1.65$) and the "Dionne" curve is based on an identical maximum. The familiar discrepancy between NASCAP and Dionne expressions at high energy is evident, but more interesting is the huge difference between these results, and those for clean aluminium (Figure 3.9). In fact, Bruining⁴⁰ notes that the maximum yield can vary between 1.5 and 4.8 (at energy 350 to 1300 eV) presumably according to the thickness of the oxide layer. Levy et al quote their data for "Aluminium", but the results are so different from that of the clean metal, they were almost certainly measuring the properties of the oxide layer. For spacecraft charging simulations, however, it may be more appropriate to use data for aluminium oxide whilst noting that the yield can vary considerably according to the thickness of the layer (which is related to age and preparation of the material).

The yield curve for the final example material, gold is shown in Figure 3.11. The "NASCAP" yield curve has been fit to measurements by Levy et al (max yield = 1.3 at 800 eV, $r_1 = 88.8\text{\AA}$, $n_1 = 0.92$, $r_2 = 53.5\text{\AA}$, $n_2 = 1.73$) although the original data does not appear to have been published. The "Dionne" curve is based on the same maximum position. Experimental data have been taken from Kollath³⁸ and Warnecke⁴⁶. There is clearly some discrepancy, but it is not clear how the experimental data was corrected for backscatter. Furthermore, there is an absence of data for incident energies above 1 keV.

3.2.2 Backscattering of incident electrons

True secondary electrons are usually defined as those electrons re-emitted from a surface under electron bombardment with energy less than 50 eV. Re-emitted electrons with energy between 50 eV and that of the incident beam are termed as "backscattered". Setting this threshold at 50 eV is a somewhat arbitrary decision, but it is supposed to be indicative of the two different physical processes which cause the emission of an electron. Backscattered electrons are primary electrons which have suffered only one or two scattering events within the first few angstroms of the target material whilst true secondaries (see 3.2.1) originate within the target and have been liberated by the ionising primary. Most secondary yield measurements consist of firing a monoenergetic, unidirectional beam normally at a target, and measuring

the total yield of secondaries (true secondaries plus backscatter) of all energies which are emitted. For the purposes of modelling spacecraft charging, it is important to make a clear distinction between the two types of emission. Spacecraft tend to develop complicated systems of potential contours which often includes the formation of potential barriers. Often, backscattered secondaries (most of which have energies close to the primary electrons) are able to escape from such barrier systems, whilst true secondaries (with energy less than 50 eV) are not.

The theory of electron backscatter is based on two principles; a range-energy relationship and a scattering model. The initial theory was developed by Everhart⁴⁷ and Archard⁴⁸, then refined by McAfee⁴⁹, Darlington and Cosslett⁵⁰ and Katz³⁵. Everhart used the Thomson-Widdington slowing down law;

$$\frac{dE}{dX} \propto \frac{1}{E} \quad (3.91)$$

together with the Rutherford scattering law to formulate the following expression for backscatter yield for normally incident particles (Z = atomic number of the target material);

$$\eta(0, Z) = \frac{a-1+(1/2)^a}{a+1}; \quad a = 0.045Z \quad (3.92)$$

McAfee has extended this to include the energy distribution of backscattered electrons;

$$\eta_0(\kappa, Z) = \frac{a-1-\kappa^2(a+1)+2[\frac{1}{2}(1+\kappa^2)^{a+1}]}{(1-\kappa^2)(a+1)} \quad (3.93)$$

which is the backscatter yield at normal incidence of particles having energy κE_p to E_p (E_p is the energy of the primary beam). This reduces to Everhart's theory (equation 3.92) when $\kappa = 0$. Darlington and Cosslett extend Archard's theory to give the variation of backscatter yield with incident beam arrival angle, θ (measured from the normal);

$$\frac{\ln\left(\frac{\eta(\theta)}{\eta(0)}\right)}{1-\cos\theta} = F(Z, E) \quad (3.94)$$

where F is constant for a given material, and is independent of energy when the Thomson-Widdington law holds. According to Katz et al³⁵, the value of F may be fixed by assuming that at grazing incidence ($\theta = 90^\circ$) the total backscatter yield is unity; this gives

$$F(Z, E) = -\ln(\eta(0)) \quad (3.95)$$

and results in the following expression for the angular dependence of

backscatter yield;

$$\eta(\theta) = \eta(0)\exp[-\ln(\eta(0))(1-\cos\theta)] \quad (3.96)$$

The angle-averaged yield (or net albedo) is given by

$$\bar{\eta} = \frac{\int_{-1}^0 \cos\theta \cdot \eta(\cos\theta) \cdot d(\cos\theta)}{\int_{-1}^0 \cos\theta \cdot d(\cos\theta)} \quad (3.97)$$

which gives the following expression (using equation 3.96);

$$\bar{\eta} = \frac{2}{[\ln(\eta(0))]^2} [1 - \eta(0)(1 - \ln(\eta(0)))] \quad (3.98)$$

According to Shimizu⁵¹, for incident energies below 10 keV, the backscatter yield increases by about 0.1, almost independently of Z. According to Katz et al³⁵, this may be modelled by adding the following term to the normal incidence backscatter yield;

$$\delta\eta(0) = 0.1\exp\left(\frac{-E}{5000}\right) \quad (3.99)$$

where E is measured in eV. Physically, this may be attributed to the breakdown of the Thomson-Widdington stopping power law for incident energies below 10 keV. At incident energies below 50 eV, by definition, backscatter and secondary emission are indistinguishable, but just above this threshold, there is an absence of any measured data. Equation 3.99 is really only applicable down to 1.0 keV so there is considerable uncertainty about how to model intermediate energies. Katz et al³⁵ note that the backscatter coefficient becomes very small at low energies, and propose the following multiplication factor for normal incidence yield below 1.0 keV (without any apparent physical justification);

$$\frac{\ln\left(\frac{E}{50}\right)}{\ln(20)}; \quad 50 < E(eV) < 1000 \quad (3.100)$$

where E is the incident energy, (in eV) and the yield at 50 eV becomes equal to zero.

Combination of equations 3.92, 3.99 and 3.100 give the normal backscatter yield for a target material of atomic number, Z for incident particle energies above 50 eV. Equation 3.96 may be used to give the variation of yield with incident angle, and equation 3.98 gives the angle averaged yield (or albedo).

There are two other formulations for the normal incidence backscatter yield which appear in the literature as alternative forms of

equation 3.92. Katz et al³⁵ give the following equation;

$$\eta(0) = 1 - \left(\frac{2}{E}\right)^{0.037Z} \quad (3.101)$$

and Burke³⁷ gives the following energy dependent relationship for polymers containing H,C,N and O, based on experimental data;

$$\eta(0) = 0.115E_0^{-0.223} \quad (3.102)$$

where E_0 is the incident electron energy in keV.

Experimental backscatter yield data is scarce and mainly confined to energies above 10 keV where it is of interest to electron microscopy research. Figure 3.12 shows the theoretical value of backscatter yield at normal incidence based on equations 3.92, 3.99 and 3.100 for aluminium ($Z = 13$) and silver ($Z = 47$). Also shown are experimental results from Palluel⁵² and Sternglass⁵³ (marked "Palluel") and from Darlington and Cosslett⁵⁰ and (marked "D+C"). In both cases, the fit is rather poor, particularly at low incident energies (below 1 keV).

For Aluminium, there are no measurements below 300 eV, although inspection of the upper panel of Figure 3.12 indicates that the maximum backscatter yield might occur in this region. The measurements of Palluel and Sternglass seem to be inconsistent with those of Darlington and Cosslett, except at about 10 keV where all experimental data and theoretical models seem to agree.

For a silver target, the theoretical expression begins to approach the data of Darlington and Cosslett, at least in terms of the energy of maximum yield (1 keV) and the overall shape of the curve at lower energies. As for aluminium, the two sets of experimental data are inconsistent, except for energies above 10 keV where (by extrapolation) they appear to converge, and agree with the theoretical curve.

3.2.3 Secondary emission yield due to ion impact

The physical processes which take place when ions are incident on a solid surface are shown schematically in Figure 3.13 which is based on a summary by McCracken⁵⁴. Incident ions may deposit energy into the target via inelastic interactions with the atomic electrons, or by interaction with the lattice atoms. The latter process results in point defects, displacements of lattice atoms and sputtering which do not contribute significantly to the current balance equation. The interaction of incident ions with atomic electrons within the target gives rise to the emission of secondary electrons, x-rays and optical photons.

The theory of secondary electron emission (SEE) due to ion impact is very similar to that of SEE due to electron impact; incident particles deposit energy in the target material thus liberating secondary electrons which migrate away from their point of excitation. The model for secondary migration and escape probability discussed in section 3.2.1 applies equally well here.

Heavy ions (eg O⁺), can create extra "free" electrons in the target by means of an Auger emission process called "potential emission". An incident ion is neutralised by pulling an inner shell electron from a nearby target atom; the photon emitted as an outer shell electron fills the vacancy never leaves the atom; it is captured by another orbital electron which is then ejected. If the ionisation energy of the ion is less than twice the work function of the metal, no potential emission can occur. In any case, the yield due to potential emission tends to be less than 0.1 and is usually neglected from the current balance equation.

At higher energies, any type of incident ion (including H⁺) can cause the emission of an electron by a process called "kinetic secondary electron emission". An incident ion collides with a target atom and causes an inner shell (valence) electron to be injected into the conduction band, leaving an inner shell vacancy. A conduction band electron re-combines with the hole, releasing a photon which is captured within the same target atom (this process is called internal Auger emission) such that an electron is ejected from the conduction band.

As for SEE due to ion impact, the yield may be expressed as the product of the number of electrons liberated at a depth x (proportional to dE/dx) and the probability that an electron is able to escape from this depth, integrated over the range of the incident particle (equation 3.62). In fact, this only differs from electron impact SEE by the mechanism of incident particle energy loss, and hence the form of the dE/dx function. For a given energy, ions are much more penetrating than electrons, so that the constant dE/dx assumption may be applied with confidence for those depths from which secondary electrons are able to escape.

Katz et al³⁵ propose the following expression for SEE due to normally incident protons;

$$\gamma = \gamma_1 \frac{E^{\frac{1}{2}}}{1 + \frac{E}{E_m}} \cdot 2^{-Q} \quad (3.103)$$

$$Q = \min \left[\left[\frac{1}{\min(E, 10)} \right]^{-0.1} \right], 2 \right]$$

where SEE yields are denoted by γ ; γ_1 is the yield for incident protons of energy 1 keV, E is the incident energy in keV and E_m is the energy at maximum secondary yield. This equation is based on the following expression for dE/dx ;

$$\frac{dE}{dx} = \frac{cE^{\frac{1}{2}}}{1 + \frac{E}{E_m}} \quad (3.104)$$

and the standard migration/escape formula (equation 3.67). A low energy correction factor has been applied. This expression is based on a fit to the experimental data of Baragiola et al⁵⁵ who measured SEE yields due to

ion impact on clean metal surfaces. An alternative approach is to use a more general form of the expressions for SEE due to electron impact of Dionne³³ and Burke³⁷ (see also section 4.1.2) where the yield function is defined by three parameters, maximum yield, energy at maximum yield and the stopping power exponent, n (see equation 3.64). For ion impact, the maximum yield now occurs at several keV, and the value of n will approach 2.0; ie $dE/dx = A/E$ which is the Bohr approximation for the energy loss of heavy particles passing through matter.

There is very little experimental data on this subject; the available data is confined to H^+ (and some heavier ions) incident on a small selection of pure metal targets; no experimental data has been found for insulating targets. Figure 3.14 shows measurements for the SEE yield due to protons incident normally on an aluminium. The data points of Aarset et al⁵⁶, Hill et al⁵⁷, Cousinie et al⁵⁸ and Foti et al⁵⁹ appear to be quite consistent and display an identifiable maximum of 4.41 at 40 keV; but differs from data of Baragiola et al⁵⁵ (to which the Katz expression with $\gamma_1 = 0.244$ and $E_m = 230$ keV is fitted). The clue to this difference almost certainly lies in the preparation of the sample surfaces. Baragiola et al removed surface contaminants by sputtering and worked at a pressure of 10^{-10} Torr to ensure a pure aluminium target; it is probable that the other data quoted is for aluminium with a thin oxide layer, or with a layer of gas adsorbed during the experiment. Further evidence that surface condition accounts for the differing results is that the SEE yields for electron impact differ considerably between pure aluminium and Al_2O_3 , and that the maximum yields in each case are similar (but slightly smaller) than the SEE yields observed for proton impact. Sternglass⁶⁰ discusses the effect of gas adsorption and oxide formation on yield and notes that at low particle energies, or for surfaces with a thick oxide layer, most secondaries will be formed close to the surface, within the insulating layer. The diffusion length for secondaries is known to be several orders of magnitude greater in insulators than in conductors, thereby giving rise to a higher yield. Sternglass also notes that the measured yield at high energy (> 1 MeV) will be representative of the underlying metal; Figure 3.14 reveals consistency between all sets of measurements at high energy.

The energy distribution of the emitted secondaries is approximately Maxwellian with a temperature of a few eV³⁴ and the dependence of yield on incident angle can be modelled in a fashion identical to that for SEE due to electron impact.

3.2.4 Photoemission

The current of photoelectrons emitted from a sunlit spacecraft surface is usually the dominant component of the current balance equation. In the absence of potential barriers around the satellite, photoemission will tend to clamp the surface potential at a small positive voltage (relative to plasma potential) such that the number of photoelectrons which are energetic enough to escape from the satellite

is approximately equal to the number which are not. Despite the apparent ability of photoemission to limit charging levels, knowledge of photoemission yields and photoelectron temperature is important for calculating the electron density in the photoelectron sheath which may form around any partially illuminated, charged spacecraft and has a large influence on the overall current balance equation.

The work function of most materials exceeds 4 eV, so it is necessary to know the solar flux spectrum above this energy (less than 3100Å) as well as the measured photoelectron yield for photon energies greater than the work function. Figure 3.15 (top panel) shows the differential solar flux (units of photons / (m² s eV)) versus photon energy (in eV) at 1AU taken from Friedman⁶¹, Grard et al⁶² and from Allen⁶³; the Lyman α line at 1216Å (10.2 eV) is clearly visible. The lower panel for Figure 3.15 shows photoelectron yields for gold and aluminium measured by Feuerbacher and Fitton⁶⁴. Above the work function energy (Al = 4.0, Au = 4.2 eV), both curves rise steeply over several orders of magnitude before reaching a saturation plateau at about 13 eV. The integrated product of a photoelectric yield curve and the solar flux spectrum leads to a total photocurrent (in A/cm²) for a given material. Feuerbacher and Fitton give the following integrated photocurrent yields (in A/cm²) for normally incident photons; Al = 4.8x10⁻⁹, Au = 2.9x10⁻⁹, stainless steel = 2.4x10⁻⁹, vitreous carbon = 2.1x10⁻⁹, graphite = 7.2x10⁻¹⁰, indium oxide = 3.2x10⁻⁹.

As a first approximation, the yield per photon may be considered constant for all photon incident angles (ie the total photocurrent is given by the integrated photocurrent multiplied by the projected area) although there is some evidence that the yield tends to increase slightly with incident angle, and also depends on the polarisation of the light.

Measurements by Grard⁶² indicate that the photoelectrons are emitted isotropically with a Maxwellian energy distribution (mean kinetic energy between 1.3 and 1.6 eV) and that this distribution is fairly insensitive to the incident material type and to the spectrum of the incident light³⁴.

3.2.5 Bulk conductivity of an insulator

All solids can be classified as conductors, semi-conductors or insulators, according to their energy band structure. Intrinsic semi-conductors and insulators have a finite energy gap (band gap) between the upper level of the valence band and the lower edge of the conduction band. If this energy gap between a filled valence band and an empty conduction band is small (less than about 5 eV) then the material is classified as an intrinsic semi-conductor, since at non-zero temperatures, valence band electrons may be thermally excited into the conduction band. It is apparent from this argument that all solids which are classed as insulators must possess some degree of intrinsic conductivity.

It is useful to consider the insulator as a system of neutral atoms, with no free electrons. When an atom is ionised by means of thermal excitation, or by the passage of an energetic charged particle, the free

electron now moves in a field of neutral (but polarizable) atoms, and the field due to the positive ion. A thermally excited insulator may therefore be regarded as a system of neutral atoms, with a small number of "free" electrons and positive ion traps. The conductivity of the material depends on both the concentration of charge carriers, and their mobility. The concentration of carriers is given by the probability that a neutral atom will be ionised, which is a function of the temperature of the material and the ionisation energy required to liberate an electron (the depth of each trap).

Values for the bulk resistivity of insulating materials are widely available^{65,35,66}, but these refer to measurements made at low electric field strengths. At high field strengths (over 10^5 V.cm⁻¹), insulators exhibit an increase in conduction current above that predicted by Ohm's law, until at sufficiently high field strength, dielectric breakdown occurs. This is an important consideration for spacecraft charging, since situations may arise where potentials of the order of kilo-volts build up on dielectric surfaces such as thermal blankets, which are less than 1mm thick.

This effect, known as "electric field enhancement to bulk conductivity" was first considered theoretically by Frenkel⁶⁷ who realised that the electric field applied across a material modifies the form of the potential well at each trapping centre, lowering it in the "forward" direction and raising it in the "reverse" direction. Consider Figure 3.16 which shows, schematically, the potential well around a positive ion trap. The dotted curve shows the potential well when no external field is applied, assuming a simple Coulomb potential. Under the influence of a field of strength, E , the shape of the potential well is modified to the form shown as a solid line. The height of the potential well at a distance r from the centre is given by the following equation

$$V(r) = -E \cdot r - \frac{e}{(4\pi\epsilon_0)\epsilon_r r} \quad (3.105)$$

assuming that the ionisation energy is reduced by a factor equal to the relative permittivity of the material when the atom is bound into a solid. The modified potential well now has a maximum barrier height at a distance r_0 from the centre. The position of the edge of this barrier, and hence the new ionisation energy may be found from the maximum of the function $V(r)$. Differentiating equation 3.105 gives the following result for the location of the turning point;

$$r_0 = \left(\frac{e}{(4\pi\epsilon_0)\epsilon_r E} \right)^{\frac{1}{2}} \quad (3.106)$$

The height of the barrier is therefore reduced by an amount

$$\Delta U = 2eEr_o = 2 \left(\frac{e^3 E}{(4\pi\epsilon_o)\epsilon_r} \right)^{\frac{1}{2}} \quad (3.107)$$

from the barrier height on the "reverse" side. The number of free electrons at temperature T (and hence the conductivity), is proportional to the probability that an electron will be thermally ionised from a trap with barrier height U_o , or

$$\propto \exp\left[-\frac{U_o}{2kT}\right] \quad (3.108)$$

If the barrier height is reduced, then this probability will be increased accordingly, so that the barrier height reduction quoted in equation 3.107 will cause an increase in conductivity over the value at zero field in the following manner;

$$\sigma = \sigma_o \exp\left[\frac{\left(\frac{e^3 E}{(4\pi\epsilon_o)\epsilon_r} \right)^{\frac{1}{2}}}{kT} \right] \quad (3.109)$$

Frenkel⁶⁷ mentions that for an electric field of 10^6 Vm^{-1} , r_o may be up to ten times the atomic distance. At distances smaller than r_o , the electron is still attached to the parent ion despite the presence of other, neutral atoms in the vicinity.

Whilst Frenkel's theory neatly embodies the physical mechanism for electric field enhancement of conductivity, it does not include any directional effects. Adamec and Calderwood⁶⁸ amended Frenkel's theory to include the effect of particle escape direction (relative to the electric field) from the potential well. They give the following expression for the field enhancement of conductivity due to an increase in carrier concentration;

$$\frac{\sigma}{\sigma_o} = \frac{1}{3} \left[2 + \cosh\left(\frac{\beta_f E^{\frac{1}{2}}}{2kT} \right) \right] \quad (3.110)$$

$$\beta_f = \left(\frac{e^3}{\pi\epsilon_o\epsilon} \right)^{\frac{1}{2}}$$

Adamec and Calderwood⁶⁸ compare this expression against measurements made for polymers and find good agreement. They also give an expression for the increased electron mobility due to an applied field, but note that this may be neglected for fields below 10^6 V.cm^{-1} . Frenkel gives further justification for this in his original work; the illumination of a semiconductor (which liberates more charge carriers) results in an additional increase of conductivity which is independent of E. It is interesting to note that whilst the intrinsic conductivity of an insulator increases with temperature, the electric field enhancement decreases with

temperature.

Finally, Figure 3.17 shows the theoretical field enhancement of conductivity for a Kapton sheet of thickness $51\mu\text{m}$, and dielectric constant 5.0^{35} as a function of surface voltage using equations 3.107 and 3.110. Note that at high field strengths, the Frenkel expression exceeds the Adamec and Calderwood expression by a factor of six, purely as a consequence of directional effects.

The conductivity of insulators is also increased by the passage of ionising radiation. Fredrickson⁶⁹ gives a general expression for the dependence of "radiation induced conductivity" on the dose rate, dD/dt (Fowler's Law);

$$\sigma_r = k\dot{D}^\Delta \quad (3.111)$$

where k is the coefficient of radiation induced conductivity (material dependent), and Δ lies in the range 0.5 to 1.0. Clearly, k depends on the incident particle collision cross-section within the target material, and Δ on the energy level distribution of traps within the target material. Fredrickson⁶⁹ assumes that Δ is equal to unity, and gives values of k for several dielectrics (eg. Teflon, $k = 1.1 \times 10^{-16}$ to 4.5×10^{-17} s/(Ω cm rad); PVC, $k = 1.8 \times 10^{-18}$ to 6.3×10^{-18}). In geosynchronous orbit, the annual radiation dose due to high energy electrons is 5.8×10^7 rad(Si) at a depth of $50\mu\text{m}$, according to the UNIRAD prediction suite⁷⁰. Assuming this to be a constant dose rate of $1.83 \text{ rad}\cdot\text{s}^{-1}$, then by equation 3.111, the radiation induced conductivity for Teflon becomes 8.2×10^{-15} to 2.0×10^{-14} mho/m according to which value of k is chosen. This is slightly larger than the measured values of bulk conductivity for Teflon, at low fields and at room temperature (10^{-16} to 10^{-15} mho/m).

3.2.6 Surface conductivity

Intrinsic surface conductivity is measured in units of Ohms per square (Ω/\square). To understand how this unit may be related to total resistance between two electrodes, consider Figure 3.18. This is a two-dimensional diagram in which two electrodes (wires, or planar electrodes perpendicular to the paper) are separated by several "tiles" of some insulating material, each of which has an intrinsic surface conductivity of $\sigma \Omega/\square$ (or $\Omega/\text{"tile"}$). The total resistance (vertically) across each horizontal row of tiles is σ/n if there are n tiles per row. The total resistance between the electrodes is now found by assuming that there are m rows in series, each of resistance σ/n , giving the total resistance as $(m/n)\sigma$. Of course, the quantity m/n is equal to the ratio of the thickness (distance between the electrodes) of the sample to its width (distance adjacent to the electrodes).

The mechanisms by which surface conductivity occurs are not well understood. Sillars⁷¹ makes the following comment; "Surface conductivity, despite its considerable practical importance in d.c. and low frequency measurements, is little understood and allows few generalisations. It is

greatly increased by increasing the ambient humidity and by the presence of salts, acids etc. in the material, or on its surface. It can be reduced by keeping the surface a few degrees above ambient temperature or by treating with a water repellent". However, it is reasonable to assume that the presence of adsorbed impurities on the surface of an insulator tends to assist the migration of electrons along the surface.

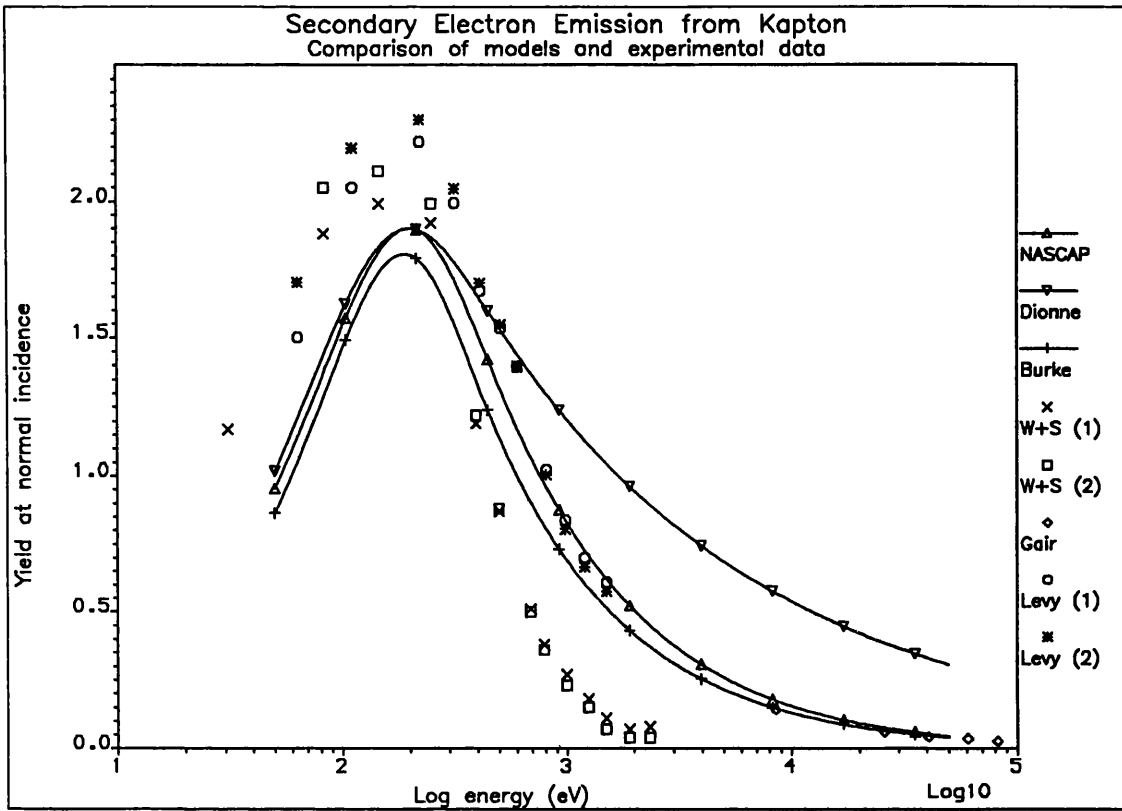


Figure 3.7

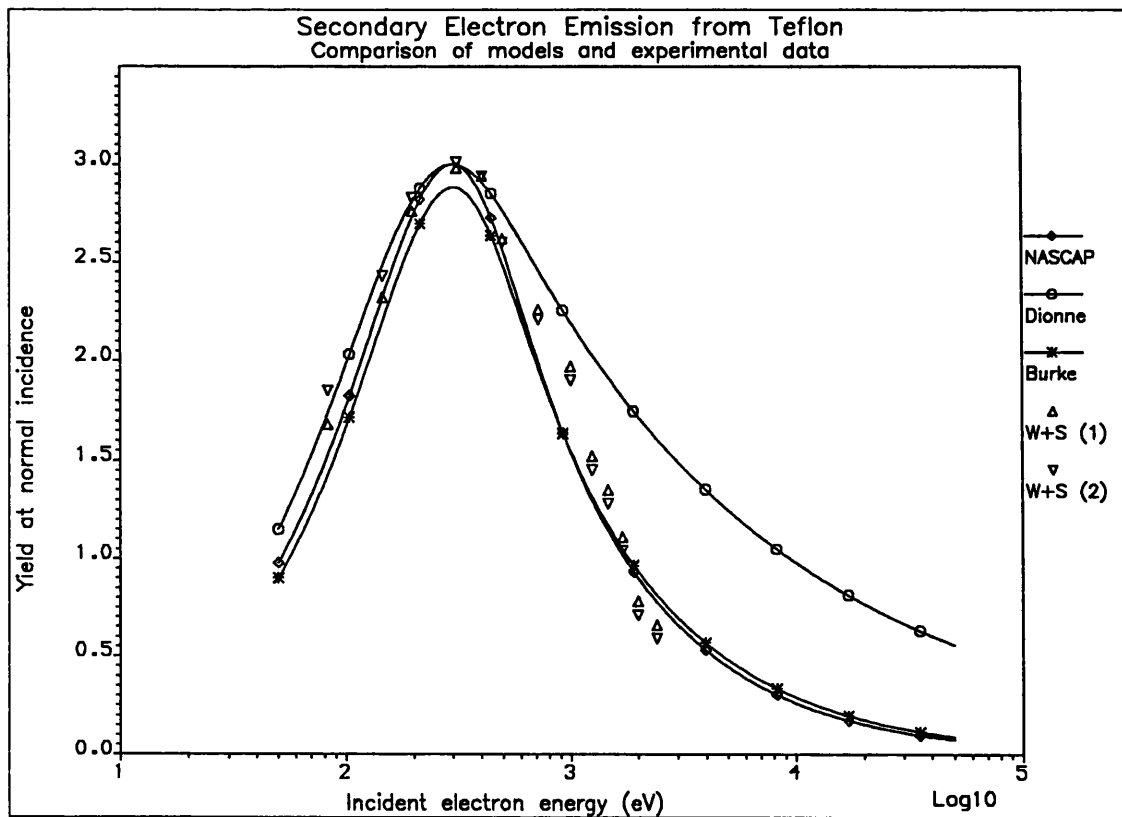


Figure 3.8

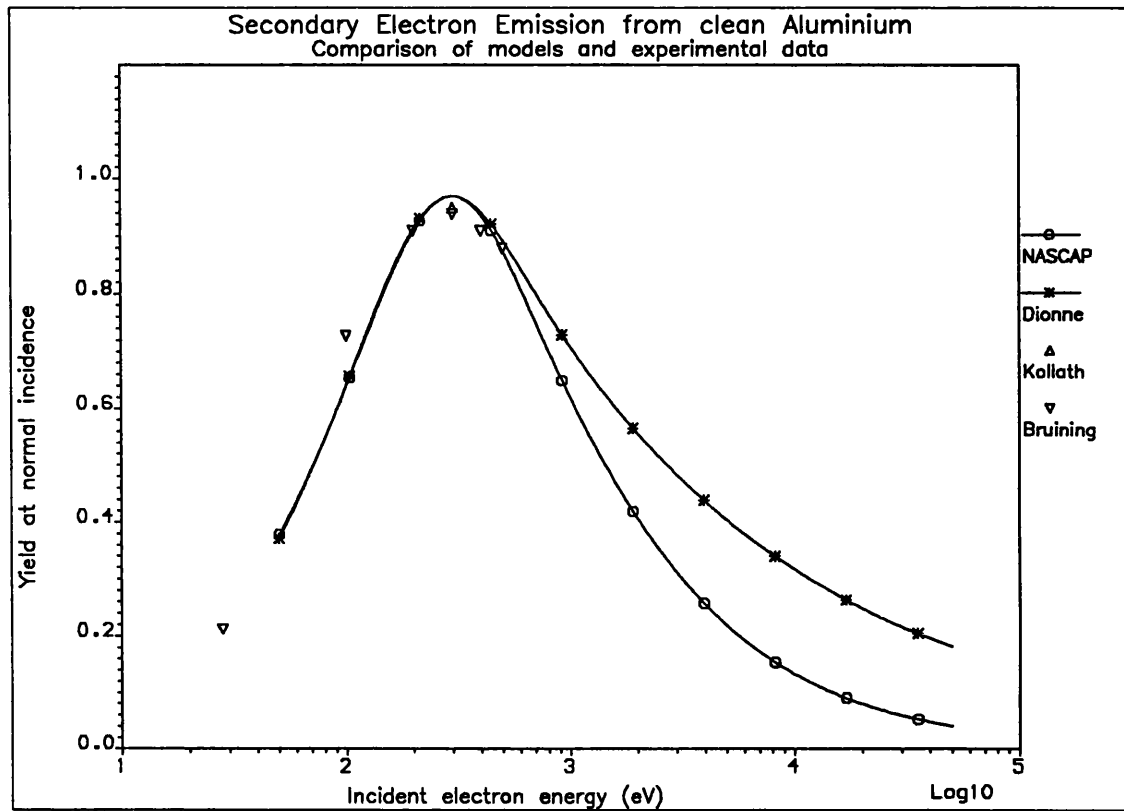


Figure 3.9

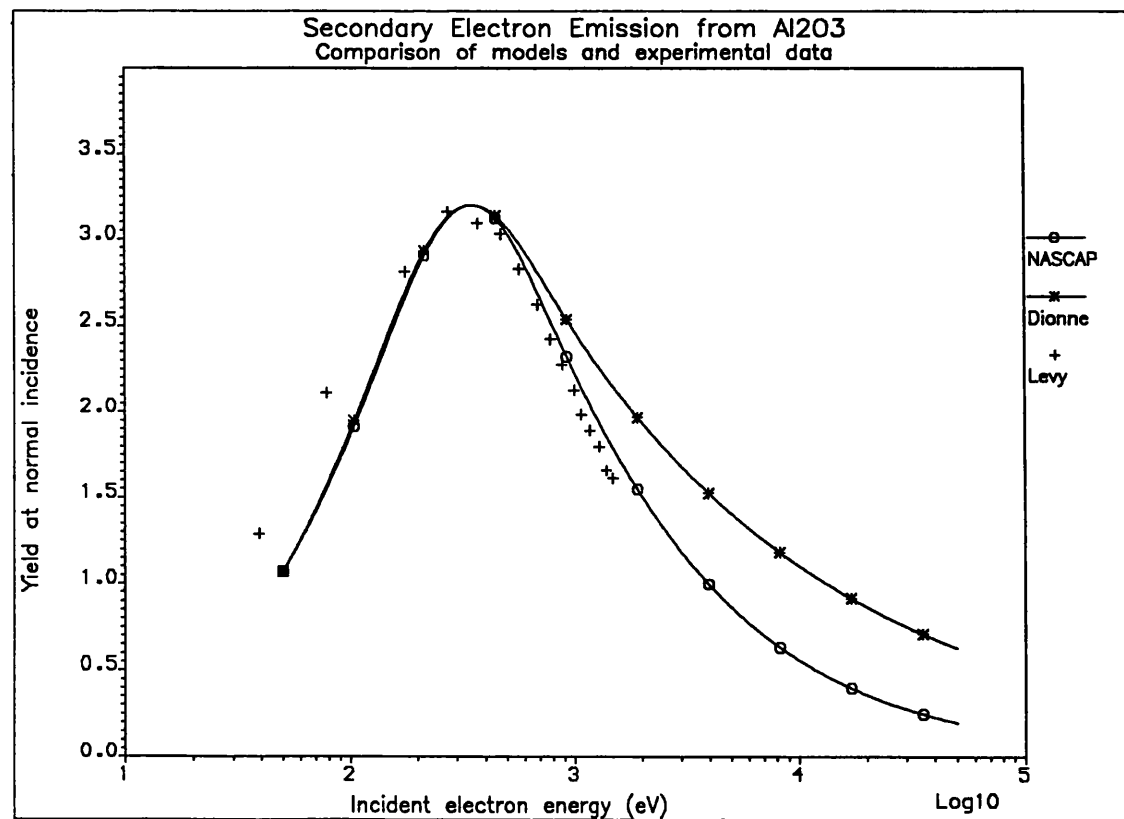


Figure 3.10

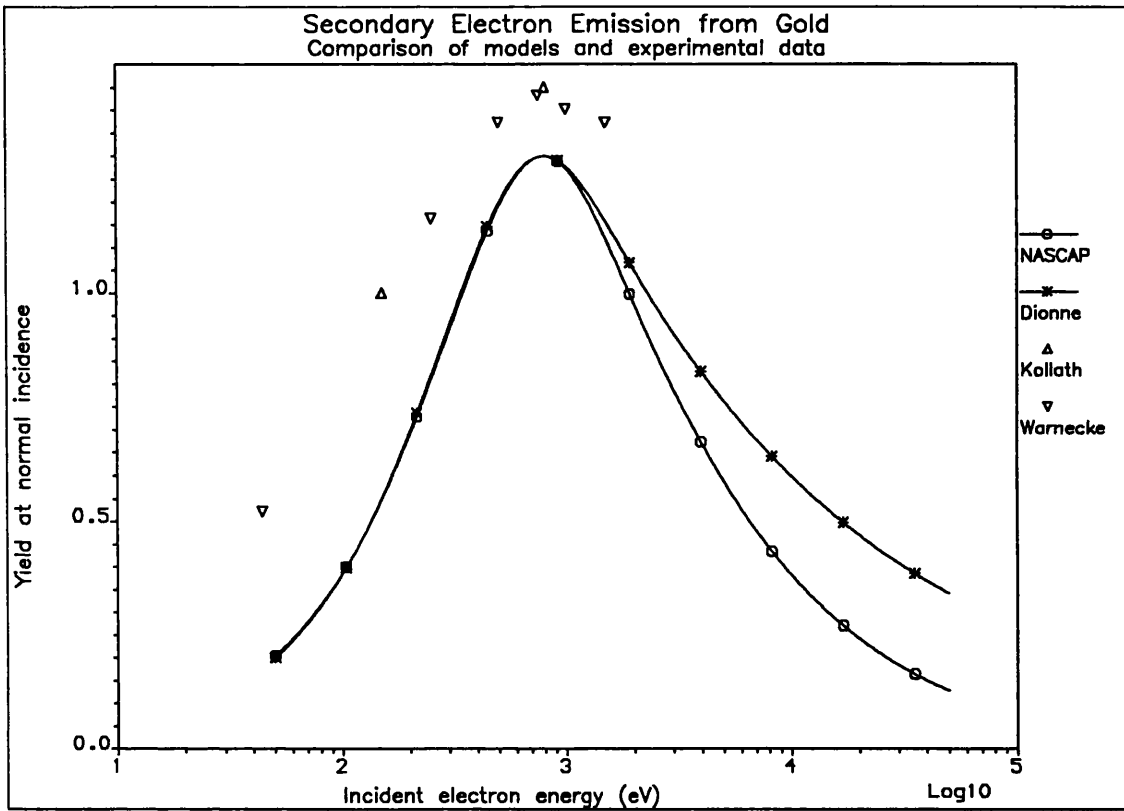


Figure 3.11

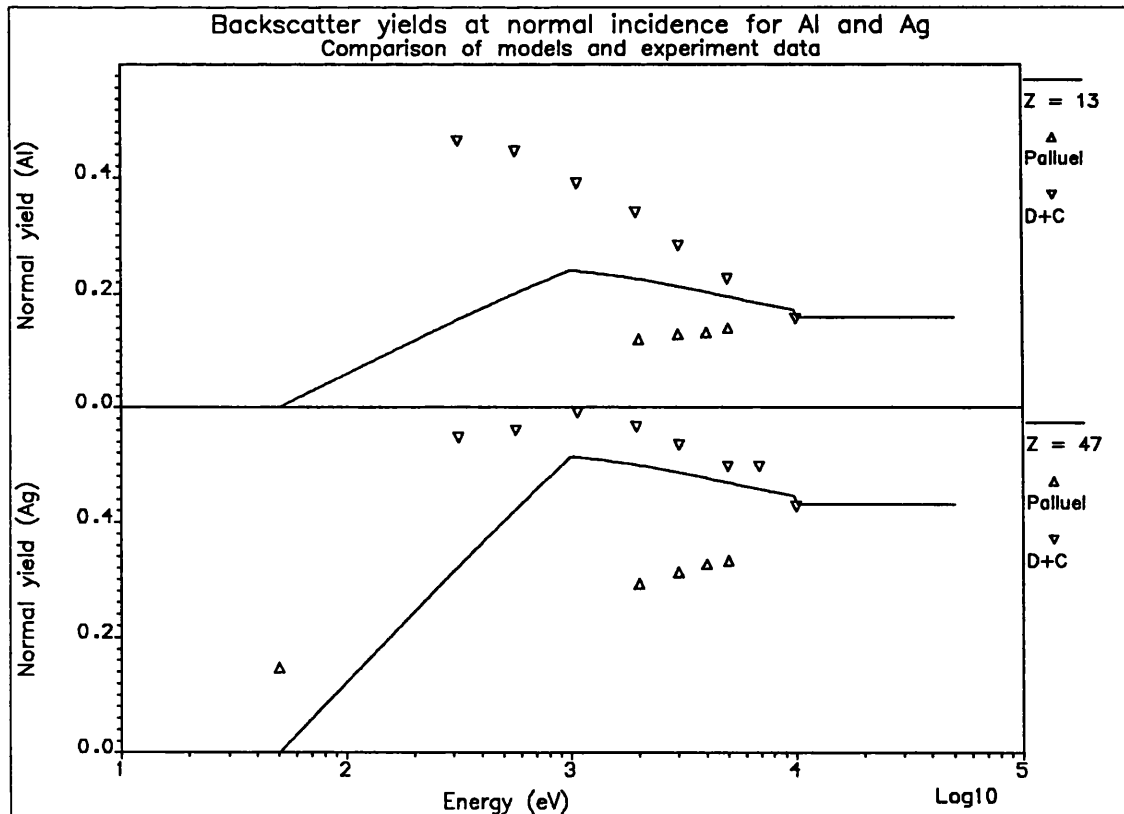


Figure 3.12

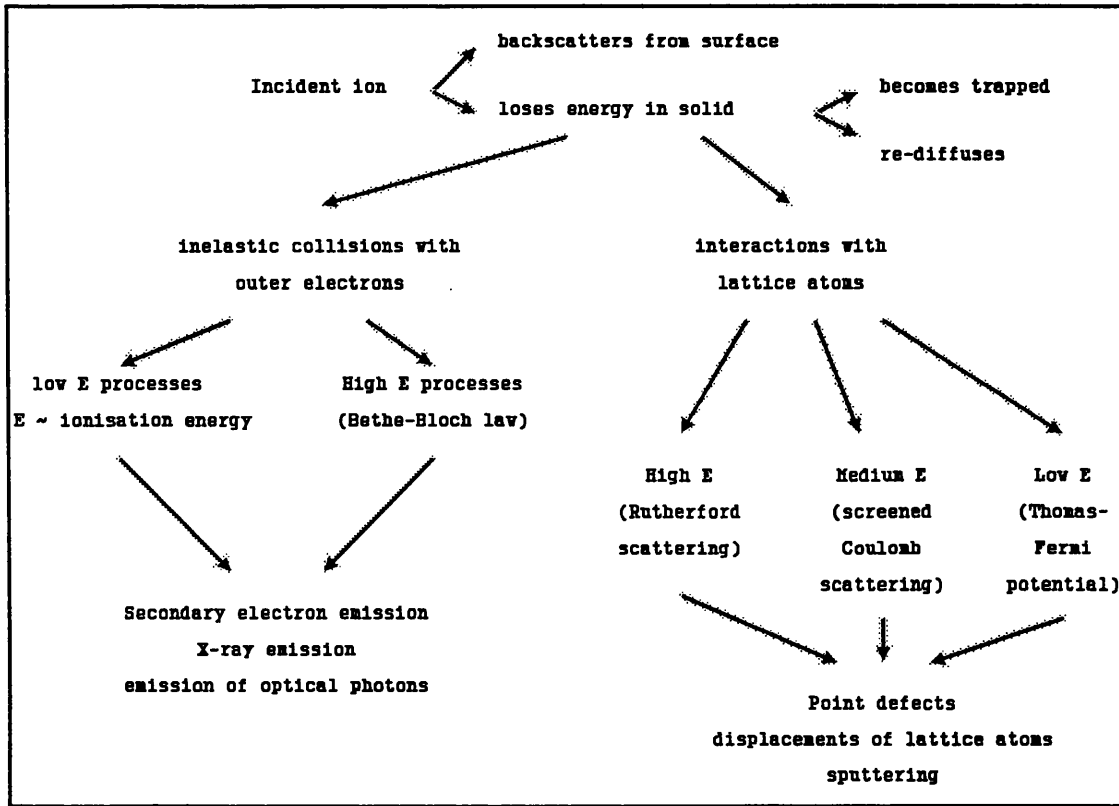


Figure 3.13 Ions incident on a solid surface

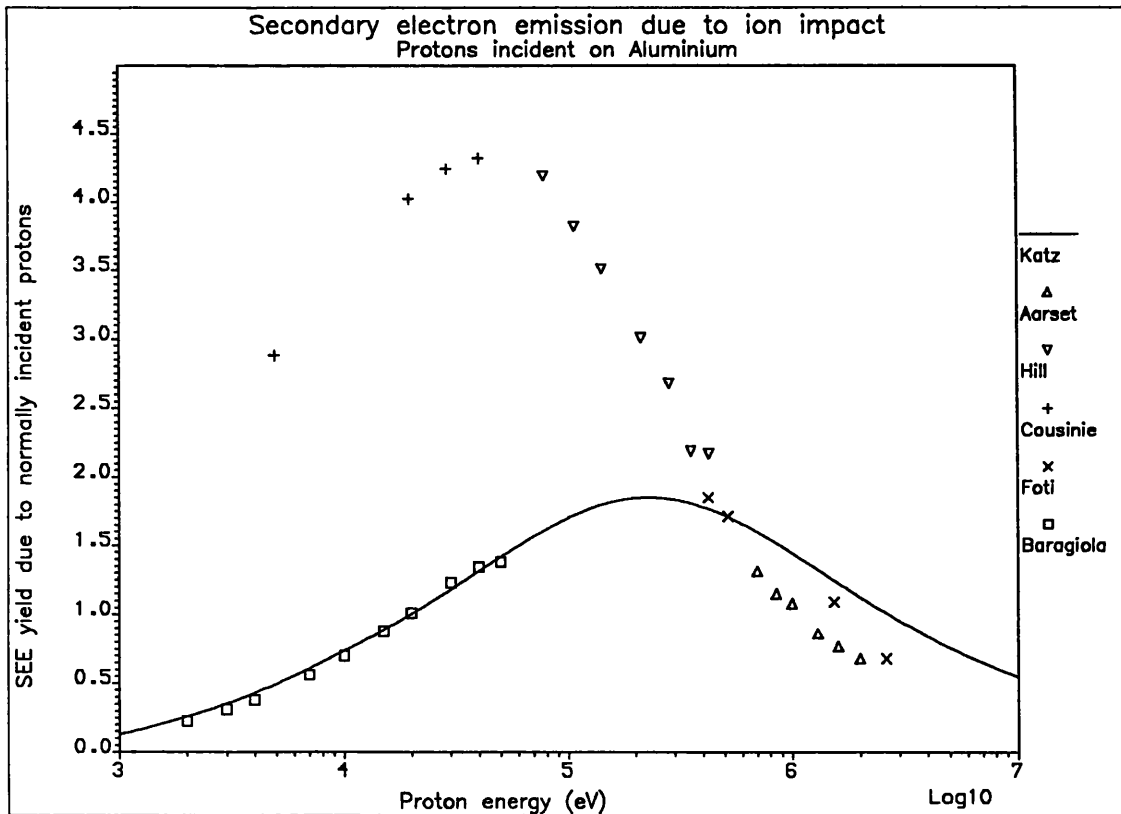


Figure 3.14

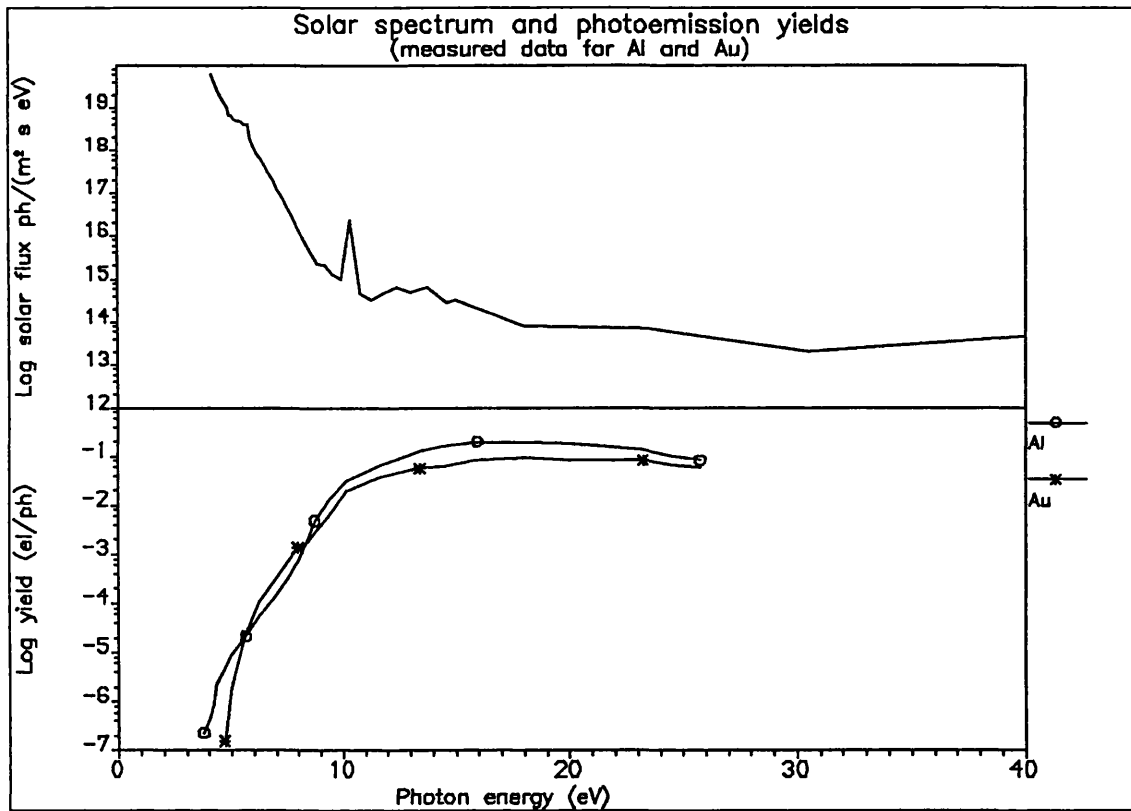


Figure 3.15

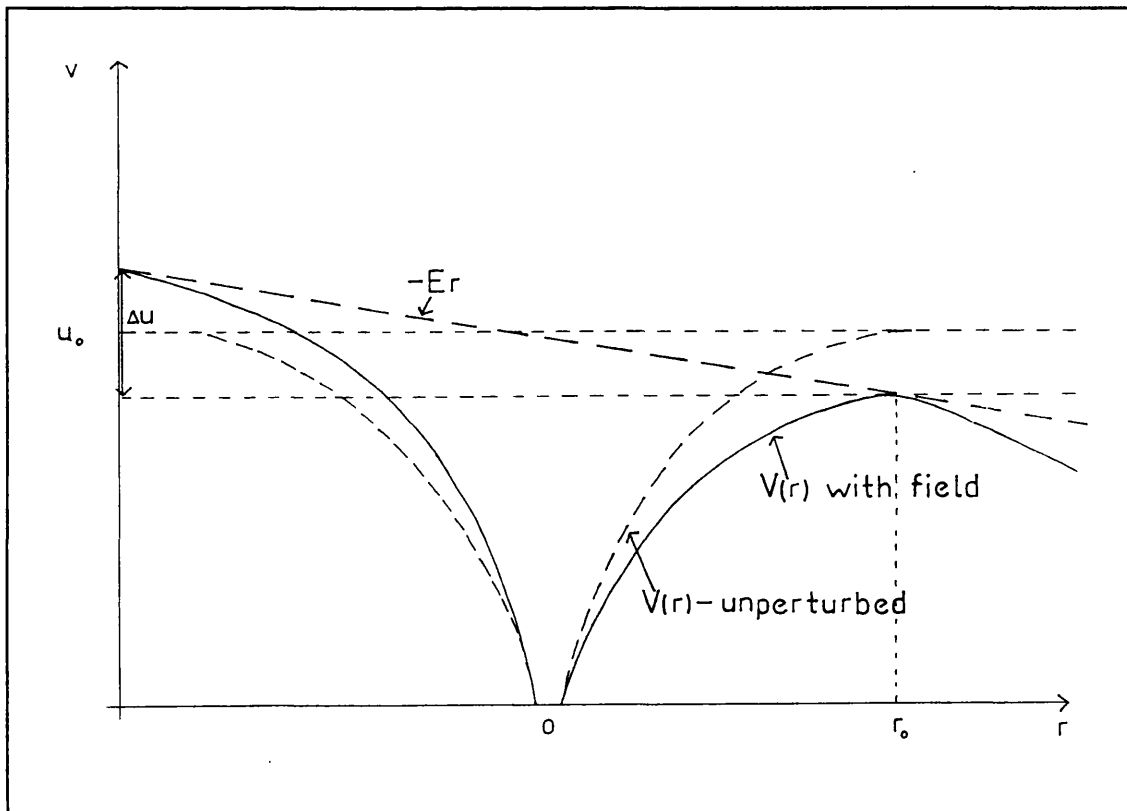


Figure 3.16 Modification of atomic potential well by an applied field

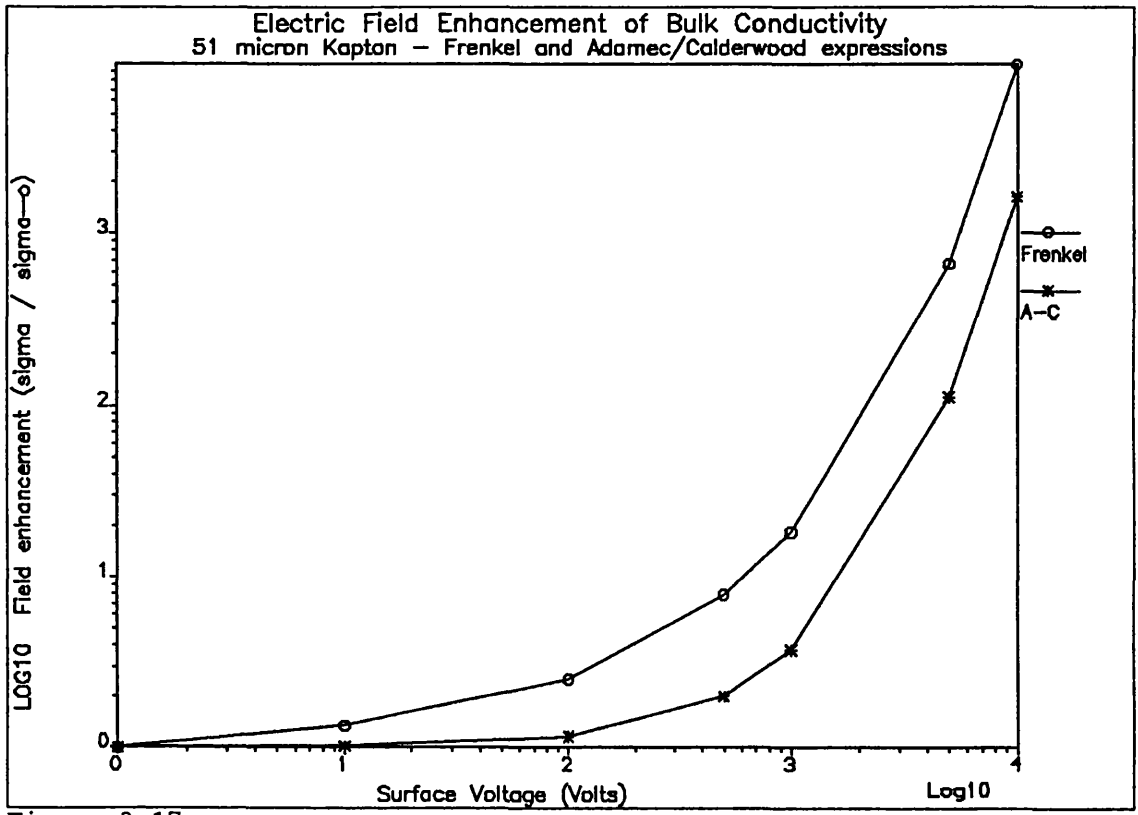


Figure 3.17

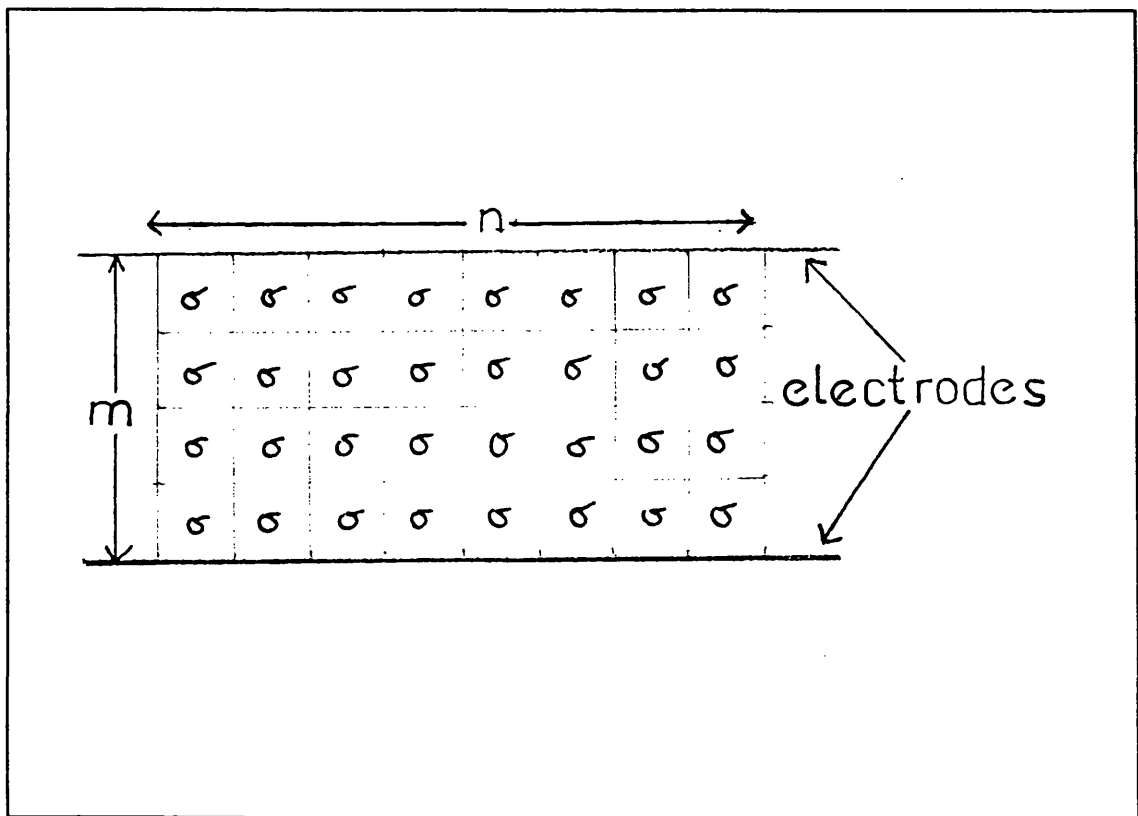


Figure 3.18 Surface conductivity calculation

3.3 THE PLASMA ENVIRONMENT AT GEOSYNCHRONOUS ORBIT

A review is presented of the plasma environment at GEO. The position of the orbit with respect to regions of the magnetosphere is discussed, and a model for geomagnetic substorms is presented. The section concludes with a review of geomagnetic indices used for studies in Chapter 5.

3.3.1 Geostationary orbit and the magnetosphere

Figure 3.19⁷² shows a cross-section through the magnetosphere in the noon-midnight meridian (for a given level of magnetic activity) on which the positions of several plasma populations have been marked. The geostationary orbit passes through the plasmasphere, the plasmasheet and, during periods of intense solar activity can cross the magnetopause (which has been compressed on the dayside) and enter the solar wind near local noon. The characteristics and boundaries of each region depend upon local time and radial distance as well as solar and magnetic activity. This section gives a review of the plasma characteristics within each region and concludes with a discussion of plasma boundaries.

The plasmasphere is a region of cool, dense, co-rotating plasma which forms the upward extension of the ionosphere and whose upper boundary is the plasmapause. To a first approximation, the plasmasphere is in diffusive equilibrium with the ionosphere, such that the density of protons (in cm^{-3}) decreases with increasing radial distance⁷³, L (Earth radii) as approximately $10^5 L^{-4}$. Particle energy, density and composition change with altitude⁷², but near the plasmapause, protons are the predominant ion species, and the number density of electrons and protons is about 10cm^{-3} with particle energies generally lower than 1eV . The plasmapause is defined as the boundary between near-Earth co-rotating plasma and plasma which is convecting from the magnetotail towards the sun as a result of the solar wind induced cross-tail electric field (see also sections 3.3.2 and 5.3). Within the plasmasphere, the corotation electric field dominates, and particles follow closed drift paths, whilst beyond the plasmapause, the convection electric field dominates and particles are "quasi-trapped", ie their drift path makes only a partial orbit of the earth. Thus, particle number density drops sharply at the plasmapause, as illustrated in Figure 3.20⁷⁴ which has been derived from several OGO-3 crossings at different geomagnetic activity levels. As the cross-tail (convection) electric field increases, the changing convection pattern causes the outer layers of the plasmasphere (especially in the afternoon sector) to be peeled off⁷⁵ and convected towards the magnetopause. Diffusion from the ionosphere along field lines re-fills flux tubes when magnetic activity subsides, but this process can take several hours or days and may not be complete before renewed magnetic activity causes further loss.

The plasmasheet (shown in Figure 3.19) extends along the anti-sunward direction, and occupies the full width of the magnetotail, but is only of the order of $4R_E$ thick at the centre, increasing to about $10R_E$

near the magnetopause. Electron energy is in the range of hundreds of eV to tens of keV and particle density is generally below 1cm^{-3} . Under steady-state conditions, a pressure balance is maintained between the kinetic pressure of the plasma and the magnetic pressure outside the sheet. The plasmashet separates two regions of oppositely directed magnetic field which represents a store of energy which is released in the form of substorms.

The position of the boundaries between these plasma populations relative to geostationary orbit determines the probability of severe charging conditions for a given longitude and local time. Particularly important for charging studies are the positions of the plasmashet inner edge and the plasmopause. Frank⁷⁶ has used data from OGO-3 to identify the spatial position of five phenomena (proton ring current, plasmopause, plasmashet, plasmashet earthward edge (EE) and the limit of stable particle trapping) near local midnight. EE is characterised by a rapid exponential decrease in average electron energy at constant density with decreasing radial distance on a length scale of $0.5R_E$. He notes that in the pre-midnight sector, the inner limit of EE lies some $2-3R_E$ beyond the plasmopause with an "electron trough" of low density and low energy electrons filling the gap. At high levels of magnetic activity, EE moves earthward and the electron trough disappears, whilst in the post-midnight sector, the inner limit of EE is coincident with the plasmopause. EE is always observed to be within the stable trapping region and therefore must require closed, quasi-dipolar field lines for its formation. With data from OGO-1, OGO-3 and Vela, Vasyliunas^{77,78} reports that within EE, electron energy density decreases as $\exp(\text{distance}/0.4R_E)$ for quiet times, and $\exp(\text{distance}/0.6R_E)$ at disturbed times; the plasmashet inner edge thins with increasing activity. He also reports enhanced energetic electron fluxes in the post-midnight sector and reduced fluxes in the dayside, together with a tongue of plasma which extends to the magnetopause in the afternoon sector.

Grebowsky and Chen⁷⁹ have modelled the plasmopause position by computing electron drift paths in the equatorial plane of the magnetosphere assuming a dipolar magnetic field, and a system of electrostatic potential contours which is based on a co-rotation electric field plus a cross-tail (convection) electric field in the sunward direction (defined as a function of K_p). This model is applied in section 5.3 to explain some plasma boundary measurements by Meteosat F2. Kennel⁸⁰ has developed a model for the inner edge of the plasmashet by balancing the earthward convection rate of plasma from the magnetotail to the rate of particle precipitation by strong (pitch angle) diffusion of plasma in the midnight sector. A limit is proposed for electron lifetime as a function of position and energy, which may be incorporated into magnetospheric convection models to predict the position and thickness of the plasmashet inner edge. Such a model is discussed in section 5.3.

3.3.2 Geomagnetic storms and substorms

Magnetic disturbances within the magnetosphere which occur at irregular intervals and last for periods of hours or even days before the magnetosphere returns to a quiescent state have been termed magnetic storms or substorms according to the severity of the event. The most severe disturbances manifest themselves as effects which may be observed terrestrially, such as the visible aurorae, changes to radio wave propagation through the ionosphere and voltage surges in high latitude power transmission cables. Satellite-borne detectors have shown that a magnetic storm is a disturbance which involves extensive movement of magnetic field lines and plasma populations around the magnetosphere and that the energy input which drives this movement is provided by the solar wind. Due to the dipolar nature of the magnetic field near Earth, magnetic field lines which map to the surface at auroral latitudes pass close to geostationary orbit, so that during storm or substorm conditions, the plasma characteristics in the vicinity of a geostationary spacecraft may change dramatically with timescales ranging from minutes to hours. The mechanisms by which storm activity affects magnetospheric plasma populations are generally understood, but it is true to say that use of the word "storm", in analogy to the meteorological phenomenon is a good one, since activity may only be predicted with moderate accuracy; spacecraft will have to continue to survive severe, sudden magnetic storms.

A process of reconnection⁸¹ allows solar wind energy to be transferred to the inner regions of the magnetosphere. The manner in which magnetic fields behave in a highly conductive plasma⁸² is described by three equations; Faraday's law (equation 3.112), Ohm's law (equation 3.113) for an electric field in the rest frame of the plasma, and Ampere's law (equation 3.114), where the displacement current term has been assumed negligible for high conductivity plasmas.

$$\frac{\partial \mathbf{B}}{\partial t} = -\nabla \times \mathbf{E} \quad (3.112)$$

$$\mathbf{E} + \mathbf{v} \times \mathbf{B} = \frac{\mathbf{j}}{\sigma} \quad (3.113)$$

$$\nabla \times \mathbf{B} = \mu_0 \mathbf{j} \quad (3.114)$$

Eliminating \mathbf{E} and \mathbf{j} from these equations gives the following differential equation for \mathbf{B} in terms of time;

$$\frac{\partial \mathbf{B}}{\partial t} = \nabla \times (\mathbf{v} \times \mathbf{B}) + \frac{\nabla^2 \mathbf{B}}{\mu_0 \sigma} \quad (3.115)$$

When the conductivity is very large, the first term on the right of this expression dominates over the second; by neglecting the final term, the

equation reduces to an expression which shows that no motion of the plasma is possible in a direction perpendicular to the field lines. This is termed the "frozen-in" approximation where the field lines are carried along with the motion of the plasma, but the field may modify the flow due to the $\mathbf{j} \times \mathbf{B}$ term. When the conductivity is finite, and the second term on the right of equation 3.115 dominates over the first, the expression reduces to the diffusion equation;

$$\frac{\partial \mathbf{B}}{\partial t} = \frac{\nabla^2 \mathbf{B}}{\mu_0 \sigma} \quad (3.116)$$

This has a characteristic diffusion constant, such that, for a system with length scale, L , the time taken for a magnetic field to diffuse into, or out of a region of plasma is given by

$$\tau = (\mu_0 \sigma) L^2 \quad (3.117)$$

The conductivity of magnetospheric plasmas may be estimated using Langevin's equation to be between 10^3 to 10^4 mho/m; on length scales of several Earth radii (10^4 km), typical diffusion times are of the order of 10^{12} seconds, or about 4×10^4 years; ie on magnetospheric length scales diffusion of field lines through a plasma is negligible.

Consider, however, two different regions of plasma (and magnetic field) coming together; for example the solar wind impinging on the magnetosphere. This is depicted in Figure 3.21a, where the interface is considered as being planar, and the two magnetic fields have opposite direction, but different magnitude. Application of Ampere's law over a closed path, normal to the interface plane results in a non-zero value of $\mathbf{B} \cdot d\mathbf{l}$, which implies that the interface plane is a thin current sheet. The characteristic length scale of this current sheet is very small compared to the magnetospheric length scale, so it is no longer possible to neglect diffusion of the magnetic field into the plasma, in the vicinity of the current sheet. Slowly, the field lines will diffuse into the current sheet, until they eventually touch (reconnect), as in Figure 3.21b. The magnetic field lines now have a component perpendicular to the interface plane, so they are subject to the $\mathbf{j} \times \mathbf{B}$ force, which causes the reconnected loops to contract, Figure 3.21c. Since the plasma is free to flow along field lines, the two bodies of plasma are now able to mix at the interface, also, contraction of the reconnected loops provides a mechanism for accelerating some regions of plasma.

This process is observed when the solar wind impinges on the terrestrial magnetosphere, and the interplanetary magnetic field (IMF), carried along with the solar wind, has a southward component, Figure 3.22. Reconnection between the IMF and the geomagnetic field occurs at the sunward face of the magnetosphere to create "open" field lines from the IMF to the polar cap region. Furthermore, the ends of these open flux tubes are swept towards the nightside by the solar wind to create a very long geomagnetic tail (several tens of Earth radii). As these flux tubes

are pulled further down the tail region, they tend to contract towards the central plane, where they may reconnect once more with the geomagnetic field. Whilst reconnection at the dayside is quasi-static, and occurs as long as the IMF possesses a southward component for a sufficiently long time, reconnection in the tail region tends to be sporadic; it is this which gives rise to magnetic storm and substorm effects.

During the "growth phase" of a magnetic substorm⁸³, which lasts about 1 hour, flux is transferred from the dayside magnetosphere to the nightside plasmashet⁸⁴, by virtue of the field configuration shown in Figure 3.22. A rapid reconnection event in the tail region causes the plasmashet to be split into two; a closed-loop plasmoid, accelerated towards Earth at a velocity of around 600 km/s, and a tailward moving section of the original plasmashet. The field configuration on the Earthward side contracts rapidly (1-2 minutes), Figure 3.23⁸³ until it approaches the near-dipolar, undisturbed configuration; this is the substorm onset. The rapid collapse of flux tubes in the tail region compresses and heats the plasma contained within the tubes, and injects it into the equatorial ring-current region. Satellites in geostationary orbit can observe the injection event directly, if they happen to be close to midnight (local time) at the moment of substorm onset. However, the effects of a storm, or substorm are not confined to satellites in this region, since the injected plasma immediately begins to drift in the equatorial plane.

All plasma particles in the magnetosphere are subjected to one or more types of guiding centre drift. One such example is the ring current, which is an electric current encircling the Earth at a distance of 4 to 7 R_E (Earth radii), in the equatorial plane, and consists of electrons drifting eastwards and ions drifting westwards due to the combined "grad-B" and curvature drift forces. Grad-B drift⁸⁵ occurs when the magnitude of the magnetic field changes significantly over a distance of one Larmor radius. Consider Figure 3.24, where the magnetic field is in the \underline{z} direction, but becomes weaker as y increases. The particle trajectory shown would have a smaller Larmor radius at small y than it would at large y ; so instead of describing closed, circular orbits, the particle will tend to drift in the x direction. Note that since electrons and ions orbit the field lines in a different sense, they will suffer oppositely directed grad-B drifts. The drift velocity is given by equation 3.118;

$$\underline{v}_{\nabla B} = \pm \frac{1}{2} v_{\perp} r_L \frac{\underline{B} \times (\nabla B)}{B^2} \quad (3.118)$$

positive for ions, and negative for electrons. v_{\perp} is the particle velocity perpendicular to the field, about the guiding centre, r_L is the particle's Larmor radius, for the field at the guiding centre and ∇B is a vector quantity pointing in the direction of increasing \underline{B} , and with magnitude equal to the rate of change of \underline{B} with position. Assuming the geomagnetic

field to be dipolar, with dipole moment M , and expressing the Larmor radius in terms of energy, equation 3.118 may be re-written as

$$v_{VB} = \pm \frac{3 \cdot E \cdot R^2}{(M \cdot R_E)^3 \cdot R_E} \quad (3.119)$$

where E is the particle energy, in eV, R_E is the radius of the Earth, R is the distance of the guiding centre from the dipole centre in Earth radii, and MR_E^3 is the geomagnetic field strength at the equator, equal to 0.32 Gauss. Table 3.2 gives the magnitude of this drift velocity for 10 keV protons and 20 and 30 keV electrons, together with the drift period at $6.6R_E$, assuming that the particles have a pitch angle of 90° . Also included in this table are the thermal, or perpendicular velocities of each particle, together with the Larmor radius, for a guiding centre at $6.6R_E$. Particles with a component of velocity directed along \underline{B} (pitch angles less than 90°) suffer curvature drift due to centrifugal force. For each species of particle, curvature drift is in the same direction as the gradient drift, such that the magnitude of the combined gradient-curvature drift, v_{CG} for particles with equatorial pitch angle α in a magnetic field with radius of curvature R_c is⁸⁶

$$v_{CG} = \frac{T}{qBR_c} (1 + \cos^2 \alpha) \quad (3.120)$$

where T is the thermal kinetic energy, q is the charge and B is the magnitude of the field. From Table 3.2, which considers particles with 90° pitch angles only, it is apparent that drift speeds exceed the orbital velocity of satellites in GEO. Thus, particles injected during a substorm will be observable by satellites located several hours away from the point of injection. At geostationary altitudes, the electron minimum lifetime prior to loss by pitch angle diffusion will in general be less than one drift period for particles in the keV energy range, such that injected electrons will tend not to drift far beyond the dawn sector. Also, there will be some energy dispersion of injected particles as they drift, with the more energetic drifting more rapidly.

3.3.3 Geomagnetic Indices

Currents which flow in the magnetosphere as a result of storm and substorm activity will induce magnetic fields which are observed at the surface of the Earth as small perturbations superimposed on the internal geomagnetic field. Such perturbations are recorded by a planetary network of magnetic observatories in the form of magnetograms for each of the three components of the magnetic field. For the purposes of studying magnetospheric phenomena, it is generally not convenient to directly interpret such magnetograms; instead, several indices have been derived to summarise observations from selected groups of magnetic observatories. These indices are used to express the level of energy dissipation within the magnetosphere for a particular current system over a period of

minutes or hours. The four magnetic indices in common use⁸⁷ are described below;

(i) The Kp index is a three-hourly index of the world-wide level of activity calculated from thirteen sub-auroral stations, introduced by Bartels⁸⁸ in 1949. It is a quasi-logarithmic index, computed from the maximum variation of each magnetic field component at each observatory, and averaged for all the thirteen observatories. It is expressed in integers, on a scale from 0 to 9, with each interval sub-divided into thirds, giving a total of 28 possible values; 0o, 0+, 1-, 1o, 1+, 2-, through to 8o, 8+, 9-, 9o. There are two major disadvantages with this index. Firstly, the observatories are not distributed evenly around the planet; in particular, there is no coverage in the Soviet sector, or over the North Atlantic. Secondly, during storm activity, the auroral zone tends to move towards the equator, so that Kp may increase either due to a true increase in the auroral electrojet current (see iii), or simply because this current system has moved closer to the observing stations.

(ii) The a_p index. This is equivalent to the Kp index, but is expressed on a linear scale which is more convenient for numerical correlations. There is a one-to-one relationship between the 28 possible values of Kp, and the 28 values of a_p which range from 0 to 400. Furthermore, the value of a_p can be directly related to the magnitude of the disturbance measured at a mid-latitude station by multiplying the a_p value by two to give the disturbance in gammas (nT). The Ap index is the average of the eight three-hourly a_p indices over one day.

(iii) The Dst index is used to represent the strength of the equatorial ring current; auroral and equatorial electrojet effects are excluded by using only the H component of the magnetic field from stations at low magnetic latitude. It is expressed as the average change in the H component of the magnetic field (in gammas, or nT) averaged over all the low latitude observatories, and normalised such that Dst = 0 represents the undisturbed case (internal field only). During a magnetic storm⁸⁹, Dst becomes slightly positive (less than +20nT) for a few hours during the substorm growth phase, then rapidly decreases following the injection event, reaching perhaps -100nT before slowly recovering towards zero over a period of two to three days. The decrease in H component is consistent with an equatorial current of westward drifting ions and eastward drifting electrons. Dst is calculated from as few as three stations, so whenever the ring current is fragmented such as during a substorm, Dst may not show any significant increase. However, Dst does respond to all magnetic storms, but there is evidence⁹⁰ for a statistical link between substorms and ring current strength.

(iv) The AE (Auroral Electrojet) index is intended to represent high latitude auroral activity, and is therefore calculated from several stations at high magnetic latitude (including some Southern hemisphere) stations and has a time resolution of 2.5 minutes. As with Dst, only the H component of the magnetic field is considered, using the undisturbed field as a reference. AE is taken as the difference between AU (the

amplitude of the maximum positive value of dH for all stations) and AL (the amplitude of the maximum negative value of dH for all stations). AU and AL represent the eastward and westward auroral electrojets respectively. As with the previous three indices, AE is limited by a lack of coverage, compounded by localised auroral activity. Furthermore, the auroral oval moves to lower latitudes during high levels of activity, causing some stations to be well outside the auroral region for much of the event.

Rostoker⁸⁷ notes that indices tend to define the lower limit of geomagnetic activity and that they should only be used in long-term statistical studies, rather than for the study of individual events. Wrenn⁹¹ introduced the time-weighted accumulation $ap(\tau)$ in an attempt to quantify long-term trends in geomagnetic activity as defined by the (three-hourly) ap index. The $ap(\tau)$ index is defined as follows;

$$ap(\tau) = (1-\tau) [ap+(\tau)ap_{-1}+(\tau)^2ap_{-2}+..] \quad (3.121)$$

where ap_{-1} , ap_{-2} etc. are ap values for the previous 3 hour periods. The parameter, τ (which lies between 0 and 1) is a three hour attenuation multiplier which controls the "persistence time", or time over which a delta-function type event would decay to 1/e of its original value. The persistence may be approximated by $3/(1-\tau)$ hours and is 4.3 hours, 10.4 hours, 1.2 days, 2.4 days, 4.9 days and 12.4 days for τ values of 0.5, 0.75, 0.90, 0.95, 0.975 and 0.99 respectively. The $ap(\tau)$ index is normalised to lie within the same limits as the ap index.

Table 3.2 Grad-B drift velocities at 6.6R _E				
	Drift Velocity (m.s ⁻¹)	Drift Period (hours)	Thermal velocity (m.s ⁻¹)	Larmor radius (km)
Protons, 10keV	6.40x10 ³	11.5	1.4x10 ⁶	132.0
Electrons, 20 keV	1.28x10 ⁴	5.7	8.4x10 ⁷	4.3
Electrons, 30 keV	1.92x10 ⁴	3.8	1.0x10 ⁸	5.1

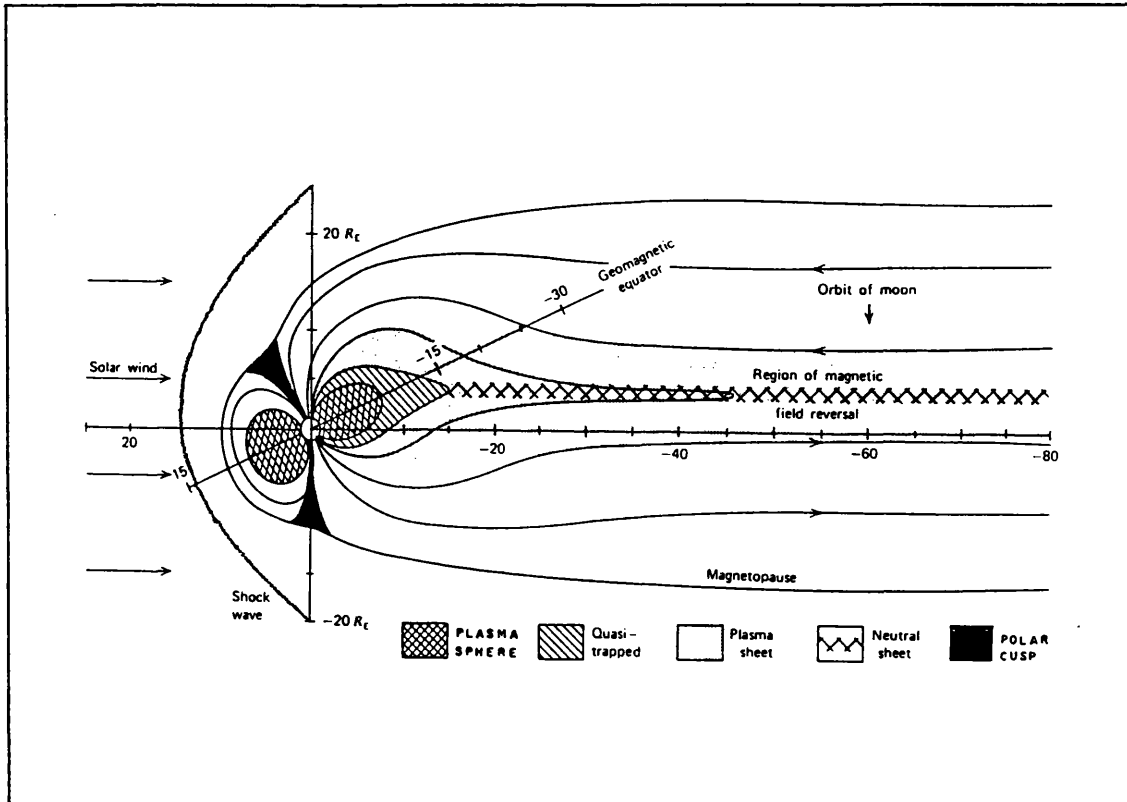


Figure 3.19 A noon-midnight meridian plane cross-section through the magnetosphere and geomagnetic tail showing several components of the charged particle populations.

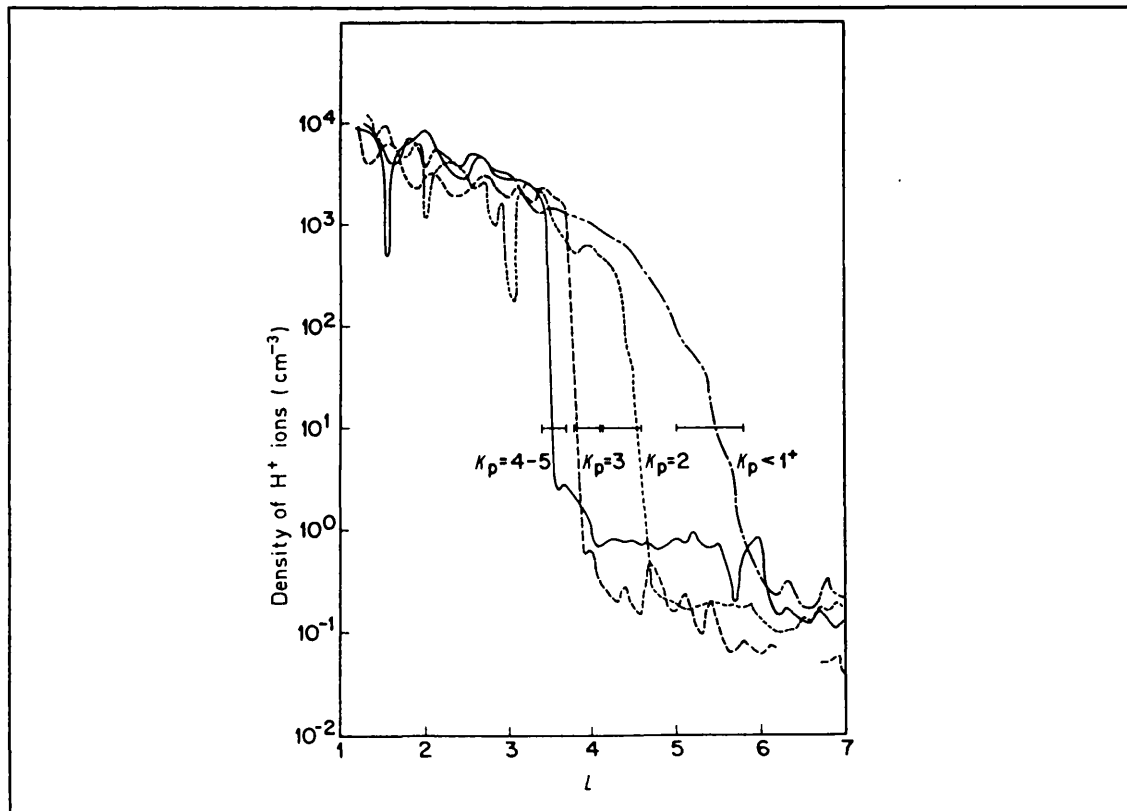


Figure 3.20 Location of the plasmapause

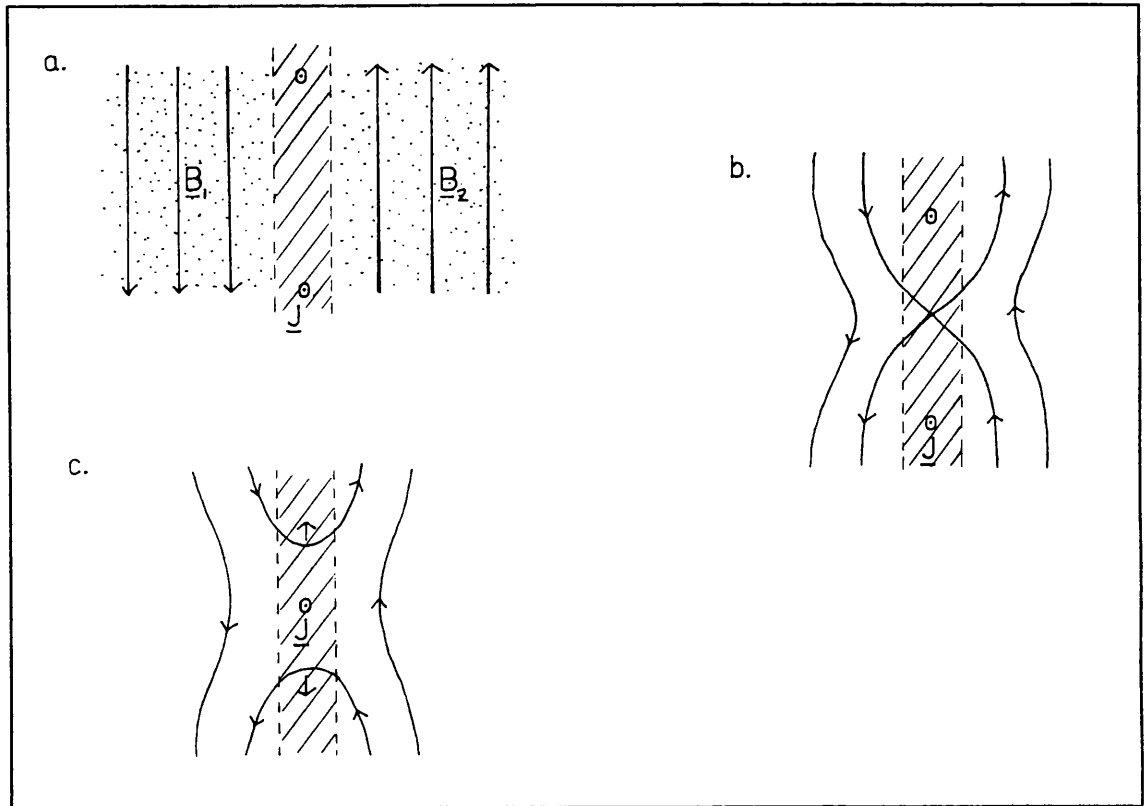


Figure 3.21 The process of reconnection

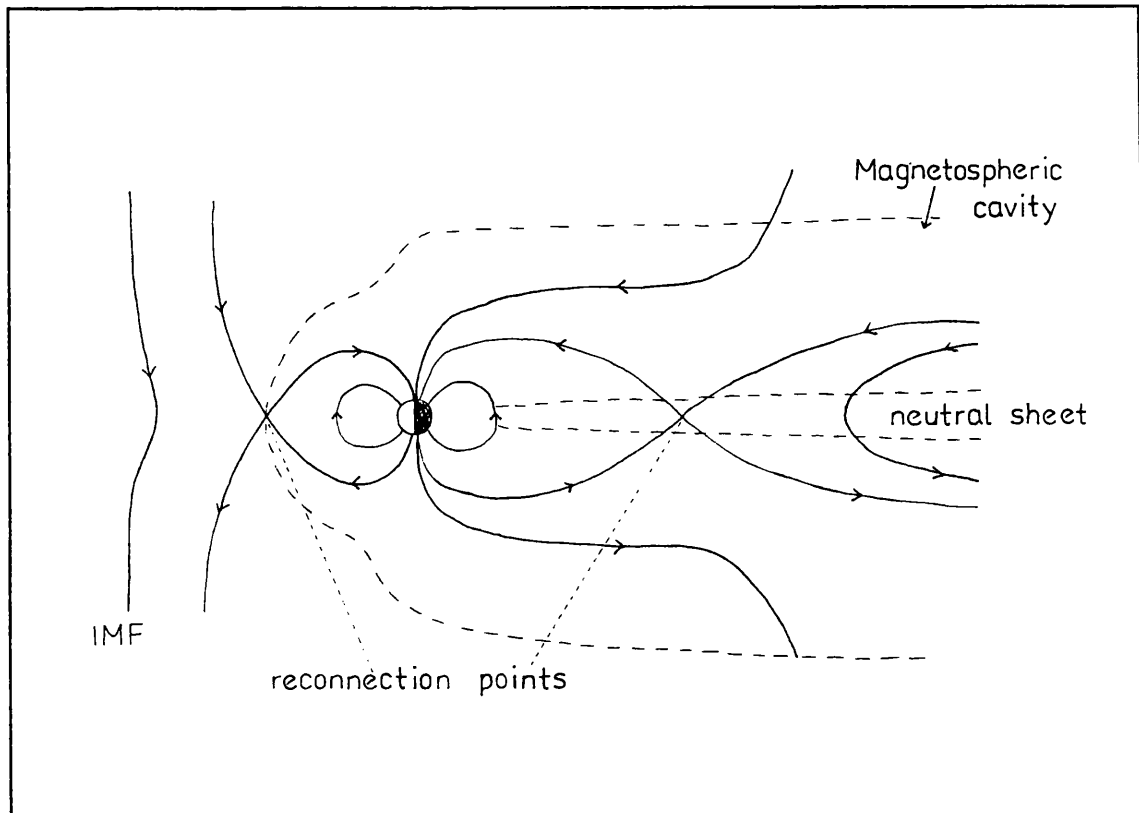


Figure 3.22 Reconnection in the magnetosphere

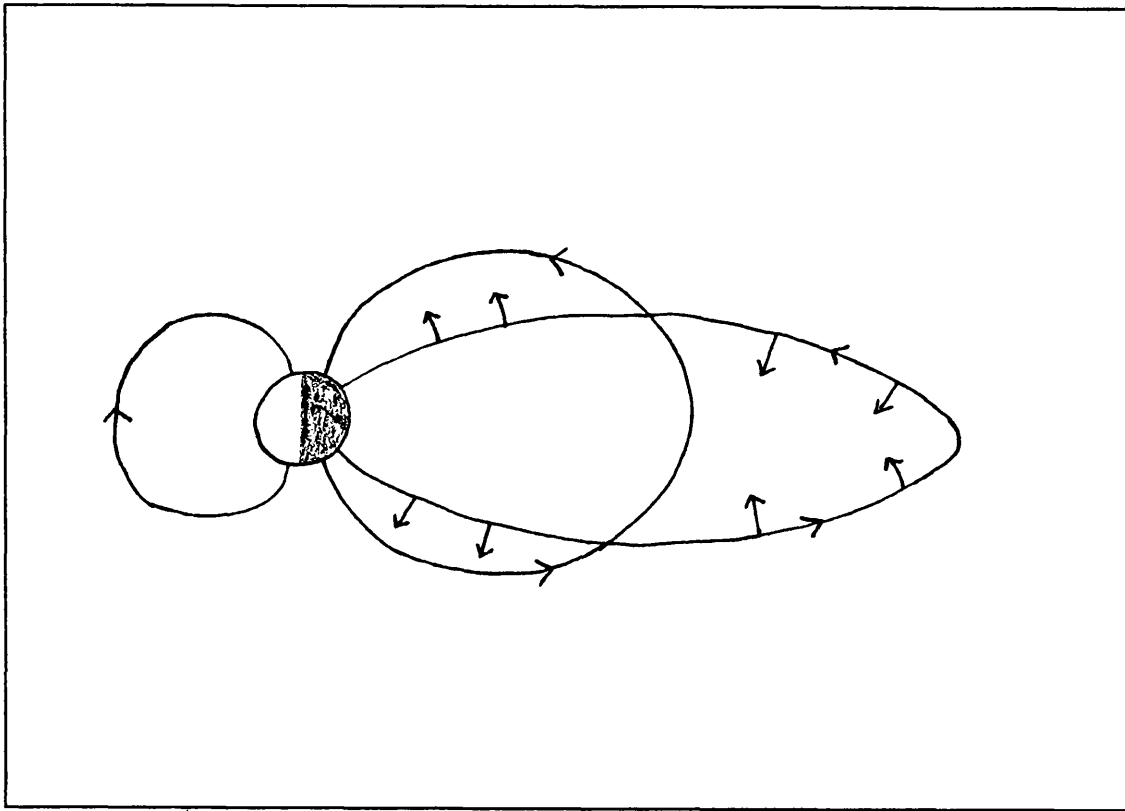


Figure 3.23 Field collapse during a substorm

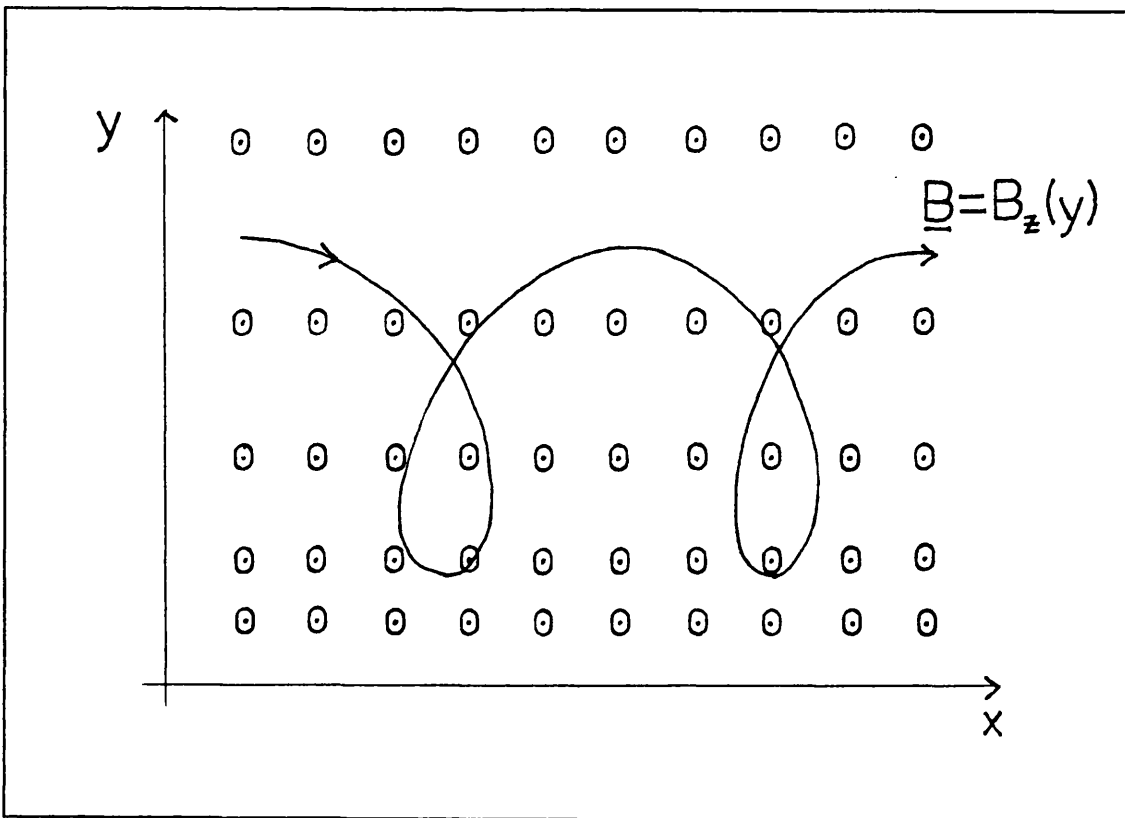


Figure 3.24 Grad-B guiding centre drift

4. THE SIMULATION CODES EQUIPOT, BEAM AND NASCAP

The physical principles and scope of three numerical spacecraft charging simulation codes are discussed. A new model with three free parameters is introduced for calculating the yield of true secondary electrons from a surface.

4.1 EQUIPOT

This code⁹² has been developed from an earlier program, "EQPOT" written by the author. It is an interactive tool which finds the equilibrium potential of a surface exposed to a space plasma. Equilibrium surface potential is determined from an input list of material properties, solar illumination conditions and plasma parameters. The central feature of the code is the ability to change any one of these input parameters in order to assess its effect on the equilibrium potential.

EQUIPOT assumes that the "spacecraft" is a sphere of diameter 1m which is covered in one type of material (usually conducting) with an infinitesimally small patch of a second material representing an insulating surface, or an isolated conductor. The current balance equation is solved to find the equilibrium potential of each surface, from which the degree of differential charging can be inferred. Collection of incident current is calculated using spherical or planar probe theory (see section 3.1) for which analytical expressions are available. There are two main limitations to this approach; firstly, analytical probe collection expressions represent limiting cases and secondly, without explicitly calculating the equipotential contours around the whole object, potential barrier formation cannot be modelled. Consider a typical simulation which consists of a spherical, sunlit, conducting satellite structure (near to plasma potential) with a shadowed, insulating patch material (at a large negative potential). For a plasma with Debye length much greater than the radius of the satellite, the equipotential contours which develop around the infinitesimal patch will appear spherical. Thus, spherical orbit limited probe collection theory (for one hemisphere only) is appropriate, but represents one of the limiting cases (the other is given by applying plane probe collection theory).

4.1.1 Voltage stepping algorithm

A simple voltage stepping algorithm is employed to solve the current balance equation for the structure and the patch material. A structure potential is determined such that the current components due to incident electrons, incident ions, secondary and backscattered electrons and photoelectrons are balanced. The conduction current of electrons from the negatively charged patch is negligible compared with the other components since the patch is infinitesimally small. If the structure charges positively with respect to plasma potential, the secondary and photo-

electron temperatures are used to determine the fraction of electrons can escape from the sphere. Thus, an illuminated conductor will normally acquire an equilibrium potential of a few volts positive. If the sphere charges negatively with respect to plasma potential, all emitted electrons are assumed to escape to infinity (or to a distance greater than the Debye length). The same current components are considered for the patch material with the addition of a conduction current to the structure which may be significant compared to the other components for the patch. If the patch is an exposed dielectric, the total resistance and capacitance between the patch and the structure are computed from the material thickness, resistivity and dielectric constant. If the patch is an isolated conductor, the capacitance and resistivity of the intermediate dielectric are specified.

EQUIPOT finds roots of the function $j(V)$ by successively stepping the probe voltage from an initial value V_0 . If the sign of $j(V)$ changes between steps, the step size dV is reduced and the process repeated until the root of $j(V)$ has been determined to within a pre-defined accuracy. If $j(V)$ has multiple roots, the initial potential V_0 can be altered until the algorithm converges to a different stable root. Although the surface voltage V is used as the dependent variable, the charging time, t can also be estimated at each step from the relation $CdV = I_{net}dt$, assuming that the capacitance between satellite elements is much greater than that between the whole satellite and space. Thus, EQUIPOT can be used to predict the differential time history of a sample exposed to a plasma, as well as the value of the root. This is useful for assessing the levels to which differential charging will develop during the timescales of natural events, such as severe substorm fluxes, or Low Earth Orbit traversals of the auroral zones.

4.1.2 A three parameter model of SEE

A new model for the secondary electron emission yield function is introduced. It is based on the work of Dionne^{32,33} and Burke³⁷ but has three free parameters; the maximum yield at normal incidence, the energy at maximum yield and the stopping power law index, n . This model requires much less computation time than the model of Katz et al³⁵ which takes six input parameters and performs a lengthy root-finding exercise before the yield at a given energy can be determined. The strength of the models of Dionne and Burke lies in their simplicity, but whilst they allow the user to fix the position of maximum yield based on measurements, they often produce significant disagreements with experimental data at incident energies well above the maximum yield.

A general expression for the total secondary yield, δ , for incident electrons with energy, E is written in terms of the product of the number of secondaries liberated at a depth x and the migration/escape probability of such a liberated electron from that depth, integrated over all depths (equation 3.62). The number of liberated electrons at a given depth $n(x,E)$ may be written in terms of the stopping power, dE/dx and the

electron liberation energy, e_0 (equation 3.63), and the migration/escape probability is assumed to decrease exponentially with depth with a scale factor, α , and normalisation constant, B , (equation 3.67). It is assumed that the stopping power, dE/dx remains constant with depth over the range of interest (Katz assumes that this is linear in x which introduces complications later) and that it depends on incident energy according to the following equation;

$$\frac{dE}{dx} = -\frac{A}{E_0^{n-1}} \quad (4.1)$$

where A is a constant, and n is the stopping power law parameter, which must always be greater than 1. Integration of equation 4.1 gives the range, R , of an electron of energy, E as

$$R = \frac{E_0^n}{A \cdot n} \quad (4.2)$$

Combining equations 3.62, 3.63, 3.67, 4.1 and 4.2 and performing a direct integration over a range of depths from 0 to the electron range, R , gives the following expression for yield at energy E ;

$$\delta = \frac{B \cdot A}{e_0} \left(\frac{A \cdot n}{\alpha} \right)^{\frac{1}{n}} (\alpha \cdot R)^{\frac{1}{n}-1} [1 - e^{-\alpha \cdot R}] \quad (4.3)$$

$$\therefore \delta = c_1 x^{\frac{1}{n}-1} (1 - e^{-x})$$

where

$$c_1 = \frac{B \cdot A}{e_0} \left(\frac{A \cdot n}{\alpha} \right)^{\frac{1}{n}} \quad x = \alpha R$$

c_1 is a dimensionless constant for given n and x is a dimensionless electron range. The task now is to find values of c_1 and α (for a given value of n) which produce the measured value of maximum yield and energy at maximum yield. The electron range (and hence energy) at which the expression for yield (equation 4.3) is a maximum may be found by setting the derivative of δ with respect to x to zero. This yields the following relationship between x_m (dimensionless range at maximum yield) and n ;

$$x_m = \left(1 - \frac{1}{n} \right) (e^{x_m} - 1) \quad (4.4)$$

For a given value of n , x_m must be found by a numerical method. Since the function is monotonous, a simple Newton-Raphson iteration process will converge to a solution of adequate accuracy within a few steps given a sensible starting value of x_m such as 2.0. The next step is to evaluate

x in terms of incident energy, and other known quantities. Using equation 4.2, x may be written in terms of the incident energy, energy at maximum yield, E_m and n as follows;

$$x = x_m \left(\frac{E_o}{E_m} \right)^n \quad (4.5)$$

Equation 4.3 may be used directly to find c_1 in terms of the maximum yield, x_m and n, then combined with equation 4.5 to give a general expression for the yield at normal incidence in terms of known quantities;

$$\delta = \frac{\delta_m}{(1-e^{-x_m})} \left(\frac{E_m}{E_o} \right)^{n-1} \left(1 - \exp \left[-x_m \left(\frac{E_o}{E_m} \right)^n \right] \right) \quad (4.6)$$

and x_m is evaluated from equation 4.4.

Dionne chose $n = 1.35$ which gives a value for x_m of 2.28, whilst Burke chose $n = 1.725$ which gives a value for x_m of 1.50. Putting these numbers into equation 4.6 recovers the respective published expressions (equations 3.71 and 3.72).

The angle-averaged yield may be found by replacing α in equation 4.3 with $\alpha \cdot \cos(\theta)$ which results in the following expression for yield as a function of c_1 , x, and θ ;

$$\delta(\theta) = \frac{c_1 x^{\frac{1}{n}-1}}{\cos\theta} (1 - e^{-x \cos\theta}) \quad (4.7)$$

This may be integrated according to equation 3.73 to give the angle-averaged yield;

$$\bar{\delta}(E_o) = \frac{\delta_m}{(1-e^{-x_m})} \left(\frac{E_m}{E_o} \right)^{n-1} 2 \left[\frac{x + e^{-x} - 1}{x} \right] \quad (4.8)$$

where x is related to x_m , E_o and E_m according to equation 4.5. For $n = 1.35$, equation 4.8 reduces to the angle-averaged Dionne equation 3.74.

This model is implemented as a FORTRAN77 function which is listed in Appendix A. The input arguments EMAX, DELMAX and N define the SEE yield curve parameters, EEV is the incident energy in eV and the yield is for normal or isotropic particle populations according to the value of ITYPE.

4.1.3 Material and environment definitions

EQUIPOT specifies each material in terms of twelve parameters; these are listed in Table 4.1. The first three parameters are used only when the material is selected for the patch and the material is an insulator. The atomic number is needed to compute the backscatter yield, based on the model described in section 3.2.2. In those cases when the material is not an element, the average atomic number for all constituents is the best estimate. Properties 5, 6 and 7 define the secondary emission characteristics of the material according to the model described in the previous section; the value and energy of the maximum yield at normal

incidence must be defined, together with the energy-loss parameter, n which determines the shape of the yield curve at high energies. Properties 9 and 10 define the shape of the electron yield curve due to incident ions (equation 3.103); property 9 is the yield for normally incident, 1 keV protons and property 10 is the incident proton energy which produces maximum secondary yield. Property 11 is the integrated photocurrent yield assuming normal illumination, and property 12 is the surface resistivity. Note that all four types of secondary yield are specified in terms of normally incident primary radiation; EQUIPOT uses these parameters to compute the true secondary yield based on the selected solar illumination conditions and plasma environment (normal or isotropic).

The plasma environment is described by specifying one or more of the following three elements; (a) three Maxwellian electron populations where the density and temperature of each are specified, (b) three Maxwellian ion populations where density, temperature and ion mass is specified for each, (c) an electron flux spectrum in the form of up to 100 (energy, flux) pairs and up to three ion spectra, each in the form of up to 100 (energy, flux) pairs, with one spectrum per ion species. In the energy range where measured spectra and Maxwellian components overlap, the total flux of that species is taken as the measured value (ie that part of the Maxwellian component is ignored). This is especially useful for fitting a high energy Maxwellian tail to a measured spectrum.

4.2 BEAM

The physical basis of the BEAM code is discussed, following a short review of electron beam charging theory.

4.2.1 Theory of electron beam charging

When one or more electron beams impinge on an unilluminated sample of material in a vacuum, the net current density to the sample, j_{net} has four components;

$$j_{net} = -j_e + j_{se} + j_b + j_c \quad (4.9)$$

where j_e is the current density of incident electrons, j_{se} is the current density of true secondary electrons, j_b is the current density of backscattered electrons and j_c is the conduction current per unit area between the sample surface and Earth. A monoenergetic beam of electrons with energy E_b impinging on a planar sample at uniform potential V arrive at the surface with energy E_s ;

$$E_s = E_b + V \quad (4.10)$$

Assuming that simple planar probe collection theory applies, the incident electron current, j_e is equal to the beam current j_{beam} , providing that E_b

exceeds the absolute value of V . Writing the total secondary yield (true secondary emission plus backscatter) at normal incidence as $Y(E_s)$, the current balance equation becomes

$$j_{net} = j_{beam}[-1 + Y(E_s)] + j_c \quad (4.11)$$

The behaviour represented by this equation may be classified as either **emission limited** (when the bulk conduction current or leakage current is small compared to the beam current), or **conduction limited**⁹³ when the conduction current is comparable to the beam current.

(a) Emission limited behaviour.

Conductivity is negligible and j_c may be set to zero in equation 4.11. Equilibrium occurs when $j_{net} = 0$, ie when $Y(E_s)$ is unity, or when j_{beam} is zero. If the net secondary yield function, Y has a maximum less than unity, equilibrium is achieved when the incident beam current becomes zero; ie when the negative potential of the sample (in Volts) is numerically equal to the beam energy (in eV). More commonly, the maximum net yield exceeds unity, and two points are defined where the net yield is equal to unity; E_- (lower crossover point) and E_+ (upper crossover point). Consider a sample which is initially uncharged. If the electron beam energy exceeds E_+ , electrons reach the sample with an energy E_b ($> E_+$) such that the net secondary yield is less than unity and the sample begins to acquire a net negative charge. The energy with which electrons reach the surface is reduced, and therefore the net secondary yield increases, until eventually, the sample reaches a negative potential $V = E_b - E_+$ such that the net secondary yield is unity and the current balance equation is satisfied. If the initial beam energy E_b lies between E_- and E_+ (for an uncharged sample), the sample will initially acquire a net positive charge. Once the potential of the sample becomes positive, a fraction of the true secondary electrons will be prevented from escaping to infinity by the electric field around the sample but backscattered electrons are able to escape, since their energy is almost equal to that of the incident particles. However, backscattered yields are always less than unity, so the sample will reach equilibrium at a few volts positive, when the current due to backscattered electrons plus the current due to those secondaries which are sufficiently energetic to escape is equal to the incident current. When the beam energy is less than the lower crossover energy, E_- , the sample will acquire an initial net negative charge, and therefore subsequent electrons arrive with reduced energy. Since dY/dE is positive in this region, Y decreases with decreasing electron energy and equilibrium will be achieved when the sample potential (in Volts negative) is numerically equal to the beam energy (in eV).

Figure 4.1 is a theoretical curve giving the equilibrium potential of Kapton as a function of incident beam energy. For the two regions where negative charging occurs, the curve is a straight line of slope unity. Note also the discontinuity when $E_b = E_-$. This is point of unstable

equilibrium, since a small increase in beam energy will cause the sample to make a large change in equilibrium.

(b) Conduction limited behaviour.

If the sample has a conductivity σ , and thickness d , the conduction current j_c may be written as

$$j_c = \frac{\sigma V}{d} \quad (4.12)$$

and the current balance equation 4.11 becomes

$$\frac{1-Y(E_B-V)}{V} = \frac{\sigma}{j_{beam}d} \quad (4.13)$$

For a given beam energy, the equilibrium surface potential must be found by a numerical technique, and can no longer be calculated directly from a secondary emission yield curve as for emission limited behaviour.

4.2.2 Code description

The previous section has shown that for the case of finite conduction current, or for multiple beams, the equilibrium potential of the sample surface must be determined by a numerical method. The BEAM code has been written (by the author) to perform such a calculation. It is a derivative of EQUIPOT and finds the solution to the current balance equation by converging towards the root from one side; thus the total charging time may be computed at each step. Whilst this is not necessarily the most efficient root-finding technique, it yields the potential time development history as well as the final equilibrium potential.

BEAM does not contain any explicit probe collection theory algorithms; the total incident electron current from each beam is specified, and assumed to remain constant for all sample potentials (implicit planar probe theory). If the target is chosen to be a conductor, the conductivity, thickness and dielectric constant of the intermediate insulator must be specified. BEAM is also able to include the effects of field enhanced conductivity according to the theory described in section 3.2.5. Models for true secondary electron emission and backscatter are identical to those used for EQUIPOT.

4.3 NASCAP

The NASA Charging Analyser Program (NASCAP)^{19,35} is a full three dimensional spacecraft charging analysis tool. Its primary purpose is to assist with the design of satellite surfaces in order to minimise surface charging, but it is also suitable for modelling the effect of spacecraft potential on plasma analyser experiments and the effect of emitted electron and ion beams.

Satellite models are defined within a rectangular 17x17x33 grid where the mesh size may be chosen freely. The material properties of each satellite surface cell must be defined by a list of parameters similar

to those described for the EQUIPOT code. Detailed surface features cannot be modelled due to the coarseness of the grid, but it is normally possible to achieve a good overall picture of the satellite whilst retaining roughly correct proportions of different surface materials. NASCAP allows the electrical characteristics of the satellite to be defined explicitly; for example the resistance and capacitance between a floating conductor and satellite ground. NASCAP is limited to plasma conditions where the Debye length is much greater than the satellite dimension, since spherical, orbit-limited probe collection theory is assumed to apply for each surface cell. This is the first major weakness of NASCAP since, even for a long Debye length regime, surface cells which are part of a cavity, or adjacent to surface cells at a very different potential will not behave like a spherical probe.

The plasma environment is defined in terms of single or double Maxwellian components which may be isotropic or anisotropic. It is possible to define a measured plasma spectrum, but if this is highly non-Maxwellian the potential solver algorithm may become unstable. This is NASCAP's second major weakness; it is seldom possible to assess the charging behaviour in measured space plasmas.

NASCAP computes the potential of each surface cell at specified time steps. The computational grid consists of several nested grids, each with 17x17x33 nodes and each with twice the mesh size of the grid which it surrounds. The model is defined within the innermost grid. At the end of each time step, the NASCAP potential solver algorithm finds the potentials of each surface cell, and at each node of the computational grid by self-consistently solving the current balance equation for each cell together with Laplace's equation for the empty grid points by a variational method. This self-consistent approach is necessary because changes in the current to a surface cell (perhaps due to changes in surrounding cell voltages) will alter the potential of the cell which in turn changes the incident current. Based on the configuration of potential contours around the spacecraft, NASCAP assesses whether low energy secondary electrons (true secondaries plus photoelectrons) are able to escape from any surface cell to infinity, or whether a potential barrier has formed which inhibits their escape. However, each simulation timestep requires several thousand seconds CPU time on a typical mini computer. Thus, it is not suitable for an extensive sensitivity analysis.

NASCAP incorporates a module called "Test-Tank" which is designed to simulate the behaviour of material samples, or satellite models in vacuum tanks under electron or ion gun bombardment. The usual environment definition in terms of Maxwellian distributions is replaced by a series of electron or ion gun definitions, where the total current, particle type, beam energy and beam divergence are specified for each gun. The location of the tank walls is also specified, and set at zero potential. In its normal mode, NASCAP fixes the potentials at the extremities of the computational grid by assuming that the potential contour configuration far from the body is the same as that surrounding a charged sphere, but

for the Test-Tank module, the potentials at the tank walls are fixed and the stray capacitance between the object and the tank walls is calculated and incorporated into the overall time constant.

The Test-Tank module may be executed in one of two modes. The first mode (TYPE1) performs current balance calculations by explicitly tracking charged particles through the potential contour configuration surrounding the object and re-computing the potentials in a self-consistent manner at each timestep. The second mode (TYPE6) uses a spherical probe collection theory approximation to compute the incident current to each surface cell. The latter method is appropriate for near-spherical objects which do not develop high degrees of differential charging; the former method is more accurate (but slower) for any configuration and has been used for the simulations described in Chapter 6.

Table 4.1
EQUIPOT material property list

no.	name	units	range
1	Relative permittivity	-	-
2	Thickness	m	-
3	Conductivity	mho/m	-
4	Atomic number	-	1 to 92
5	Max normal SEE yield	-	-
6	Energy at max yield	eV	-
7	Energy loss power, n	-	> 1.0
8	Material density	g/cm ³	-
9	SEE yield due to 1 keV protons	-	-
10	Proton energy at max yield	keV	-
11	Integrated photocurrent yield	A.m ⁻²	-
12	Surface resistivity	Ω/\square	-

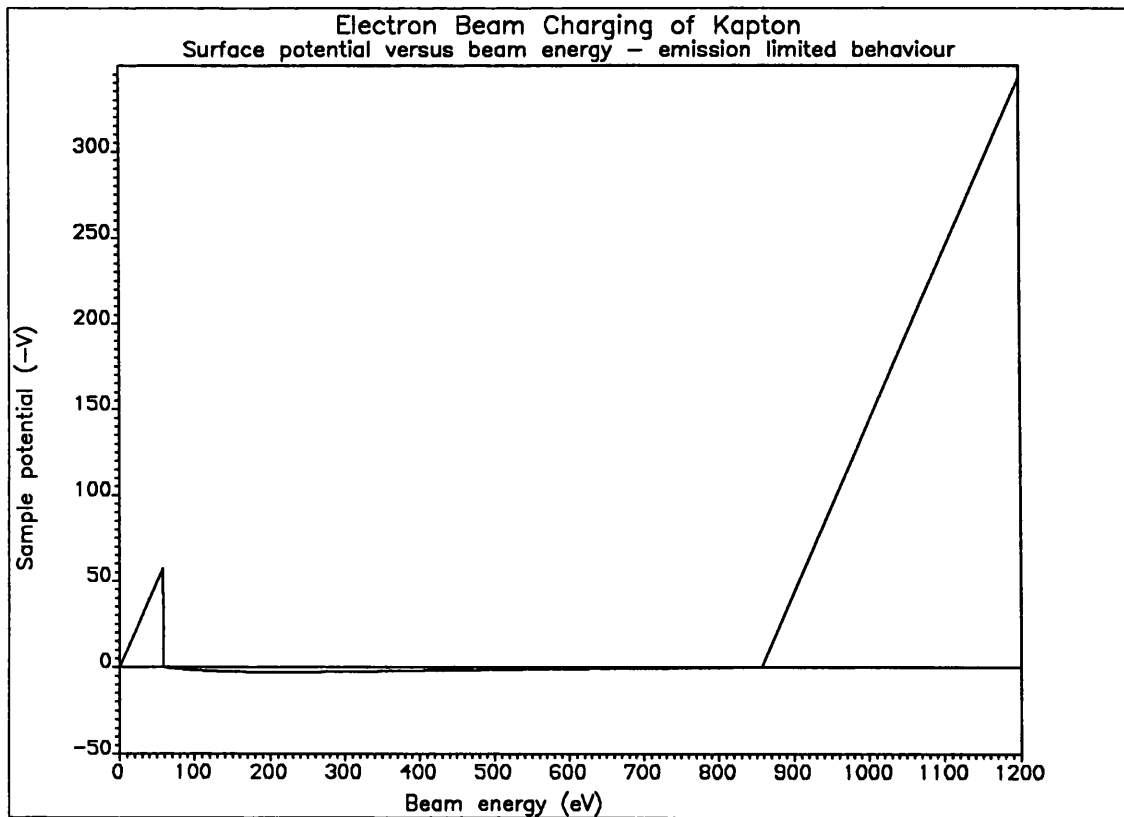


Figure 4.1

5. THE ELECTRON ENVIRONMENT AT GEOSTATIONARY ORBIT

Data from the electron spectrometer flown on Meteosat F2 has been used to identify the main regions of plasma encountered in geostationary orbit and to examine enhanced electron fluxes during geomagnetic storm and substorm events. Long-term (5 year) statistical studies are presented for the location of plasma boundaries as a function of local time (LT) and geomagnetic activity, and for the occurrence frequency and intensity of substorm events.

5.1 DATA REDUCTION

The data set from the Meteosat F2 electron spectrometer consists of a fifteen point energy spectrum measured every 100.6 seconds for five years. Two derived quantities which prove to be convenient for identifying plasma regions and substorm characteristics are total flux (TF) and mean energy (E_M). For a differential flux spectrum $f(E)$, these quantities are given by

$$TF = \int_0^{\infty} f(E) dE \quad E_M = \frac{\int_0^{\infty} E f(E) dE}{\int_0^{\infty} f(E) dE} \quad (5.1, 5.2)$$

These integrals may be evaluated for a fifteen point spectrum using the trapezium rule;

$$TF = \frac{1}{2} \sum_{i=1}^{i=14} [f(i) + f(i+1)] \cdot [E(i+1) - E(i)] \quad (5.3)$$

and

$$E_M = \frac{1}{2} \sum_{i=1}^{i=14} [E(i) \cdot f(i) + E(i+1) \cdot f(i+1)] \cdot [E(i+1) - E(i)] \quad (5.4)$$

where $f(i)$ is the differential flux, in $(\text{cm}^2 \cdot \text{s} \cdot \text{st} \cdot \text{eV})^{-1}$ for channel i ; total flux TF has units of $(\text{cm}^2 \cdot \text{st} \cdot \text{s})^{-1}$ and the mean energy, E_M is in eV. It is convenient to convert total flux into incident current; for a spherical collector (see section 3.1), incident current density J (in nA/m^2) is related to total flux TF ($\text{cm}^{-2} \cdot \text{st}^{-1} \cdot \text{s}^{-1}$) by the following relationship;

$$J = e \cdot \pi \cdot TF \quad (5.5)$$

$$J(\text{nA}/\text{m}^2) = 5.03 \times 10^{-6} \cdot TF(\text{cm}^2 \cdot \text{st} \cdot \text{s})^{-1}$$

where e is the magnitude of the electronic charge. For a plasma with a Maxwellian distribution function, the mean energy E_M (in eV) and incident

current density J are related to electron density n_e and temperature kT_e as follows

$$kT_e = \frac{E_m}{2} \quad n_e = \frac{2J}{e} \left(\frac{m_e}{E_m} \right)^{\frac{1}{2}} \quad (5.6, 5.7)$$

where m_e is the electronic mass. Using these relations, it is possible to estimate electron density and temperature from measured spectra, together with the electron pressure $p = n_e \cdot kT_e$. However, it should be noted that where the spectrum is highly non-Maxwellian, or when the mean energy is high with respect to the maximum energy of the detector, equations 5.6 and 5.7 should be used with caution.

5.2 RESULTS

Total flux and mean spectral energy are used to identify four distinct plasma regions encountered in GEO. The effect of geomagnetic activity on plasma boundaries is investigated using the Kp index. Long-term average plasma sheet spectra are presented for several levels of activity and will be used as reference spectra for charging studies presented in Chapter 7. Over two thousand geomagnetic storm and substorm onsets have been detected from the data set; correlations of the frequency and intensity of these events with terrestrial magnetometer data are presented. Finally, probability distributions are given for the electron density and pressure increases following substorm activity.

5.2.1 Plasma regions in GEO

Mean electron energy and incident current density were computed for intervals of 5.03 minutes (an average over three 100.6 second accumulation periods) for the entire data set. A scatter plot of these quantities was created for each hour of local time, with approximately 20,000 points per plot. Four such plots, for local times 00-01, 03-04, 12-13 and 20-21 are shown in Figures 5.1, 5.2, 5.3 and 5.4 respectively. Several distinct regions of increased point density are discernable; firstly, for current densities below about 300 nA/m², the detector count rate is comparable with background noise levels and therefore the mean energy is not a meaningful quantity. Each plot shows a concentration of points with current density below 300 nA/m² (designated as region I) which can be associated with the spacecraft being immersed in cold plasma with a thermal energy much less than the detector energy threshold of 50 eV. Evident from almost all the scatter plots is an increased concentration of points in the region bounded by the limits 300 to 800 nA/m² incident current and 0 to 3000 eV mean energy (designated as region II) representing a transition between region I (thermal plasma) and the large, diffuse point distribution which covers most of the rest of the frame (designated as region IV) and is associated with the plasmashield. In the midnight to dawn sector, increased point density is observed in

the region bounded by 5 keV to 8 keV mean energy, and 500 to 2000 nA/m², which is a subset of region IV and is designated region III.

So far, the boundaries between four distinct regions have been identified from scatter plots in terms of electron current and spectral mean energy according to a somewhat arbitrary, visual criterion. However, the distribution of points falling into each region as a function of local time and geomagnetic activity relates these regions to distinct plasma populations within the magnetosphere. First, consider the local time distribution; for each hour of local time, the number of points (5.03 minute intervals) in each region was expressed as a fraction of the total number of points within that local time range; the results are shown in Figure 5.5. The satellite is most likely to be in region I between 0900 and 2200 LT; in fact between 1100 and 1800 LT the probability of being in region I exceeds 90%. This is generally consistent with the times when the geostationary orbit is expected to be within the plasmasphere, or at least to be earthward of the inner plasmasheet boundary. Following prolonged periods of geomagnetically quiet conditions, the plasmopause extends beyond 6.6R_E for all local times which explains why the probability of being in region I during the midnight to dawn sector does not fall to zero, but is of the order of 10%. The local time dependence of region II shows a peak in the dusk to midnight sector which is coincident with the local time for which the probability of being in region I is falling sharply. This is consistent with the idea that region II is a transition zone between the plasmopause and the plasmasheet, referred to as a distinct region⁷⁶; the plasmasheet "earthward edge". The probabilities of being within regions III and IV fall nearly to zero during the noon to dusk sector, but rise to a maximum (both centred on 03-05 LT) during the midnight-dawn sector, which is typical of plasmasheet behaviour. The probability distribution for region III covers a much narrower spread of local times than region IV and is associated with the central plasmasheet. In fact, the peak in region III probability distribution between 02-07 LT is exactly coincident with the secondary minimum in the region IV distribution providing further support to the view that regions III, IV (and partially II) represent the plasmasheet as a whole whilst region III is appropriate to central plasmasheet conditions.

The response of each of the probability distributions shown in Figure 5.5 to changes in geomagnetic activity was examined by using the Kp planetary index. Although the Kp index has a coarse time resolution of 3 hours which makes it unsuitable for analysis of individual events, it is well suited to this type of long-term statistical study. There are 28 possible values of Kp ranging from 0o (very quiet geomagnetic activity) through to 9o (very disturbed); in order to achieve adequate statistical confidence and to aid clarity in presentation of results, values of Kp have been grouped together into four categories, each containing seven values; Very Quiet (VQ) for Kp = 0o to 2o; Quiet (Q) for Kp = 2+ to 4+; Disturbed (D) for Kp = 5- to 7-, and Very Disturbed (VD)

for $K_p = 7_0$ to 9_0 . Values of K_p do not occur with equal frequency, therefore the probability of being in a particular plasma region at given values of local time and K_p range is found by dividing the number of records falling into a (LT, K_p range, plasma region) bin over the whole data set by the total number of records which fall into the appropriate (LT, K_p range) bin. Taken over all local times, the value of K_p spends 41.5% of the time in the VQ range, 48.7% in Q, 9.1% in D and only 0.7% in the VD range, which can lead to statistical fluctuations when correlating measured quantities with the most active range. Furthermore, the occurrence frequency of a given K_p range is not constant for all local times; the uneven planetary distribution of magnetic observatories results in the VQ range being most probable around 12UT whilst active ranges are more probable in the dusk to midnight and midnight to dawn sectors. This indicates that the calculation of K_p is biased towards European observatories, and is important for this study since K_p falls into the Very Disturbed range near noon very seldom (only 38 times in five years).

Figure 5.6 shows the probability (expressed as a percentage) of Meteosat being in region I for given values of local time and K_p range. As expected, the only non-zero probability in the midnight-dawn sector is for the Very Quiet range which includes periods of prolonged geomagnetic quiet. At increasing levels of activity, the satellite enters region I at later local times and exits earlier. Despite the wide range of activity levels within each K_p range together with solar cycle variations, the transitions into and out of region I are very sharply defined, particularly for the higher K_p ranges where the mean boundary position (taken as the 50% point) differs from the 10% and 90% points only by about 2 hours of local time. Figure 5.7 shows the probability of being in region II as a function of local time and K_p . The small peak in the Very Disturbed curve near 12LT is due to poor statistical coverage and should be ignored. Plasma conditions attributed to region II behaviour are most probable for Very Quiet conditions, and become less probable as geomagnetic activity increases. For a given activity level, the probability distribution for region II is singly peaked in local time, and the position of this peak moves to earlier times as geomagnetic activity increases; near 03LT for Very Quiet conditions, near 20LT for Quiet conditions, near 19LT for Disturbed conditions and near 15LT for Very Disturbed conditions. The positions of these peak values are coincident with the local times for which the satellite leaves region I, but significantly, the satellite does not enter region II before entering region I during the dawn to noon sector. Figure 5.8 shows the probability distributions for plasmashet conditions (regions III and IV together) as a function of local time and K_p . This is almost a mirror image of Figure 5.6 and shows many of the same features. For very quiet conditions during the midnight to dawn sector, the probability is close to 50%, compared with more than 90% for the more active cases; this is consistent with the expansion of the plasmopause beyond $6.6R_E$ during prolonged quiet

periods. As activity increases, the satellite remains in the plasmasphere until later local times on the dayside and re-enters the plasmasheet earlier during the dusk-midnight sector. In addition, the local time spread of plasmasphere exit times as a function of K_p is much smaller than the corresponding spread of entry times.

5.2.2 Average plasmasheet spectra

In general, averaging the Meteosat data over long periods has limited value, even if the average is confined to one plasma regime (ie plasmasheet) and one level of geomagnetic activity, as the scatter plots of section 5.1 bear witness. However, average spectra provide a reference against which more or less disturbed conditions can be assessed.

Five-year average electron spectra for the plasmasheet (regions III and IV) were calculated for the four geomagnetic activity levels (VQ, Q, D, VD) defined above. Results are expressed in terms of current spectra where the contribution to total incident current from each channel is plotted against the channel mid-point energy. Strictly, such spectra should be drawn as histograms, but in the interests of clarity, the height of each histogram bar is drawn as a point at the mid-interval energy. Figure 5.9 shows the results (four curves marked VQ, Q, D, and VD). For each level of activity, the greatest contribution to current is from high energy, and the curves are truncated above the peak energy due to the upper energy limit of the detector. Visual extrapolation of these curves to higher energy implies that there will be a significant incident current of plasmasheet electrons beyond the range of the detector. The total current at each energy increases smoothly with geomagnetic activity, but the energy of the peak remains close to 7 keV for all activity levels.

Figure 5.9 also shows the equivalent Maxwellian distributions for each of the four mean current spectra, where the Maxwellian temperature, T_e , and density n_e are related to the total flux and mean energy of each spectrum according to equations 5.6 and 5.7. The fit is generally poor, with the peak of the measured distribution being much broader than its associated Maxwellian. This may be explained in part by noting firstly that the average of several Maxwellian distributions with different densities and temperatures is not mathematically equal to a single Maxwellian distribution with density equal to the mean density and temperature equal to the mean temperature. Secondly, the total flux of a Maxwellian distribution is given by an integral to infinity, but the total flux of each mean distribution has been computed by an integral only up to 20 keV.

5.2.3 Frequency and intensity of substorm events

The diffuse nature of the scatter plots introduced in 5.2.1 for region IV is largely due to the action of geomagnetic storms and substorms which cause a rapid flux increase at geostationary altitudes in the pre-midnight to dawn sector. The energy range and time resolution

of the Meteosat detector are ideal for making long-term measurements of substorm frequency and intensity at $6.6R_E$ in the equatorial plane. There is no universally accepted definition as to what constitutes a magnetic "storm" or a magnetic "substorm", but a "storm" is usually designated as such whenever a given terrestrial magnetometer records a deviation which exceeds some threshold. However, ground based magnetometers are not always an ideal indicator of magnetospheric activity, so in the context of this work, it is convenient to describe all magnetospheric disturbances as "substorms" of varying degrees of intensity. Figure 5.10 shows a summary plot of the Meteosat spectrometer data for the 6th June 1982. The top panel is a spectrogram where the 15 energy channels are plotted along the y axis and the differential flux value for each channel is plotted as a shaded rectangle (with two grey shades per decade from 10^2 to 10^7 electrons/($\text{cm}^2 \text{ s st eV}$)). The next two panels show total flux (TF) in nA/m^2 and mean energy (E_m) in eV, calculated according to equations 5.3 and 5.4. The narrow band at the base of the top panel gives the eclipse status (filled = umbra, partially filled = penumbra, open = illuminated). Each point represents an average over three successive 100.6 second accumulation periods. There is a sudden increase in total flux, characteristic of substorm injection at about 01:30 UT, followed by another at 05:30 UT. A storm sudden commencement (SSC) was reported at 02:43 UT. The onsets are also apparent from the spectrogram and from sudden changes in mean spectral energy, but the total flux is the clearest indicator.

Substorm onsets were detected automatically from the data set according to a criterion set by visual inspection of many spectrograms, such as Figure 5.10. An onset is recorded if there are three successive monotonically increasing points and the total flux of the third point is at least 700 nA/m^2 greater than that of the first. The magnitude of the substorm is recorded as the absolute value of total flux at the maximum of the substorm onset peak. Thus, the storm is detected as the magnitude of the fluctuation whilst its size is recorded as the maximum absolute magnitude of the electron flux.

Using this technique, a total of 2333 substorm onsets were detected between April 1982 and March 1987. Figure 5.11 shows the distribution of these events in local time, relative to local midnight. Most events occur during the hours around midnight, but some events have been observed as early as 17UT, and as late as 10UT. Since electrons drift eastwards, the distribution is skewed towards the dawn side, but it is evident that injected electrons are unable to drift beyond about 10UT at this altitude and remain recognisable as injected particles. The spectrometer data will be affected by vehicle charging; therefore, all eclipse periods and barrier charging events have been removed from the data set for this analysis. The absence of any data during eclipse explains the secondary minimum immediately around local midnight.

During the period of this analysis, 138 SSC's were reported by the Observatorio del Ebro, Roquetas, Spain, and by the Institut fur Geophysik

der Gottingen Universitat, Germany, based on world-wide magnetometer data⁹⁴. Figure 5.10 shows that there are at least two injection events associated with the same burst of activity which caused the SSC threshold to be exceeded. In general, the frequency with which substorm onsets are observed increases close to the time when an SSC is reported. For this analysis, a substorm onset is deemed to be associated with an SSC if it occurs in a 13 hour long period starting one hour before the SSC and ending 12 hours afterwards. This choice is somewhat arbitrary, but has to be comparable to the persistence time of the storm, such that injected particles which drift are also associated with the reported SSC, and must not be too wide, or else the fraction of time deemed to be associated with an SSC will become a significant fraction of the total data set, thereby increasing the number of chance correlations. Table 5.1 gives the substorm onset frequency (normalised to number per day) for periods associated and unassociated with a reported SSC; the errors are uncertainties in the mean rate assuming Poisson statistics. For all but the largest magnitude onset, the substorm occurrence frequency for times close to a reported SSC exceeds the observed rate at other times by a statistically significant amount. Furthermore, the near-SSC enhancement factor increases with substorm onset size which implies that the events with the largest fluxes of injected electrons are most likely to be detected by ground based magnetometers whilst smaller events are less likely to be detected.

Table 5.1 implies that a link exists between substorm intensity and the deviations observed with ground-based magnetometers during active periods. To investigate this possible link more fully, a correlation was sought between the intensity of a substorm event (maximum total electron flux at the peak of the event) and an appropriate geomagnetic index (a_p or Dst). Standard linear regression techniques assume that the error can be attributed to one or other parameter and give a correlation coefficient which describes the relation between the two parameters, not the degree of fit to a straight line. The method applied here is due to Wrenn⁹⁵ which assumes that an error exists in both parameters and determines the best-fit slope and a "Linear Fit Coefficient (LFC)" which is a measure of the goodness of fit to a straight line. This is achieved by minimising the sum of the quadratic distances between measured points and the regression line. The method was applied to find the correlation between the peak substorm flux and the hourly $a_p(\tau)$ index at the time of the injection (see section 3.3 for a description of this index) for several values of persistence time, τ . The best value obtained for the LFC was for $\tau=0.0$, which is simply an hourly interpolation of a_p . Figure 5.12 shows the scatter plot of this data, together with the best-fit straight line for which the LFC is 0.881. Although a clear trend is discernable, there is considerable scatter and it is not practical to use the best-fit slope as a one-to-one relationship. Furthermore, the fact that LFC maximises at $\tau=0.0$ implies that substorm activity is not related to the past history of a_p , although the converse may be true. On the

assumption that storm activity enhances the ring current, a correlation was sought between the peak substorm flux and the maximum negative value achieved by the Dst index in the 36 hour period following the onset. The scatter plot and best-fit straight line are shown in Figure 5.13, for which the LFC is 0.809. Thus, the peak substorm flux correlates more closely with the a_p index than the Dst index.

The continuous, five year Meteosat F2 data set spans the latter half of solar cycle 21 (minimum sunspot number in July 1976, maximum in October 1979 and minimum in September 1986). Since substorms are driven by the interaction between the solar wind and magnetosphere, it is expected that substorm frequency will be linked to solar activity. Figure 5.14 shows histograms of the observed number of substorm onsets per calendar month (N_{ss}) from April 1982 to March 1987 and the monthly count of grouped solar flares (N_{GF}) for the same period⁹⁶. Figure 5.15 presents the same data in the form of a scatter plot, with the best-fit straight line (LFC = 0.933) obtained by the same method as above, given by

$$N_{ss} = 5.218 \times 10^{-2} N_{GF} + 26.11.$$

This result raises the possibility that optical solar flare observations could provide some warning of forthcoming severe charging conditions, perhaps several tens of hours in advance.

5.2.4 Changes in density and pressure during substorms

Figure 5.16 shows three current spectra for the substorm onset observed at 0114UT on 6th June 1982 (see also Figure 5.10), marked "Before" for the spectrum immediately before the onset, "Peak" for the peak spectrum and "Delta" for the difference, or the injected current. In this case, the injected electrons arrive with a characteristic energy of about 3 keV, but it is more meaningful to classify substorms in terms of the change in electron density (computed from total flux and mean energy via equation 5.7), and the change in pressure between pre-storm spectra and peak-storm spectra. For this event, the electron pressure increases from 0.08 nPa before the injection to 0.584 nPa at the peak, whilst the electron density increases from 0.44 cm^{-3} to 2.01 cm^{-3} . The increase in electron density and electron pressure has been computed for each of the 2333 substorm onsets detected from the data set. The results are shown in Figures 5.17 and 5.18, in the form of probability distributions (ie the fraction of the total number of observed onsets falling into each density or pressure "bin"). Such probability tables may be used to compute the likelihood that any given substorm will enhance the local electron density and temperature by a certain amount.

5.3 DISCUSSION

Results presented in section 5.2 are discussed with particular reference to theoretical predictions of plasma boundaries and statistical studies of substorms.

(a) Near-Earth Plasma Boundaries.

Long term scatter plots of total flux versus mean electron energy have been used to identify four plasma regions. Region III represents a state to which the plasmashet tends at certain times and levels of activity such that there is no sharp transition between regions III and IV. Similarly, region II represents the plasmashet inner edge, and there is a smooth transition between regions II and IV. From the scatter plots, a much sharper boundary is evident at the outer edges of region I; moving from region I to II in the dusk sector, and from IV to I in the dawn-noon sector. However, since the detector energy threshold is 50eV, region I physically corresponds to a region devoid of energetic electrons, not to a region of cold plasma, although these may be coincident under certain circumstances. The boundaries of region I can be understood by combining a model for magnetospheric convection with a model for the expected lifetime of an electron (with given energy and at given position) due to pitch angle diffusion. Such a model has been constructed following Grebowsky and Chen⁷⁹ (who used a similar technique to predict the plasmopause position) and Kennel⁸⁰ who gives a model for the lifetime of an electron prior to being lost by pitch angle diffusion. Electron drift velocity in the equatorial plane of the magnetosphere is calculated by adding the $\underline{E} \times \underline{B}$ drift velocity vector (where \underline{E} is the vector sum of the solar-wind induced convection electric field and the corotation electric field) to the grad-B drift velocity vector (which is energy and charge dependent). Drift paths are computed by integrating the drift velocity vector over one timestep, then re-computing kinetic energy by conservation of the first magnetic moment, M (equal to the ratio of kinetic energy to magnetic field strength) at the new position. It is assumed that electron mirror points are close to the equatorial plane, such that curvature drifts are negligible with respect to grad-B drifts. The magnetic field is taken as dipolar in the equatorial plane and in the near-Earth region ($L \leq 10$), which leads to a corotation electric field of magnitude $94.4/r^2$ kV/ R_E (where r is measured in Earth radii) directed towards the centre of the earth and the grad-B drift velocity of an electron with kinetic energy T (in eV), of $Tr^2/68.0$ ms⁻¹, directed in the easterly ($+\phi$) direction. Two models for the convection electric field have been used; a uniform dawn-dusk field⁸⁶ with magnitude 0.5 to 2.0 kV/ R_E depending on activity, and a model proposed by Volland⁹⁷ which gives equipotentials of the form $Ar^2 \sin(\phi)$ where ϕ is the local time angle measured from noon and A is a constant which determines the field magnitude and is a function of K_p . The latter model includes the effect of shielding in the near-Earth region. Kennel⁸⁰ notes that for strong (pitch angle) diffusion, particle lifetime approaches a minimum lifetime,

T_M which depends only on the size of the loss cone (α_o = equatorial loss-cone pitch-angle) and the quarter-bounce period of the particle, T_B .

$$T_M = \frac{2T_B}{\alpha_o^2} \quad (5.8)$$

Assuming a dipolar field, and a precipitation altitude of 100km, the minimum lifetime of an electron with energy T (in keV) on a field line with equatorial radius L can be approximated by⁸⁰

$$T_M = \frac{L^4}{\sqrt{T}} \quad (5.9)$$

This model has been used to compute the position of the inner edge of the plasmashet for a given particle energy. The initial kinetic energy and position of an electron are specified, then the drift motion of the particle is traced backwards in time, choosing a timestep $-dt$ which produces an integrated drift velocity vector with magnitude less than $0.05R_E$. The minimum lifetime T_M , and fraction of lifetime dt/T_M is computed for each step of the trajectory; if the particle escapes from computational space ($R > 10R_E$) before its accumulated fractional lifetime exceeds unity, then the initial particle position is deemed "allowed" for that energy, otherwise, the initial position is deemed "forbidden". Physically, a forbidden initial position corresponds to one for which the drift time of a particle from the magnetotail exceeds the minimum lifetime of an electron before it precipitates. Figure 5.19 shows the near-Earth magnetosphere in the equatorial plane on which the magnetopause (modelled as a paraboloid) and geostationary orbit have been marked. The edge of the forbidden region (inner edge of the plasmashet) has been computed for several particle energies within the range of the Meteosat detector assuming a uniform cross-tail field of magnitude $1.0 \text{ kV}/R_E$. Figure 5.20 is similar, but has been computed with Volland's convection field model⁹⁷ with a K_p value of 6- representing disturbed conditions. Figure 5.21 has been derived by an identical method, and shows the maximum particle kinetic energy which can be observed at various local times at the geostationary altitude for a number of K_p values. This simulation provides a clear illustration of regions I, II and (III,IV). On the dayside, part of the orbit is always in the forbidden region for particles in the energy range of the detector; this is region I. Region II corresponds to that part of the orbit in the dusk sector which intersects plasmashet inner edge boundaries at increasing energy. As activity increases, this boundary region moves to later local times and becomes thinner (Figures 5.19 and 5.20) which is also consistent with observation. Figure 5.21 should be compared with Figure 5.8 which shows the fraction of time spent in regions III and IV; the time of post-dawn plasmashet exit (for a given energy) is predicted to be much less sensitive to changes in K_p than the position of the dusk plasmashet entry, which is clearly observed. This is also apparent from

Figures 5.19 and 5.20 which show that the dusk boundary region moves sunwards as activity increases. At the dusk boundary, corotation drifts and convection drifts tend to be in opposite directions, and therefore the boundary is highly sensitive to changes in the convection field, whilst near the post-dawn boundary, convection drifts and corotation drifts are in the same sense, such that changes in the convection field alter the magnitude of the net drift velocity, rather than the direction. This analysis also shows that in all but the most extreme levels of activity, the inner edge of the plasmashet (for the detector energy range) lies astride the geostationary orbit altitude for the greater part of the night-time sector, such that Meteosat is rarely in the central plasmashet where electron loss due to pitch angle diffusion is small compared to convection rates.

(b) Substorm onset distributions.

The local time distribution of substorm onsets (Figure 5.11) can be considered in the context of the plasmashet inner edge position (Figures 5.19 and 5.20). The models for deriving the position of this boundary assume a quasi-static convection field magnitude, but they may be used as a guide for determining the geostationary orbit local time to which injected particles can penetrate during a substorm event. Concentrating on the dusk-midnight sector, electrons visible to Meteosat can penetrate to GEO altitudes after about 21UT for all but extreme quiet conditions. At increased activity, the penetration boundary moves to earlier local times, hence those onsets observed at the dusk tail of the distribution are expected to be associated with disturbed conditions. The movement of this boundary during the dusk-midnight sector is also apparent from Figure 5.8.

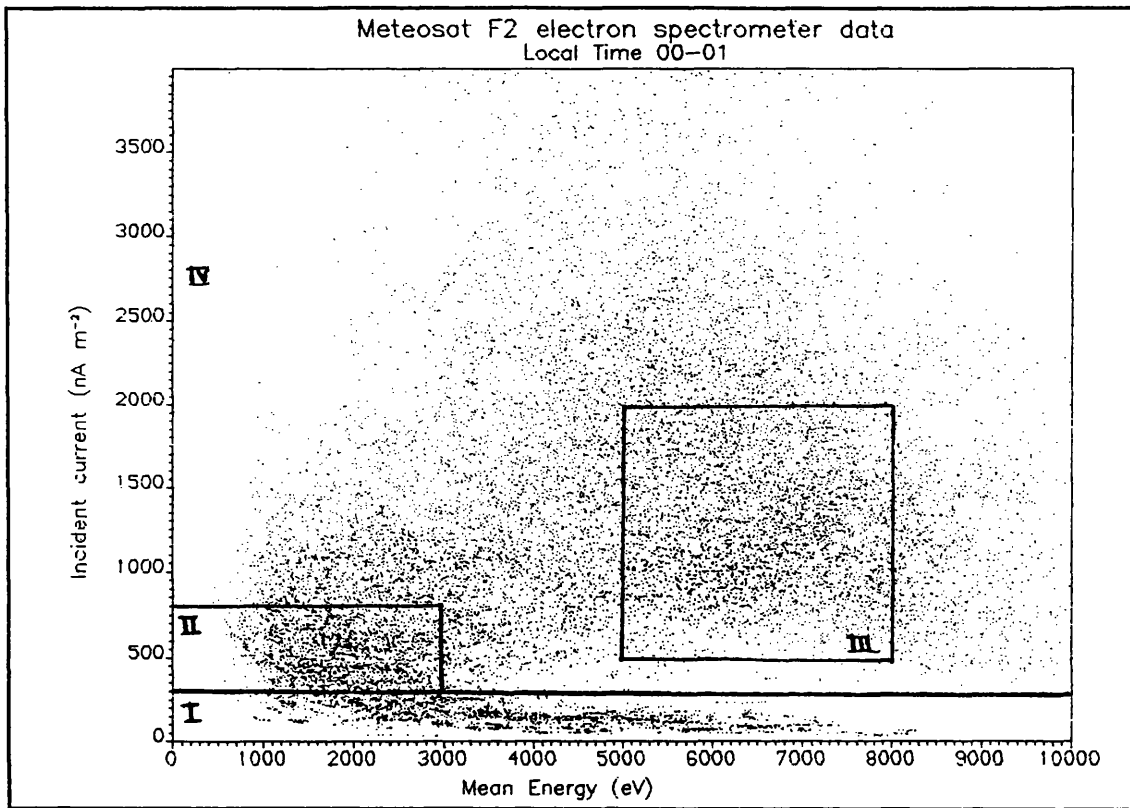


Figure 5.1

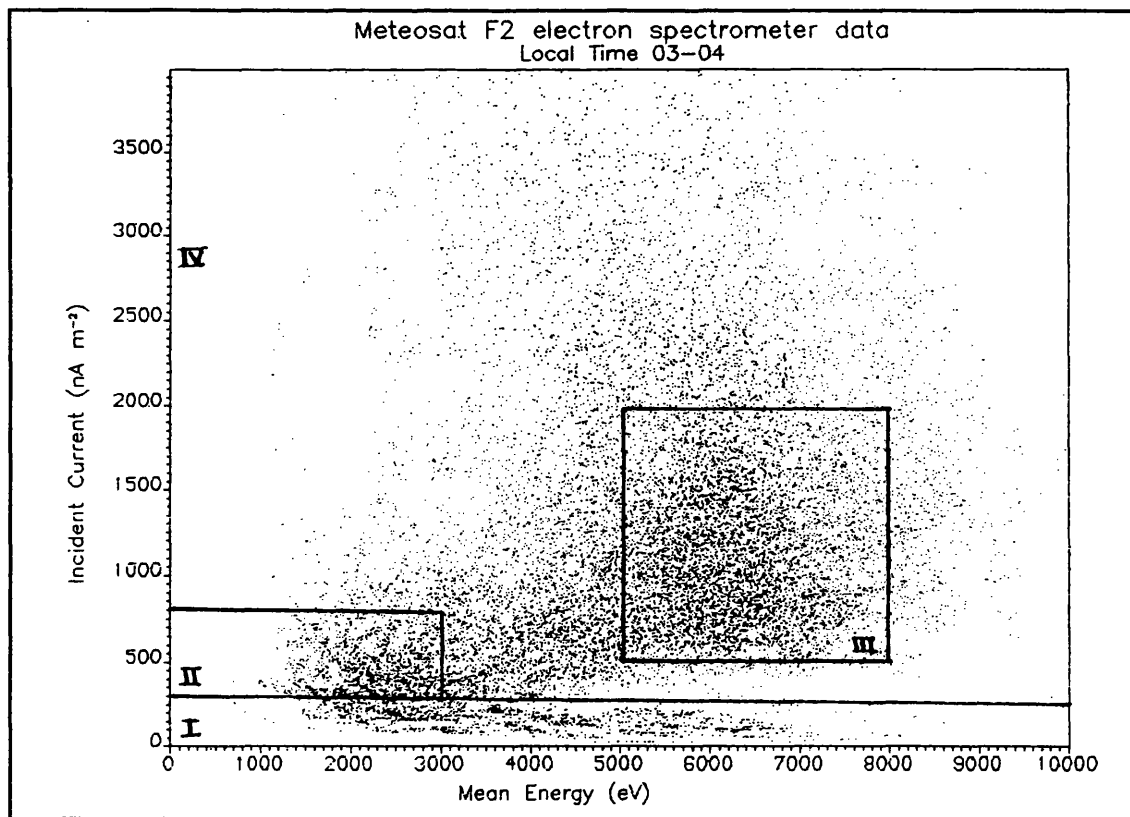


Figure 5.2

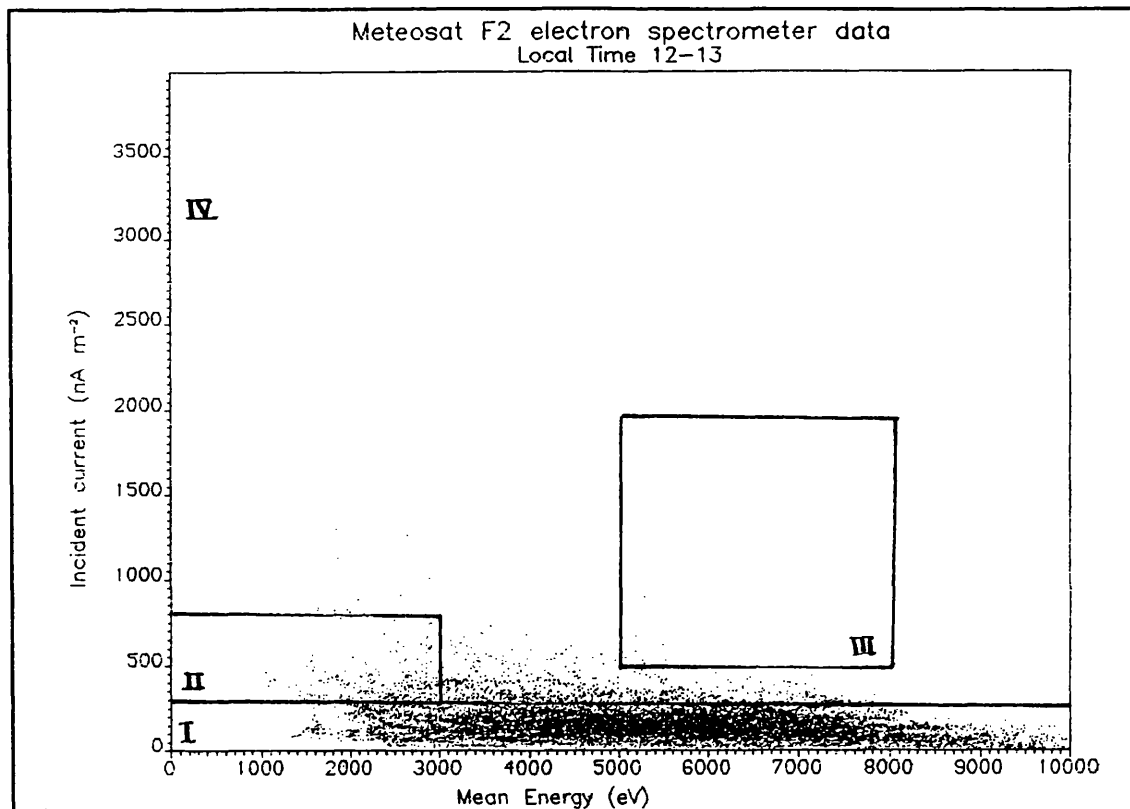


Figure 5.3

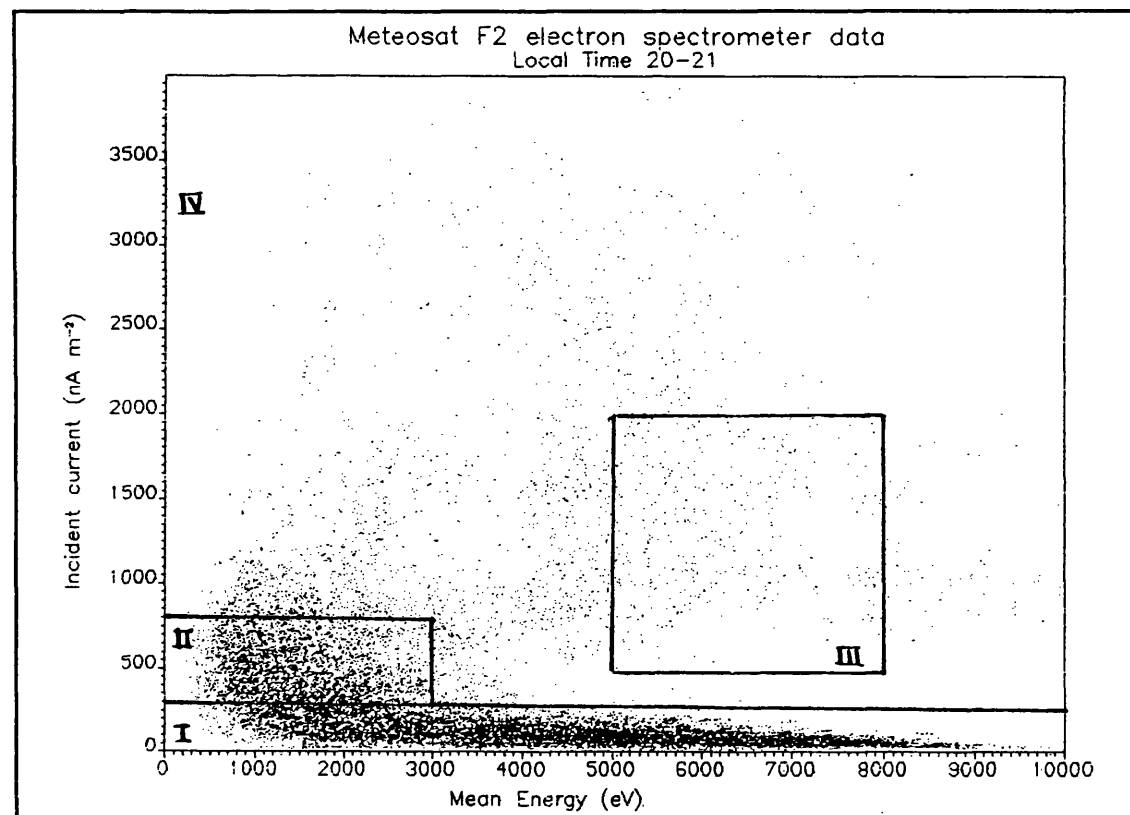


Figure 5.4

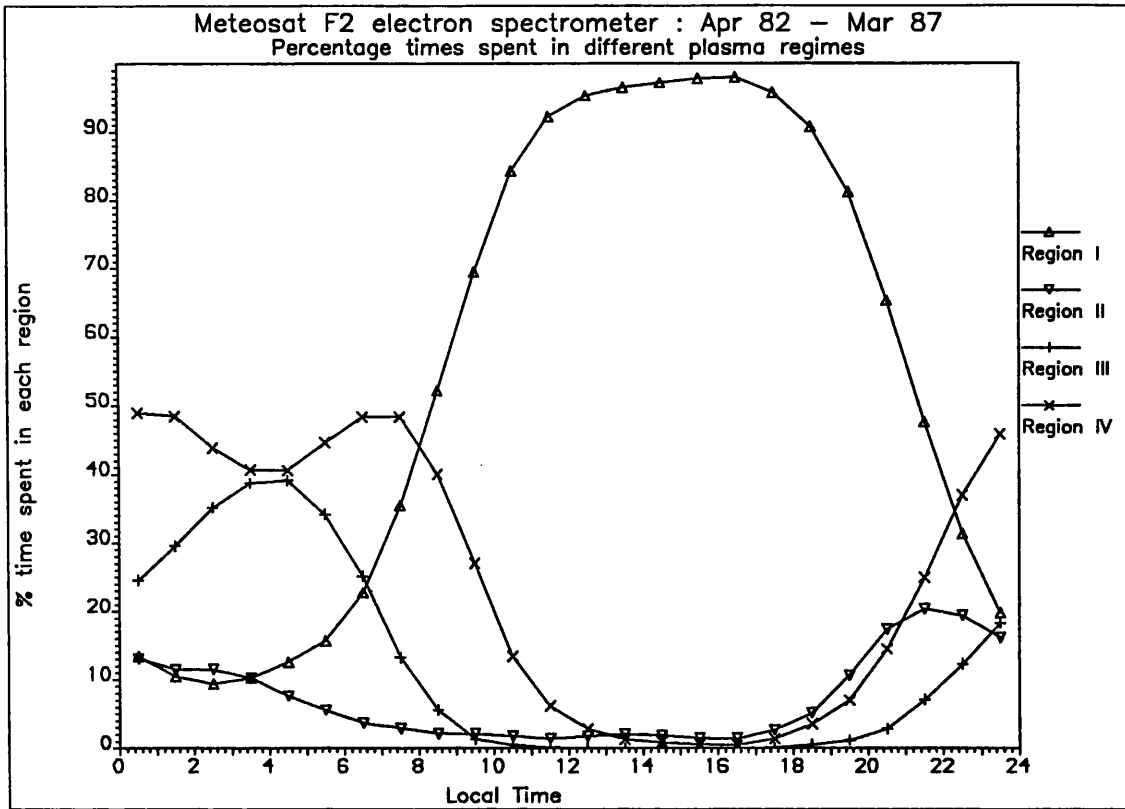


Figure 5.5

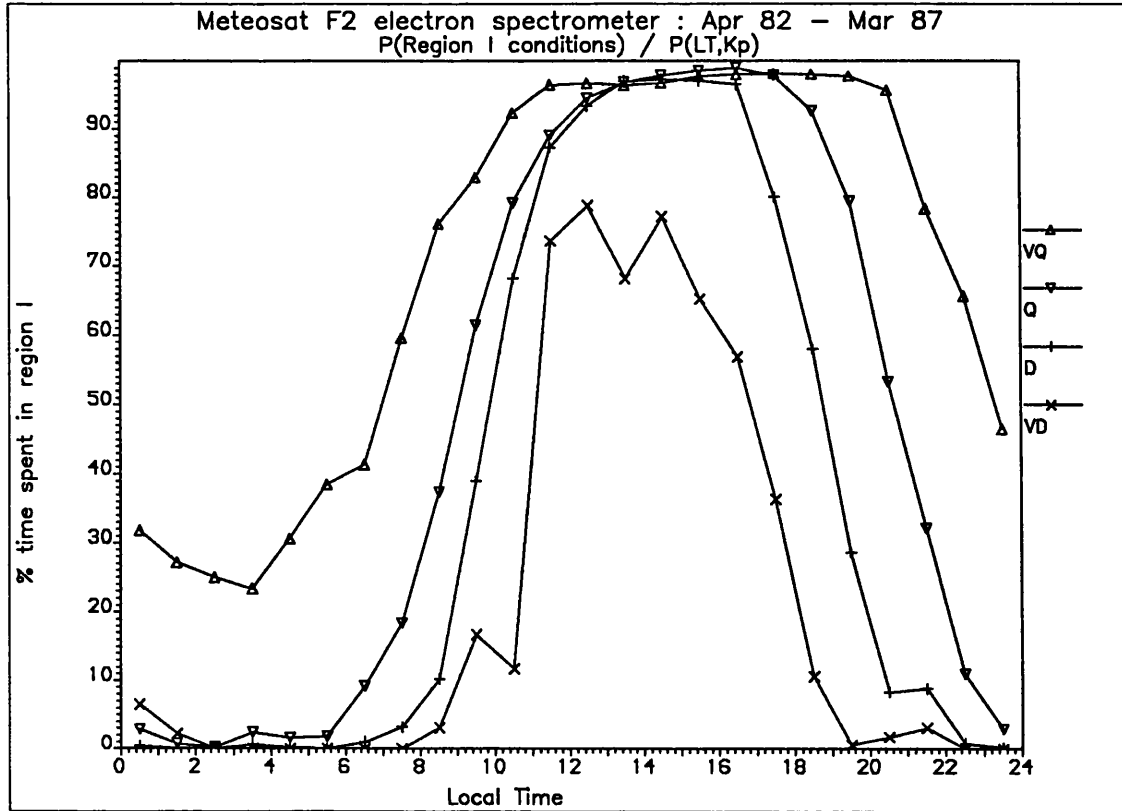


Figure 5.6

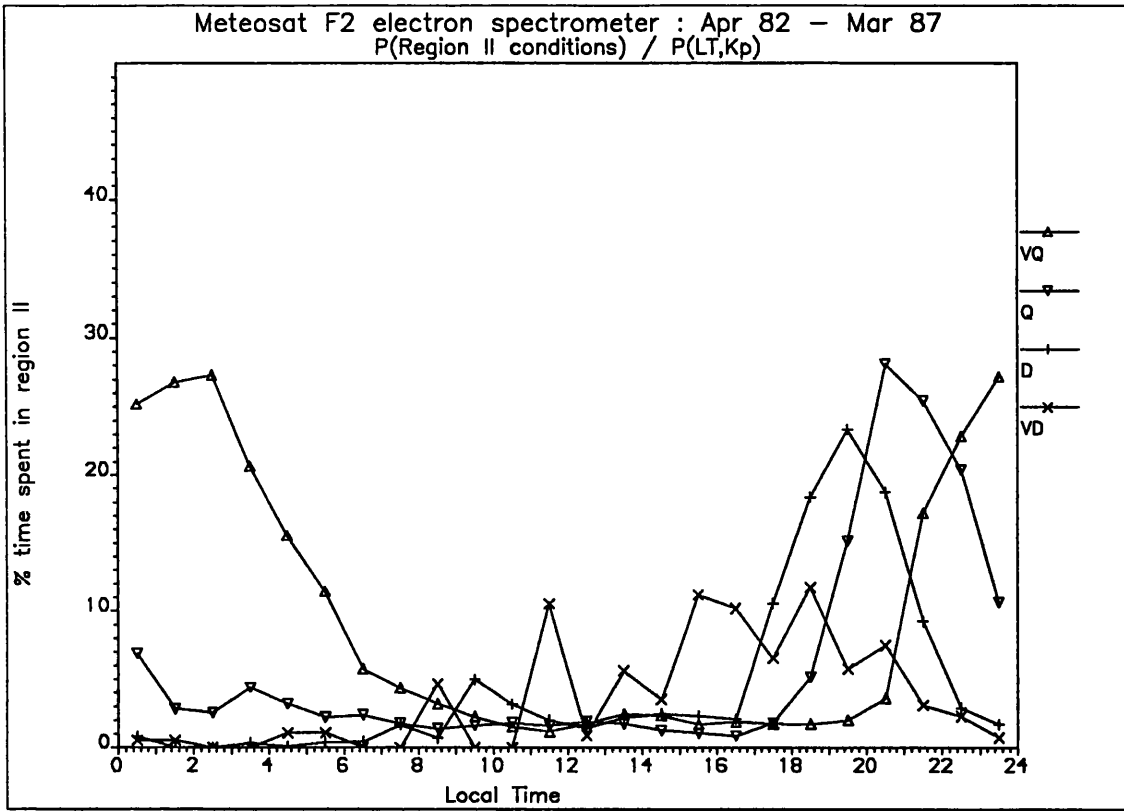


Figure 5.7

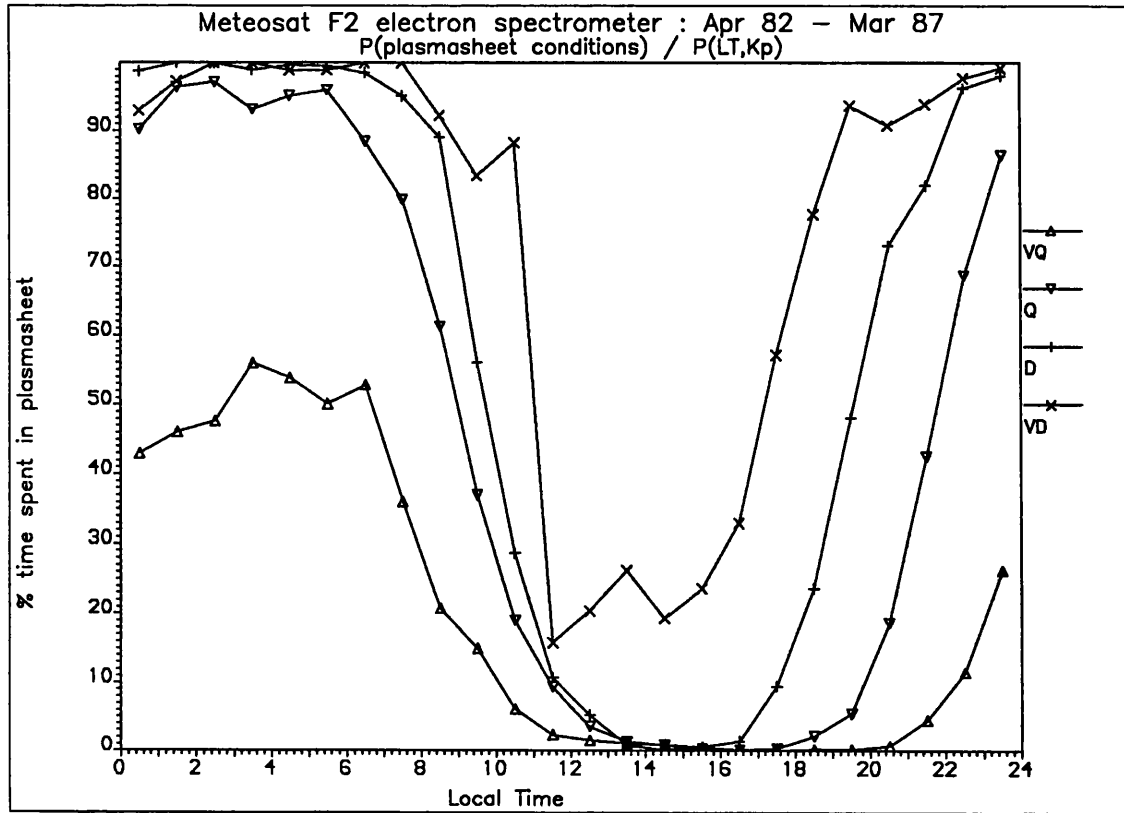


Figure 5.8

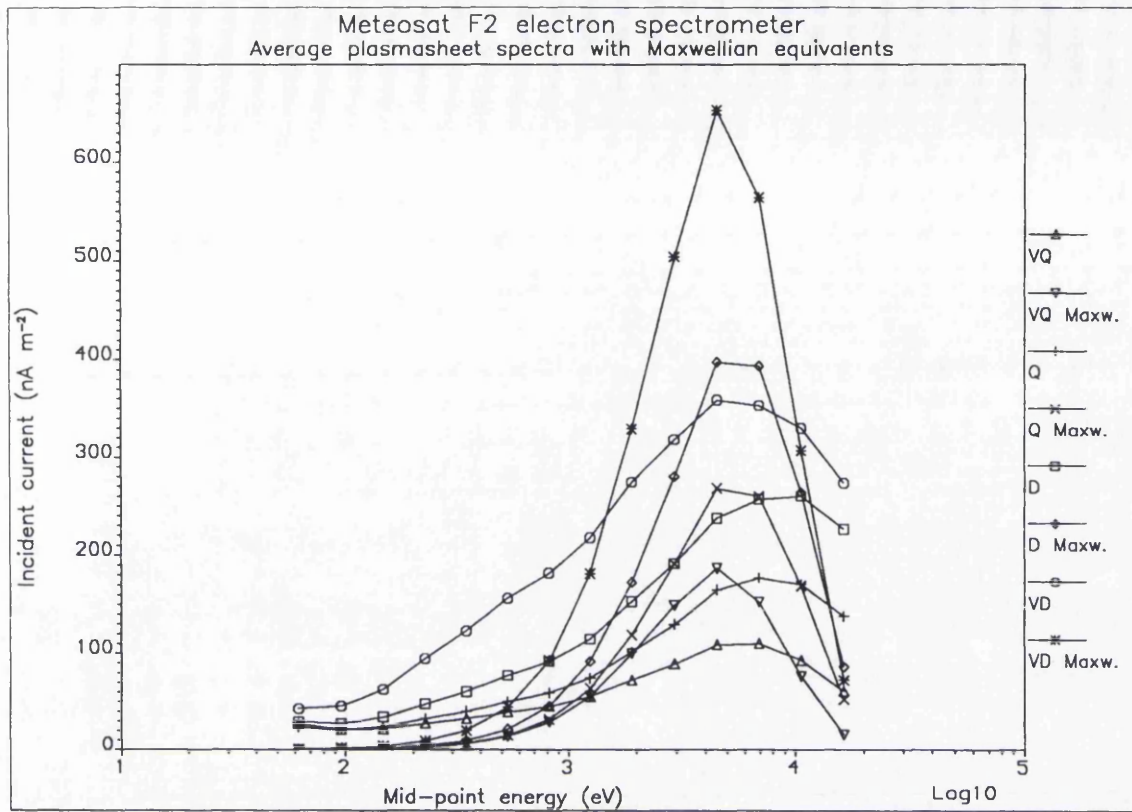


Figure 5.9

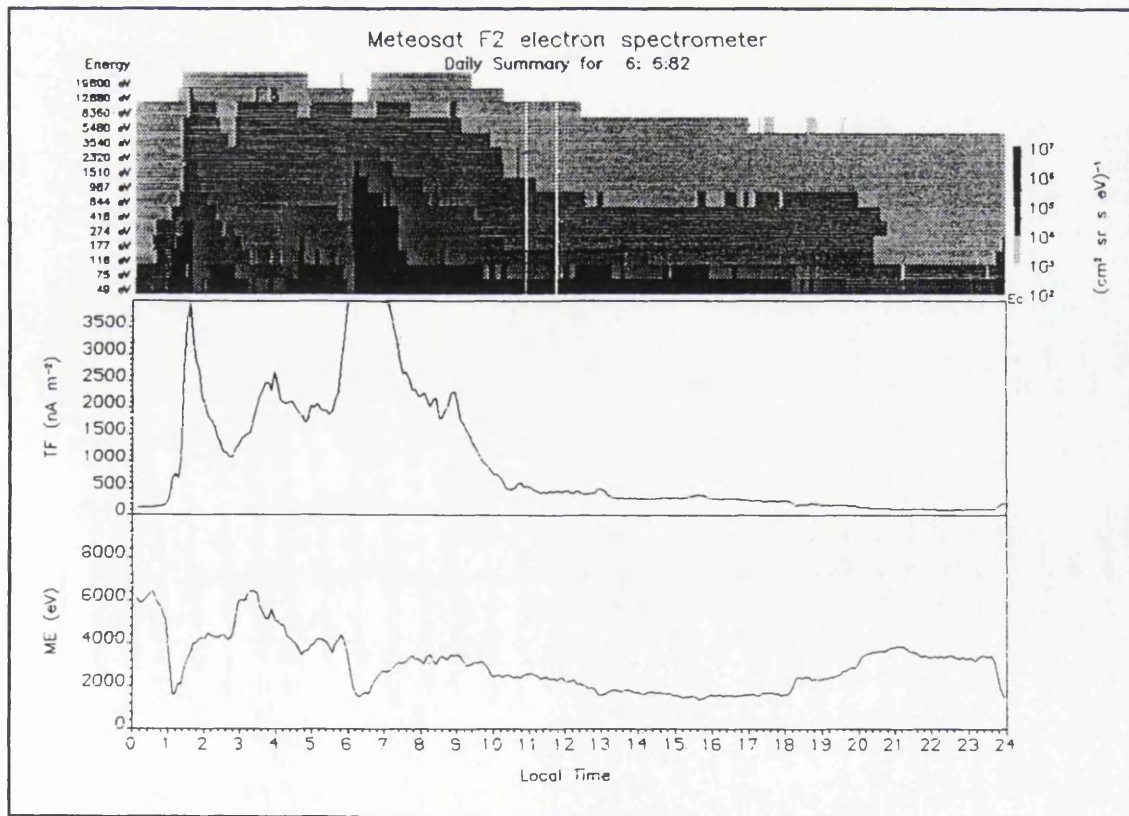


Figure 5.10

Table 5.1
Correlation between observed substorm onset flux increase and reported
SSC's.

Increase (nA/m ²)	Total onsets	Associated with SSC		Unassociated with SSC	
		Number	Number per day	Number	Number per day
700-1500	1587	153	2.05±0.17	1434	0.82±0.02
1500-2000	399	55	0.74±0.10	344	0.20±0.01
2000-2500	177	25	0.33±0.07	152	0.09±0.007
2500-3000	90	21	0.28±0.06	69	0.04±0.005
3000-3500	39	10	0.13±0.04	29	0.02±0.003
3500-4000	22	3	0.04±0.02	19	0.01±0.002
4000-4500	10	5	0.07±0.03	5	0.003±0.001
4500-5000	6	5	0.07±0.03	1	0.001±0.001
5000-5500	3	1	0.01±0.01	2	0.001±0.001

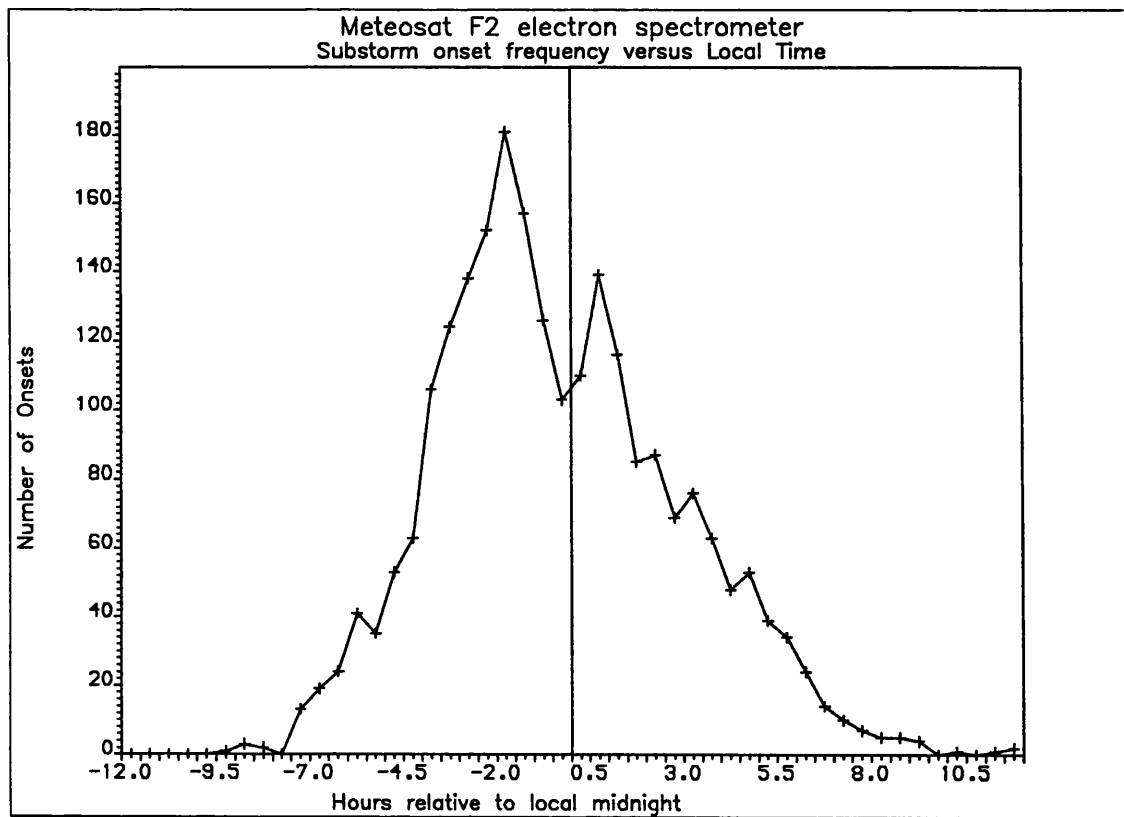


Figure 5.11

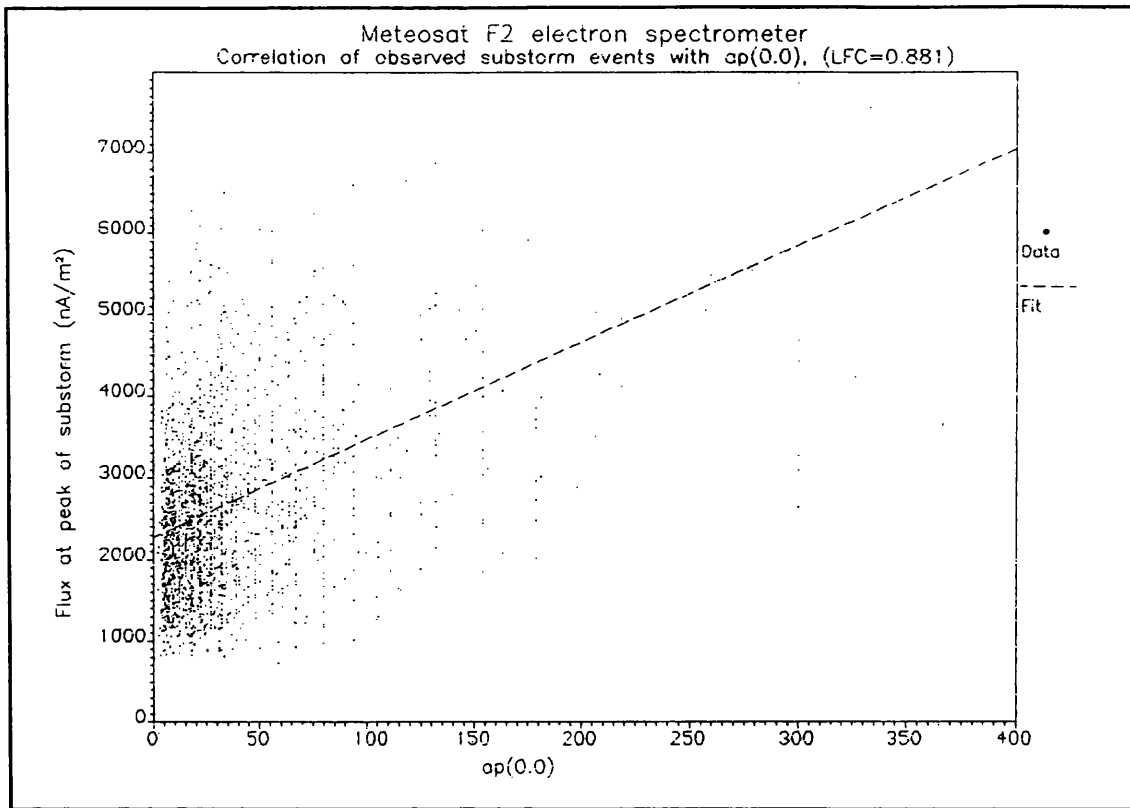


Figure 5.12

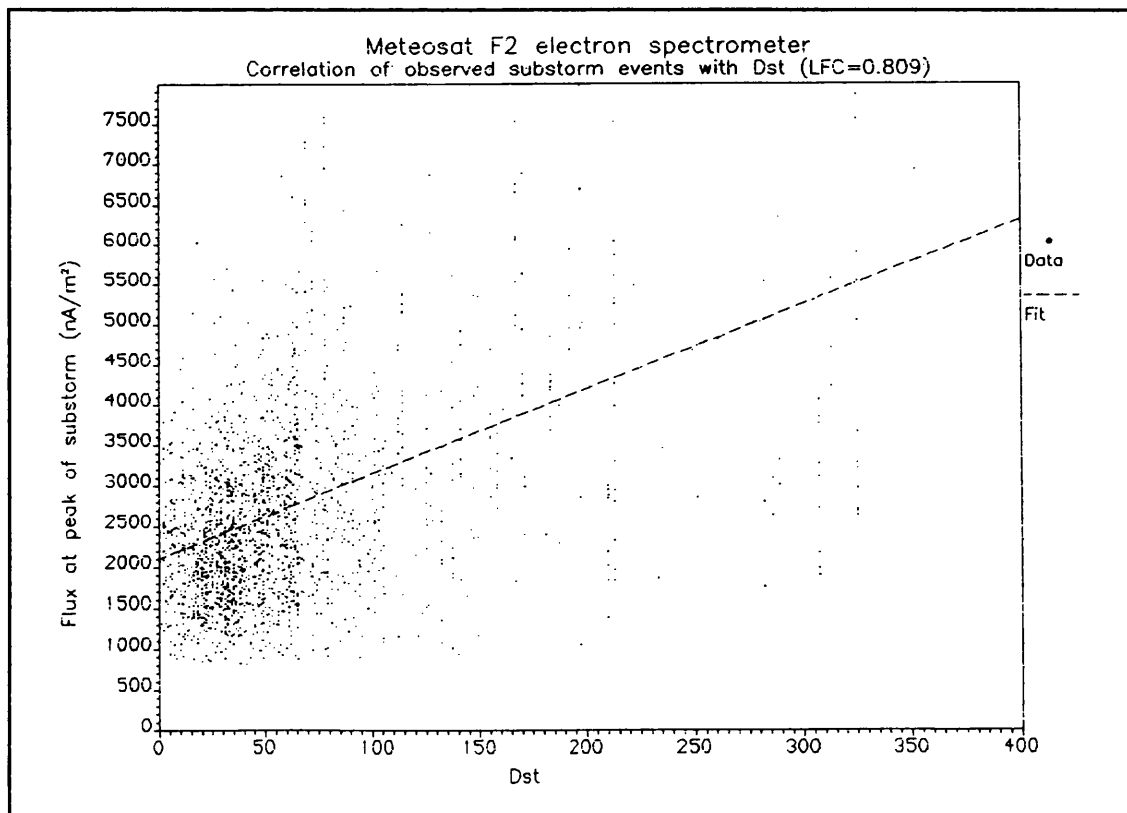


Figure 5.13

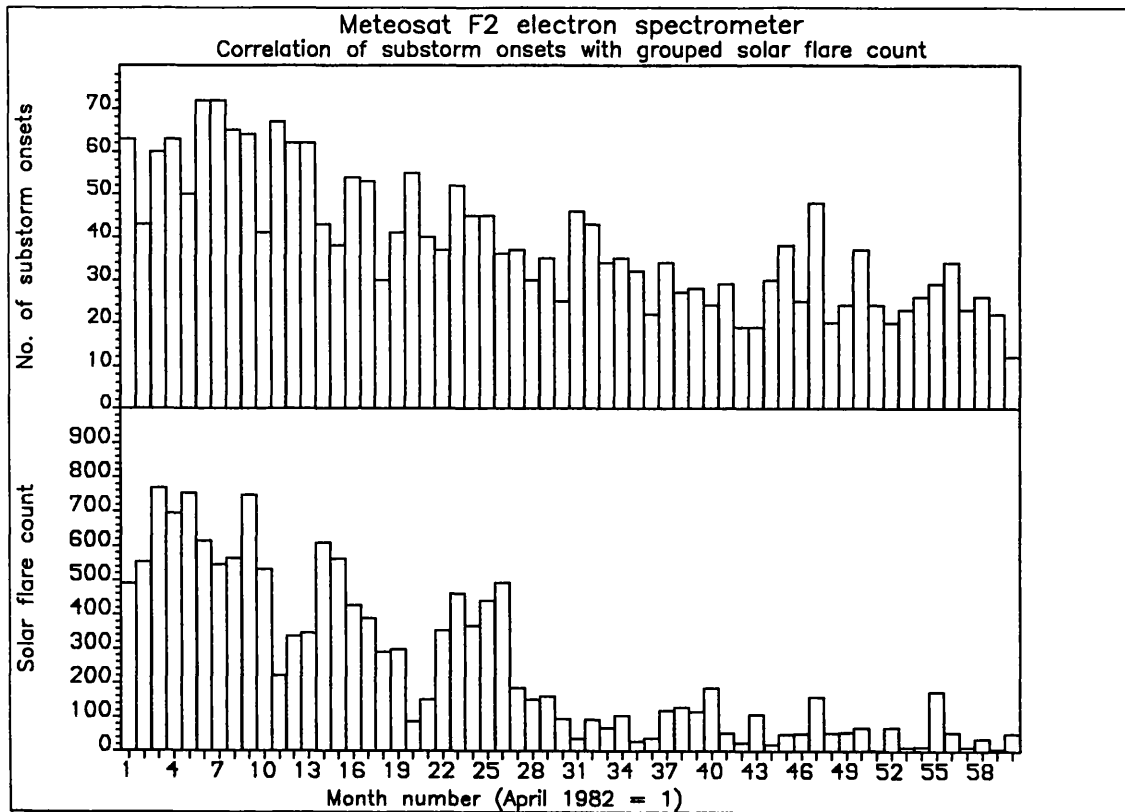


Figure 5.14

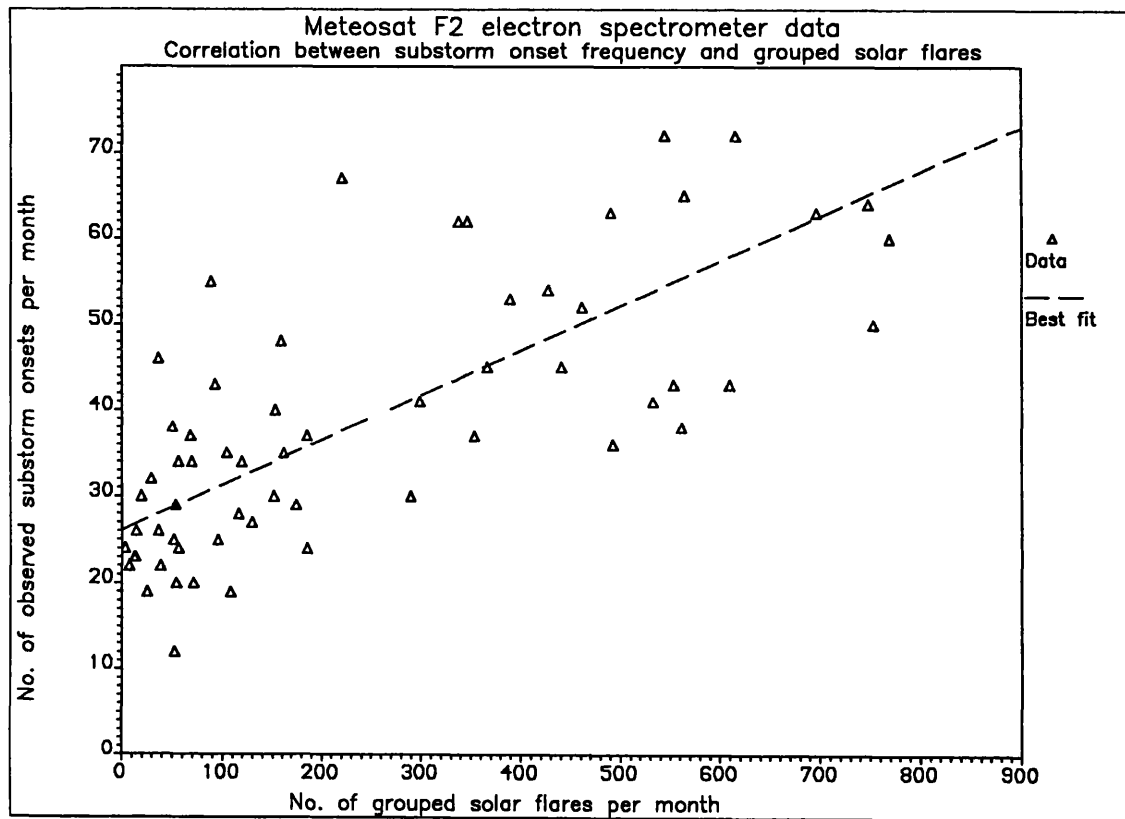


Figure 5.15

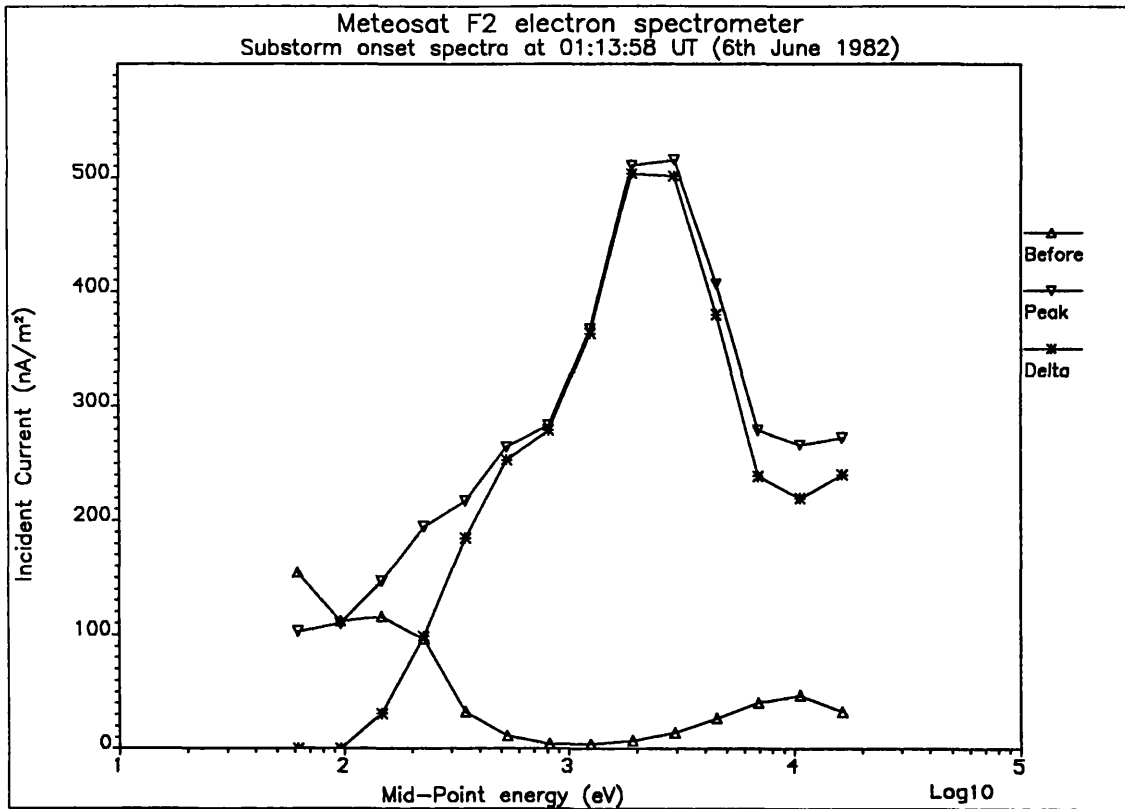


Figure 5.16

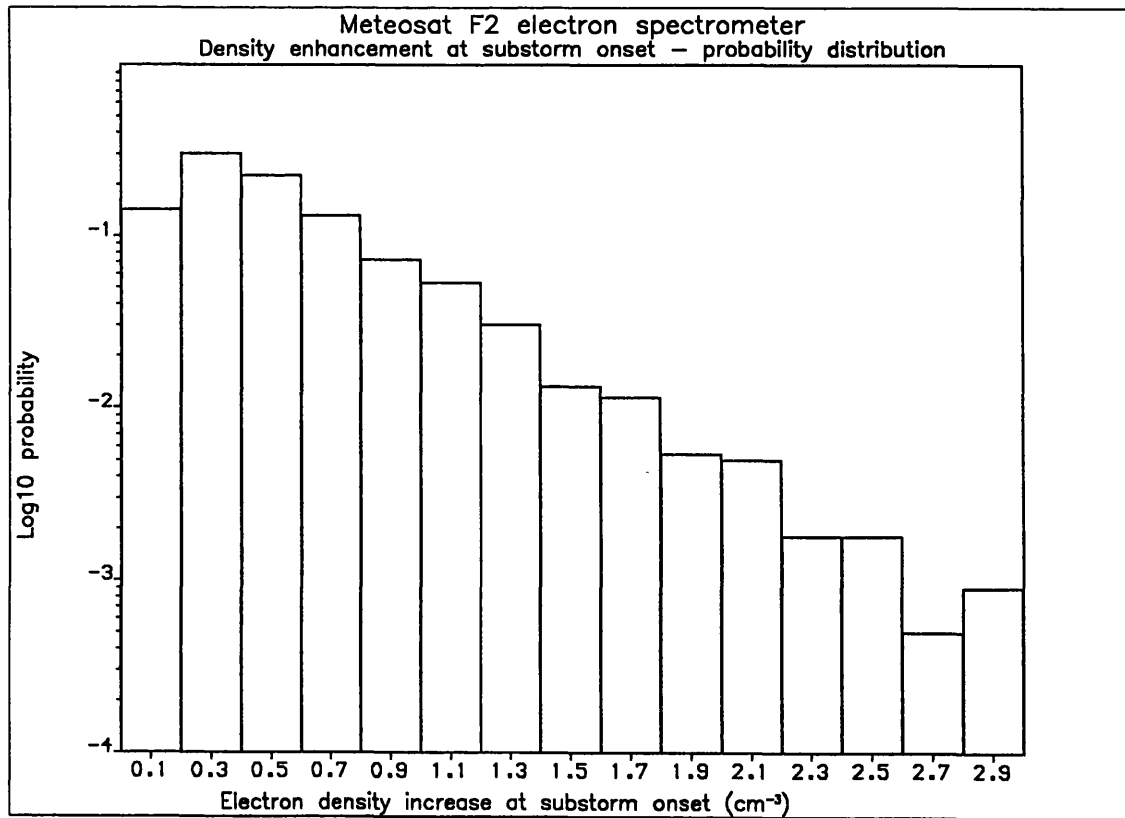


Figure 5.17

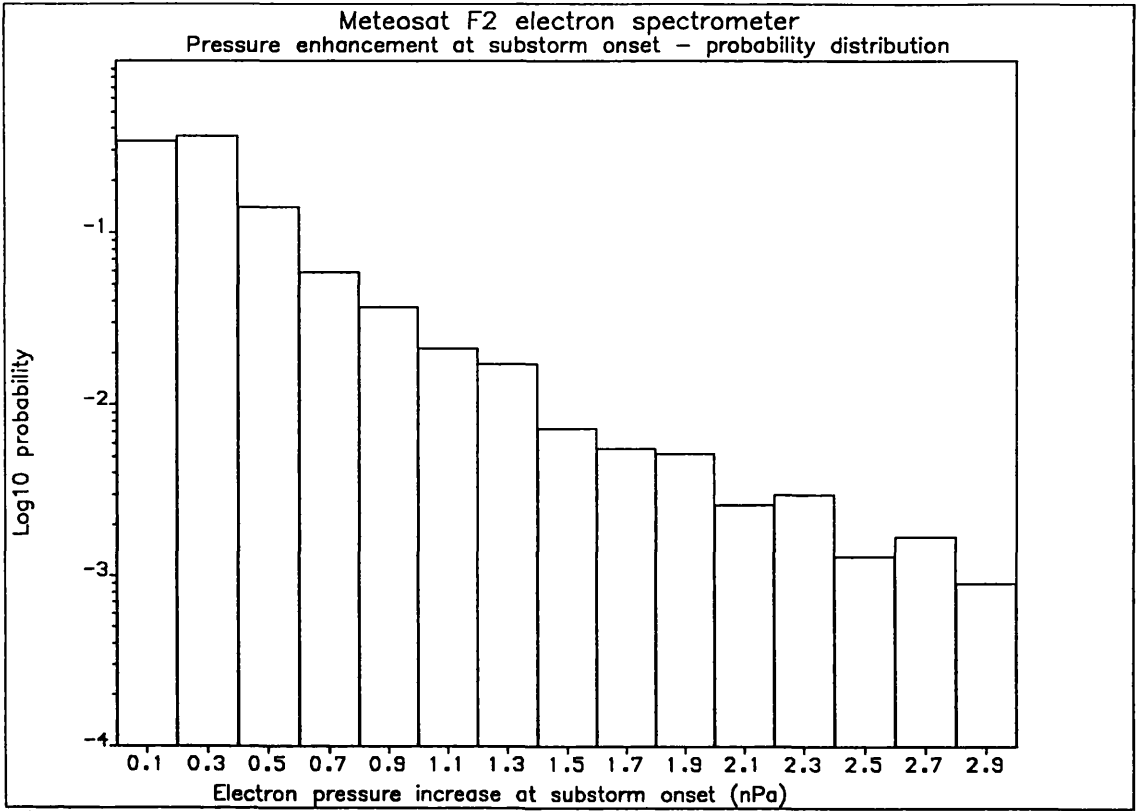


Figure 5.18

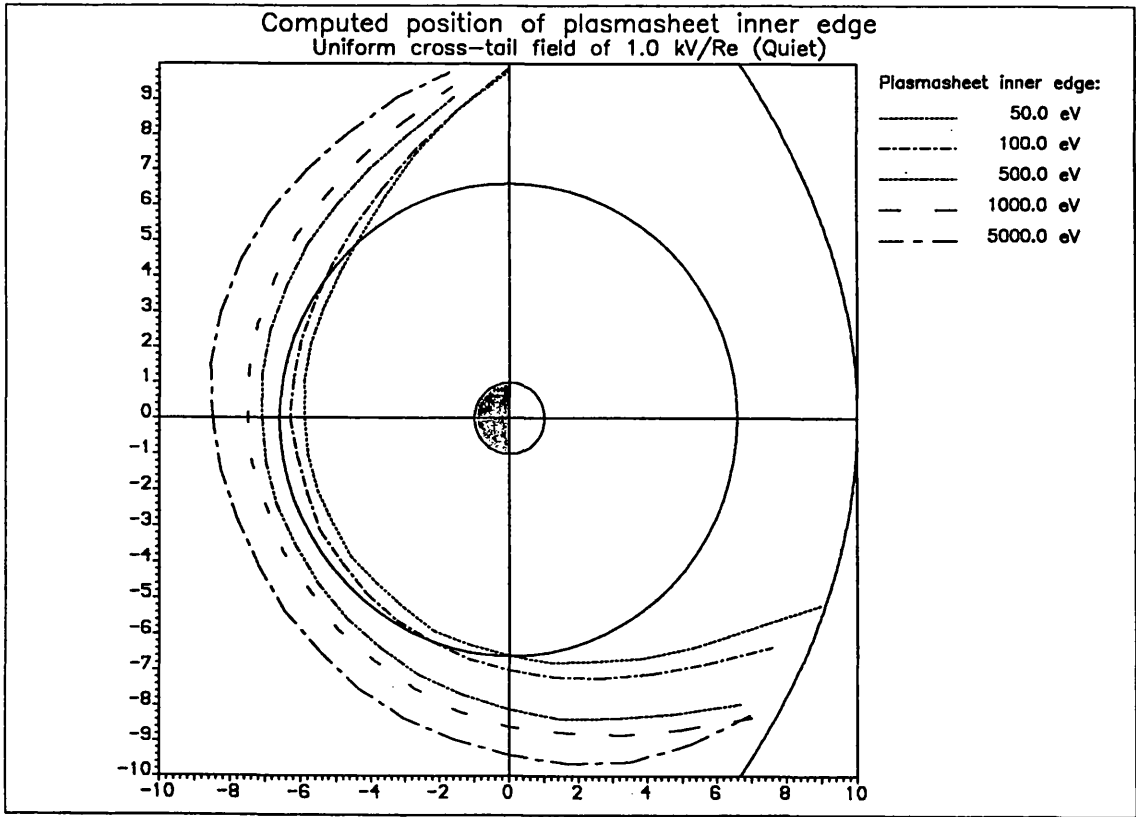


Figure 5.19

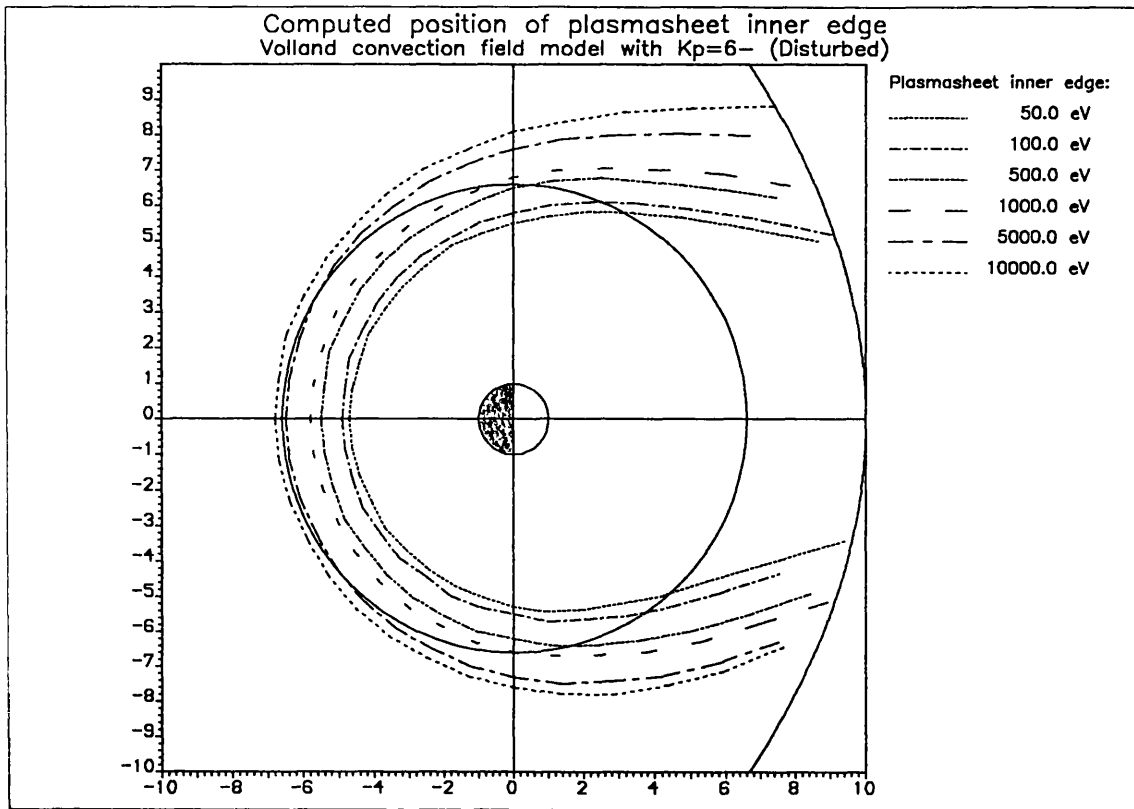


Figure 5.20

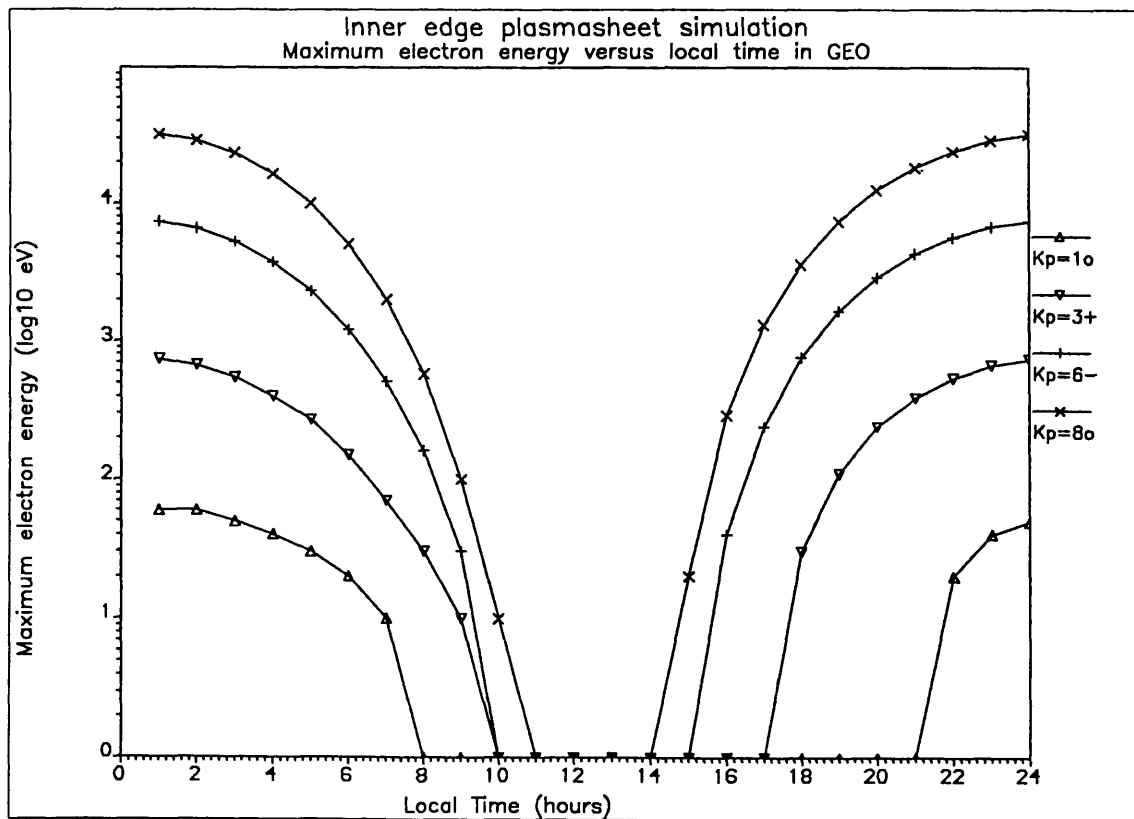


Figure 5.21

6. CHARGING PROPERTIES OF SATELLITE SURFACE MATERIALS

This chapter describes a series of experiments carried out using an electron beam test facility to measure the surface charging properties of some common spacecraft materials. Results are presented for the bulk and surface resistive properties of Kapton and Teflon, and the secondary emission properties of gold. Experimental data is compared with the results of two numerical simulation codes; the one-dimensional current balance equation solver, BEAM (see Chapter 4), and a full three-dimensional particle-tracking code, NASCAP test-tank.

6.1 EXPERIMENT AND SIMULATION DETAILS

The experimental facility and test method is described, together with the parameters used to define the numerical simulations.

6.1.1 Experimental facility and test method

The monoenergetic, single electron beam facility used for the experiments described in this chapter is located at Harwell Laboratory, Oxfordshire and is used for the routine ESD testing of new spacecraft materials⁹⁸. Figure 6.1 shows a cross-section of the vacuum chamber. The electron gun and flight tube assembly provide a monoenergetic, stable electron beam which irradiates the sample mounted on a copper block at the bottom of the chamber. Sample surface potential is measured by a non-contacting probe which may be scanned across the sample. Beam current, energy and sample temperature can all be varied.

The electron gun assembly is mounted on a vacuum flange which is connected directly to a variable (3 to 30 kV) EHT supply, such that the whole flange is biased negatively with respect to ground and forms the top of an insulating glass flight tube (painted grey to prevent light entering the chamber). The EHT supply voltage has been checked with a voltmeter and the agreement between setting and voltage is better than 1% at potentials up to 20 kV. The filament, grid and first anode are powered by an isolated, 230V a.c. supply connected to the 30KV EHT unit. The filament supply unit delivers up to 7A at 12V (a.c.) to a thoriated tungsten filament which is biased at about 5V negative with respect to the flange. The grid, which is a stainless steel mesh, is mounted just below the filament, and is at the same voltage as the flange. The first anode, mounted just below the grid, and made of the same type of stainless steel mesh can be biased at 0 to 1KV positive with respect to the grid by means of a second EHT supply mounted on the top flange. A disc of 27mm diameter is welded to the centre of the grid to prevent light from the filament reaching the sample. The cathode assembly is surrounded by an aluminium cup arrangement, at the same voltage as the main flange which provides some beam collimation. The principal anode is another stainless steel grid mounted at the base of the flight tube, and grounded to the main vacuum chamber which is constructed from 5.5mm thick stainless steel; it is 750mm high, has an internal diameter of 1275mm and

is evacuated by means of a diffusion pump and a liquid nitrogen cooled vapour trap which open into the base of the chamber. Operating pressure varies between 2×10^{-7} and 1×10^{-6} Torr, which can be achieved in less than one hour. All experiments described here were at room temperature. A wire mesh, mounted at the base of the flight tube acts as a beam flux monitor and forms the first element in a feedback system designed to maintain a constant beam current.

The sample surface potential is monitored using a non-contacting probe supplied by Trek Inc. (USA) which has a resolution of 5mm at a distance of 2.5mm, although the absolute measurement of potential is independent of probe to surface distance. The probe sensor head is connected to an electrostatic voltmeter with a range of 0 to 20KV and an x-y scanning mechanism allows the sensor to be located above any desired point on the sample. The outer casing of the probe head is automatically biased to the voltage being measured via a high gain feedback loop which causes minimum disruption of the beam in the vicinity of the probe and reduces the possibility of arc discharges occurring between the probe and the sample. The performance of the Trek probe has been checked by placing it above an extended aluminium plate biased at potentials up to 4.0 kV using a stabilised EHT power supply. Agreement between plate potential and Trek measurement is better than 1% over this voltage range.

A Faraday cup is mounted next to the probe sensor head to measure the beam current above the sample and is designed to collect all electrons which enter the main aperture (7mm diameter), and to minimise the escape of secondary electrons emitted by the collector. The cup is connected to an electrometer (Keithley model 610C) via a 3 metre long 75Ω coaxial cable. The system was calibrated by supplying known d.c currents into the cable at its connection point to the Faraday cup and the electrometer readings were found to be within 1.2% of the supplied current in the range 10 to 30 nA. Beam uniformity has been measured at 25 keV and 0.64 nA/cm^2 over the entire sample holder, and varies by less than 8% over the extent of the gold sample.

The experimental test rig characteristics are summarised in Table 6.1. Figure 6.2 is a general view of the vacuum tank and instrumentation and Figure 6.3 is a view inside the chamber showing the sample holder, Trek probe and Faraday cup assembly and the x-y scanning mechanism.

The electron beam was used to irradiate a rectangular gold sample of area 150 cm^2 and thickness $25 \mu\text{m}$, isolated firstly with Teflon and then with Kapton. The energy and current density of the beam were varied and the gold sample was allowed to reach equilibrium for each setting, whereupon the Trek probe reading together with the filament current, grid and first anode potentials and Faraday cup current were recorded. At high beam energies, discharges were observed between the gold sample and the grounded copper sample holder, and the subsequent time development of surface potential was logged with a chart recorder. The dynamic response of the sample proved to be a very useful method for calculating some resistive properties of the insulating material.

6.1.2 Simulation using the BEAM code

The code has been described in section 4.2. For input, it requires the surface properties of the target material, the total resistance and capacitance between the target surface and ground, the beam energy and the total beam current which impinges on the sample. Incident current and total resistance are assumed to remain constant throughout the charging process. The incident current density above the sample, measured by the Faraday cup was used to compute the total incident current, taking account of the shielding effect of the Trek probe assembly. This approach therefore incorporates the small variation in actual beam current density which is observed during a voltage sweep at constant filament current setting. For the purpose of these simulations, it is assumed that the insulating layer resistance is constant for all sample potentials. This is a first approximation, but provides a good demonstration of the role of the conduction current in the current balance equation.

The secondary electron emission model described in section 4.1.2 has been used, together with the model for electron backscatter described in section 3.2.2. SEE parameters have been chosen to fit those used in NASCAP³⁵ to ensure consistency with NASCAP test-tank results.

6.1.3 Simulation using NASCAP test-tank

Length scales for the experimental configuration range from about 1m (test tank diameter) down to about 50 μ m (Kapton thickness). If the inner computational grid spacing was chosen to be equal to the minimum length scale, many computational grids would be required to accommodate the entire test tank. NASCAP allows the resistance and capacitance between conductors to be specified explicitly, so the insulator can be made 1 grid square thick and an adequate model of the experiment may be constructed completely within the innermost computational grid (Figure 6.4) with a grid spacing of 5cm. The gold sheet has been modelled as a square plate of size 20cm by 20cm so that the simulation is symmetrical in the x-y plane, to simplify the interpretation of results. Although the area of the sheet is larger than the experimental arrangement, the total current can be adjusted to the experimentally measured value by altering the electron gun current.

The computational space is defined in order to simulate a cylindrical vacuum chamber with its axis in the z-direction, a radius of 0.75m (15 code units), and a height of 1.25m (25 code units). Constraints imposed by NASCAP force the height of the simulation tank to be shorter than the actual distance between tank base and electron gun, but this is acceptable since the geometry near the top of the tank does not affect the development of potential contours around the target. All tank walls and the copper sample holder are fixed at Earth potential, which requires NASCAP to perform lengthy calculations to find the stray capacitances between each element of the object and each element of the test tank. However, these stray capacitances are much smaller than the capacitances

of the Teflon and Kapton sheets, and have negligible effect on the simulation charging time constant.

NASCAP allows the electron gun to be placed outside computational space so that the separation between electron gun and sample surface may be modelled exactly. As well as specifying the position and direction of the gun (shown in Figure 6.4), the beam divergence (expressed as a half angle) and total beam current must be defined. Throughout these simulations, the beam half angle was fixed at 7.7° in order to irradiate the entire sample and the beam current was adjusted so that the total electron current incident on the sample surface was in accordance with experimental measurements. The "TYPE1" test tank environment was chosen in order to perform the calculation by particle tracking, rather than by an analytical approximation ("TYPE6" environment).

6.2 RESULTS

Results are presented for the irradiation of a gold sample with an electron beam. Two types of insulator are used, Teflon and Kapton. The gold sample potential is measured as a function of beam energy and beam current.

6.2.1 Gold on a Teflon insulator

The gold sample was placed on a 2.6mm thick Teflon sheet, cut slightly smaller than the gold so that no Teflon was directly exposed to the electron beam, then positioned at the centre of the copper block, in direct contact with it. After setting up the beam for a given current density, by adjusting the grid and first anode potentials and filament current, the beam energy was swept from 2.0 keV to 28 keV in steps of 2.0 keV, and then back down to 2.0 keV. The TREK probe and Faraday cup assembly were left in place above the sample throughout the entire experiment. Whilst the feedback system between the beam flux monitor and the grid potential control acted to keep the beam flux monitor reading constant, changes of the beam profile cause the Faraday cup current to be a weak function of beam energy.

A voltage sweep was performed at two current settings of approximately 1 nA/cm^2 and 5 nA/cm^2 . The surface potential at a given beam energy is taken as the average of the two values obtained during the "up" and "down" phases of the voltage sweep. For each beam energy, the average surface potential and Faraday cup current (converted to current density) are computed and the error taken as the difference between the mean value and each of the two actual readings. Figure 6.5 shows the average surface voltages as a function of incident beam energy with error bars representing the difference between "up" and "down" voltage sweeps. The actual current at the sample, as measured by the Faraday cup, varied slightly between each beam energy setting which accounts for the non-smooth nature of each curve. From the discussion in section 4.2.1, it is expected that for emission-limited behaviour, surface potential will be independent of beam current, but Figure 6.5 shows that surface potential

is a strong function of beam current such that larger potentials may be induced on the gold at higher beam currents. In addition, the gradient of each curve is significantly less than the theoretical value of unity (section 4.2.1). These observations lead to the conclusion that the conduction current through the Teflon to ground is significant compared to the net incident electron current (total incident minus secondary and backscattered electrons), ie the system is behaving in a conduction limited manner.

The resistance of the insulating layer can be found from analysis of the voltage time history of the gold sample following a discharge. A typical event occurred at a beam energy of 24 keV and a beam current of 0.83 nA/cm², (observed visually to be a discharge between a corner of the gold and the sample holder) after which the sample took several minutes to reach an equilibrium potential of -4085V. Other discharges were observed at sample potentials of -3800V, -4220V, -4580V, -5130V, -5600V, -4900V, -4750V and -4500V. The time history of the re-charging process is shown as the curve marked "Exp" in Figure 6.6. The form of this curve can be derived by assuming that the insulator acts as a capacitor with capacitance C which permits a leakage current V/R_T to flow, where V is the sample potential and R_T is the total resistance of the Teflon layer. The total current which flows from the gold into the insulator, I_g therefore satisfies the following equation;

$$C \frac{dV}{dt} = I_g - \frac{V}{R_T} \quad (6.1)$$

The current balance equation for the gold sample may be written in terms of the total secondary yield of gold, Y (which is a function of beam energy, E_B and sample potential, V) and the total current flowing into the Teflon, I_g ;

$$-I_B + I_B Y(E_B - V) + I_g = 0 \quad (6.2)$$

Equations 6.1 and 6.2 may be combined to give the following expression which describes voltage time history development;

$$\frac{dV}{dt} = \frac{I_B \cdot (1-Y)}{C} - \frac{V}{R_T \cdot C} \quad (6.3)$$

Since Y is a function of V, for a given beam energy, equation 6.3 cannot be integrated directly without making some approximations. However, it is evident from Figure 6.5 that for a beam energy of 24 keV, the sample only reaches an equilibrium potential of -4085 V, so that immediately following the discharge, electrons reach the sample with an incident energy of 24.0 keV whilst at equilibrium, the incident electron energy has been reduced to 19.9 keV. The secondary emission yield for gold varies slowly with incident electron energy in this region, so to a first approximation, Y may be considered as constant throughout this experiment. Equation 6.3 may now be integrated to give the familiar form

of exponential growth of V with a charging time constant $R_T C$. This may be expressed in terms of t as;

$$t = -R_T \cdot C \cdot \ln\left(1 - \frac{V}{V_\infty}\right) \quad (6.4)$$

where

$$V_\infty = I_E \cdot R_T \cdot (1-Y) \quad (6.5)$$

(V_∞ is the final equilibrium potential). The total resistance of the Teflon layer, R_T can be computed from a series of (t,V) data points, such as those shown in Figure 6.6 by plotting values of t (y axis) against $\ln(1-V/V_\infty)$ on the x axis. The theory above predicts this to be straight line through the origin with slope $-R_T C$; a linear least-squares analysis of the data points (including the origin) is used to give a best-fit value for the charging time constant. If C is known, then a value for total resistance may be inferred. Furthermore, having evaluated R_T , and measured the incident electron current to the sample with the Faraday cup, one can infer a value for the average secondary electron emission yield over this energy range using equation 6.5. The capacitance of the Teflon layer, C is calculated as 1.02×10^{-10} F, assuming that³⁵ $\epsilon_r = 2.0$, an area of 150 cm^2 and a thickness of 2.6mm. For the voltage versus time curve of Figure 6.6, such an analysis gives the following results:

$$\text{Slope (time constant)} = 21.7 \pm 0.8 \text{ s}$$

$$\text{Linear least squares correlation coefficient} = 0.992$$

$$\text{Number of data points} = 13 \text{ (including origin).}$$

Assuming that any errors in the estimate of C are negligible, this value of charging time constant implies that the total resistance of the Teflon sample, R_T is $(2.13 \pm 0.08) \times 10^{11} \Omega$. The incident electron current density during the charging process was 0.84 nA/cm^2 , but to compute the total current to the sample, account must be taken of the shielding effect of the Trek probe assembly, which directly shields 16.6 cm^2 of the gold surface, leaving 134.4 cm^2 of area exposed to the beam and therefore the total incident current is 112.9 nA . Putting these known values into equation 6.5 gives a value of $Y = 0.83 \pm 0.03$ for the average normal, net secondary yield of gold for incident energies between 19.9 keV and 24.0 keV.

The BEAM code was used to compute equilibrium potentials of the gold sample at the experimental values for beam current density (assuming an exposed area of 134.4 cm^2) and beam energy with derived values for the bulk resistance and capacitance of the Teflon insulator. Results are shown in Figure 6.7 (upper panel) for a 1 nA/cm^2 beam current and Figure 6.7 (lower panel) for a 5 nA/cm^2 current (curves marked "BEAM"), along with the experimental curves for reference. In both cases, BEAM correctly predicts the threshold beam energy and for the low current case, agreement is good for beam energies up to 28 keV. However, at the higher beam current, agreement at energies above the threshold voltage is poor;

this will be discussed in section 6.3. In addition, BEAM has been used to simulate the behaviour of the gold following a discharge; the results are shown in Figure 6.6, marked "BEAM" and are in excellent agreement with experimental results.

NASCAP test-tank was employed to predict sample equilibrium potentials versus beam energy, and to model dynamic behaviour following a discharge. Resistance and capacitance of the insulator were specified to be the experimental values and one complete NASCAP simulation is required per beam setting (taking several thousand CPU seconds). Results of the dynamic simulation are shown in Figure 6.6, and static simulation in Figure 6.7, marked "NASCAP" which may be compared with the results of experiment and BEAM simulations. These are discussed in section 6.3.

6.2.2 Gold on a Kapton insulator

The gold sample was isolated using a 51 μ m thick Kapton sheet, and the equilibrium potential was determined as a function of beam energy using a high current density (7 nA/cm²) to keep charging times down to several minutes, rather than hours. The experimental method was identical to that for a Teflon insulator, and the results are shown in Figure 6.8, marked "7 nA/cm²"). This figure shows that, as for Teflon, the system is behaving in a conduction-limited fashion such that the slope of the curve above beam threshold energy is much less than unity. The resistance of the insulating layer was found from a voltage time history record following a discharge at 25 keV (Figure 6.9) when the sample had reached -5100V (several discharges were observed at potentials close to this value), using an identical method to that of section 6.2.1. Linear least squares fit to a plot of t versus ln(1-V/V_∞) gives the following results, where V_∞ = -5100V:

Slope (time constant, R_TC) = 113.8 ± 6.9s.

Linear least-squares correlation coefficient = 0.971

Number of data points (including origin) = 19

Taking the capacitance of the Teflon layer as 1.3x10⁻⁸F ($\epsilon_r = 5.0$)³⁵ implies that the total resistance of the Kapton sheet is (8.74±0.53)x10⁹ Ω . At equilibrium, the beam current density was measured as 7.4 nA/cm² which implies a total current of 987.2 nA to the sample, taking into account beam shadowing by the Trek probe assembly. By equation 6.5, this gives an average total secondary yield at normal incidence for gold in the energy range 19.9 keV to 25 keV of 0.41±0.02.

These computed values of resistance and capacitance were used as a basis for the BEAM code simulation; the equilibrium potential was predicted for each experimental beam energy and current density setting and the results are shown in Figure 6.8, marked "BEAM1" (constant resistance) and "BEAM2" (field enhanced conductivity effects are included). Also shown is a simulation based on the theoretical bulk resistance of Kapton which includes the effect of field enhanced conductivity ("BEAM3").

6.3 DISCUSSION

The results presented in section 6.2 are discussed with particular reference to the deflection of electrons away from the charged target, the electron beam energy threshold for charging, field emission currents prior to a discharge, measured secondary yields for gold, and the effects of surface conductivity and non-Ohmic conduction.

(a) Deflection of electrons away from a charged target.

Although the sample is a flat sheet of gold, its dimension is much less than the diameter of the vacuum chamber, therefore at high negative potentials, the equipotential contours far from the target will resemble those around a charged sphere. Since the Faraday cup is placed above the centre of the sample, directly beneath the electron gun, the measured current will not depend on sample potential; however, the divergence inherent in the electron beam will cause some electrons to be deflected towards the edges of the tank by the electric field due to the charged sample, thereby introducing an error into the computation of total incident current. It is expected that incident electron current to the sample will reduce as the sample becomes more negatively charged; in the limiting case, the incident electron current will be reduced by a factor $(1-qV/E)$ assuming a unidirectional beam incident on a system of concentric equipotential contours (see section 3.1.5). For a beam energy of 24 keV and sample potential of -5186V, incident electron current would be reduced by 22% of the incident current to the uncharged sample. In practice, however, the influence of the tank walls, and the finite size of the sample prevent the equipotential contours from becoming completely spherical, so that the fraction of incident current lost as the sample charges negatively will always be less than the limiting case given above. Figure 6.10 shows equipotential contours around the gold sample as predicted by NASCAP for a sample potential of -6520V and including the effect of grounded tank walls. At large distances, the contour lines are nearly spherical, but become planar close to the sample. For a 24 keV beam, NASCAP predicts the incident current to reduce by 6% for a sample potential of -5186V compared with the current to an uncharged sample which is small compared to the 22% reduction predicted on the basis of spherical probe theory; thus, the unidirectional beam assumption made by the BEAM code is a good one for this experimental geometry. A further consideration is that the secondary emission yield function increases for non-normal incidence (section 3.2.1). However, for beam energies below the charging threshold, the sample is close to zero volts and electrons will be near-normally incident, (except for a slight beam divergence) such that geometrical probe effects will not influence the threshold charging energy, and will have a second order effect on the SEE current at negative sample potentials.

(b) Threshold energy for charging.

The threshold beam energy for charging cannot be determined accurately from the experimental data due to the effects of conduction current and to uncertainties in the Trek probe measurements at surface

voltages smaller than about 50V. However, if the threshold is chosen as the beam energy for which the sample potential exceeds -50V, one obtains the values of 6.5 keV (gold on Teflon, high current), 6.0 keV (gold on Teflon, low current) and 6.0 keV (gold on Kapton) with uncertainties of the order of 0.5 keV. Table 6.2 gives theoretical values of the total secondary yield upper crossover point for gold (normal electron incidence) using the SEE function described in section 4.1.2 and backscatter model described in section 3.2.2 for six sets of SEE yield curve parameters. Set number 1 is based on measurements by Levy et al⁴⁴ and set number 2 on data from Katz et al³⁵ (on which the BEAM and NASCAP simulations are based) with the remainder being variants on these. The measured threshold exceeds that of parameter set 2 by about 1 keV, but is significantly less than that of set number 1, even accounting for experimental error. Recent measurements by Troim⁹⁹ with a similar gold sample show a much clearer threshold at 6.4 ± 0.2 keV which is within the experimental error of these measurements. Data presented here, together with more recent measurements suggest that the SEE data for gold within the NASCAP code predict a threshold which is too low, and should be replaced with a set of SEE yield curve parameters such as set 6 in Table 6.2.

(c) Field emission as a mechanism for discharge.

Discharges were observed visually between one of the corners of the gold sheet and the grounded sample holder. Various mechanisms have been proposed for vacuum breakdown¹⁰⁰ according to the residual pressure and electrode separation. In each case, there must be a source of electrons or ions on one or both electrodes which introduces particles to the inter-electrode space according to some increasing function of the electric field. The discharge process is initiated by a steady release of electrons from the cathode by field emission which liberate positive ions and photons from the adsorbed gas layers on the anode. A fraction of these ions and photons are incident on the cathode and liberate further electrons, leading to a rapid growth of current and eventually to breakdown. In the context of this study, it is necessary to establish two factors; the sample potential at which field emission currents become significant (to justify their exclusion from the current balance calculation), and why the sample potential at discharge appears to be independent of electrode separation (insulator thickness). These may both be understood in terms of the Fowler-Nordheim theory of electron field emission^{100,101} which describes the escape of electrons by wave mechanical tunnelling through a surface potential barrier which has been thinned by

an external electric field. The current density of electrons emitted from a surface with applied electric field F is given by

$$I = \frac{e}{2\pi h} \frac{\zeta^{\frac{1}{2}} F^2}{(\phi + \zeta) \sqrt{\phi}} \exp \left[-\frac{4}{3} \left(\frac{8\pi^2 m}{h^2} \right)^{\frac{1}{2}} \frac{\phi^{\frac{3}{2}}}{eF} \right] \quad (6.6)$$

where I is in A/cm^2 , F in V/cm and ξ (Fermi level) and ϕ (work function) are in eV . Figure 6.11 shows field emission current density, I as a function of electric field, F over the range 1×10^7 to 2×10^8 V/cm according to the Fowler-Nordheim relation for gold ($\phi = 4.3eV$, $\xi = 5.5eV$) and Figure 6.12 shows how the total emission current varies as a function of V (the sample potential), assuming the radius of curvature of the field emission region to be $2\mu m$. This curve is derived with the additional assumptions that the emitting area is a quarter sphere (at the corner of the gold) and that the electric field very close to the surface is V/r , from which one can deduce that just prior to discharge ($V \approx -4500V$ and emission current of the order of the net incident current ≈ 50 nA) r must be about $2\mu m$. These figures show clearly that field emission current is not significant until the sample potential is very close to the discharge potential and therefore justifies its exclusion from current balance calculations. Furthermore, this theory agrees with the experimental observation that the discharge potential is controlled by the curvature of the field emission surface, and not by the electrode separation distance.

(d) Resistance of the insulating layers.

Table 6.3 gives measured and theoretical values for the resistance of the Teflon and Kapton insulating layers, assuming the bulk conductivities to be $10^{-16} mho/m$ (Teflon³⁵) and $10^{-15} mho/m$ (Kapton⁴⁴) and surface resistivities to be $10^{16} \Omega/\square$ (Teflon³⁵) and $10^{15} \Omega/\square$ (Kapton⁴⁴). The field-enhanced resistance has also been computed using the equation of Adamec and Calderwood⁶⁸ (see section 3.2.5) for a sample potential of $-5100V$. For Kapton, the field enhanced bulk resistance is an order of magnitude smaller than the surface resistance and within a factor of three of the measured value. Thus, at low potentials, surface conductivity effects dominate, giving way to enhanced bulk conduction at larger sample potentials. For Teflon, the theoretical bulk resistance is almost four orders of magnitude greater than the measured value, and is only reduced by a factor of 1.5 by the maximum applied field prior to vacuum breakdown. The calculated surface resistance of the edges of the Teflon sheet is almost two orders of magnitude less than the bulk value and is therefore the primary conduction path, although this resistance is still well in excess of the measured value. The reason for this excess is two-fold. Firstly, the standard test method for measurement of surface conductivity¹⁰² is subject to the effects of charge injection or field-dependent conduction mechanisms¹⁰³ which may introduce significant errors. Secondly, the presence of contaminants or solvents absorbed into the surface layers of an insulator can influence surface conductivity by an

order of magnitude¹⁰³. The Teflon used for these experiments was untreated, although periods of at least 30 minutes at pressures of 10^{-6} Torr was allowed for out-gassing prior to the tests.

(e) Agreement with simulations.

Figure 6.7 shows that for a Teflon insulator, agreement between BEAM and NASCAP with experimental results is good at low current densities and higher beam energies where field enhanced conduction is considered, but the agreement is less convincing at high current density and for low beam energy. This can be explained by Figure 6.13 which gives BEAM code predictions for surface potential (28 keV beam, including field enhanced conductivity effects) versus incident current. Uniformity of the electron beam over the sample area has been demonstrated at 25 keV and $< 1\text{nA}/\text{cm}^2$ current density⁹⁸ but changes in beam energy, cathode current, grid voltage and first anode potential may introduce non-uniformities into the beam such that the Faraday cup measures a maximum current density and it may not be appropriate to assume this is constant over the whole sample. Ideally, the beam profile should be measured at each beam setting, but Figure 6.13 shows that this effect is sufficiently important to account for the discrepancy in Figure 6.7, lower panel. Simulation of dynamic behaviour (Figure 6.6) using BEAM included field enhanced conductivity effects, and the agreement with experiment is excellent whereas the NASCAP simulation assumes constant resistance and predicts a higher final potential. For Kapton, the situation is quite different (Figure 6.8); at the measured value of resistance, BEAM predictions are significantly lower than observations, but at the theoretical value of bulk resistance, including field enhancement effects, BEAM predictions are too high at low beam energies, but in good agreement at 25keV. Once again, this can be explained partly by a beam focusing effect at low beam energies which reduces the actual incident current and partly by a failure of the method described in section 6.2.1 to accurately predict the time constant if total resistance does not stay constant during the charging process.

(f) Secondary emission yields.

During the charging process shown in Figure 6.6 for gold on Teflon, field enhancement effects are small, and the resistance stays almost constant up to -5kV. Thus, the approximation of constant R_T used in section 6.2.1 to derive equation 6.4 is valid, and equation 6.5 was used with confidence to infer the total secondary yield at normal incidence, (over the energy range 19.9 to 24.0 keV) to be 0.83 ± 0.03 . Table 6.4 shows predicted SEE yield values using the model described in section 4.1.2 and the Katz model³⁵. The measured yield lies between the predicted values, but agrees with both to within the experimental error.

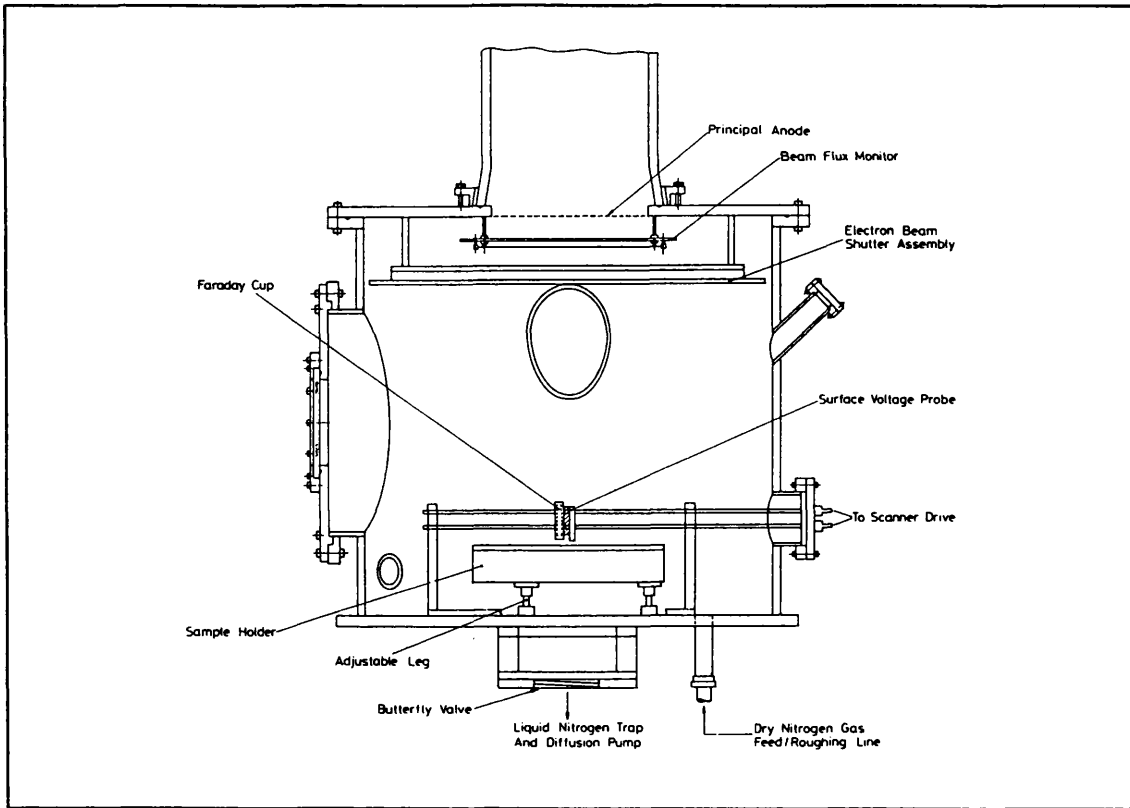


Figure 6.1

Table 6.1 Specifications for the electron beam facility	
Operating vacuum	2×10^{-7} to 1×10^{-6} Torr
Max sample diameter	350 mm
Sample temperature range	-196°C to +150°C
Beam energy range	3 to 30 keV
Beam flux	≤ 10 nA/cm ²
Voltage monitoring range	0 to -20 kV

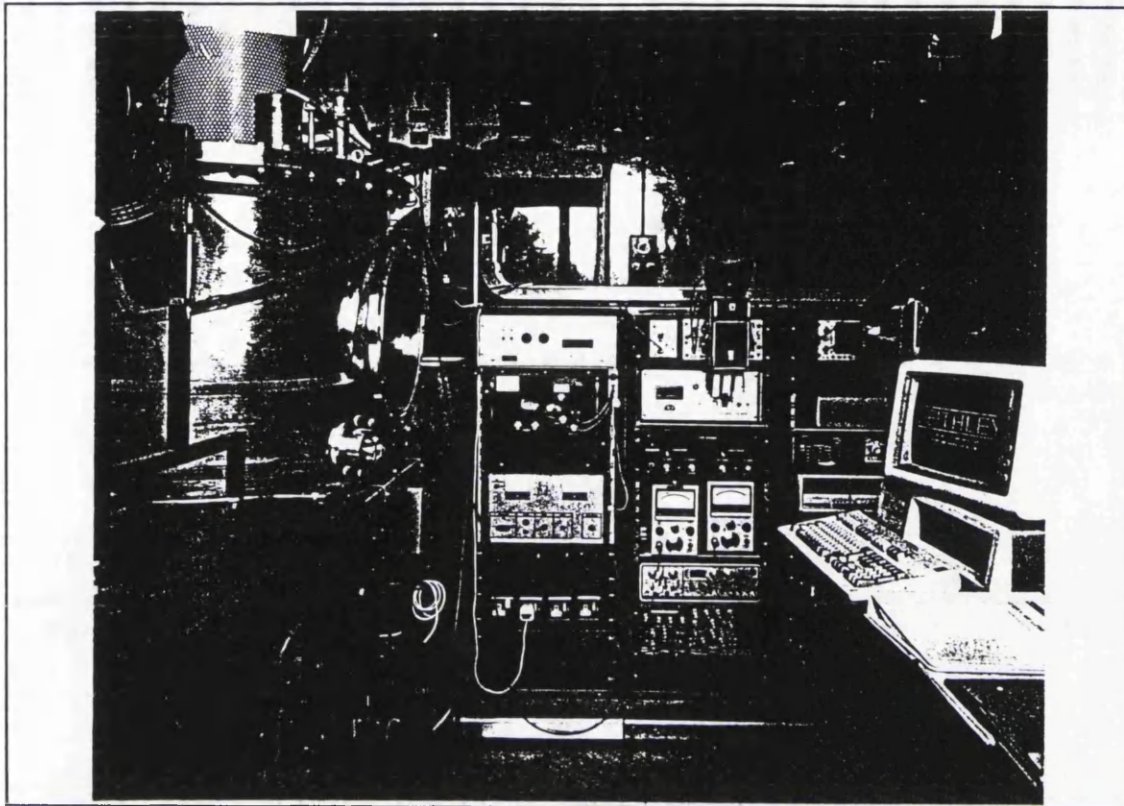


Figure 6.2 Vacuum chamber and instrumentation

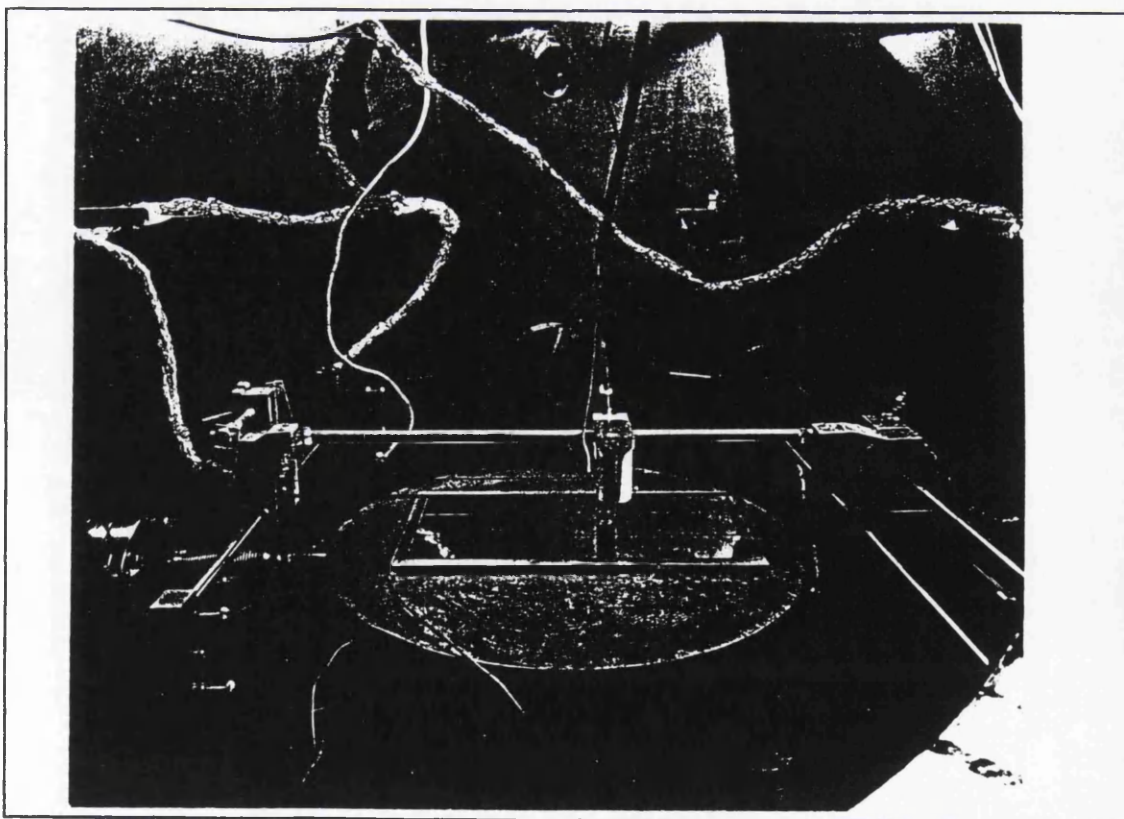


Figure 6.3 Sample holder and probe assembly

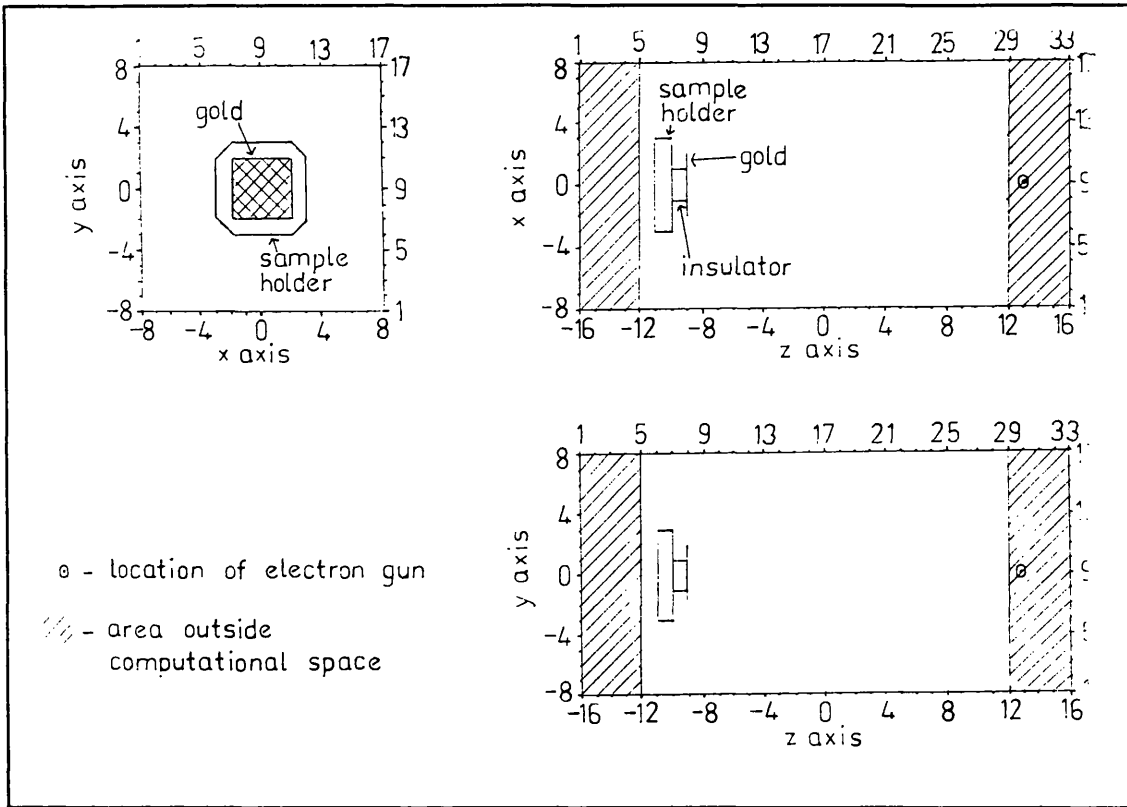


Figure 6.4 NASCAP model of BEAM experiment

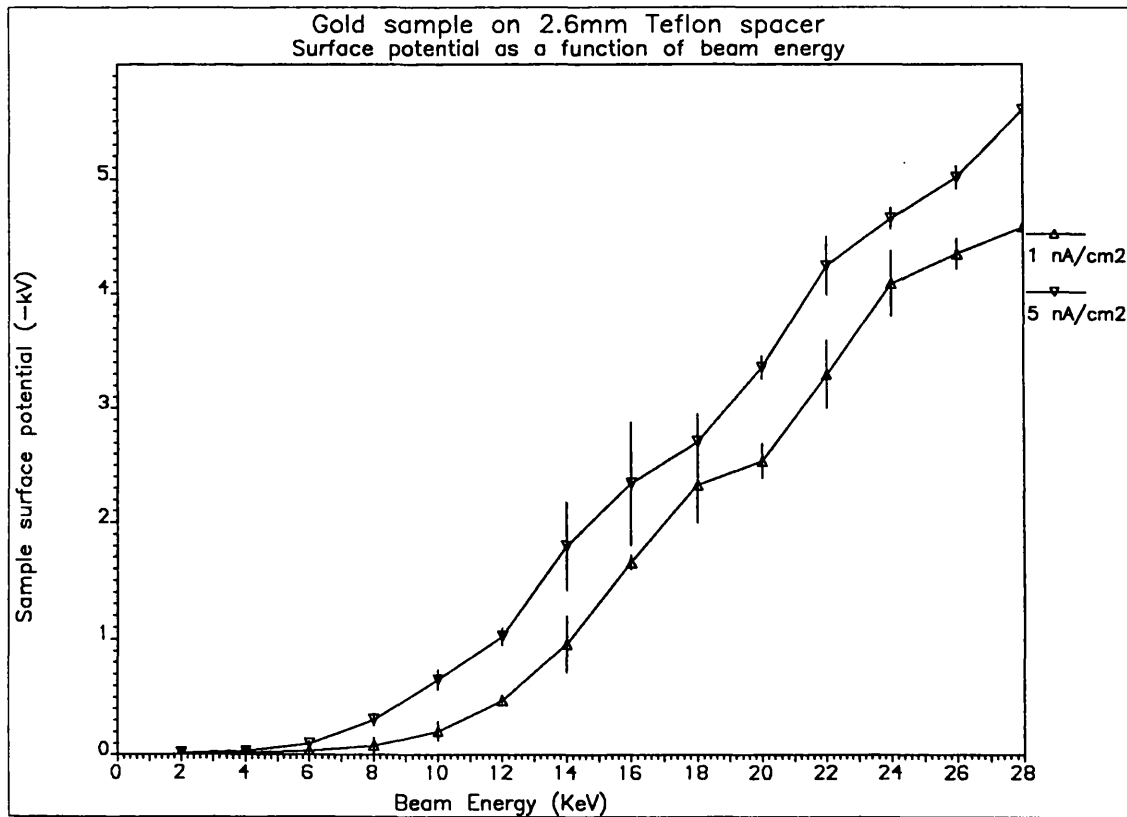


Figure 6.5

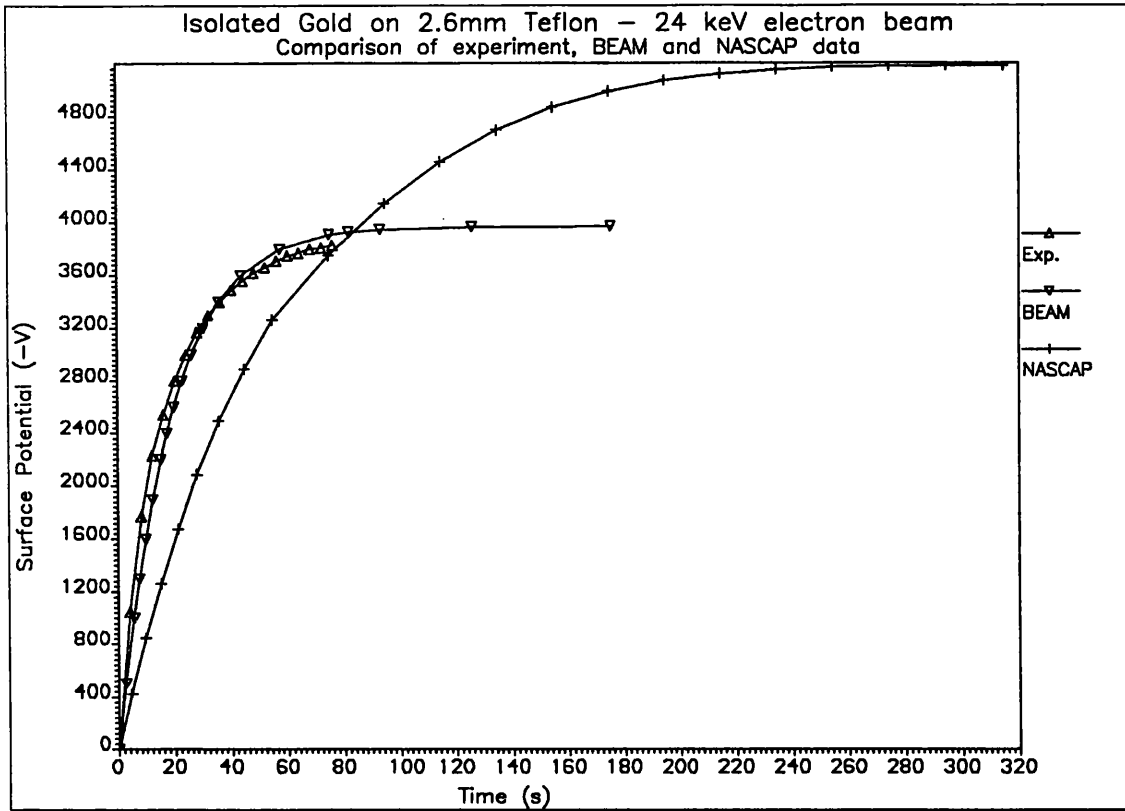


Figure 6.6

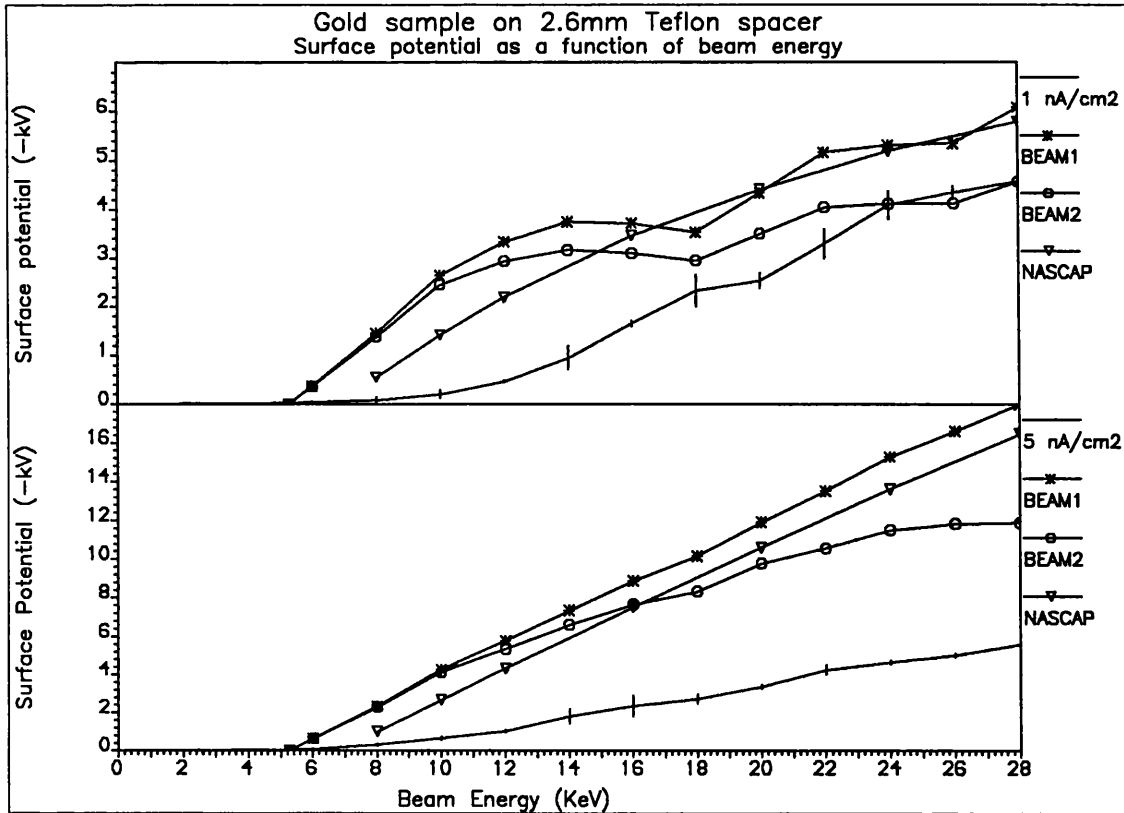


Figure 6.7

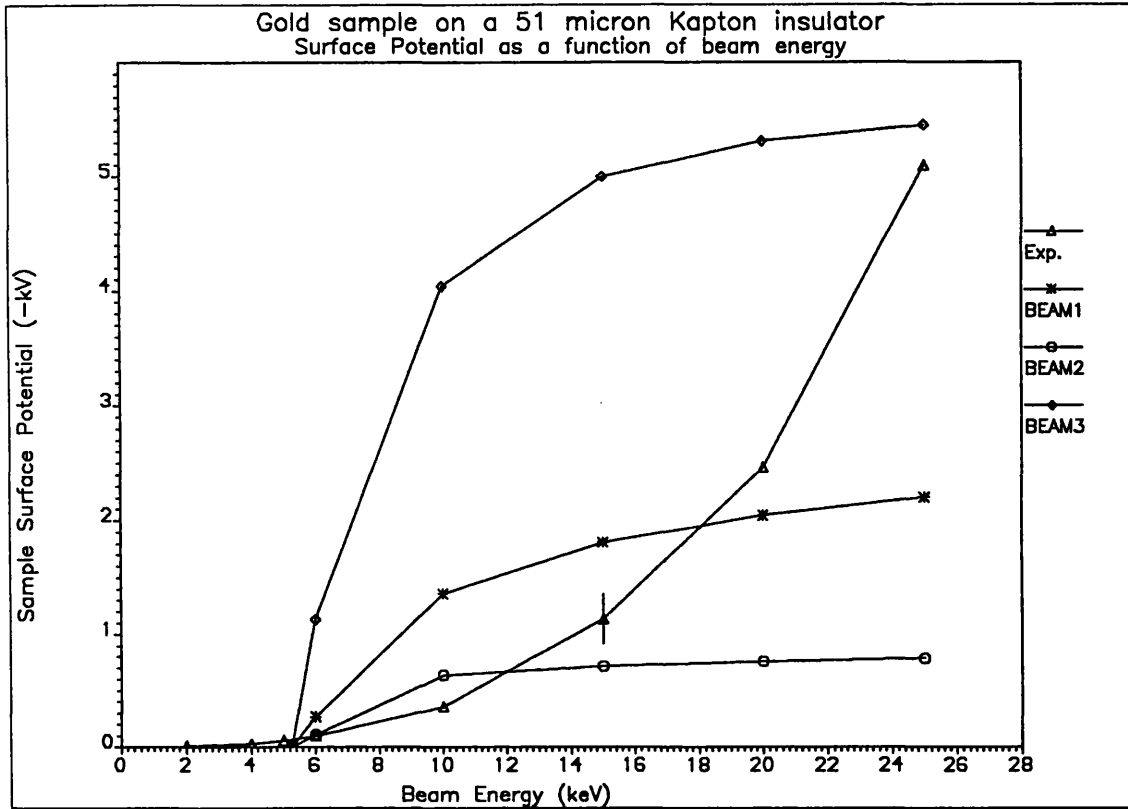


Figure 6.8

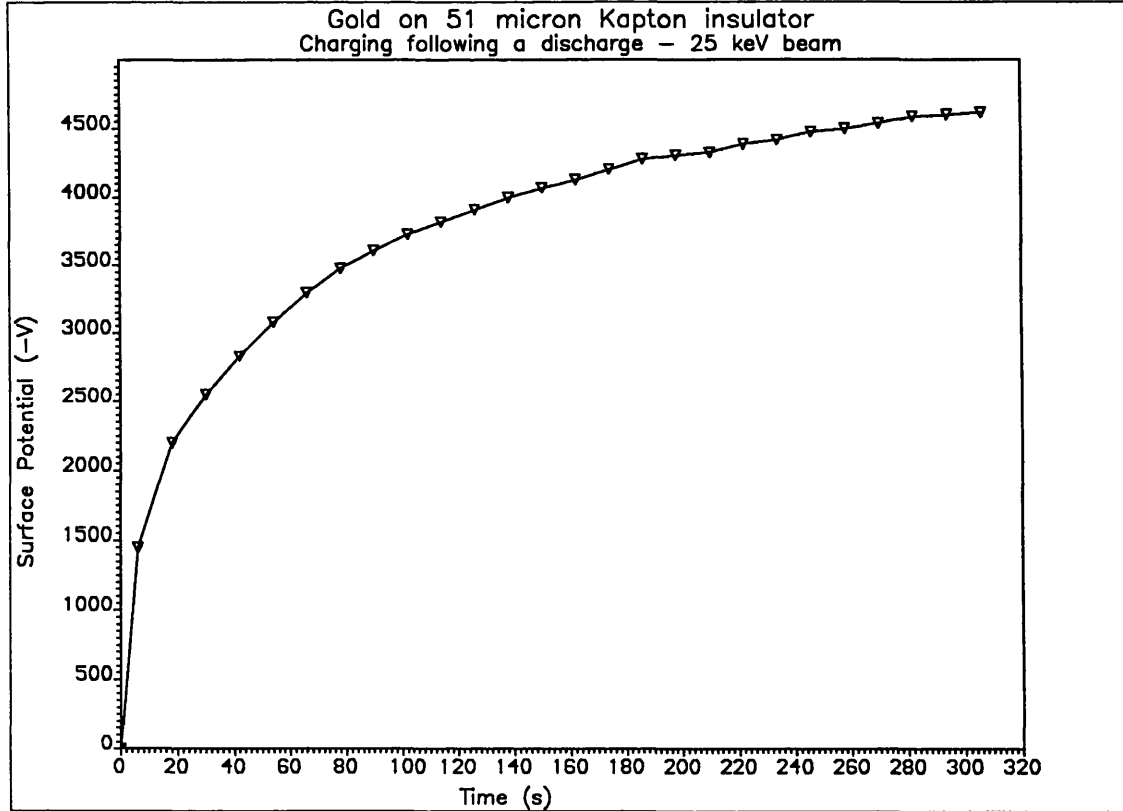


Figure 6.9

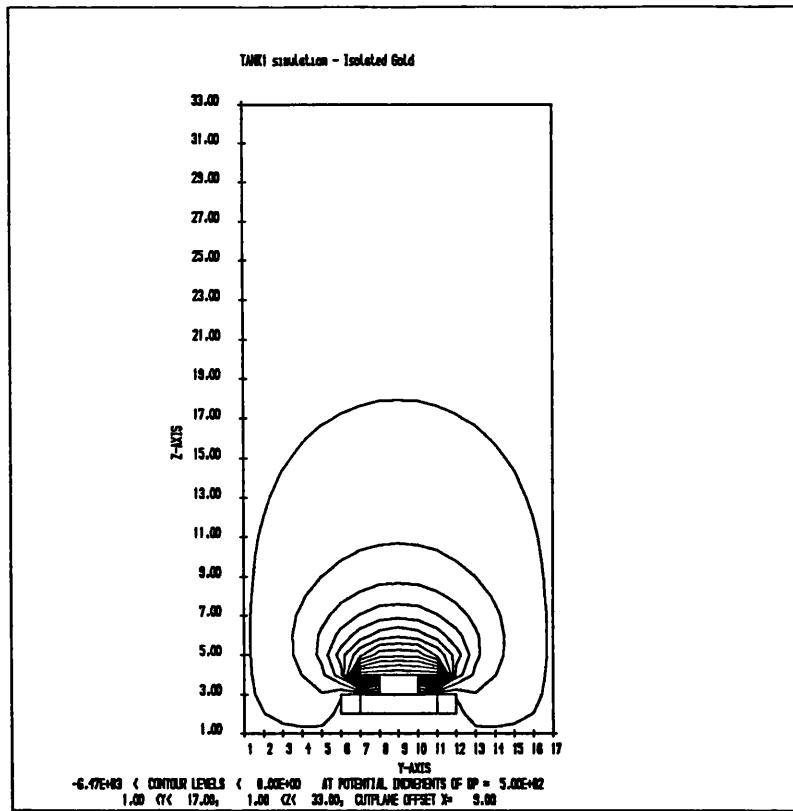


Figure 6.10 NASCAP Test-Tank contour plot

Table 6.2
 Upper crossover points for total yield of gold

Max yield, δ_m	Energy at max yield E_m (keV)	Energy loss power, n	Upper crossover (eV)
1.300	0.800	1.551	9696.0
0.880	0.800	1.551	5263.2
0.880	0.800	1.500	5995.3
0.880	0.800	1.450	6981.7
0.950	0.800	1.551	5922.7
1.000	0.800	1.551	6411.2

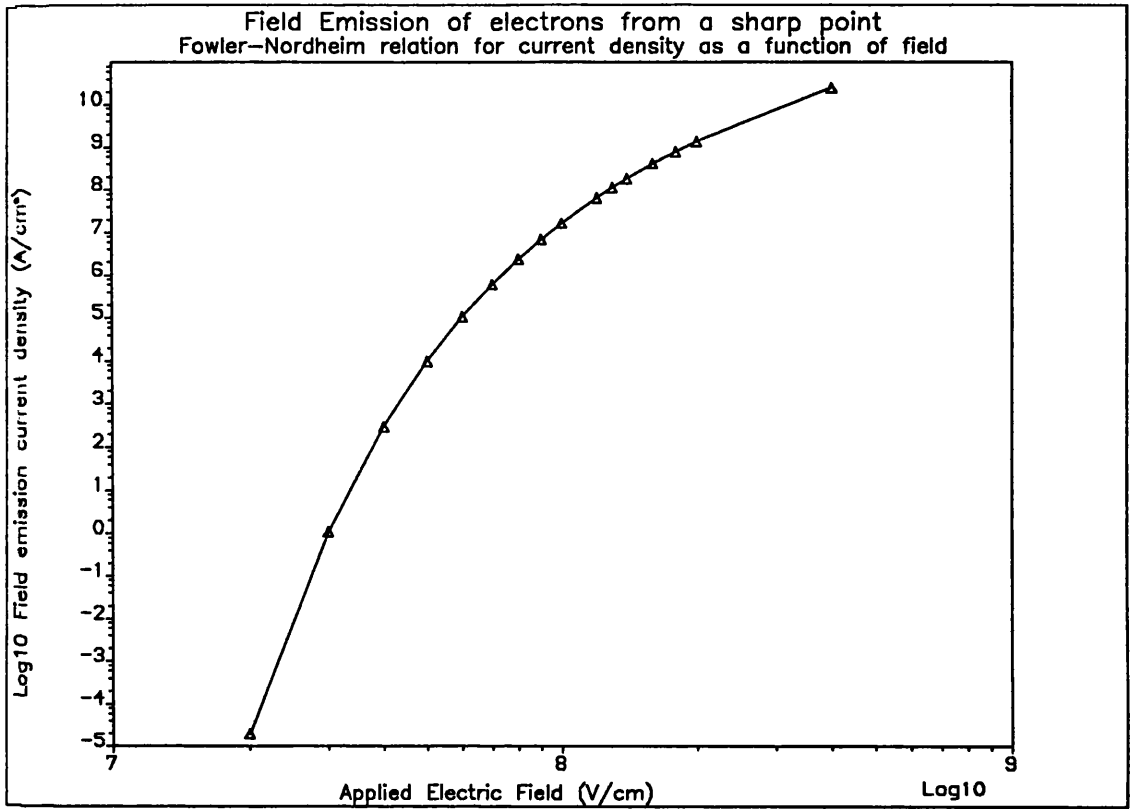


Figure 6.11

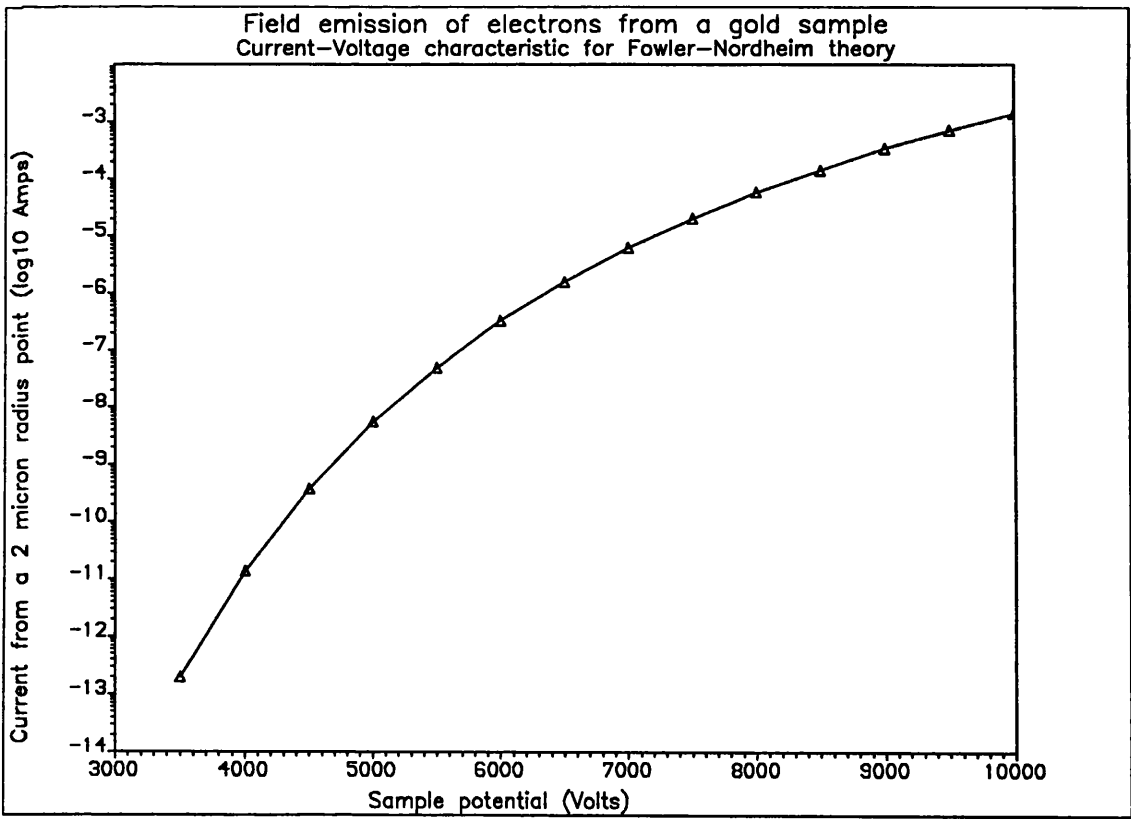


Figure 6.12

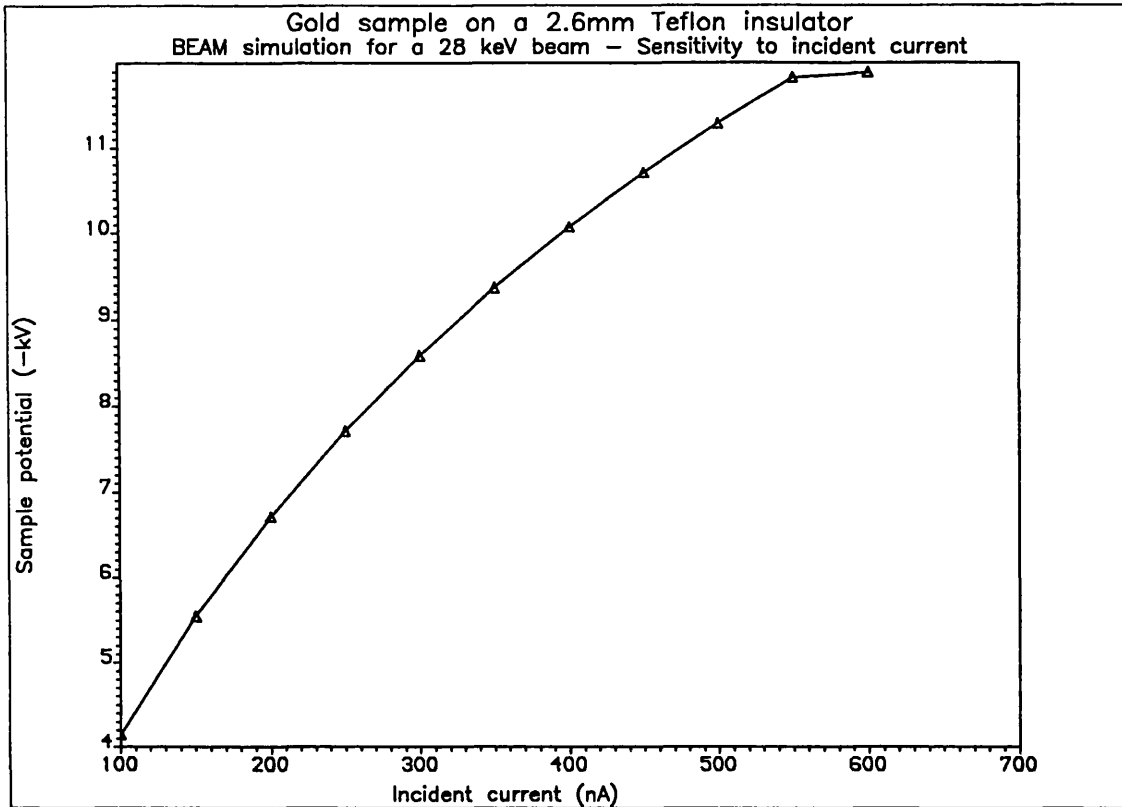


Figure 6.13

	Teflon	Kapton
Measured	$(2.13 \pm 0.08) \times 10^{11} \Omega$	$(8.74 \pm 0.53) \times 10^9 \Omega$
Theoretical bulk	$1.7 \times 10^{15} \Omega$	$3.4 \times 10^{12} \Omega$
Field enhanced at -5.6 kV	$1.2 \times 10^{15} \Omega$	$2.9 \times 10^{10} \Omega$
Surface	$5.2 \times 10^{13} \Omega$	$3.4 \times 10^{11} \Omega$

	"EQUIPOT" SEE model		"NASCAP" SEE model	
	19.9 keV	24.0 keV	19.9 keV	24.0 keV
Y_{SEE}	0.179	0.162	0.243	0.214
Y_B	0.592	0.592	0.592	0.592
Y_{TOT}	0.771	0.754	0.835	0.806

7. SENSITIVITY ANALYSIS USING EQUIPOT

EQUIPOT is employed to investigate the sensitivity of the equilibrium potential reached by a surface exposed to a space plasma. The results of changing material properties, and plasma characteristics are presented.

7.1 RESULTS OF VARYING MATERIAL PARAMETERS

In this section, the EQUIPOT code is used to investigate the degree to which the equilibrium potential of a surface (which is exposed to a severe charging environment) depends on each of the characteristic surface and bulk properties of the material. A set of surface properties and plasma parameters were chosen such that EQUIPOT predicts a potential of -10.0 kV to develop on the "patch" material. This set of parameters provides a convenient datum against which the effect of changes in surface characteristics may be assessed. The "baseline" configuration consists of a sunlit aluminium sphere with a shadowed Kapton patch of thickness 51 μ m. The environment is a "double Maxwellian" which is close to the published "SCATHA worst-case substorm environment"¹⁰⁴, but with a slight increase in the density of the higher temperature electron component in order to produce a patch potential of -9.98 kV (sufficiently close to the desired -10.0 kV). The default list of material properties for aluminium and for Kapton are listed in Table 7.1, and the modified worst-case substorm environment is given in Table 7.2. This environment was chosen, rather than using results from Chapter 5 for two reasons; Firstly, the SCATHA worst case environment is commonly used as an input to NASCAP simulations and it is interesting to investigate how material parameters affect current balance equation solutions in this environment; Secondly it is supposed to be a worst-case environment, so that the results of a sensitivity analysis will be exaggerated, but clearly visible. Section 7.2 is devoted to investigating the effect of different plasma characteristics on the current balance equation solution; the severity of this environment relative to those derived from Meteosat data is therefore quantified.

Since the fraction of the aluminium covered by the Kapton patch is assumed to be negligible, the conduction current between the aluminium and Kapton may be ignored when computing the equilibrium potential of the aluminium (structure) material. This value is largely determined by the photoelectron temperature and turns out to be +6.7V relative to space plasma potential. All results presented for the remainder of this section assume that the structure is maintained at this constant potential.

7.1.1 Sensitivity to conduction

Although the conductivity current is usually a small fraction of the incident current, it can play a significant role in the current balance equation, especially close to equilibrium, where other components change very slowly with surface potential. EQUIPOT considers only the bulk

conductivity between the patch and the structure, and can incorporate field enhanced conductivity according to the model of Adamec and Calderwood⁶⁸. Thus, there are four parameters which affect the conduction current; patch thickness, conductivity of the patch material, together with temperature and relative permittivity of the patch material, if field enhanced conductivity is included.

Figure 7.1 shows the equilibrium potential of the Kapton patch as a function of Kapton thickness, for five different cases; (i) Assuming that the bulk conductivity current can be calculated according to Ohm's law (marked "Default"), (ii) Assuming field enhanced conductivity according to equation 3.110 with a patch temperature of 273K (marked "273K"), (iii) as for (ii), but with a patch temperature of 173K (marked "173K"), (iv) as for (ii) but with a patch temperature of 373K (marked "373K") and (v) as for (ii), but assuming that the relative permittivity of Kapton is 4.0. The three temperatures were chosen on the basis that these are the minimum, most probable, and maximum temperatures likely to be attained by satellite surface materials. At thicknesses of 1mm or greater, all five curves converge since the conductivity current becomes negligible for thick samples; the equilibrium potential is a result of detailed balancing of surface currents only. The most striking feature of these results, however, is the effect of including field enhanced conductivity, which appears to inhibit differential charging for thin dielectric films. Patch temperature has a significant effect on the enhancement of conductivity due to electric fields; as the temperature increases, the degree of enhancement is reduced, although this should be offset against the normal effects of temperature on bulk conductivity at low electric fields. The relative permittivity of Kapton is reported⁶⁶ as lying between 3.0 and 4.0. According to Figure 7.1, a small change in relative permittivity has only a second order effect on the equilibrium potential of the Kapton patch compared to other factors.

There are several reported values for the bulk conductivity of Kapton; the differences perhaps arise from uncertainties in the various measurement techniques, slight differences in the characteristics of the sample, temperature effects or ageing. Figure 7.2 gives the effects of varying the bulk conductivity over almost four orders of magnitude, for Ohmic conduction only (marked "Normal" on the figure) and for field enhanced conductivity at 273K (marked "enhanced" on the figure). Two effects are apparent; the field enhancement effect is most important for low values of conductivity, and the equilibrium potential is especially sensitive to the conductivity when its value exceeds 10^{-15} mho/m.

7.1.2 Sensitivity to changes in electron backscatter

To estimate the current of backscattered electrons from a surface, EQUIPOT uses the model described in section 3.2.2, for which the only free parameter is the atomic number of the target material, Z. The sensitivity of the equilibrium potential to changes in Z for the target material were investigated by using the default configuration and

environment described earlier and varying the atomic number of the patch material (Kapton). Variation of Z may be thought of as a convenient device for changing the importance of the backscattered electron current relative to the other components.

The results of this analysis are given in Figure 7.3. Z has been varied over atomic numbers from 5 to 90 which ensures that all possible backscatter yield functions are sampled. Although there is a significant variation in equilibrium potential over the full range of Z , the solution is relatively insensitive to small changes in Z . Also, the effect of making a small change in Z decreases slightly for high Z materials.

7.1.3 Sensitivity to changes in electron SEE current

The model for secondary emission of electrons due to electron impact described in section 4.1.2 is based on three parameters; the maximum yield at normal incidence, the energy of maximum yield, and the energy loss power. A sensitivity analysis over the full range of all three variables would generate a prohibitive number of results; however, if the study is confined to polymers, Burke's relations (equations 3.85, 3.86 and 3.87) can be used to relate both the maximum yield and energy at maximum yield to an "emission coefficient", K which is computed from the properties of a repeating polymeric unit. Thus, for polymers, a sensitivity analysis can be performed with two free parameters; K which can range from 0.682 (Kapton) through to 1.546 (Teflon) and the energy loss power, n which can range from about 1.3 to 2.3.

The results are shown in Figure 7.4 where the equilibrium potential has been plotted against n for several values of K , giving a family of curves. At high energies, beyond the peak in the yield curve, the secondary emission yield is inversely related to n . When n exceeds 2.0, (for this severe environment), the current of secondary electrons is virtually suppressed, thus at high values of n , there is almost no dependence on K , and the equilibrium potential asymptotically approaches a value determined by the balance between incident current, backscatter, ion-induced SEE and conductivity. For each value of K , there is a threshold value of n , above which negative charging occurs. The position of this threshold also depends on the spectrum of incident radiation and represents the point where the incident electron current is exactly equal in magnitude to the sum of the true SEE current, backscatter, incident ion and ion-induced SEE currents. Just above this threshold value of n , the equilibrium potential increases rapidly for small changes in n such that if n is raised above the threshold by 0.1, the equilibrium potential may change by several kilovolts. In addition, that part of the curve just above the threshold value of n is the region where changes in K have their greatest effect, ie the vertical separation of the family of curves is at a maximum.

In summary, for a given polymer, the energy loss power must be measured with great care, especially if it lies close to the threshold value. The precision with which the position of maximum yield (or K

value) must be measured depends on the appropriate value of n for a given material. Previous measurements of the secondary yield properties of materials have tended to concentrate on determining the maximum yield, and the energy at which this occurs; this work has demonstrated that it is more important to concentrate on measuring the yield at high incident energy, from which n can be determined with greatest accuracy.

7.1.4 Sensitivity to changes in ion-induced SEE

Secondary electrons liberated from a surface as a result of ion impact (SEI) are modelled according to the theory described in section 3.2.3, which permits the secondary yield function to be characterised in terms of two parameters; the yield for normally incident, 1 keV protons, and the incident proton energy at which the normal yield is a maximum. Variation of two parameters is ideally suited to a sensitivity analysis, and a search of lists of material data from NASCAP^{19,44} revealed that for common satellite surface materials, the yield at 1 keV varies between 0.2 and 0.5, whilst the energy for maximum yield occurs between 100 and 300 keV.

Figure 7.5 shows the results of the analysis for the default configuration of a shaded Kapton patch subjected to a severe substorm environment. The effects of changing the energy of maximum yield are small since this energy is an order of magnitude greater than the temperature of the hottest plasma component. The sensitivity to changes in E_m will be further reduced for less severe environments. Changing the yield for 1 keV protons has a much greater effect, but large changes are necessary to cause the equilibrium potential to be affected significantly.

Although this current component is always a significant constituent of the current balance equation, it is relatively insensitive to small changes in the two properties which define the yield function. In addition, the sensitivity to variations in these two parameters will diminish as the spectrum softens.

7.2 RESULTS OF VARYING THE ENVIRONMENT

This section examines the effect of subjecting the default configuration satellite (a sunlit aluminium sphere with a shadowed Kapton patch) to different forms of plasma environment. A threshold plasma temperature for negative charging is identified which is related to material properties. Charging levels induced by average plasmashet spectra, and geomagnetic substorms are determined. Finally, a relationship is established between threshold charging temperature and the onset of triple root current voltage characteristics.

7.2.1 A threshold temperature for charging

Based on analysis of spectrogram data from the satellites ATS-5, ATS-6 and SCATHA, Olsen¹⁰⁵ showed that there existed a threshold plasma temperature (about 15 keV) above which eclipse charging was likely to

occur. However, there was no apparent relation between plasma temperature and the eventual equilibrium potential attained by the vehicle. Theoretically, the threshold plasma temperature occurs at the point where the incident electron current is numerically equal to the sum of the current components due to true electron secondaries, backscatter, ion impact and secondaries due to ion impact. Conduction current is not considered since at the threshold temperature, the satellite potential will be zero (relative to plasma potential). For a Maxwellian plasma, it is possible to predict the threshold temperature directly, by integrating all the secondary yield functions with the incident currents; but the resulting expression would need to be solved numerically. EQUIPOT provides a mechanism for finding this threshold temperature, although it is necessary to change the plasma environment interactively until the patch equilibrium potential becomes zero.

The default satellite configuration was subjected to a single Maxwellian plasma environment where the ions (protons) and electrons had equal density and temperature. For a Kapton patch, the threshold temperature was found to be 2520 eV, for a density of 1.0 cm^{-3} . The threshold temperature is insensitive to changes in plasma density; for a density of 0.1 cm^{-3} , the threshold temperature increases to 2540 eV and for an increase on plasma density to 3.0 cm^{-3} the threshold temperature is reduced to 2515 eV.

From Figure 7.4 it is apparent that the threshold temperature for negative charging will also depend very strongly on the secondary electron emission yield function, and specifically on the energy loss power, n . Thus, for a fixed plasma density (1.0 cm^{-3}) and with all other material parameters as for the default case, it is possible to find combinations of energy loss power and plasma temperature which determine the threshold for negative charging. EQUIPOT was used to find the locus of such pairs, for a default Kapton patch, and for a polymer with emission constant, K equal to 1.8 (representing a polymer with high secondary yield, such as Teflon). The results are given in Figure 7.6. The two curves are the loci of the charging threshold; a combination of plasma temperature and energy loss power which lies on one of the curves will result in an equilibrium patch potential of 0.0V; points lying in the region above the curve will cause negative charging, whilst those lying below the curve will cause the patch to float at a small positive potential. Of course, this threshold locus will depend on every other parameter which enters the current balance equation, but plasma temperature and energy loss power are the most influential.

7.2.2 Charging properties of average plasmasheet spectra

In section 5.2.2 four plasmasheet electron spectra were derived from average fluxes measured by Meteosat F2 according to four levels of geomagnetic activity. The level of charging induced by these "average" environments, and by their Maxwellian equivalents has been calculated. The corresponding ion spectra are essential for this exercise, but were

not measured by Meteosat; therefore the ion flux at each energy range was estimated by dividing the average electron flux by the square root of the proton to electron mass ratio. This ensures bulk neutrality of the plasma, and is correct for a single Maxwellian environment. The equilibrium potential of the shaded Kapton patch (ie the default satellite configuration) was computed for each of the average plasmashet spectra (with the equivalent ion fluxes), and also for the Maxwellian equivalent plasma characteristics of each spectrum shown in Figure 5.9. Since the measured spectra end abruptly at 19.8 keV, and the flux greater than this energy may be significant, the equilibrium potential was also computed for each measured average spectra plus its Maxwellian equivalent for energies greater than the upper limit of the detector. (EQUIPOT allows Maxwellian definitions to be added to measured spectra, but where these overlap, the Maxwellian is ignored and the measured spectrum used to compute the current). The results are shown in Table 7.3. Only the Maxwellian equivalents to the quiet and disturbed average spectra demonstrate any negative charging, whilst all other cases do not. The reason for this is two-fold. First consider the current equivalent spectra for the four average spectra and their Maxwellian equivalents (Figure 5.9); the measured average spectra are much flatter than their Maxwellian equivalents, such that there is less flux at high energies near the peak, where the secondary electron emission yield function is much less than unity. Secondly, the equivalent Maxwellian temperatures (equal to half the mean spectral energy) for the Very Quiet and Very Disturbed cases are less than the threshold charging temperature of 2620 eV for the default satellite configuration.

Where the spectrum becomes significantly non-Maxwellian, there is a possibility of multiple-root charging (see, for example Whipple³⁴) which can be detected by examination of the current-voltage relationship for a given set of input parameters. Figure 7.7 shows the current-voltage relationships for the four average spectra with Maxwellian high energy tails above 19.8 keV (note that the positive x axis has been expanded by a factor of 100 for clarity). Although none of these curves exhibits more than a single root, they all contain two turning points and both the Quiet and Disturbed cases come very close to a triple root characteristic, where the most negative stable root is close to the potential predicted for the single Maxwellian equivalent of each case.

These results are highly significant for several reasons; firstly, none of the measured average spectra will induce negative charging on the shaded Kapton patch, even with the addition of a realistic high energy tail component, but in certain cases, a Maxwellian equivalent, based on the same mean energy and total current will induce negative charging. Secondly, all the average spectra are sufficiently non-Maxwellian to exhibit a current-voltage characteristic with two turning points, and the addition of extra electron flux at high energies (eg during certain substorm events) would be sufficient to induce a triple-root characteristic.

7.2.3 Charging in a model substorm environment

In section 5.2.4, a substorm model was introduced, based on the probability of a change in plasma density and pressure (energy density) for a substorm onset. This model has proved to be ideally suited to a study using EQUIPOT whereby the effect of adding an injected plasma (characterised by a change in density and pressure) to a quiet-time plasmashet spectrum may be assessed. However, the substorm model assumes that the injected plasma has a Maxwellian energy distribution which EQUIPOT will only superimpose onto a background environment if the background is itself Maxwellian. Therefore, a quiet-time background plasmashet spectrum was chosen which corresponds to the Maxwellian equivalent of the "Quiet" average plasmashet spectrum, given in the previous section (density = 0.483 cm^{-3} , temperature = 2822.3 eV) which induces a potential of -543.7V on the default satellite configuration. To this was added various different Maxwellian components corresponding to combinations of density and pressure change observed during substorms.

According to Figures 5.17 and 5.18, the density of injected plasma observed during a substorm onset varies between about 0.5 and 3.0 cm^{-3} whilst the pressure varies over the range of 0.5 to 3.0 nPa . The mean energy of the injected plasma may be approximated by dividing the pressure by the density and converting to the appropriate units (this assumes a Maxwellian form for the injected plasma). The results are shown in Figure 7.8 which shows the equilibrium potential achieved by the shaded Kapton patch for a range of density and pressure increases superimposed onto the quiet-time plasmashet background spectrum. It should be noted that whilst dn (change in density) and dp (change in pressure) can be used to define the severity of a substorm event, they do not influence the equilibrium potential independently since the plasma temperature is derived from them both. Thus, the most negative potentials are achieved when the pressure increase is high and the density increase low, ie most of the injected plasma is energetic. It is also interesting to note from Figure 7.8 that the contours giving the probability of a substorm with a given magnitude are perpendicular to the equilibrium potential contours, so that the events which induce the most negative potentials are not the least common.

7.2.4 Charging during measured substorm environments

Although the substorm severity model introduced in section 5.2.4 is useful for assessing the likelihood of a substorm of given magnitude, it relies on the approximation that the injected plasma may be described by a Maxwellian distribution function. When used in conjunction with EQUIPOT, it is also necessary to assume that the quiet-time background plasma is Maxwellian. It was shown in section 7.2.2 that if the plasma energy spectrum becomes significantly non-Maxwellian, then the system may develop a multiple-root current-voltage characteristic. This section examines the behaviour of the default satellite configuration when exposed to an electron environment measured by Meteosat, at the peak of

a substorm onset. Once again, the ion flux at a given energy has been approximated by dividing the corresponding electron flux by the square root of the proton to electron mass ratio.

A subset of the substorm onsets observed by Meteosat F2 were chosen to study the effect of such events on surface charging. Table 7.4 shows the patch equilibrium potential when exposed to the spectrum measured at the peak of each of 11 substorm events selected at random from April 1982. The table shows the temperature (in eV, and equal to one half of the mean energy), and the total flux (in nA/m²) for each spectrum. All the spectra induced a single-root current-voltage characteristic, but only three produced any negative charging. The reason why these three events induced negative charging is apparent from Figure 7.9 which shows the electron spectra for each of the substorm events (on two panels for clarity). The three charging spectra (denoted S04, S10 and S11) have a lower flux at low energy, and a higher high energy flux; ie they have a greater mean energy than the rest. This is also apparent from Table 7.4 where the three charging events are the only ones with a temperature greater than the charging temperature threshold of 2620 eV for this configuration (see section 7.2.1).

The analysis was extended to a total of 63 substorm onset events, observed during April 1982. Of these, nineteen substorm spectra induced negative charging with a single root characteristic (although not necessarily with a monotonic current-voltage relationship), five resulted in triple-root characteristics and the remainder did not induce any negative charging. Figure 7.10 shows the equilibrium patch potential (of the default satellite configuration) as a function of the temperature of the electron spectrum for each of the 63 recorded substorm onsets during April 1982. The positive x-axis has been magnified by a factor of 100 for reasons of clarity, and the triple-root charging events (marked "TR") have been plotted for the most negative stable root. Spectra for which no negative charging was induced are marked "No Chg" and those which induced single-root negative charging are marked "SR chg". There is a clear threshold temperature of about 2950 eV, above which negative charging can occur. This threshold temperature is somewhat higher than that for a Maxwellian environment (2620 eV) since the measured spectra are artificially truncated at 19.8 keV; ie the net negative current contribution from electrons above this energy is absent. Furthermore, the triple-root charging characteristic is found only when the plasma temperature just exceeds the threshold value. Thus, triple-root charging and threshold temperature are related for non-Maxwellian spectra; when the mean energy is close to twice the threshold temperature for a Maxwellian plasma, triple-root charging is most likely to occur.

Table 7.1
Default material properties for aluminium and Kapton

No.	Name	Aluminium	Kapton
1	Relative permittivity	-	3.0
2	Thickness [m]	-	51x10 ⁻⁶
3	Conductivity [mho/m]	-	1.0x10 ⁻¹⁵
4	Atomic number	13	5.0
5	Max. SEE yield	0.970	1.9
6	Energy for max SEE yield [keV]	0.3	0.2
7	Energy loss power, n	1.621	1.698
8	Density [g/cm ³]	2.698	-
9	SEE yield for 1 keV protons	0.244	0.455
10	Proton energy for max yield [keV]	230.0	140.0
11	Photoelectric yield [A/m ²]	4.0x10 ⁻⁵	2.0x10 ⁻⁵
12	Surface resistivity [Ω/\square]	-	1.0x10 ¹⁵

Table 7.2
Modified SCATHA worst case environment used for EQUIPOT sensitivity analysis.

	n ₁ (cm ⁻³)	T ₁ (eV)	n ₂ (cm ⁻³)	T ₂ (eV)
Protons	1.1	350.0	0.95	28800.0
Electrons	0.15	450.0	1.1	27650.0

Table 7.3
Equilibrium potentials for average plasmashet spectra

	Equilibrium pot. in Volts			Equivalent Maxwellian	
	Ave. spectra	Ave. + HE tail	Equiv. Maxw.	n (cm ⁻³)	T (eV)
V. Quiet	+1.19	+1.20	+0.18	0.352	2359.9
Quiet	+0.75	+0.75	-543.7	0.483	2822.3
Disturbed	+0.72	+0.72	-730.1	0.714	2893.4
V. Disturbed	+1.22	+1.23	+0.04	1.208	2485.0

Table 7.4
Temperature, total flux and equilibrium potential for eleven selected substorm events during April 1982.

Label	Date	Time (UT)	T (eV)	TF (nA/m ²)	V _p Volts
S01	01.04.82	20:34:56	1079	4668.7	+2.3
S02	02.04.82	19:21:47	1253	2313.5	+2.3
S03	03.04.82	06:17:50	1199	4211.7	+2.8
S04	03.04.82	00:33:43	4296	3202.2	-2930
S05	10.04.82	04:33:44	2021	3976.3	+0.77
S06	10.04.82	19:27:48	2207	3071.8	+0.65
S07	11.04.82	04:48:35	2050	3883.1	+1.40
S08	20.04.82	23:06:13	2139	2993.7	+1.05
S09	25.04.82	02:56:31	2417	4327.8	+0.92
S10	28.04.82	04:15:05	3363	3672.8	-1810
S11	29.04.82	23:12:55	3427	1683.7	-1700

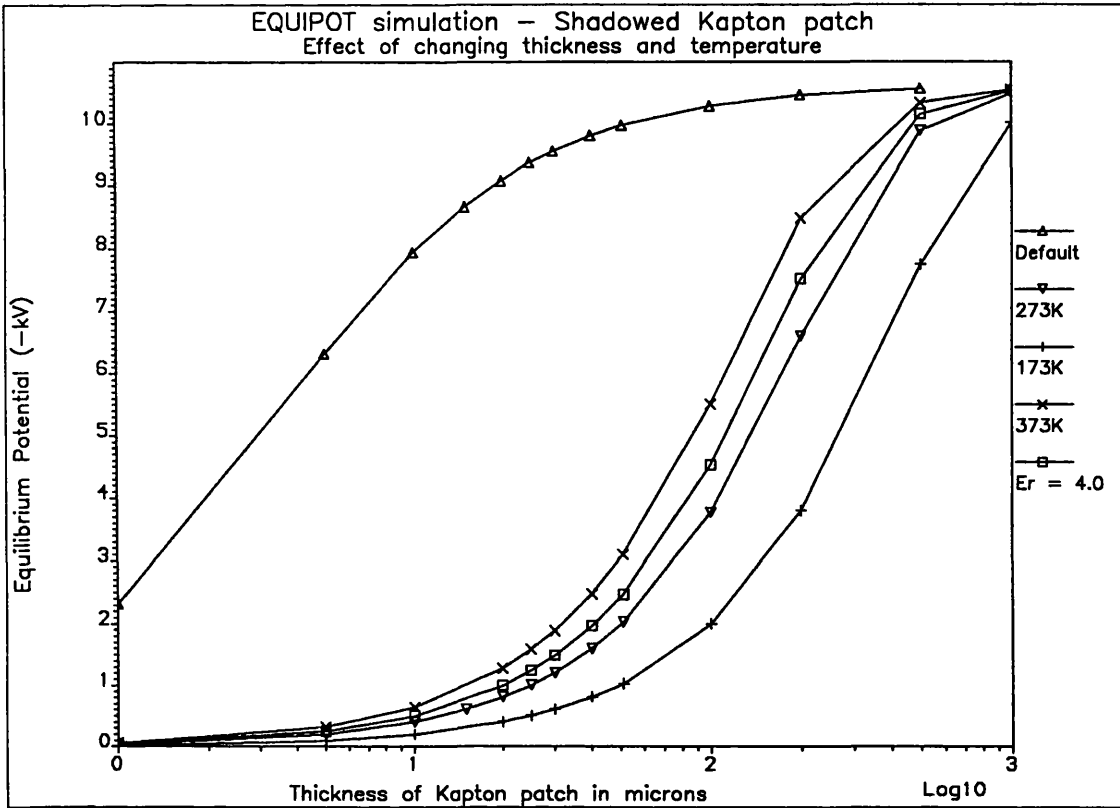


Figure 7.1

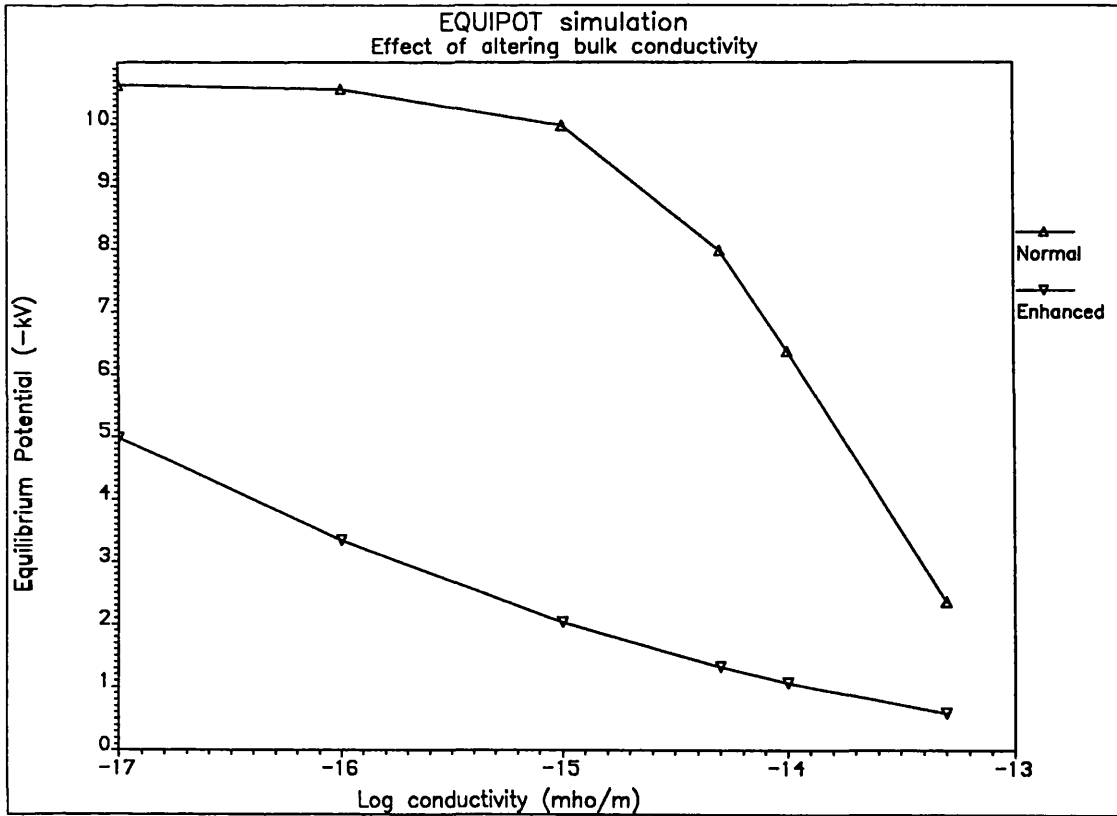


Figure 7.2

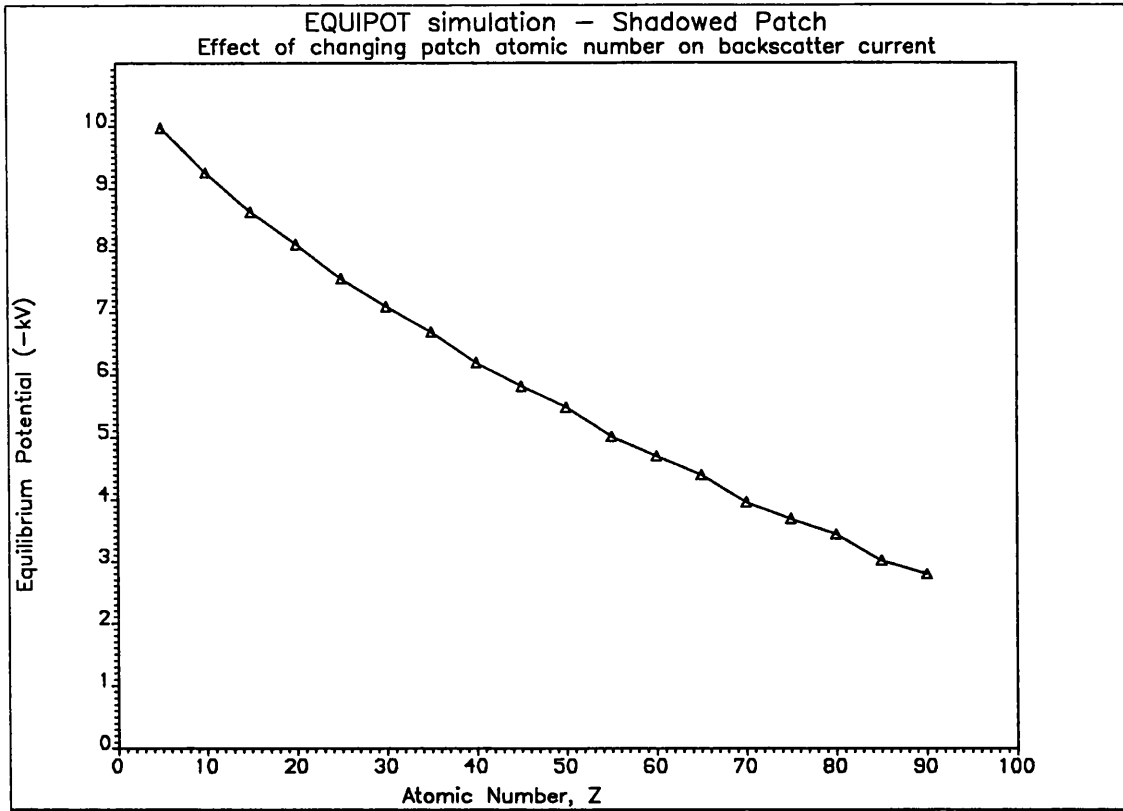


Figure 7.3

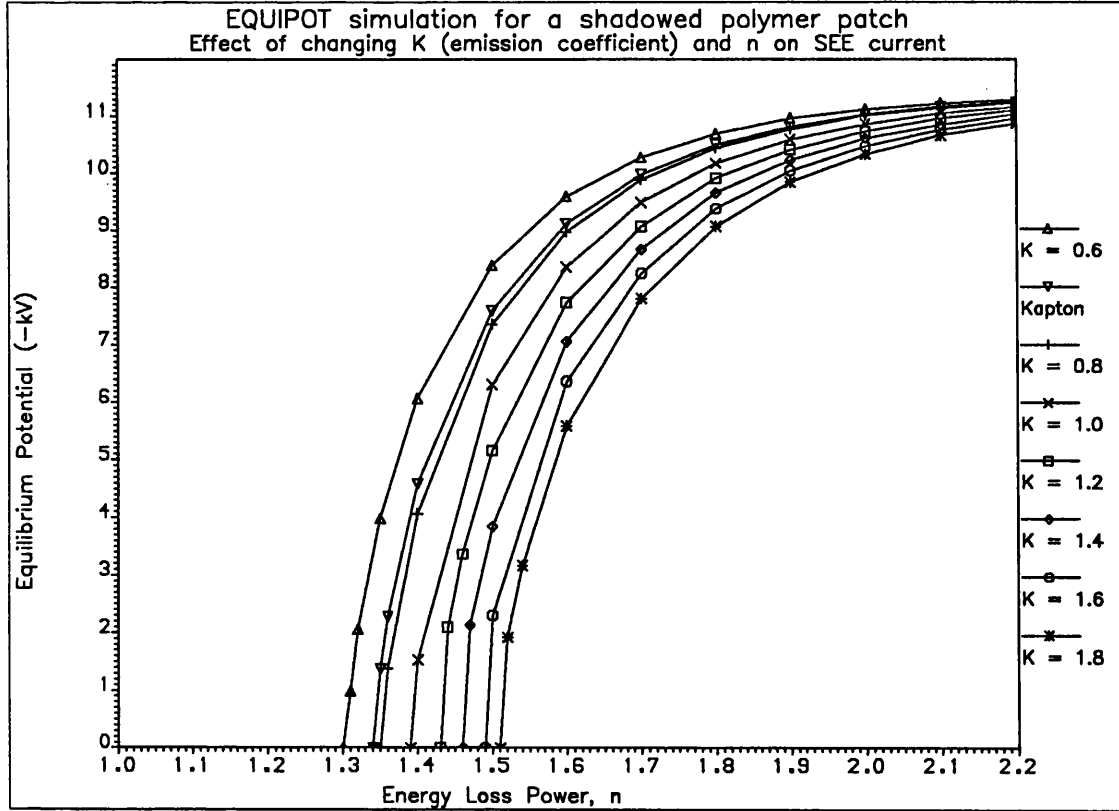


Figure 7.4

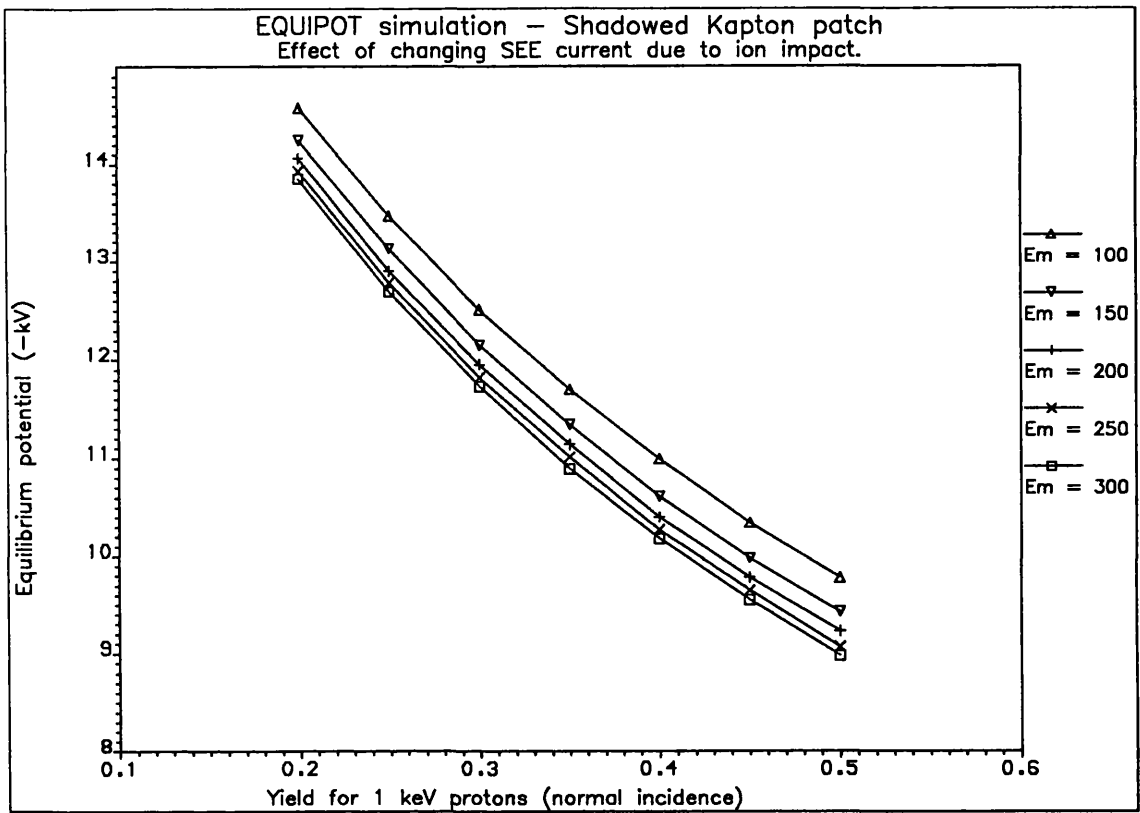


Figure 7.5

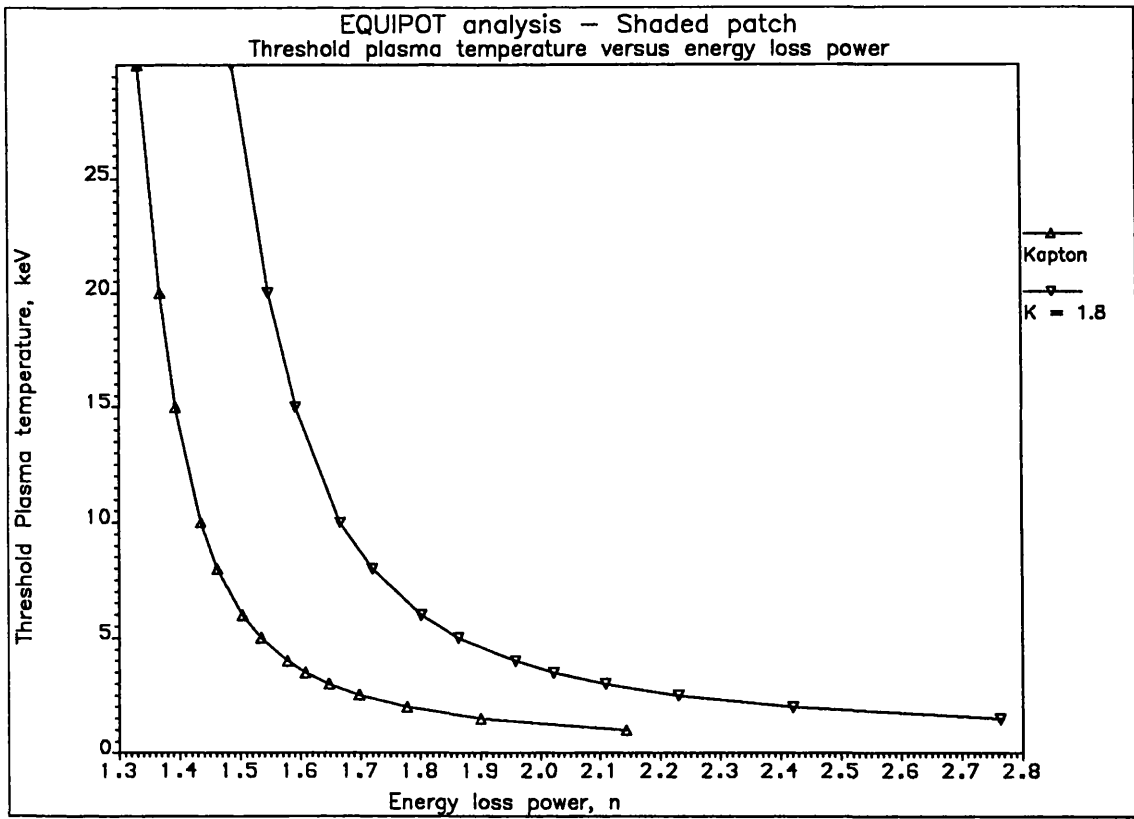


Figure 7.6

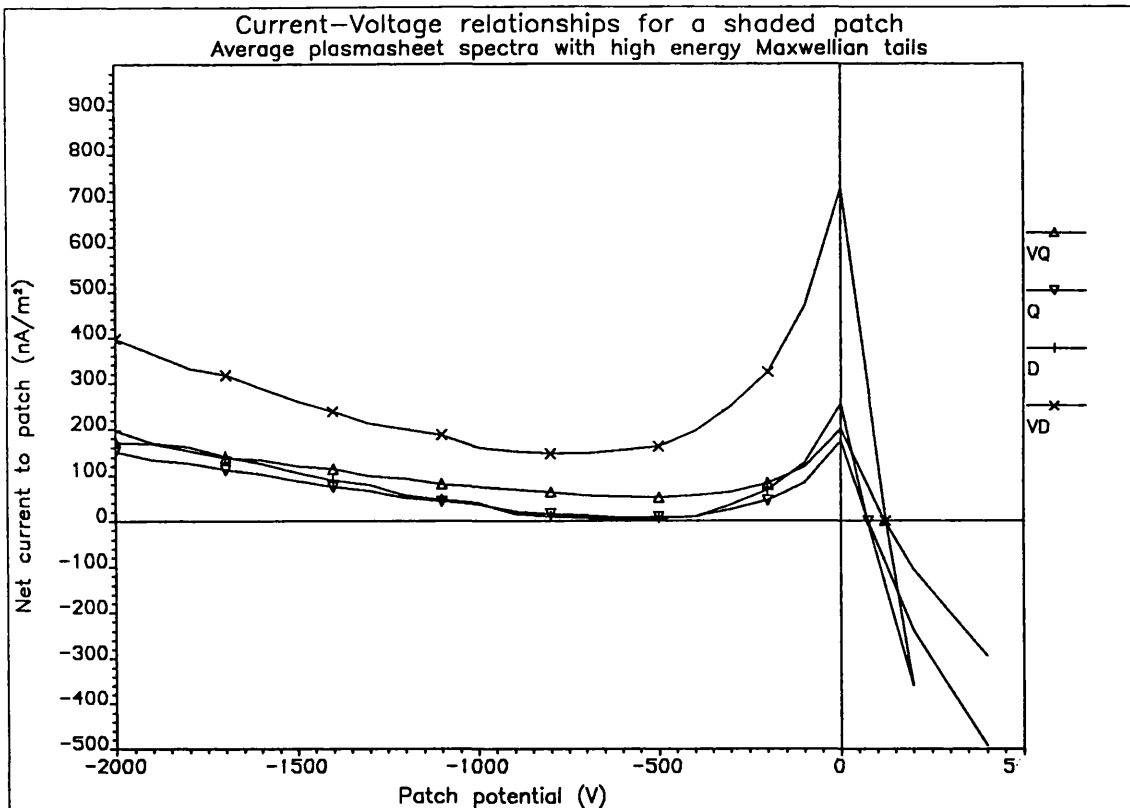


Figure 7.7

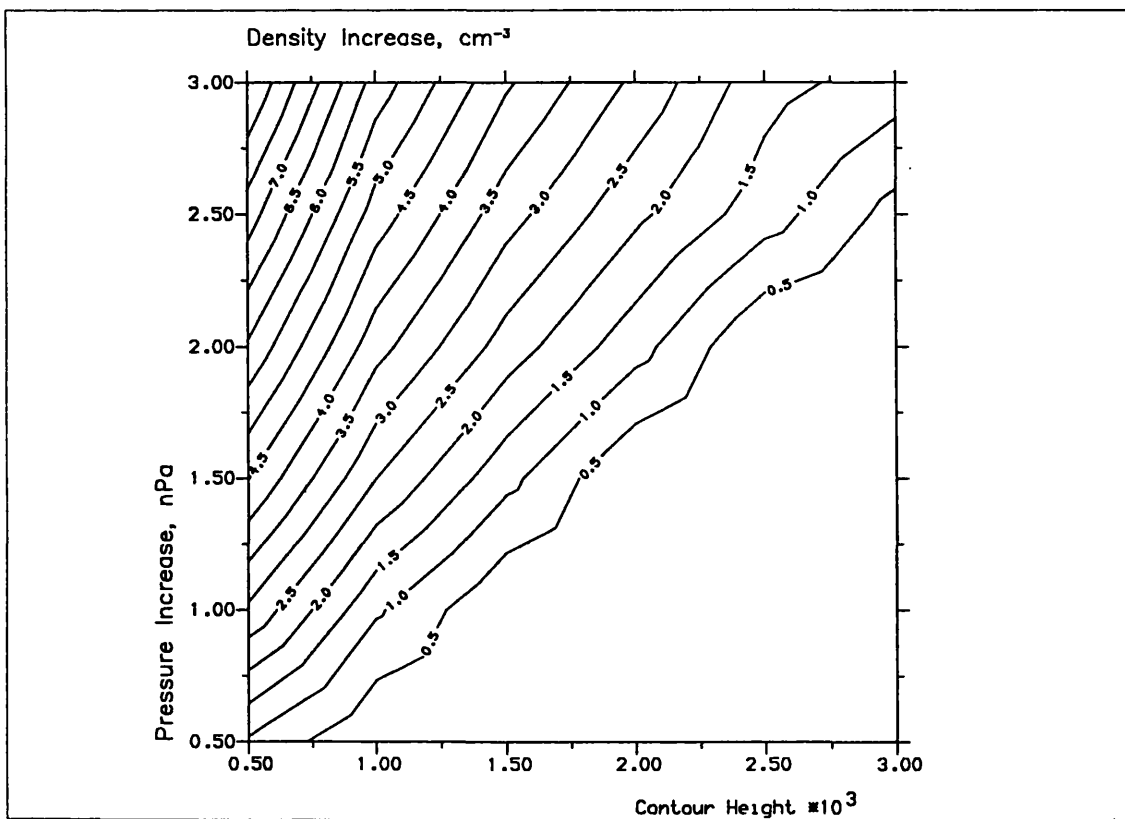


Figure 7.8 Equilibrium potential contours for substorms of various severity.

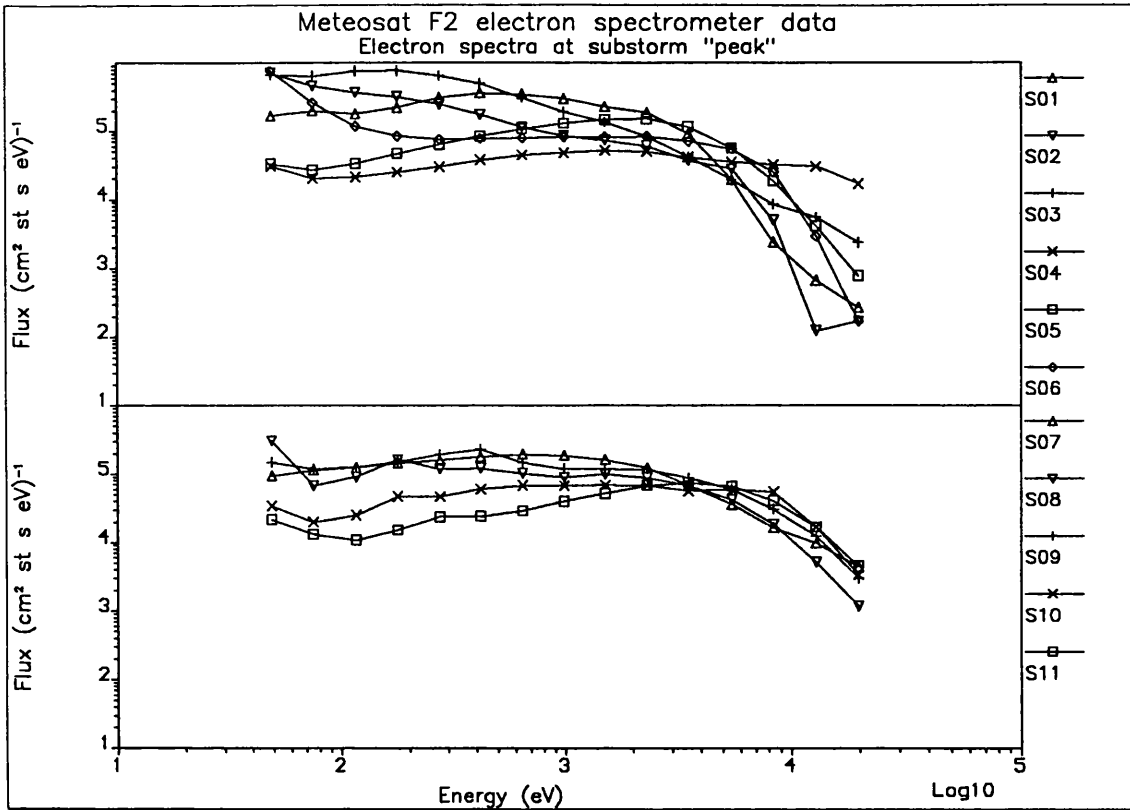


Figure 7.9

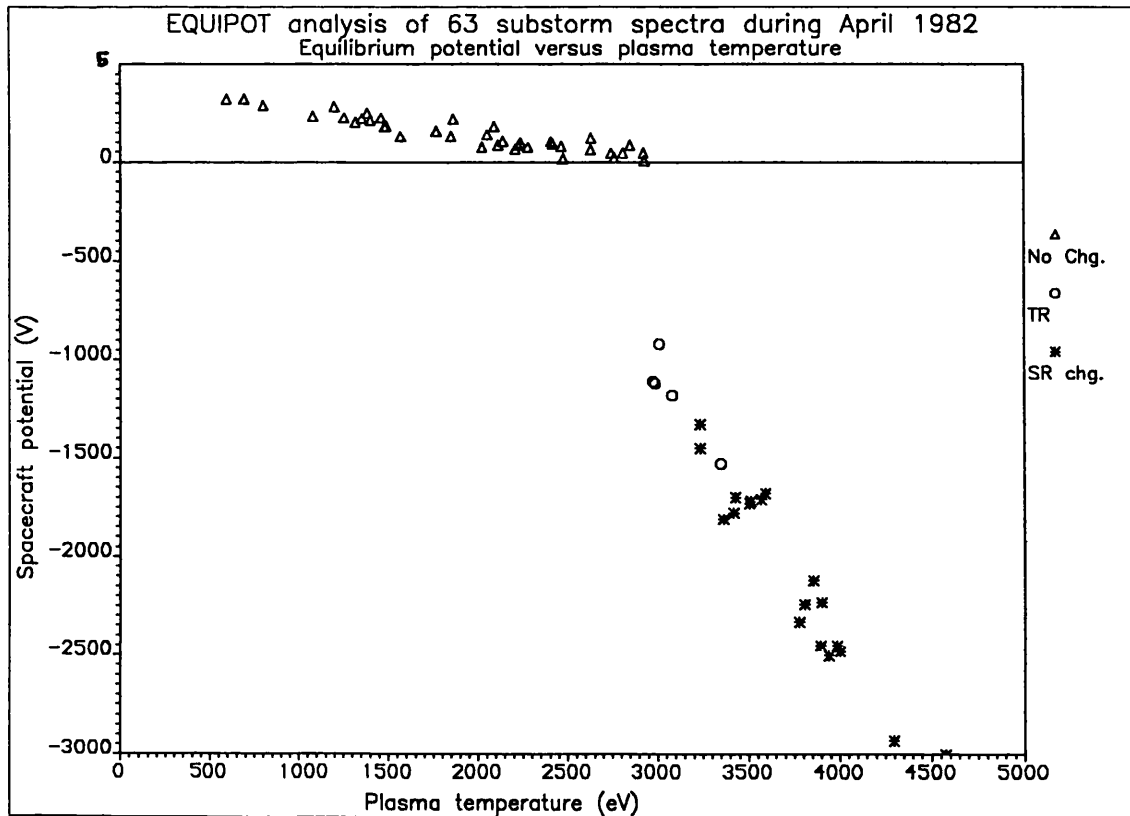


Figure 7.10

8. BARRIER CHARGING EVENTS ON METEOSAT F2

Anomalous operational events reported for both the Meteosat F1 and Meteosat F2 satellites occur at all local times, ie when the satellite is in sunlight, and are not confined to the short geostationary eclipse periods near the equinoxes. Although the highest recorded geostationary satellite potentials have been measured during eclipse (see Introduction), anomalies tend to occur when the satellite is sunlit, since large differential potentials are able to develop.

Two types of surface charging event were observed from Meteosat F2 electron spectrometer data by Johnstone et al¹²; Firstly, "eclipse events" occurred only during eclipse periods and were recognised by a very large current of electrons in one channel. As the event developed, the large electron current appeared in successively higher channels, reaching a maximum energy at about 640 eV. This large electron flux was much higher than the ambient plasma flux, and was attributed to secondary electrons being emitted from a surface more negative than the detector, and being focused into the detector by the local electric field configuration. The second type of event identified from the spectrometer data is the "barrier event". These occur when most of the satellite is sunlit, but some surfaces are shadowed, and can charge negatively. Eventually, the potential contours around the charged surface envelop all or part of the satellite and form a potential barrier. A statistical study of barrier event occurrence is presented, followed by a numerical simulation of one such event, using the NASCAP code.

8.1 STATISTICAL STUDY

The phenomenon of "barrier" charging occurs when a highly negative potential forms on a shaded surface element of a sunlit satellite and creates a system of negative potential contours which envelop all or part of the spacecraft. Thus, photoelectrons and secondary electrons emitted from the illuminated surfaces are not sufficiently energetic to cross this barrier and escape; the photoelectron term of the current balance equation is effectively zero which leads to overall negative charging. This effect has been predicted by Fahleson¹⁰⁶ and has been observed on ATS-6 by Whipple¹⁰⁷ by identifying (from spectrometer data) an electron distribution function which is consistent with photoelectrons emitted from the satellite surface. Where a barrier forms around an illuminated satellite, the situation is complicated by an accumulation of space charge (due to trapped photo- and secondary electrons) in the region between the satellite and the potential contour which represents the barrier. However, to a first approximation, the effects of this space charge may be neglected, since in an ambient plasma with a long Debye length, the volume of space enclosed by the "barrier" contour is generally much greater than the volume of the satellite itself.

Barrier events were first identified from the Meteosat F2 electron spectrometer data by Johnstone et al¹² by means of an enhancement in

electron flux in one or more of the first four energy channels (49 eV, 75 eV, 116 eV, 177 eV) to a level much greater than ever observed due to ambient plasma. This is attributed to photo- and secondary electrons emitted from the satellite surface which become trapped within the potential barrier. The maximum energy at which electrons originating from the satellite are observed is equal to the (absolute) height of the potential barrier minus the (absolute) potential of the detector, since secondary electrons emitted from surfaces at potentials more negative than the barrier are able to escape (ignoring space-charge effects). Figure 8.1 shows a typical example of a barrier event which started at 0300 (UT) on the 20th July 1982 and lasted for about 3 hours. A barrier event detection algorithm was devised based on the following criteria: the total count rate (see section 2.3) in channels 1, 2 and 3 should exceed 150,000 for a single record, and there should be at least two successive half-hour periods containing barrier records in order to constitute a barrier event. These criteria are based on visual inspection of the spectrometer data and their use will inevitably lead to some barrier events being missed, and to sequences of records which meet the criteria for barrier events, but which, on closer inspection are due to some other cause. As barrier events develop, the barrier height, and the potential of the detector and other spacecraft surfaces vary, such that at certain times, the energy of the maximum reflected secondary flux falls into the gap between detector energy channels (Table 2.3), before re-appearing at a later time in another channel. It is important for statistical studies that barrier events which persist for several hours are registered as one event, rather than several, separated by false disappearances of the barrier. This was incorporated into the auto-detection algorithm by recording the number of "barrier" records which fall into a half-hour period (18 records), and then defining the duration of the barrier event as the number of contiguous half-hour periods which contain barrier event signatures.

A total of 139 distinct events meeting these criteria were detected from the five-year data set (all records were analysed, except for those during eclipse). Visual inspection of each event revealed that 10 of these were due to magnetopause crossings near mid-day, where solar wind plasma fluxes are high in the lowest channels, and 49 were due to injections of plasma following substorms, where most of the injected flux appeared in the lowest four energy channels. The remaining 80 barrier events were used for four statistical studies; their distribution in local time, solar aspect angle, Kp value, and electron mean energy prior to the event. Figure 8.2 shows the distribution of barrier event start times (in hours UT) in which a peak during the midnight to dawn sector (plasmashet) is evident. Figure 8.3 shows the distribution of barrier events with solar aspect angle (at the equinoxes, solar aspect angle (SAA) is 90°) which demonstrates that barrier events tend to occur when the SAA is less than 78° , or greater than 104° , near the solstices with a marked preference for the summer solstice. There is also some evidence

for barrier events when the solar aspect angle lies close to 90° . Similar results have been published previously by Johnstone et al¹², but this analysis has been included because a different form of barrier event detection has been used. The dependence on solar aspect angle is perhaps the most interesting, since, as Johnstone et al point out, the solar aspect angles for which barrier events occur are those for which the primary radiometer mirror is shadowed from the sun during the entire satellite spin period. Figure 8.4 shows the distribution of barrier events as a function of Kp (Kp = 0 is at $x = 1$, and Kp = 9 is at $x = 28$) at the start of the event (top panel). The same data is presented in the lower panel as a scatter plot but has been normalised such that the y axis represents the average number of barrier events which have occurred per three-hourly Kp interval, during the five years of Meteosat data collection (April 1982 to March 1987). For example, a Kp value of 9 was recorded for 3 three-hour intervals during the five year period, and 2 barrier events started when Kp had this value. Once again, the Kp index has proved to be a good indicator of the probability of charging, but is inadequate for the purposes of predicting individual events.

Figure 8.5 is a scatter plot of the maximum electron mean energy achieved in the six hour period prior to each summer solstice barrier event versus the value of the a_p index at the start of each event. This plot shows that there exists a threshold plasma temperature, above which charging can occur. In addition, the figure shows some evidence that this threshold is reduced when a_p increases. The EQUIPOT analysis which investigated the effects of a threshold temperature for charging assumed that the electron and ion plasma populations were of equal density and temperature, and also showed that small changes in density had a negligible effect on the plasma threshold temperature. An explanation for charging threshold temperature reducing with increased a_p lies in the presence (or absence) of a cold ion component. Fluxes of cold ions tend to mitigate charging, and their presence causes the effective threshold plasma temperature to increase, i.e. the incident electron current must become more energetic to compensate for the enhanced cold ion current. When a_p is high, the cold ion population is swept out of the plasmashield region, and the charging threshold is reduced accordingly. There are two data points which appear in the lower part of Figure 8.5 and seem to violate the threshold temperature theory. However, both these events occur immediately after the satellite enters the plasmashield; it is therefore difficult to establish the plasmashield temperature prior to the charging event with certainty.

8.2 NASCAP SIMULATION

The electron spectrometer analysis results presented in section 8.1 showed that during barrier events; (a) the spectrometer was at a less negative potential than the barrier height, and (b) that some surfaces were a maximum of 177 eV (channel 4) more negative than the spectrometer, but still less negative than the barrier potential. However, it is

difficult to establish the absolute detector potential during events and impossible to measure the absolute potential of the most negative surface (ie the radiometer primary mirror). Some attempt could be made to measure the absolute detector potential by application of Liouville's theorem (equation 3.3) to the spectral energy shift before and after charging, but the results are confused by the presence of accelerated secondary electrons trapped within the potential barrier.

Since the process of barrier formation is a truly three dimensional effect, NASCAP has proved to be a necessary tool for modelling the configuration of potential contours around the satellite, at least qualitatively. In particular, NASCAP is able to demonstrate the relationship between barrier height and primary mirror potential, and also to show how the satellite structure potential develops after the potential barrier has formed. Figures 8.6 to 8.8 show three views of the NASCAP model of Meteosat. The model is necessarily a rather crude representation of the satellite for several reasons; Firstly, all NASCAP objects must be defined in a 17x17x33 grid, and the maximum number of surface cells per object is limited to 1250. Secondly, it was intended to model the overall global shape and surface material composition of the satellite without including any fine details of the surfaces. Such an approach is rather dangerous in some senses, since it is often the detailed surface features which give rise to charging, but in this case, NASCAP is not being used to identify a region where negative charging occurs (a task already attempted by Frezet et al¹⁸) but to assess the effect of charging a surface which has already been identified from spectrometer data. Each grid square has a side of 15cm, and Meteosat is represented by three octagonal cylinders whose axes lie along the Z axis. The main body is covered in solar cells except for a narrow Teflon equipment bellyband, and a cavity of about 1m diameter and slightly more than 1m deep with the radiometer primary mirror at the rear (see Chapter 2). The surfaces of the cavity are assumed to be covered in conducting black paint, and the mirror itself is constructed of Zerodur and silvered on the front surface. The mirror is electrically isolated from the satellite structure, and for simplicity, the secondary and first 45° folding mirror are not modelled. The base of the satellite is assumed to be aluminium and the top to be Teflon, representing thermal blanket and second surface mirror materials. Most of the EDA assembly is assumed to be covered in black paint. Solar illumination was modelled using the "SPIN" module which computes average solar illumination for several sun angles during one spin phase (at 100 rpm, the satellite spin period is much less than any charging time constant). The season was taken as northern hemisphere summer solstice so that the primary mirror was shadowed from the sun throughout one entire satellite rotation.

Perhaps the most serious limitation imposed by NASCAP for a simulation of this sort is its implicit use of spherical probe theory for collection of plasma particles by charged surfaces. This is quite clearly inadequate for surfaces within the cavity, especially those behind the

radiometer mirror. A further approximation is introduced in the way that NASCAP handles barrier formation; where the electric field near a surface cell is inverted (ie secondary electrons are not able to escape to infinity) NASCAP applies a "limiting factor". This represents the fraction of secondary electrons able to escape and is calculated according to the cell potential, barrier height and secondary or photoelectron temperature. The current of secondaries is then reduced to the limiting factor multiplied by the secondary electron current in the absence of any barrier. No account is therefore taken of the space charge effect of trapped secondary electrons.

Before discussing the results of the full three dimensional NASCAP simulation, it is useful to study the idealised case of a small number of surface cells, together with an electron detector subjected to a limiting potential barrier (Figure 8.9a). Assume that the detector cell is grounded to the satellite structure which remains fixed at -200V and that the detector cell and other two floating cells (initially at -200V) are enclosed within a potential contour of -500V. The system will tend to evolve towards equilibrium such that a current balance is maintained for each of the two floating cells whilst any net current into the detector cell is assumed to have negligible effect on the structure potential. Figure 8.9b shows how the potential varies along a line AB (see Figure 8.9a) and illustrates the potential barrier. True secondary and photoelectrons are emitted isotropically with a temperature of a few eV relative to the surface, so are unable to escape from the surface (cell 1), or become trapped in the potential well and do not contribute to the current balance equation of which only the terms for incident particles and backscattered electrons are significant. The potential of cells 1 and 2 will be driven more negative in an attempt to reduce the incident electron current, and in most practical situations, current balance will only be achieved when the cell potential comes to within a few volts of the barrier height such that a fraction of secondaries are able to cross the potential barrier. However, even at equilibrium, secondaries with lower energy are just unable to escape and remain trapped in the barrier, or are collected by the detector element with an apparent energy of about 300 eV. In fact, during the approach to equilibrium, the detector will collect a large flux of secondaries all with an energy close to the potential difference between the cells and the detector. In the three-dimensional case the situation is more complicated since the detector may collect trapped secondaries from cells at different potentials; but good evidence is provided for the mechanism above since the barrier event signature disappears from time to time during an event which is consistent with the potential difference between the emitting cells and the detector falling into one of the detector energy gaps.

In an attempt to simulate charging behaviour during a barrier event, a relatively severe charging environment was chosen with solar illumination conditions applicable to northern hemisphere summer solstice

such that the radiometer mirror assembly is shadowed throughout one satellite spin. The environment chosen was a "double" Maxwellian, modified SCATHA "worst-case" environment used for the EQUIPOT material properties sensitivity study (Table 7.2). Figure 8.10 shows an equipotential contour plot in the Y=3 plane after 1 NASCAP cycle (210 seconds). The radiometer mirror has already reached a potential of -450V whilst most of the sunlit surfaces of the satellite are at a small, positive potential (eg the aluminium South end of the satellite is at +1.4V). It is not meaningful to show a contour plot for a plane which includes the radiometer mirror since the contouring algorithm is swamped by the magnitude of the mirror voltage relative to the other surfaces; instead the plot in Figure 8.10 is taken in a plane offset from the mirror. This shows the large potential well outside the satellite which is due to the negatively charged mirror in addition to the positive potential contours around the sunlit satellite body. Figure 8.11 shows the potential contours in the Z=15 plane, also after 1 cycle. The picture is dominated by the negative potential well that has formed outside the mirror cavity, but the contour surrounding the satellite is at a small positive voltage. Taken together, Figures 8.10 and 8.11 show that the negative potential well around the radiometer mirror emerges from the mirror cavity and "mushrooms" out into the space around the satellite. At this stage, however, the potential barrier has not yet formed around the whole satellite, although some of the surface cells adjacent to the mirror cavity experience an inverted electric field leading to the suppression of secondary and photoelectron emission.

By the time the system has come close to equilibrium, the potential contour configuration has changed significantly. Figure 8.12 shows the equilibrium contours after 21 cycles (1700 seconds) in the Y=2 plane. The radiometer mirror has now achieved a potential of -12 kV and the contours in this plane have a height of several hundred volts negative, as opposed to magnitudes of several volts for the same plane after 1 cycle. A potential barrier, controlled by the radiometer mirror has now formed around the whole satellite with the "closing" contour having a height of about -390V. The aluminium South end of the satellite, and parts of the EDA assembly at the North end have achieved a potential of -890V whilst some parts of the solar array, near the bellyband and on the -Y face (opposite to the cavity) have developed potentials as small as -380V. Figure 8.13 shows the equilibrium potential contours after 21 cycles for the Z=15 plane. This demonstrates clearly that it is the radiometer mirror which is controlling barrier height and shape and also that the surface cells close to the radiometer cavity achieve the most negative potential; this is consistent with the idea that local insulating cells reach an equilibrium potential close to that of the adjacent barrier contour height. Figure 8.14 shows the potentials which have developed on solar cells in the plane Z=11, immediately below the equipment bellyband. The potentials become more negative close to the cavity entrance due to the potential barrier, whilst NASCAP predicts the structure potential to

be -389V. The electron spectrometer aperture is situated at about 60 degrees from the centre of the radiometer cavity, measuring clockwise in the x-y plane and since it is grounded to the satellite structure, it will detect secondary electrons from adjacent surface cells which have become trapped in the potential barrier. Thus, according to this simulation, SSJ/3 will observe electrons from solar cells closer to the cavity at energies near to 59 eV, 93 eV, 150 eV and 317 eV, considering only the Z=11 plane. Of course, these energies assume that the primary mirror has reached -12 kV and will therefore scale for different mirror potentials, but these predicted energies are very close to those observed experimentally.

This simulation has proved that when the radiometer mirror is continuously shadowed and the satellite is subjected to a "severe" environment, very large potentials, exceeding -10kV develop on the mirror and cause the formation of a system of potential contours which creates potential barriers, preventing secondary and photoelectrons escaping from surface cells. Insulating, illuminated solar cells near to the radiometer cavity charge to potentials in the range of -381V to -706V given a potential of -12kV on the radiometer mirror. These results are consistent with several pieces of experimental evidence; (a) NASCAP predicts the satellite structure potential to be -389V, thus, as the potential barrier develops, the detector will collect secondaries trapped by the barrier with energies in the range 59 eV to 317 eV which is close to the observed values; (b) The high flux of trapped, accelerated secondaries periodically disappears from the spectrograms, consistent with the view that the potential difference between "source" cells and detector falls into a detector energy blind spot; (c) Laboratory testing (Chapter 2) showed that several kilovolts could be applied directly to the radiometer mirror assembly without discharges being observed; the NASCAP analysis shows that potentials of this magnitude are necessary to support barrier potentials of the observed magnitude.

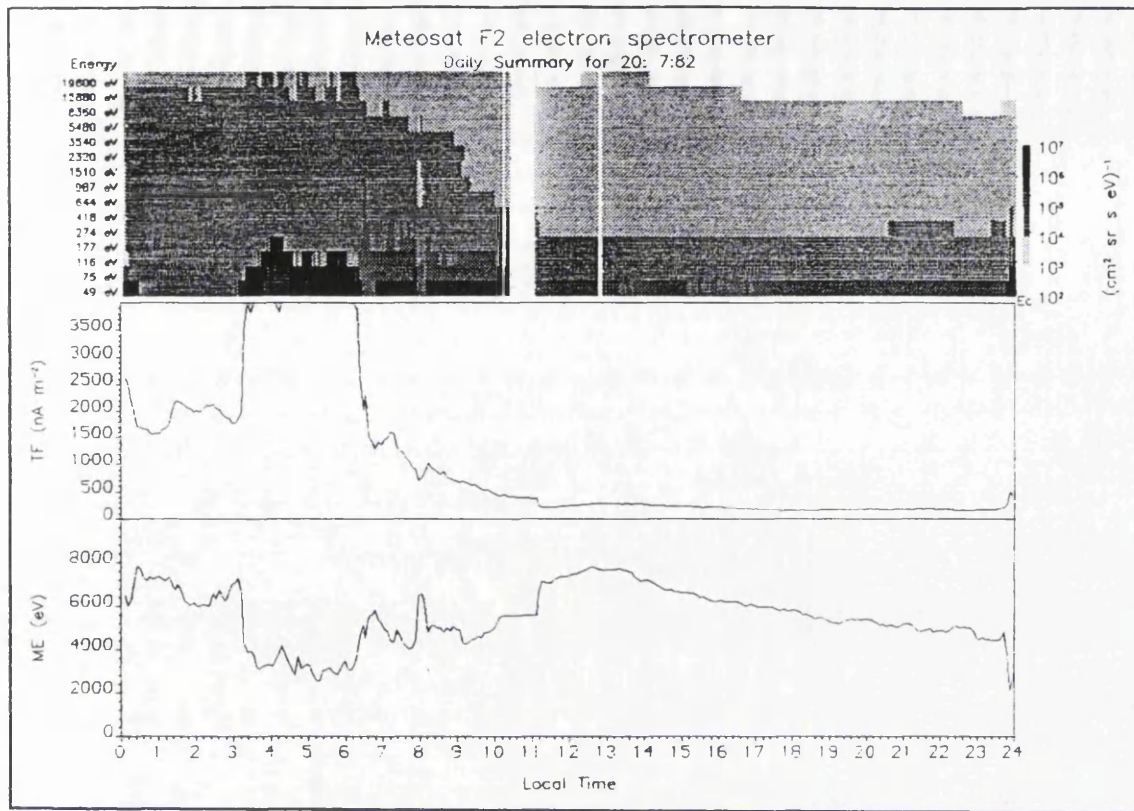


Figure 8.1

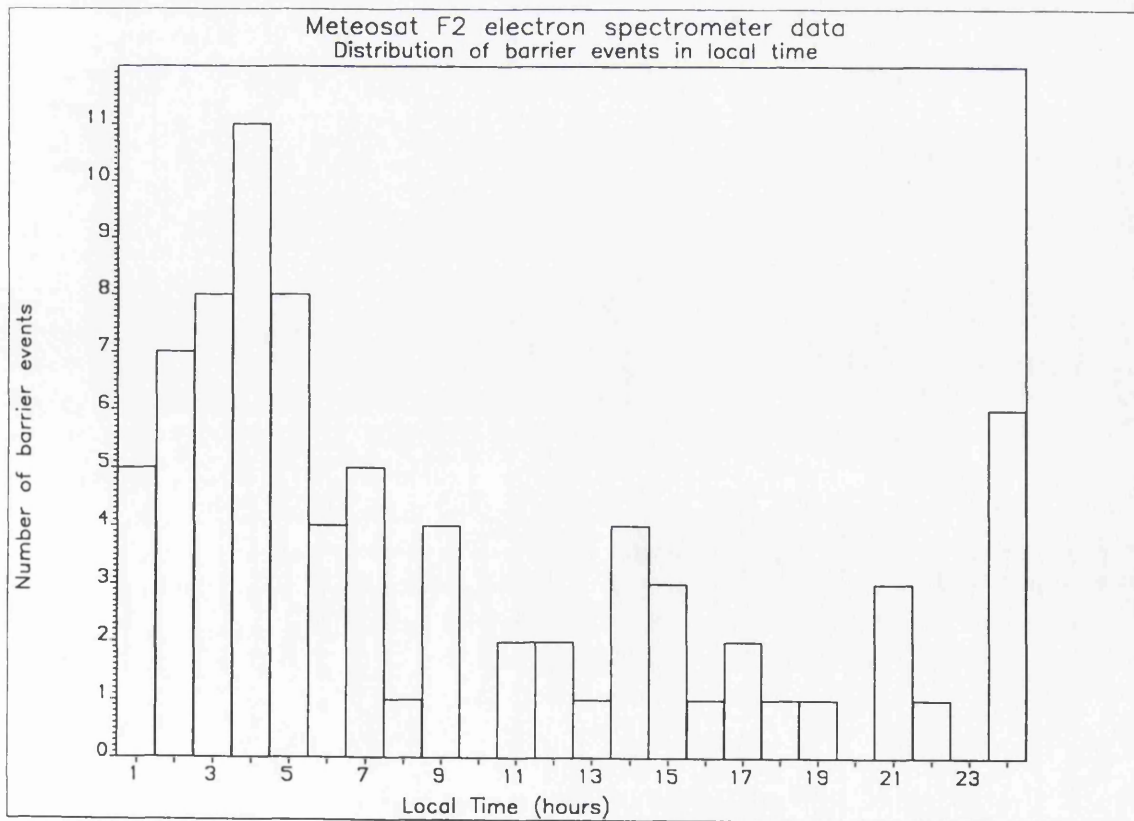


Figure 8.2

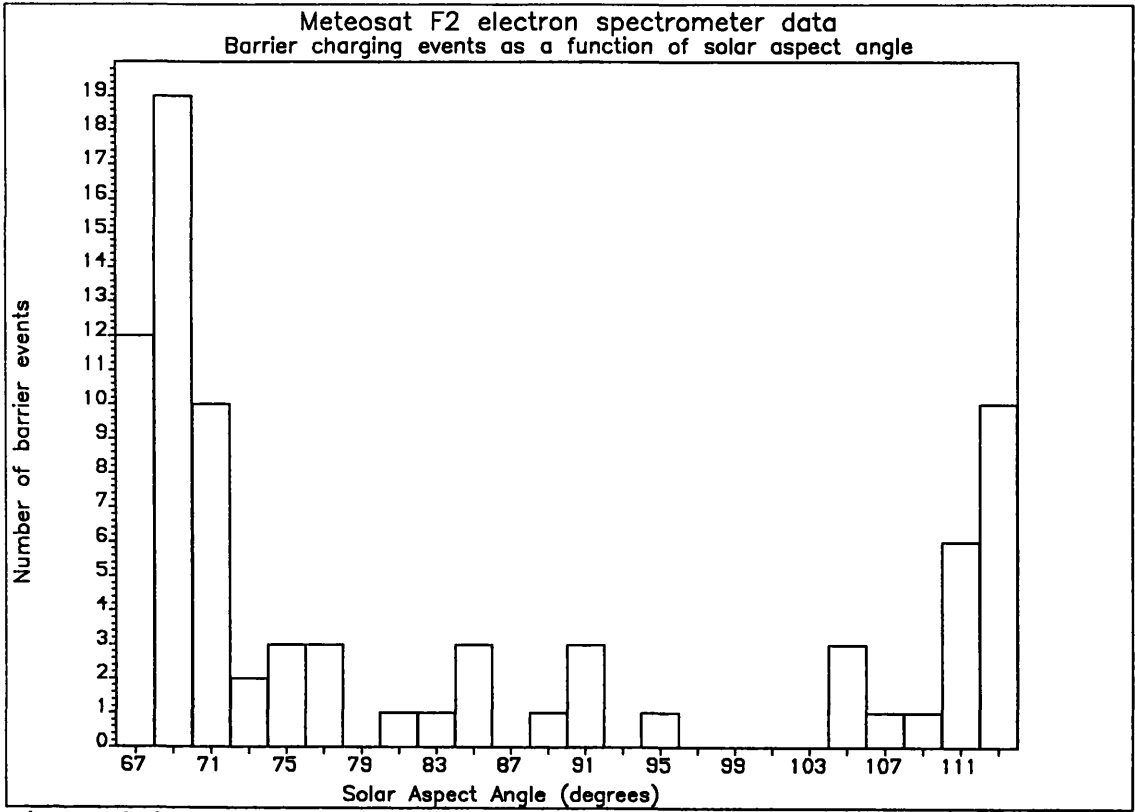


Figure 8.3

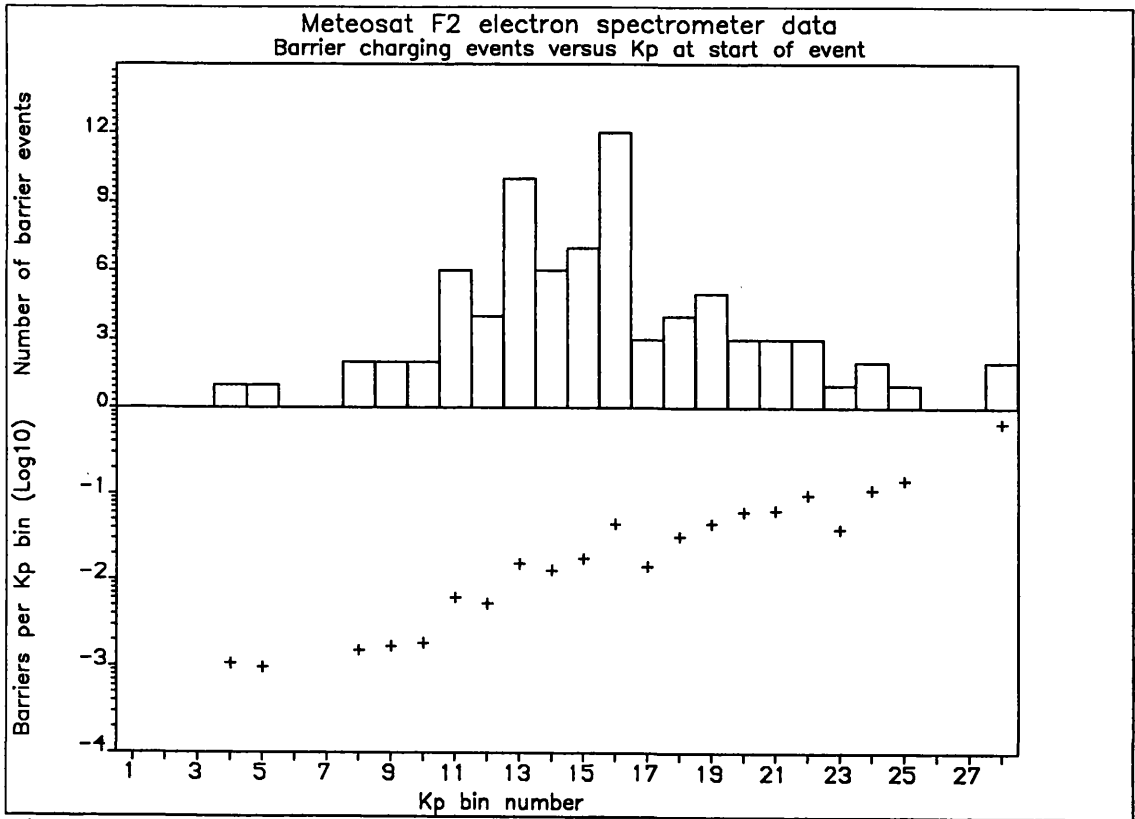


Figure 8.4

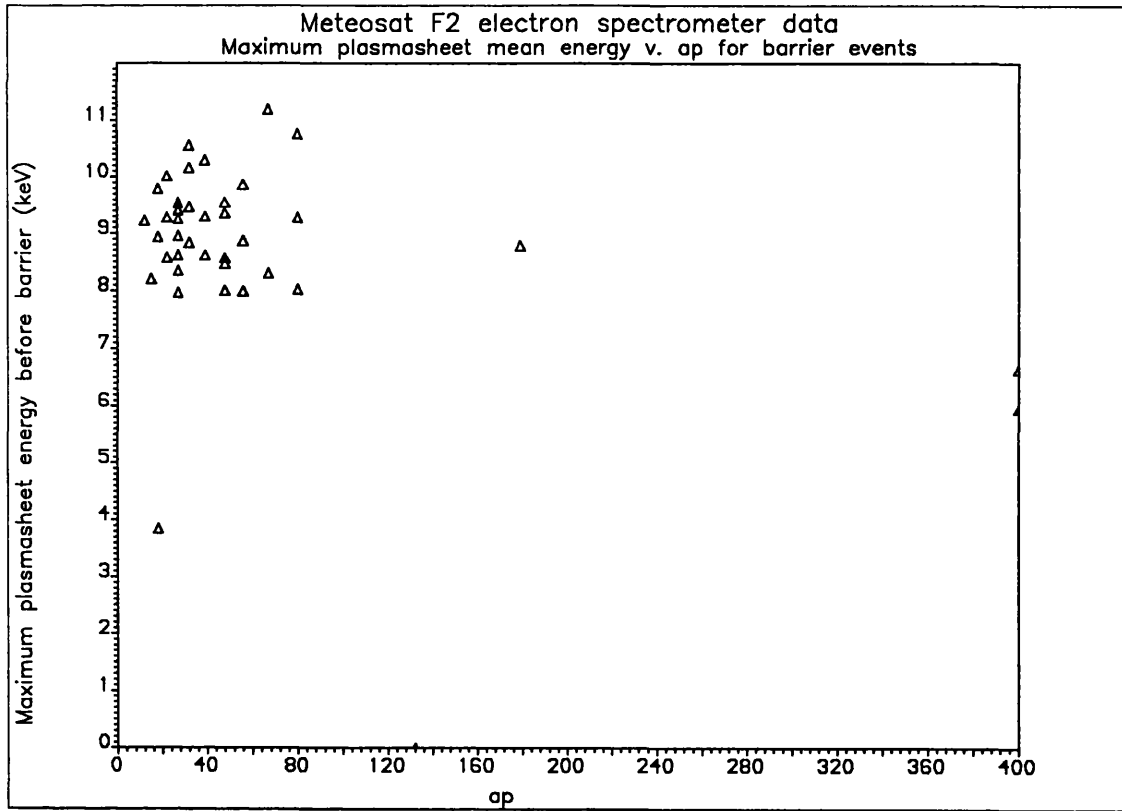
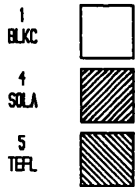


Figure 8.5

MATERIAL LEGEND



SURFACE CELL MATERIAL COMPOSITION AS VIEWED FROM THE POSITIVE Y DIRECTION
FOR Y VALUES BETWEEN 1 AND 17

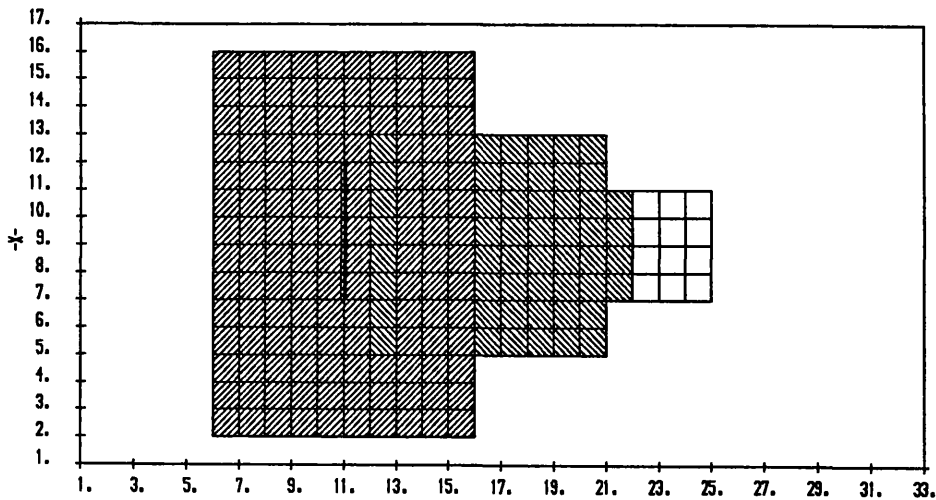
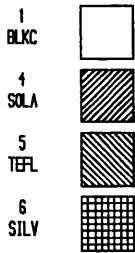


Figure 8.6 ^{-z-} NASCAP model of Meteosat F2 (+Y view)

MATERIAL LEGEND



SURFACE CELL MATERIAL COMPOSITION AS VIEWED FROM THE POSITIVE X DIRECTION
FOR X VALUES BETWEEN 1 AND 17

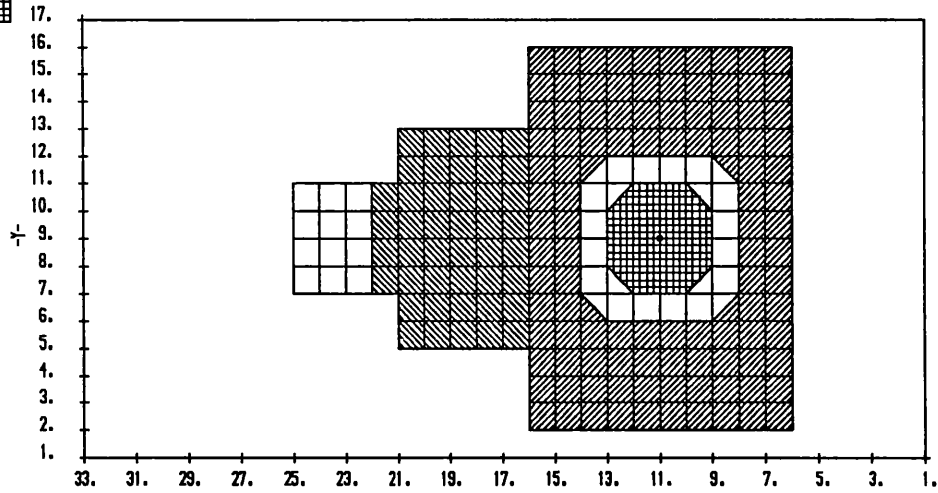
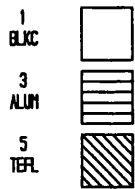


Figure 8.7 NASCAP model of Meteosat F2 (+X view)

MATERIAL LEGEND



SURFACE CELL MATERIAL COMPOSITION AS VIEWED FROM THE POSITIVE Z DIRECTION
FOR Z VALUES BETWEEN 1 AND 33

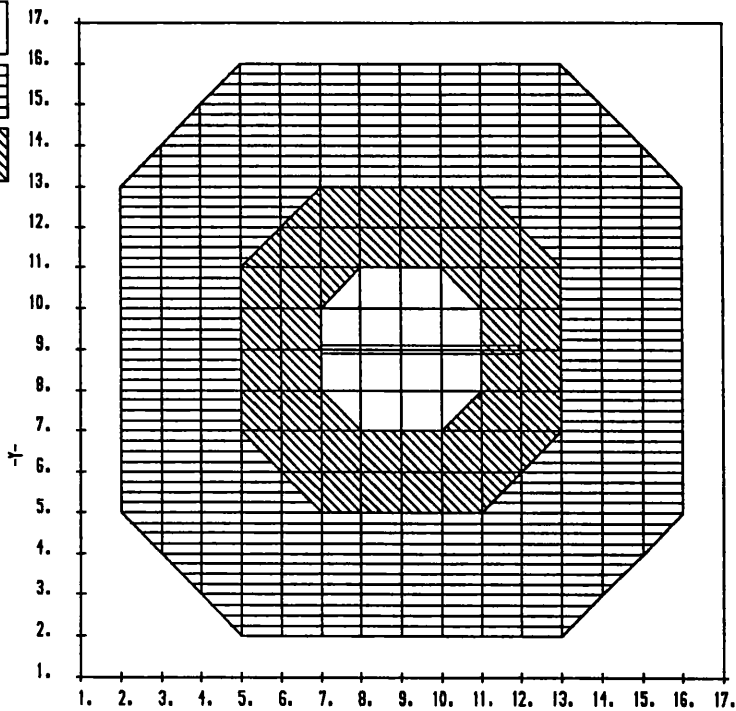


Figure 8.8 NASCAP model of Meteosat F2 (+Z view)

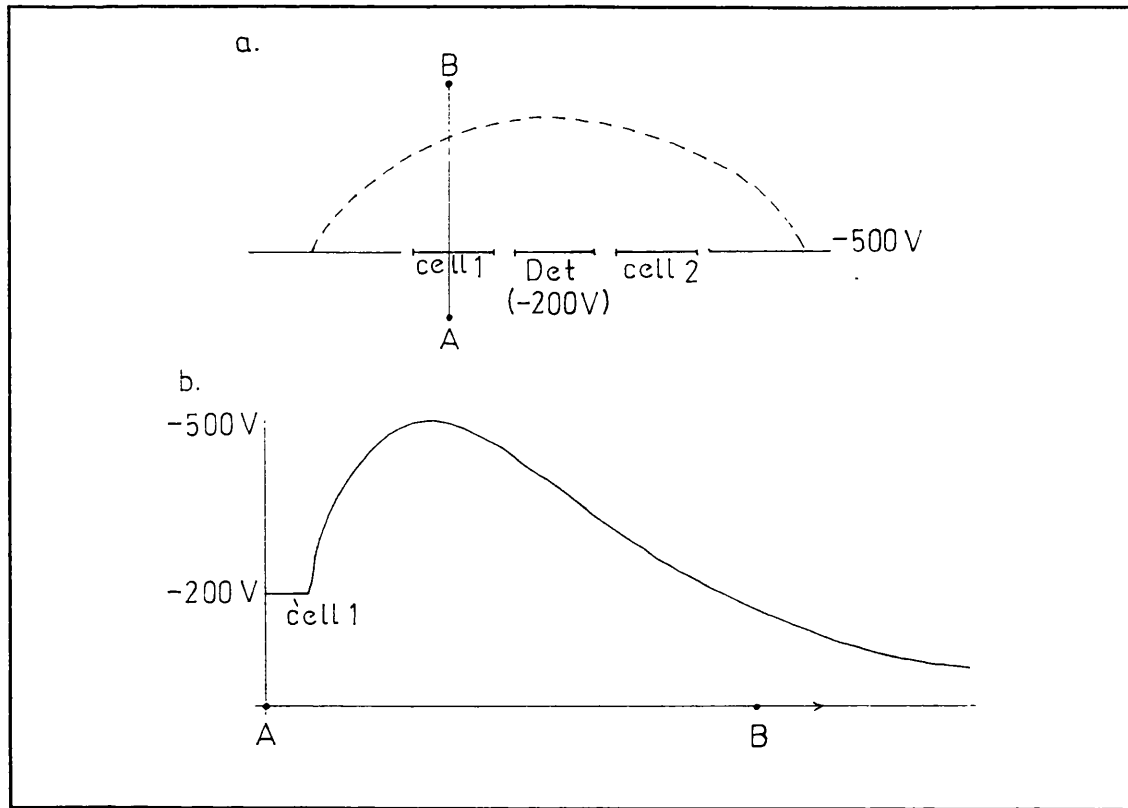


Figure 8.9 Barrier charging process

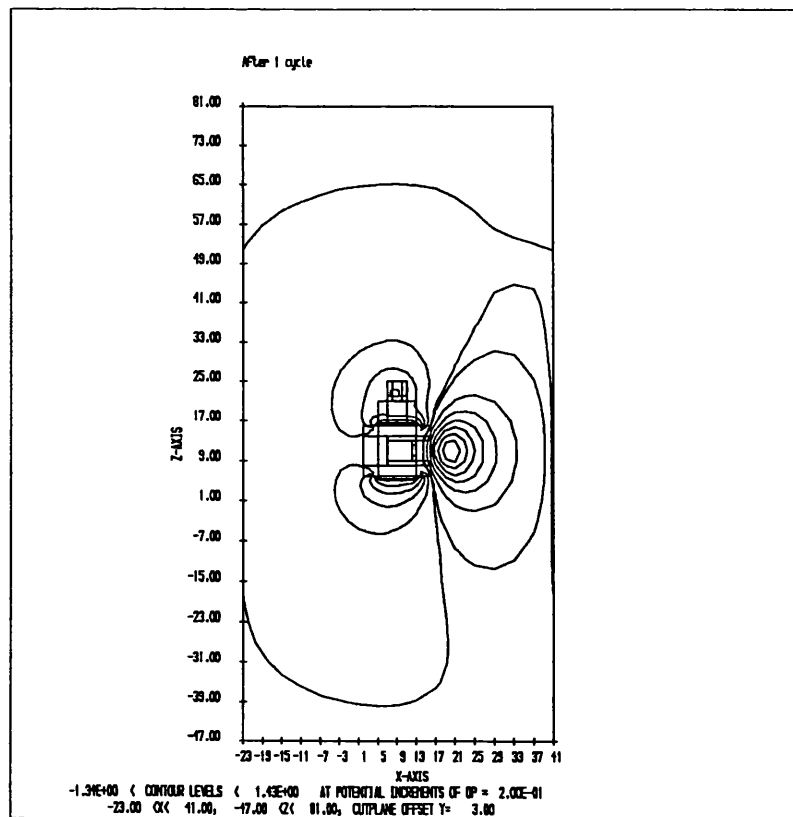


Figure 8.10 NASCAP contour plot, Y=3 plane after 1 cycle

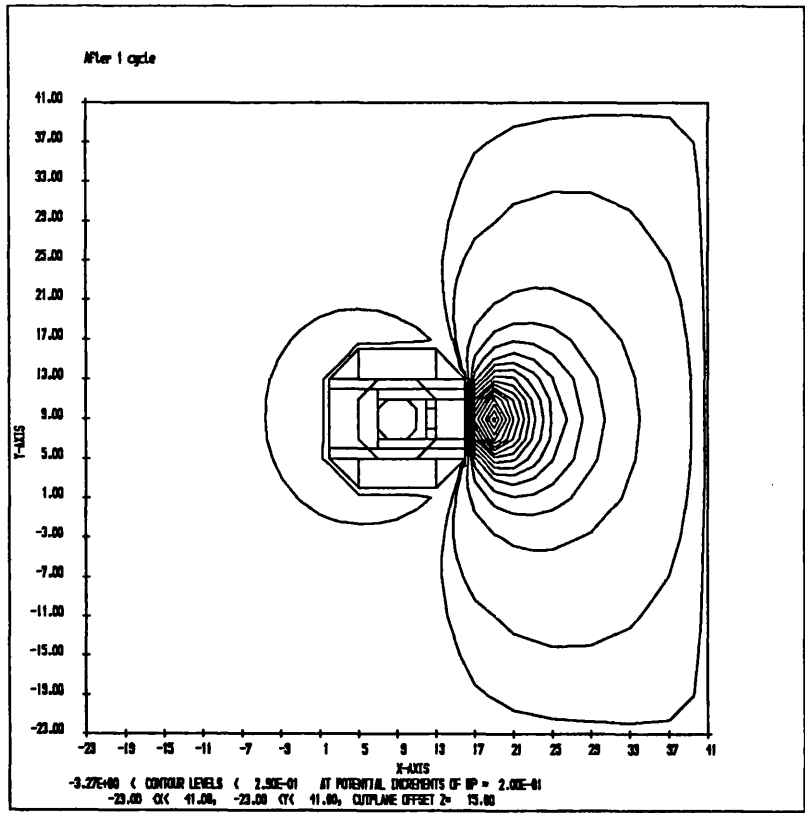


Figure 8.11 NASCAP contour plot, Z=15 plane after 1 cycle

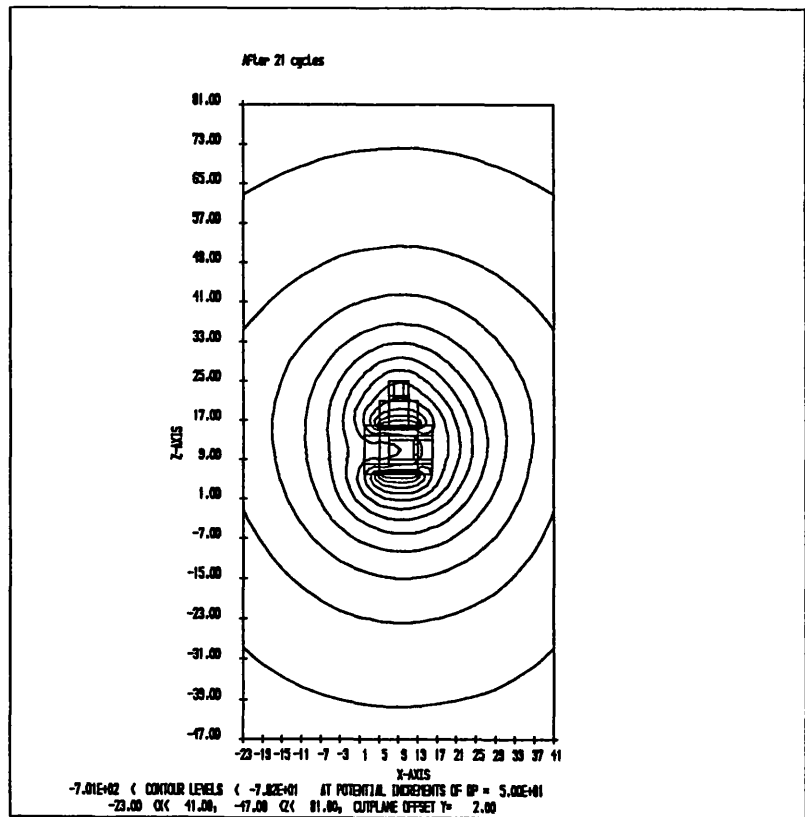


Figure 8.12 NASCAP contour plot, Y=2 plane after 21 cycles

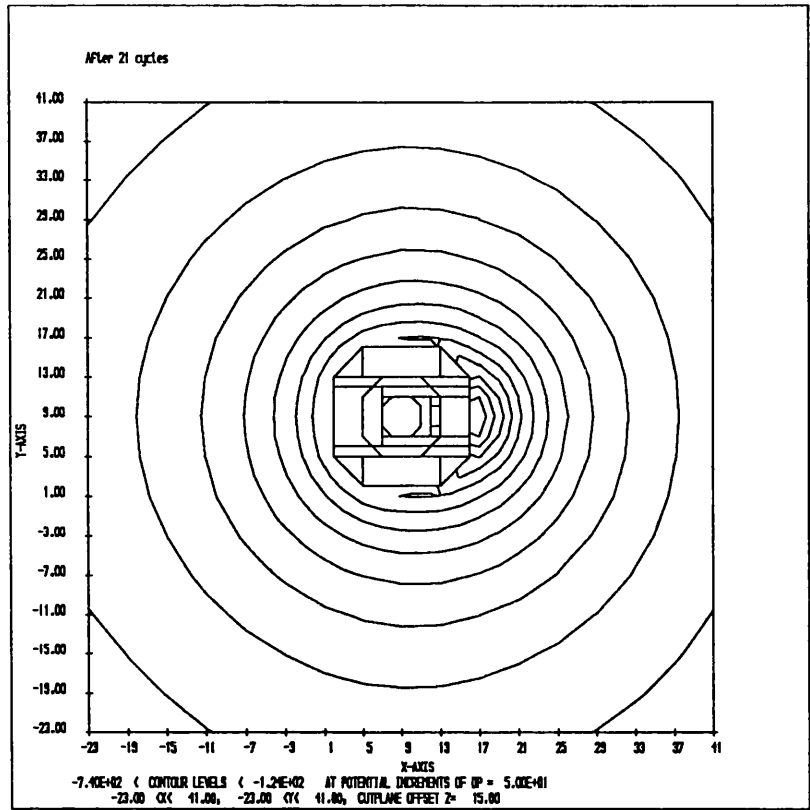


Figure 8.13 NASCAP contour plot, Z=15 plane after 21 cycles

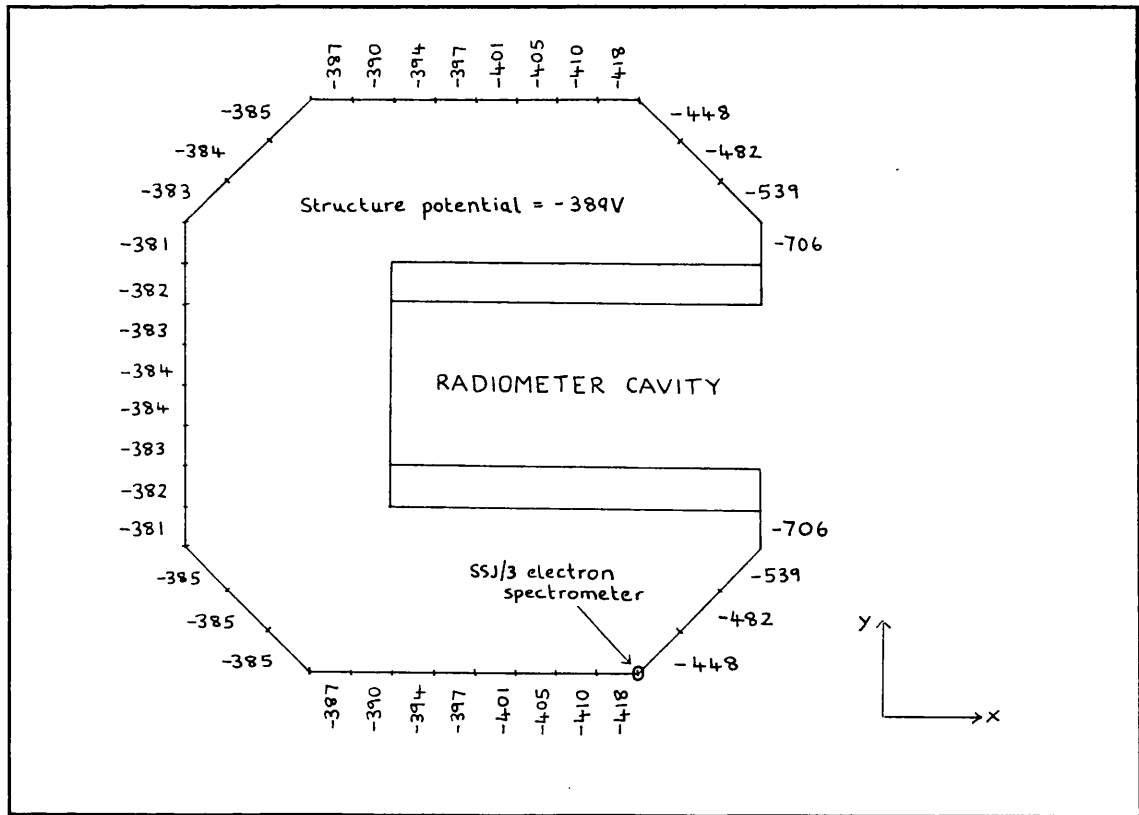


Figure 8.14 Solar cell potentials predicted by NASCAP

9. CONCLUSIONS

Nine main conclusions are presented, based on the results of Chapters 5, 6, 7 and 8.

1. The Meteosat F2 electron spectrometer data set has been used to identify three plasma regimes encountered in geosynchronous orbit; the plasmasphere, the plasmashet and the inner edge of the plasmashet (or "transition region"). The position of boundaries between these regions has been determined as a function of local time, and of the planetary geomagnetic activity index, K_p . Except during very high levels of geomagnetic activity, the plasmasphere (denoted by an absence of energetic electrons) is encountered once per orbit. Conditions associated with the transition region (or plasmashet inner edge) are encountered much more frequently at dusk (plasmashet entry) than at dawn. The probability of being within a given plasma regime as a function of local time and K_p has been determined in order to assess the likelihood of severe charging conditions prevailing at any given time.

2. Geomagnetic storm and substorm onsets have been detected from the Meteosat F2 electron spectrometer data set by means of a simple signature; a sharp increase in total flux. The most significant of these events have been shown to correspond to storm sudden commencement (SSCs) reported by terrestrial magnetometers. The distribution of onsets in local time has been measured, and is found to peak close to local midnight, and to extend further towards dawn than dusk, due to the eastward drift of electrons. A statistically significant relationship has been established between the magnitude of the substorm onset and the value of the a_p index at the time of onset and also with the maximum negative value of the Dst index during the same 36 hour period. A new index, $a_p(\tau)$ which takes into account the time history of geomagnetic activity was found to give maximum correlation with substorm onset magnitude for a persistence time of zero hours. The most interesting aspect of these results is that although there is a clear link between substorm onset magnitudes (proportional to flux of injected plasma) and geomagnetic indices, it is far from being a one-to-one relationship and that geomagnetic indices are unsuitable for the purposes of forecasting substorm activity and hence severe spacecraft charging conditions.

A clear correlation has been established between the number of observed substorm onsets per month and the reported number of grouped solar flares during the same period. This result helps to determine the probability of severe charging conditions as a function of phase within the solar cycle, and also introduces the possibility of severe condition forecasting based on optical flare observation.

3. The plasma injected during each of the 2333 observed substorm onsets has been characterised in terms of the measured increase in particle density and energy density. These parameters have been computed from differential electron flux spectra based on the observation that the injected plasma has an approximately Maxwellian velocity distribution.

The results have been presented as histograms which give the probability of a certain magnitude of pressure or energy enhancement for a substorm onset. For the purposes of spacecraft design, it is now possible to estimate the number of substorms of a given severity which will occur during a mission, or part mission.

4. Surface conductivity and field-enhanced bulk conductivity have been shown to be important components of the current balance equation under certain circumstances. During laboratory electron beam materials characterisation, an isolated, conducting sample tended to behave in a conduction-limited fashion, rather than the emission-limited fashion predicted on the basis of published bulk and surface conductivities for the insulating polymer. For a Teflon layer, the increased conductivity is attributed to the presence of surface contaminants which appear to increase the surface conductivity by as much as two orders of magnitude above the published value. For a thin Kapton layer, surface conductivity is also important, but the electric field enhancement to bulk conductivity accounts for most of the increased conduction current. Where the total conductivity (bulk plus surface) may be specified, and remains constant with sample potential (for a thick insulator), both one and three dimensional simulation codes give good agreement for sample potentials versus beam energy, and for charge time history development. Much poorer agreement is obtained where field enhanced conductivity is important.

5. The EQUIPOT code was used to assess the effect of making small changes in the conduction current term of the current balance equation. The most important result to emerge was that for thin dielectric films, if the conduction current model includes the effect of field enhanced conductivity, then the results are very different from those obtained assuming pure Ohmic conduction. This is consistent with the experimental results of Chapter 6, where field enhancement effects dominate.

6. A new model for secondary emission of electrons due to electron impact was introduced and incorporated into the EQUIPOT simulation code. The secondary emission yield curve is described in terms of three parameters; the maximum yield and energy at maximum yield for normal incidence, and the energy loss power, which is assumed to be constant for a given material. A sensitivity analysis using these parameters revealed that the equilibrium potential is highly sensitive to small changes in n , the energy loss power. Furthermore, if all other material definition parameters remain constant, it is the value of n which is most critical in determining the plasma temperature above which negative charging occurs. The equilibrium potential was shown to be most sensitive to changes in energy loss power when this quantity just exceeded the threshold charging value for a given plasma temperature.

7. The EQUIPOT code was used to verify that, for a Maxwellian plasma, there exists a threshold plasma temperature, above which negative charging occurs. EQUIPOT was used to determine the locus in (n, T) space, where n is the energy loss power for a given material, which (for all

other material parameters being constant) represents the negative charging threshold boundary. Furthermore, for measured non-Maxwellian electron spectra (taken from the Meteosat F2 data set), EQUIPOT was used to demonstrate that the mean spectral energy (equal to twice the plasma temperature) could be used in place of a Maxwellian temperature to determine a charging threshold. However, for a given material, where the plasma mean energy only just exceeds twice the threshold temperature, a "triple-root" current-voltage relationship tended to develop, which is not observed with single Maxwellian environments.

8. A statistical survey of Meteosat F2 barrier events on a "per-event" basis reaffirms earlier results that events tend to occur in the midnight to dawn sector of local time (plasma sheet conditions), become increasingly likely when K_p is high and are observed only when the radiometer primary mirror is shadowed throughout the whole satellite rotation. Further analysis reveals a clear electron energy threshold, below which barrier events are not triggered which is consistent with EQUIPOT results of Chapter 7. In addition, there is evidence that this threshold electron temperature reduces as a_p increases which can be attributed to the increasingly efficient removal of cold ions at higher activity levels.

9. A three-dimensional charging analysis of Meteosat F2 using the NASCAP code has successfully simulated a "barrier event". A severe plasma environment caused the shadowed primary mirror to charge to about -12 kV creating a potential barrier around the whole spacecraft which leads to absolute and differential potentials of the order of several hundred volts to develop on the solar array surfaces. The predicted potential contour configuration around the electron spectrometer location will cause trapped secondary and photo-electrons to be accelerated and detected by the spectrometer with energies in good agreement with those observed experimentally.

Inevitably, this work leads to further questions concerning future areas of research. There are two immediate areas of work which would add greatly to the value of the results presented here. Firstly, it would be interesting to consider ion data as well as electron data for the identification of plasma regimes, substorm studies and EQUIPOT charging threshold calculations. Suitable ion data sets for comparison include the ion spectrometer on ATS-5¹⁰⁸ and the SC9 ion detector on P78-2 (SCATHA)¹⁰⁹ in addition to measurements of cold ions by the GEOS spacecraft⁹¹. The CRRES¹¹⁰ satellite, launched in July 1990 spends a large fraction of its time at near-GEO altitudes and will generate a large database of plasma measurements in the tens of eV to tens of keV range. However, these measurements were not made simultaneously and the effects of solar cycle variation may well prevent serious comparison with the Meteosat F2 electron data set.

Secondly, there is much scope for improved measurements of secondary electron emission for materials using the electron beam facility described in Chapter 6. Recent studies using a different facility⁹⁹ have

proved that good isolation of the target sample may be achieved such that results are emission limited. Further study into the effect of sample surface preparation is necessary along with the adoption of a new technique due to von Seggern¹¹ for measuring the SEE yield of dielectric materials.

Acknowledgements

I would like to thank my employers (Space Department, Royal Aerospace Establishment, Farnborough) for the opportunity to carry out this research as part of my normal duties. Special thanks to my supervisor at RAE, Dr. Gordon Wrenn for his guidance and interest over the last five years, and to my supervisor at Mullard Space Science Laboratory, UCL, Dr. Alan Johnstone for his suggestions on the direction of research, and for providing the Meteosat electron spectrometer data. The electron beam tests would not have been possible without the enthusiastic support of Mike Duck of Chemistry Division, Harwell Laboratory. Data processing, analysis and simulation were carried out on a PRIME 2655 mini computer which has proved to be ever-reliable thanks to the Space Computing Service, RAE. Last but not least, thanks to Helen for her patience and encouragement throughout.

Appendix A

```

REAL FUNCTION DELTA(EEV, DELMAX, EMAX, N, ITYPE)
C
C 20.02.91 AJS
C Computes the true secondary electron yield due to incident
C electrons of energy EEV (in eV) given material definition
C parameters DELMAX (max yield), EMAX (energy at maximum yield
C in keV) and n, the stopping power coefficient where
C  $dE/dx = A/E^{n-1}$ , and  $n > 1$ .
C ITYPE < 0 : Normal incidence
C ITYPE > 0 : Isotropic incidence
C
C Declarations..
INTRINSIC EXP,      /* F77 functions
+      ABS

REAL EEV,          /* incident electron energy (eV)
+      EK,          /* incident energy in keV
+      X,           /* x = alpha*range
+      XMAX,        /* max value of x for this n
+      C,           /* C = 1 - 1/N
+      F,F1,        /* functions in Newton-Raphson
+      ERR,         /* Newton-Raphson error
+      Y            /* internal yield var.

INTEGER I,         /* loop counter
+      MAXITR,      /* max no. of iterations
+      ITYPE        /* normal/isotropic flag

REAL DELMAX,       /* maximum yield
+      EMAX,        /* energy at max yield (keV)
+      N            /* stopping power power

C Check input value of n..
IF (N .LT. 1.001) THEN
  WRITE(1,*) ' n < 1.001 , SEE yield set to zero '
  DELTA = 0.0
  RETURN
END IF

C Get value of XMAX for this n..
C n.b. Strictly only need to re-evaluate XMAX
C whenever n is changed, but the simple
C Newton_raphson method requires negligible
C computation time, so it is most convenient
C to re-do it each time the function is called.
C = 1.0 - 1.0/N      /* compute constant
X = 2.0             /* best guess for x (n = 1.456)
MAXITR = 100        /* max no. of iterations allowed
I = 0              /* initialise loop counter

1  I = I + 1
   F = (X / (EXP(X) - 1.0)) - C
   F1 = ((1.0-X)*EXP(X) - 1.0)/(EXP(X)-1.0)**2
   ERR = F/F1
   X = X - ERR
   IF (ERR .GT. 1.0E-5) THEN
     IF (I. LT. MAXITR) GOTO 1
   END IF
   XMAX = X

C Compute constant part of yield..
EK = EEV / 1000.0   /* convert to keV
Y = DELMAX/(1.0-EXP(-XMAX))
Y = Y * (EMAX/EK)**(N-1.0)
X = XMAX * (EK/EMAX)**N /* define 'x'

C Get secondary yield for normal or isotropic incidence
IF (ITYPE .LT. 0) THEN
  Y = Y * (1.0 - EXP(-X))
ELSE
  Y = Y * (2.0/X) * (X + EXP(-X) - 1.0)
END IF

C Finish off..
DELTA = Y
RETURN
END

```

References

- [1] K. Knott, The Equilibrium Potential of a Magnetospheric Satellite in an Eclipse Situation, *Planet & Space Science*, 20, pp 1137-1146, January 1972.
- [2] S.E. DeForest, Spacecraft Charging at Synchronous Orbit, *J. Geophys. Res.*, 77, pp 651-659, 1972.
- [3] R.C. Olsen, C.E. McIlwain and E.C. Whipple, Observations of Differential Charging Effects on ATS-6, *J. Geophys. Res.*, 86, p6809, 1981.
- [4] C.K. Purvis, H.B. Garrett and N.J. Stevens, Design Guidelines for Assessing and Controlling Spacecraft Charging Effects, NASA Technical Paper 2361, 1984.
- [5] C. Kalweit and A. Pitt, Electromagnetic Cleanliness - An Important Characterisation of the GEOS Satellite, *ESA Bulletin 9*, May 1977, pp 28-34.
- [6] J.H. Allen and D.C. Wilkinson, NGDC Satellite Anomaly Data Base and Solar Terrestrial Activity, IFAC Workshop on Electrostatic Charges and Discharges and Cosmic Ray Interactions in Satellites, Paris, France, 15-17th December 1986, pp 93-119.
- [7] E.J. Daly, Simulations of the Electrostatic Charging of ESA Communications Satellites, *ESA STM-239*, December 1987.
- [8] D. Breton, The Meteosat System and its Missions, *ESA Bulletin 11*, Dec 1977, pp 11-15.
- [9] D. Leverington, The Meteosat Space Segment, *ESA Bulletin 11*, December 1977, pp 20-27.
- [10] M. Reynolds, Meteosat's Imaging Payload, *ESA Bulletin 11*, Dec 1977, pp 28-33.
- [11] A. Robbins, Meteosat Spacecraft Charging Investigations, *ESA Contract 3561/78F/GG/SC*, Final Report, 1979.
- [12] A.D. Johnstone, G.L. Wrenn, H.E. Huckle, and R.F. Scott, Meteosat F2 Spacecraft Charging Monitors, *ESA Contracts 4715/81 and 5911/84* Final Report, November 1985.
- [13] G.L. Wrenn and A.D. Johnstone, Spacecraft Charging : Meteosat Experience, "The Aerospace Environment at High Altitudes and its Implications for Spacecraft Charging and Communications", *AGARD Conference Proceedings*, No. 406.
- [14] G.L. Wrenn, A.D. Johnstone, D.N. Baker and R. Robinson, Meteosat Spacecraft Anomalies : High Energy Electron Effects?, *IFAC Workshop, CNES Paris*, Dec 15-17 1986.
- [15] L. Levy and D. Sarrail, Comparative Study of Two Configurations of Thermal Shields Tested in a Simulated Geomagnetic Substorm Environment, *ONERA/DERTS CR/REV/06* July 1978.
- [16] M. Andrau and G. Burle, Meteosat P1 Arcing Tests, *Aerospatiale 2683/83 TGA*, September 1978.
- [17] D. Hoge and D. Leverington, Investigation of Electrostatic Discharge Phenomena on Meteosat Spacecraft, *ESA Journal 1979*, Vol 3.

- [18] M. Frezet, J.P. Granger and L. Levy, Assessment of Charging Behaviour of Meteosat Satellite in Geosynchronous Environment, IEEE Trans. Nucl. Sci., NS-35, No. 6, December 1988.
- [19] M.J. Mandell, P.R. Stannard and I. Katz, NASCAP Programmers Reference Manual, NASA Contract no. 22826, Revised under contract 23058, March 1984.
- [20] M. Frezet, Computer Aided Analysis of the Electrostatic Behaviour of a Geostationary Satellite, IFAC Workshop, Paris, Dec 1986, pp 229-251.
- [21] J. Pantazis, A. Huber and M.P. Hagan, Design of the Electrostatic Analyzer SSJ/3, AFGL-TR-77-0120, April 1970.
- [22] A.J. Sims, Processing of the Meteosat F2 Spacecraft Charging Data, RAE Working Paper SP(87)WP44, December 1987.
- [23] J.A. Bittencourt, Fundamentals of Plasma Physics, Pergamon, 1986. ISBN 0-08-033923-9.
- [24] G. Medicus, Theory of Electron Collection of Spherical Probes, J. App. Phys., 32, 12, pp 2512-2520, December 1961.
- [25] H. Mott-Smith and I. Langmuir, Collectors in Gaseous Discharges, Phys. Rev. 28, p727, 1926.
- [26] G.L. Wrenn, Ph.D Thesis, University College London, 1966.
- [27] J. Rubinstein and J.G. Laframboise, Theory of a Spherical Probe in a Collisionless Magnetoplasma, Phys. Fluids, 25, p1174, 1982.
- [28] L. Austin and H. Starke, Uber die Reflexion der Kathodestrahlen und eine damit verbundene neue Erscheinung sekundarer Emission, Ann. Physik. Lpz., 9, p271, 1902.
- [29] I. Katz, M. Mandell, G. Jongeward and M.S. Gussenhoven, The Importance of Accurate Secondary Electron Yields in Modelling Spacecraft Charging, J. Geophys. Res. 91, A12, pp 13739-13744, December 1986.
- [30] R.C. Alig and S. Bloom, Secondary Electron Escape Probabilities, J. App. Phys., 49, 3476, 1978.
- [31] O. Hachenberg and W. Brauer, Secondary Electron Emission from Solids, Adv. Electronics and Electron Physics, 11, pp 413-499, 1959.
- [32] G.F. Dionne, Effects of Secondary Electron Scattering on Secondary Emission Yield Curves, J. Appl. Phys., 44, 12, pp 5361-5364, December 1973.
- [33] G.F. Dionne, Origin of Secondary Electron Emission Yield Curve Parameters, J. Appl. Phys. 46, 8, pp 3347-3351, August 1975.
- [34] E.C. Whipple, Potentials of Surfaces in Space, Rep. Prog. Phys, Vol 44, 1981, pp 1197-1250.
- [35] I. Katz, D.E. Parks, M.J. Mandell, J.M. Harvey, D.H. Brownell, S.S. Wang and M. Rotenberg, A Three Dimensional Dynamic Study of Electrostatic Charging in Materials, NASA CR-135256, August 1977.
- [36] S. Ono and K. Kanaya, The Energy Dependence of Secondary Emission Based on Range-Energy Retardation Power Formula, J. Phys. D: App. Phys. 12, pp 619-632, 1979.

- [37] E.A. Burke, Secondary Emission from Polymers, IEEE Trans. Nucl. Sci. NS-27, p 1760, 1980.
- [38] R. Kollath, Handbuch. der Physik, Vol 21, p232, 1956.
- [39] H. Bruining and J.H. de Boer, Secondary Electron Emission Part I; Secondary Electron Emission from Metals, Physica, 5, 17, pp 901-913, 1938.
- [40] H. Bruining, Physics and Applications of Secondary Electron Emission, Pergamon Press, London, 1954.
- [41] A.J. Dekker, Secondary Electron Emission, Solid State Physics, 6, p251, 1958.
- [42] R.F. Willis and D.K. Skinner, Secondary Electron Emission Yield Behaviour of Polymers, Solid State Communications, 13, p685, 1973.
- [43] T.L.Matskevitch, Fiz. Tverd. Tela. Adad. Nauk, SSSR, 1, p277, 1959.
- [44] L. Levy, D. Sarraill, J.M. Siguiet, Conductivity and Secondary Emission Properties of Dielectrics as Required by NASCAP, Proc. 3rd. Int. Symposium on Spacecraft Materials in Space Environment, Noordwijk, Netherlands, ESA-SP-232, November 1985.
- [45] S. Gair, Electron Backscattering and Secondary Yield Measurements, Proc. IEEE Conf. Nucl. Space rad. Effects, July 1974, p177.
- [46] R. Warnecke, Emission Secondaire des Metaux Purs, J. Phys. Radium, 7, p270.
- [47] T.E. Everhart, J. App. Phys. 31, pp 1483, 1960.
- [48] G.D. Archard, J. App. Phys. 32, p1505, 1961.
- [49] W.S. McAfee, Determination of Energy Spectra of Backscattered Electrons by Use of Everhart's Theory, J. App. Phys. Vol 47, no. 3, March 1976.
- [50] E. H. Darlington and V.E. Cosslett, Backscattering of 0.5 - 10 keV Electrons from Solid Targets, J. Phys. D. 5, p1969, 1972.
- [51] R. Shimizu, Secondary Electron Yield with Primary Electron Beam of Kilolectron Volts, J. App. Phys, 45, 5, pp 2107-2111, May 1974.
- [52] P.C.R Palluel, Rediffused Component of Secondary Radiation from Metals, Comptes Rendus., Acad. Sci. Paris, 224, p1492, 1947.
- [53] E.J. Sternglass, Backscattering of Kilovolt Electrons from Solids, Phys. Rev. 95, 2, pp 345-358, 1954.
- [54] G.M. McCracken, The Behaviour of Surfaces Under Ion Bombardment, Rep. Prog. Phys. 38, pp 241-327.
- [56] B. Aarset, R.W. Cloud and J.G. Trump, Electron Emission from Metals Under High Energy Hydrogen Ion Bombardment, J. App. Phys., 25, p1365, 1954.
- [57] A.G. Hill, W.W. Buechner, J.S. Clark and J.B. Fisk, The Emission of Secondary Electrons under High Energy Positive Ion Bombardment, Phys. Rev., 55, p463, 1939.
- [58] P. Cousinie, N. Colombie, C. Fert and C. Simon, Variation du Coefficient d'emission Electronique Secondaire de Quelques Metaux

- avec l'énergie des Ions Incidentes, Comptes Rendus, 249, p387, 1959.
- [59] G. Foti, R. Potenza and A. Triglia, Secondary Electron Emission from Various Materials Bombarded with Protons at $E_p < 2.5$ MeV, Lett. al Nuovo Cim. 11, p659, 1974.
- [59] R. Baragiola, E.V. Alonso and A. Oliva Florio, Electron Emission from Clean Metal Surfaces Induced by Low Energy Light Ions, Phys. Rev., B19, no. 1, pp 121-129, 1979.
- [60] E.J. Sternglass, Theory of Secondary Electron Emission by High Speed Ions, Phys. Rev., 108, no. 1, pp 1-12, 1957.
- [61] H. Friedman, "Rocket Spectroscopy", Space Science, ed. J.P. LeGalley, p549, John Wiley, N.Y.
- [62] R.J.L. Grard, K. Knott and A. Petersen, The Influence of Photoemission and Secondary Electron Emission on Electric Field Measurements in the Magnetosphere and Solar Wind, "Photon and Particle Interactions with Surfaces in Space", ed. R.J.L. Grard, D. Reidel Co., Holland, pp 163-189.
- [63] C.W. Allen, Astrophysical Quantities, Page 171, Athlone, London.
- [64] B. Feuerbacher and B. Fitton, Experimental Investigation of Photoemission for Satellite Surface Materials, J. App. Phys., 43, p1563, 1972.
- [65] R.C. Weast, CRC Handbook of Chemistry and Physics.
- [66] K.L. Mittal, Polyimides : Synthesis, Characterisation and Applications, Volume 1, Plenum Press, New York, 1984.
- [67] J. Frenkel, On Pre-Breakdown Phenomena in Insulators and Electronic Semi-Conductors, Phys. Rev. 54, pp 647-648, 1938.
- [68] V. Adamec and J.H. Calderwood, Electrical Conduction in Dielectrics at High Fields, J. Phys. D. 8, p551, 1975.
- [69] A.R. Fredrickson, Radiation Induced Currents and Conductivity in Dielectrics, IEEE Trans. Nucl. Sci., NS-25, 6, pp 2532-2539, December 1977.
- [70] J. Cl. Debruyne and L.H. Jensen, The "UNIFLUX" System, ESTEC Working Paper 1308, July 1983.
- [71] R.W. Sillars, Electrical Insulating Materials and Their Application, P. Peregrinus Ltd., 1973.
- [72] G.L. Siscoe, The Particle Environment in Space, "Photon and Particle Interactions with Surfaces in Space", Proceedings of 6th ESLAB symposium, 26-29 Sep 1972, D.Reidel Publishing Co, Astrophysics and Space Sci. Lib, Vol 37, 1973, Ed. R.J.L. Grard, p23,
- [73] D.L. Carpenter and R.L. Smith, Whistler Measurements of Electron Density in the Magnetosphere, Rev. Geophysics, 2, p415, 1964.
- [74] C.R. Chappell, K.K. Harris and G.W. Sharp, A Study of the Influence of Magnetic Activity on the Location of the Plasmapause as Measured by OGO5, J. Geophys. Res., 75, pp 50-56, 1970.
- [75] C.R. Chappell, K.K. Harris and G.W. Sharp, The Dayside of the Plasmasphere, J. Geophys. Res., 76, pp 7632-7647, 1971.

- [76] L.A. Frank, Relationship of the Plasmasheet, Ring Current, Trapping Boundary and Plasmopause Near the Magnetic Equator and Local Midnight, *J. Geophys. Res.*, 76, p2265, 1971.
- [77] V.M. Vasyliunas, A Survey of Low Energy Electrons in the Evening Sector of the Magnetosphere With OGO1 and OGO3, *J. Geophys. Res.*, 73, p2839, 1968.
- [78] V.M. Vasyliunas, Low Energy Electrons on the Dayside of the Magnetosphere, *J. Geophys. Res.*, 73, p7519, 1968.
- [79] J.M. Grebowsky and A.J. Chen, Effects on the Plasmasphere of Irregular Electric Fields, *Planet & Space Sci.*, 24, p689, 1976.
- [80] C.F. Kennel, Consequences of a Magnetospheric Plasma, *Reviews of Geophysics*, 7, p379, 1969.
- [81] J.W. Dungey, The Structure of the Exosphere or Adventures in Velocity Space, "Geophysics and the Earth's Environment", ed C. DeWitt, J. Hieblot and A. Lebeau, Gordon & Breach, NY, 1963.
- [82] S.W.H. Cowley, Magnetic Reconnection, SERC Summer School Lecture Notes, Royal Holloway and Bedford New College, September 1987.
- [83] Z.V. Lewis, S.W.H. Cowley and D.J. Southwood, Impulsive Energization of Ions in the Near-Earth Magnetotail During Substorms, *Planet & Space Sci.*, 38, no. 4, pp 491-505, 1990.
- [84] C.T. Russell and R.L. McPherron, The Magnetotail and Substorms, *Space Science Reviews*, 15, p 205, 1973.
- [85] F.F. Chen, Introduction to Plasma Physics and Controlled Fusion, Volume 1, Plenum Press, New York, 1984.
- [86] J.G. Roederer, Dynamics of Geomagnetically Trapped Radiation, *Physics & Chemistry in Space*, Volume 2, Springer-Verlag.
- [87] G. Rostoker, Geomagnetic Indices, *Reviews of Geophys. & Space Phys*, Vol 10, no. 4, pp 935-950, November 1972.
- [88] J. Bartels, The Standardized Index, Ks and the Planetary Index, Kp, International Union of Geodesy and Geophysics, IATME Bulletin number 126, p97, 1949.
- [89] J.K. Hargreaves, The Upper Atmosphere and Solar-Terrestrial Relations, Van Nostrand Reinhold, 1979, ISBN 0-442-30216-9.
- [90] T.N. Davies and R. Parthasarathy, The Relationship Between Polar Magnetic Activity DP and Growth of the Geomagnetic Ring Current, *J. Geophys. Res.*, 72, p 5825, 1967.
- [91] G.L. Wrenn, Time-Weighted Accumulations $ap(\tau)$ and $Kp(\tau)$, *J. Geophys. Res.*, 92, A9, pp 10125-10129, September 1987.
- [92] G.L. Wrenn and A.J. Sims, The EQUIPOT Charging Code, RAE Working Paper SP(30)WP37, 1990.
- [93] R.D. Reeves and K.G. Balmain, Two-Dimensional Electron Beam Charging Model for Polymer Films, *IEEE Trans. Nucl. Sci*, NS-28, 6, p 4547, 1981.
- [94] Solar-Geophysical Data, Part 453I, May 1982 to Part 514I, June 1987, U.S. Dept. of Commerce, Boulder, Co, USA, 80303.
- [95] G.L. Wrenn, Linear Fit Coefficients for Least Squares Fitting, Unpublished Communication.

- [96] Solar-Geophysical Data, Part 554II, p27, October 1990, U.S. Dept. of Commerce, Boulder, Co, USA, 80303.
- [97] H. Volland, A Semi-Empirical Model of Large-Scale Magnetospheric Electric Fields, J. Geophys. Res., 78, p171, 1973.
- [98] M.J. Duck and D. Verdin, Investigation of the Spacecraft Charging Phenomenon; Part VII : The Design and Construction of a Large ESD Test Facility, AERE-R 13064, June 1988.
- [99] A.J. Sims and J. Troim, BEAM Simulations of NDRE Charging Experiments, RAE Working Paper (in press).
- [100] C. Grey-Morgan, Fundamentals of Electric Discharges in Gases, Handbook of Vacuum Physics Vol 2, Part 1, Ed. A.H. Beck, Pergamon, 1965.
- [101] R.O. Jenkins and W.G. Trodden, Electron and Ion Emission from Solids, Routledge & Kegan-Paul, London, 1965.
- [102] American Society for Testing and Materials, Standard Methods of Test for Electrical Resistance of Insulating Materials, ASTM Designation D257-66.
- [103] R.A. Fouracre, G. Leondopoulos and R.I. Frame, Effects of Solvents on Surface Resistivity Measurement of Polymer Films, Polymer Testing, 7, pp 85-90, 1987.
- [104] M.S. Gussenhoven and E.G. Mullen, Geosynchronous Environment for Severe Spacecraft Charging, J. Spacecraft & Rockets, 20, no 1, pp 26-34.
- [105] R.C. Olsen, A Threshold Effect for Spacecraft Charging, J. Geophys. Res., 88, pp 493-499, 1983.
- [106] U. Fahleson, Plasma-Vehicle Interactions in Space; Some Aspects on Present Knowledge and Future Developments, Photon and Particle Interactions with Surfaces in Space, Ed. R.J.L. Grard, pp 563-9, D. Reidel, 1973.
- [107] E.C. Whipple, Observations of Photoelectron and Secondary Electrons Reflected from a Potential Barrier in the Vicinity of ATS-6, J. Geophys. Res., 81, pp 715-719, 1976.
- [108] H.B. Garrett, Review of Quantitative Models of the 0-100 keV Near-Earth Plasma, Reviews of Geophysics & Space Physics, 17, 1979, pp 397-417.
- [109] E.G. Mullen and M.S. Gussenhoven, High Level Spacecraft Charging Environments near Geosynchronous Orbit, AFGL-TR-82-0063, Feb 1982.
- [110] E.G. Mullen, Status Report on the CRRES/SPACERAD Program, Proc. ESA Space Env. Analysis Workshop, ESA WPP-23, 9-12 October 1990.
- [111] H. von Seggern, Charging Dynamics of Dielectrics Irradiated by Low Energy Electrons, IEEE Trans. Nucl. Sci., NS-32, no. 4, August 1985.